THE INFRARED SPECTROSCOPY OF NiCO, $Ni(CO)_3(^{13}CO)$, AND $Ni(CO)_3(C^{18}O)$ AND RESONANT TWO-PHOTON IONIZATION SPECTROSCOPY OF ZrF, ZrCl, AND PdSi

by

Alonzo Martinez

A dissertation submitted to the faculty of
The University of Utah
in partial fulfillment of the requirements for the degree of

Doctor of Philosophy

Department of Chemistry

The University of Utah

December 2012

Copyright © Alonzo Martinez 2012

All Rights Reserved

The University of Utah Graduate School

STATEMENT OF DISSERTATION APPROVAL

The dissertation of **Alonzo Martinez**

has been approved by the following supervisory committee members:

Michael D. Morse	, Chair	**08/16/2012** Date Approved
Peter B. Armentrout	, Member	**08/16/2012** Date Approved
Michael H. Bartl	, Member	**08/16/2012** Date Approved
John C. Conboy	, Member	**08/16/2012** Date Approved
Christoph Boehme	, Member	**08/16/2012** Date Approved

and by **Henry S. White** , Chair of the Department of **Chemistry**

and by Charles A. Wight, Dean of The Graduate School.

ABSTRACT

Infrared and resonant two-photon ionization spectroscopy were employed to study the bonding and electronic structure of small gas phase transition metal containing molecules. Rovibrational spectra of NiCO, $Ni(CO)_3(^{13}CO)$, and $Ni(CO)_3(C^{18}O)$ were collected using a pulsed-discharge slit-jet infrared diode laser spectrometer, while resonant two-photon ionization spectra were collected for ZrF, ZrCl, and PdSi. Analysis of these spectra allowed spectroscopic parameters to be determined, leading to an improved understanding of the chemical bonding in these molecules.

Spectra of NiCO, $Ni(CO)_3(^{13}CO)$, and $Ni(CO)_3(C^{18}O)$ were obtained by exciting a CO vibration in these molecules. For NiCO, band origins of 2010.69289(34) and 2010.64528(23) cm^{-1} were measured, along with values of B_0 = 0.151094(7) and 0.149597(6) cm^{-1} for ^{58}NiCO and ^{60}NiCO, respectively. These were used to determine bond lengths of r_0 (Ni-C) = 1.641(40) Å and r_0 (C-O) = 1.193(53) Å. The ground state constants determined for $Ni(CO)_3(^{13}CO)$ are υ_0 = 2022.075753(95) cm^{-1} and B" = 0.034736(2) cm^{-1}. For $Ni(CO)_3(C^{18}O)$, υ_0 = 2021.93683(18) cm^{-1} and B" = 0.033764(4) cm^{-1} are obtained. These values provide bond lengths of r_0(Ni-C) = 1.839 ± 0.007 Å and r_0(C-O) = 1.121 ± 0.010 Å.

The vibronic spectrum of ZrF revealed many bands in the range from 14700 to 18000 cm^{-1}, several of which can be grouped into three band systems. Rotationally resolved investigations are hampered by perturbations in the excited states, but three

unperturbed bands have revealed an $\Omega'' = 1.5$ ground state, and a bond length of $r_0'' = 1.858$ Å. Hot bands originating from $v'' = 1$ provide $\Delta G_{1/2}'' = 691.45(2)$ for $^{90}Zr^{19}F$. Based on comparisons to ZrCl and ligand-field considerations, the ZrF ground state is assigned as a $^2\Delta_{3/2}$. In addition to the ZrF measurements, vibronically resolved spectra of ZrCl were recorded over the 13000 to 18000 cm^{-1} range, and four band systems were identified.

Three vibronic bands of PdSi have been rotationally resolved and analyzed, two of which are perturbed by interactions with other states. The data show an $\Omega = 0$ ground state and a bond length of $r_0'' = 2.0824(3)$ Å. Comparisons to density functional (DFT) calculations strongly support a $^1\Sigma^+$ ground state assignment.

for my wife and children

TABLE OF CONTENTS

APPENDICES

LIST OF TABLES

Table

LIST OF FIGURES

Figure

ACKNOWLEDGMENTS

My journey through graduate school was filled with many people who have helped shape me into the scientist and person I am today. To these people I owe a great debt of gratitude. First, I would like to praise my wife, Mary. I came to the University of Utah seeking to further my education, and in the process found the most amazing person I have ever had the privilege of knowing. Without Mary's love, support, and patience I would not be celebrating my accomplishment with this letter of acknowledgments. For everything that you have done and for who you are, the least I can say is thank you. I love you.

Next, I have to thank Michael Morse. Michael has a great love for spectroscopy and a talent for being able to distill a complex subject into something that is easy to understand, two qualities that led me to join his research group. I would like to express my sincerest gratitude to Michael for accepting me into his research group, always making himself available to answer questions, and for having enough confidence in me to suggest my name when someone was needed to teach the Advanced Physical Chemistry Lab course. Without his help and support the Advanced P-Chem Lab would not have been as successful. I shall always remember Michael's dedication to teaching, as well as his infectious excitement for being among the first people to see a spectrum, an attitude I will carry with me moving forward.

I am also grateful to all of my friends in the Morse group, Maria Garcia, Olha Krechkivska, Ned Lindholm, Ramya Nagarajan, Dan Matthew, Sergei Aksyonov, and Eric Johnson. I am very thankful for their help, friendship, encouragement, and support over these past few years. From this group of people, I owe a special thanks to Maria Garcia. The friendship we developed from the many ups and downs inherent with graduate school is special and something I would not trade for anything.

I would also be remiss in not acknowledging Dale Heisler, Ron Jones, Dennis Romney, and Jeff Welsh. The data I collected and present in this dissertation would have been gathered much more slowly without their help. I will always remember these individuals for their friendliness, willingness to teach, and frequent help with broken instrumentation.

Lastly, I must give thanks to my parents, family, and core group of friends in Los Angeles. The support, encouragement, and confidence they provided over the years have been a great source of motivation. I would not be where I am today if it were not for the roles these people have played in my life.

CHAPTER 1

INTRODUCTION

1.1 Introduction

Spectroscopy, the study of the interaction between matter and electromagnetic radiation, has played a pivotal role in our modern understanding of the world, our sun, distant stars, and interstellar space. The origins of spectroscopy can be traced back to 1670 – 1672, when Sir Isaac Newton used a glass prism to disperse the white light from the sun into a continuous series of colors. In 1802, William Hyde Wollaston discovered dark lines in the solar spectrum.[1] Joseph von Fraunhofer rediscovered these lines after his invention of the spectroscope in 1814.[2] In his studies, Fraunhofer realized that the positions of these lines are characteristic of the solar spectrum. Even though Fraunhofer did not understand what gave rise to the observed spectral lines, he saw the importance of these features as landmarks and mapped out several hundred of them.[2-4] In 1860, Gustav Kirchhoff and Robert Bunsen theorized that the sun is surrounded by layers of gases that give rise to the dark lines found in the solar spectrum.[5-7] They came to this hypothesis after recognizing each element had a characteristic spectrum and found the position of Fraunhofer's dark lines matched the emission spectra of heated terrestrial elements.[3,5-7] Although the ability of an element to absorb and emit electromagnetic radiation in a specific pattern was known at the time, it could not be explained. Nevertheless, the

findings of these individuals laid the foundation for the entire science of spectroscopic analysis.

In an attempt to gain better insight into the relationship between matter and electromagnetic radiation, Kirchhoff introduced the notion of a blackbody.[8] A blackbody was defined as an idealized object that at any temperature will completely absorb all frequencies of radiation falling upon it, and which emits a continuous spectrum of radiation.[9] Blackbodies provide the simplest test case for the study of the interaction between radiation and matter, namely one in which there is no dependence on the material of the blackbody. It was soon discovered that classical physics failed to fit the experimental emission spectrum of a blackbody at short wavelengths, leading to what was termed "the ultraviolet catastrophe."[9] In 1900 Max Planck proposed a solution to the frequency distribution for blackbody radiation.[8-10] At the time, the energy in an electromagnetic field oscillating at a certain frequency was thought to be a continuous variable. Planck reluctantly abandoned this notion and treated the energy emitted by a blackbody to be quantized, relying on Ludwig Boltzmann's, Josiah Gibb's, and James Maxwell's statistical approach to thermodynamic properties to obtain an expression for the energy density per unit frequency emitted by the black body.[3,5,11] The solution Planck proposed was

$$\rho_{\nu}(T)d\nu = \frac{8\pi h}{c^3}\frac{\nu^3 d\nu}{e^{\frac{h\nu}{k_B T}} - 1}, \tag{1.1}$$

where ρ is the radiant energy density between the frequency ν and $\nu + d\nu$ at temperature T, c is the speed of light, k_B is Boltzmann's constant, and h is Planck's quantization

constant.[9] Even though Planck's revolutionary statement considered light to be in the form of discrete energy packages, he believed that these discrete packages arose solely from the "resonators" (simple harmonic oscillators) in the walls of the blackbody.[5,11] A few years later, a yet unknown Albert Einstein advanced Planck's quantum hypothesis with his studies on the photoelectron effect, another problem confronting classical physics.

Heinrich Hertz first observed the photoelectron effect in the late nineteenth century.[9,12] In this phenomenon, whether or not electrons are emitted from a metal surface illuminated with visible or ultraviolet light is dependant only on the frequency of the electromagnetic radiation and not its intensity. Furthermore, the maximum kinetic energy of the emitted electrons also depends only on the frequency and not the intensity of the radiation. Classical physics predicts that the energy of the emitted electron should increase with the intensity of the incident radiation. Furthermore, in classical physics the emission of electrons was expected regardless of the radiation frequency, as long as the intensity was sufficiently high.[9] This, however, was not what was observed. Not until Einstein proposed that light is quantized and particle-like was a proper explanation of the photoelectron effect experiment provided.[13] With these assumptions it was possible to think of electromagnetic radiation as carrying a discrete amount of energy that, when large enough, could overcome the electron's binding energy to the metal surface (the work function of the metal).[5,9] The equation that Einstein used to describe his hypothesis was

$$KE = \frac{1}{2}mv^2 = h\nu - \phi, \tag{1.2}$$

where the left portion of this equation is the kinetic energy with which the electron is emitted, $h\nu$ is the energy of the incident light, and ϕ is the work function of the metal.[9] With this equation, Einstein described the emission of an electron from a metal surface illuminated with light, showing that it is only dependent on the frequency of the incident radiation and not the intensity of the light. An increase in the light intensity only results in a larger number of electrons being emitted, provided, of course, that the light has enough energy to overcome the work function of the metal. Even though the solutions put forth by Planck and Einstein fit the experimental observations, their notions of quantization were resisted at first. Ultimately, it was the insight provided in these studies that led to an avalanche of scientists attempting to understand the world though a new set of quantized glasses.

Although the developmental history of quantum theory is fascinating, it is not the main topic of this thesis. The previous paragraphs were given only to briefly summarize the origins of spectroscopy and present its importance in the history of science. Although the development of quantum theory could have been initiated through other avenues, such as the diminishing of specific heats at low temperatures,[5] it was spectroscopic studies that paved the way to its establishment and eventual acceptance. Following the development and acceptance of quantum theory by the scientific community, the theory has been used extremely successfully to explain the nature and behavior of matter on a molecular, atomic, and subatomic level.

Over the last few decades, spectroscopy has creatively been applied to answer various questions about molecular structure and dynamics. The advancements made in the interpretation of molecular spectra have made spectroscopy one of the preferred

methods for determining molecular structure. Proton and ^{13}C nuclear magnetic resonance (NMR), microwave/millimeter wave spectroscopy, and infrared spectroscopy are all techniques commonly used to establish the structure of long-lived molecules. However, if the molecule under investigation is highly reactive, a custom spectrometer must be built to allow the molecule to survive long enough to be analyzed. Research in the Morse group at the University of Utah focuses on such reactive compounds. Custom spectrometers, such as the infrared (IR) and resonant two-photon ionization (R2PI) spectrometers discussed in Chapter 2 of this dissertation, allow for the characterization of highly reactive complexes that could not be studied under normal atmospheric conditions.

Although not all spectroscopic techniques use lasers as a light source, many do. When lasers were first developed they were fixed in frequency, severely limiting their applications in spectroscopy. The introduction of tunable lasers, such as dye lasers, greatly expanded the scope of measurements that became available to scientists. The high intensity and narrow spectral linewidth that is inherent to laser light has stimulated a great deal of interest in atomic and molecular spectroscopy. Depending on the resolution of the laser spectrometer, it is possible to probe the electronic, vibrational, or rotational structure of a molecule. The study of electronic motion has led to a better understanding of the electronic structure of atoms and molecules. From studies of vibrational motion in molecules, it is possible to identify the chemical groups within the molecule and to determine the forces between atoms. Lastly, from investigations of the rotational energy levels it is possible to obtain bond lengths and the geometrical structure for a molecule.

The laser spectroscopic studies carried out in the Morse group allow electronic, vibrational, and rotational information to be obtained, depending on the resolution of the

laser. In this lab we are interested in elucidating the nature of the bond between a transition metal and another chemical species. The goal of this research is not the mere compilation of large quantities of data in a convenient table format. Rather, the goal is to generate useful information that provides insight into the nature of these molecules.

1.2 Dissertation Outline

This dissertation is divided into five different chapters and three appendices. The first chapter provides an introduction to the subject and explains why the general categories of molecules studied are of importance. The second chapter focuses on the IR and R2PI spectrometers that were used in these studies, describing their construction and use. This chapter was written in such a way that it would be most beneficial to a spectroscopic novice. With this in mind, an effort was made to describe each instrument from first principles. Because I was responsible for the design and assembly of the IR spectrometer, I felt it necessary to describe the rationale as to why certain materials or parts were used in the instrument. The next set of chapters presents the studies that have been published using these techniques.

Chapters 3 presents spectroscopic results on NiCO, $Ni(CO)_3(^{13}CO)$, and $Ni(CO)_3(C^{18}O)$. Transition metal carbonyls and their reactive intermediates (unsaturated transition metal carbonyls) have received a great deal of attention due to their importance in catalytic processes.[14-17] Stable transition-metal carbonyls such as $Cr(CO)_6$, $Ni(CO)_4$, and $Fe(CO)_5$ are often used as starting materials in organometallic syntheses.[18] Transition metal carbonyls such as these have been studied extensively in solid and solution-phase experiments.[19,20] Despite the countless experiments that have been conducted on these molecules, a detailed understanding of their reaction chemistry is

incomplete. This is mainly because the unsaturated transition metal carbonyls that are often reaction intermediates readily elude detection due to their small concentrations. In order to gain more insight on the unsaturated transition metal carbonyls, the construction of a high-resolution IR spectrometer was undertaken to study these molecules in the gas phase, where they are isolated from interaction with their environment.

The fourth chapter of this dissertation provides the results obtained for ZrF and ZrCl when studied with the R2PI instrument. Spectroscopic studies of transition metal halides have been an active area of research because of their role as precursors to other organometallic compounds, such as ferrocene,[21] in catalysis,[22] in the industrial purification of metals,[23] and in astrophysics. To date, no transition metal halides have been identified in interstellar space.[24] However, some metal halides (NaCl, KCl, AlCl, and AlF) have been identified in the atmosphere of the carbon star IRC +10216, leaving hope that one-day transition metal halides may be found.[25-27] This optimism arises because of the relative high abundance of transition metal elements in stars.[28] On a theoretical level, transition metal monohalides have been investigated because they provide the simplest models to test the applicability of ligand field theory to other unsaturated metal molecules.[29-32]

Lastly, Chapter 5 presents the results obtained in a study of PdSi. Transition metal silicides are of interest because of their potential use in industrial applications. In particular, these molecules show a great deal of promise because of their relative hardness, favorable electronic properties, high melting points, and chemical resistance to oxidation.[33-35] When compared to a metal such as chromium (hardness of 935 kg/mm^2) or nickel (hardness of 557 kg/mm^2), transition metal silicides, such as $MoSi_2$ (hardness of

1200 kg/mm^2), have been found to be more scratch resistant.[34] Transition metal silicides have also successfully been used in Schottky barrier devices.[33,34] Finally, when placed in an oxidizing environment, transition metal silicides have been found to be highly stable, making them possible candidates for protective coatings.[34]

The final section of this thesis contains three appendices. The information in Appendix A contains detailed electrical diagrams for components used in the infrared spectrometer. Appendixes B and C contain the detailed spectroscopic data that were collected for zirconium fluoride and chloride and palladium silicide, respectively.

1.3 References

[1] T. H. Pearson and A. J. Ihde, Journal of Chemical Education **28** (5) (1951).

[2] M. W. Jackson, *Spectrum of Belief: Joseph von Fraunhofer and the Craft of Precision Optics*. (MIT Press, Cambridge, 2000).

[3] H. E. White, *Introduction to Atomic Spectra*. (McGraw-Hill Book Company, Inc., New York, 1934).

[4] F. A. Jenkins and H. E. White, *Fundamentals of Optics*, 4th ed. (McGraw-Hill, 1981).

[5] E. G. Steward, *Quantum Mechanics It's Early Development and the Road to Entanglement and Beyond*, 2nd ed. (Imperial College Press, London, 2012).

[6] G. Kirchhoff, Annalen der Physik **185** (1) (1860).

[7] G. Kirchhoff, Annalen der Physik **185** (2) (1860).

[8] T. S. Kuhn, *Blackbody Theory and the Quantum Discontinuity: 1894-1912*. (Oxford University Press, New york, 1978).

[9] D. A. McQuarrie and J. D. Simon, *Physical Chemistry A Molecular Approach*. (University Science Books, 1997).

[10] M. Planck, Annalen der Physik **4** (1901).

[11] G. Gamow, *Thirty Years that Shook Physics*. (Doubleday & Company, Inc., New York, 1966).

[12] H. Hertz, Annalen der Physik **267** (8) (1887).

[13] A. Einstein, Annalen der Physik **17** (6) (1905).

[14] M. Torrent, M. Sola, and G. Frenking, Chem. Rev. **100** (2000).

[15] J. C. Mitchener and M. S. Wrightion, J. Am. Chem. Soc. **103** (1981).

[16] W. Tumas, B. Gitlin, A. M. Rosan, and J. T. Yardley, J. Am. Chem. Soc. **104** (1982).

[17] R. L. Whetten, K. J. Fu, and E. R. Grant, J. Am. Chem. Soc. **104** (1982).

[18] L. S. Hegedus, *Transition Metal in the Synthesis of Complex Organic Molecules*. (University Science Books, California, 1999).

[19] M. Wrighton, Chem. Rev. **74** (1974).

[20] N. Greenwood and A. Earnshaw, *Chemistry of the Elements*. (BH, Boston, 1998).

[21] T. J. Kealy and P. L. Pauson, Nature **168** (1951).

[22] K. Fagnou and M. Lautens, Angewandte Chemie (International ed. in English) **41** (1) (2002).

[23] Y. Waseda and M. Isshiki, *Purification Process and Characterization of Ultra High Purity Metals: Application of Basic Science to Metallurgical Processing*. (Spinger, New York, 2002).

[24] R. S. Ram and P. F. Bernath, J. Mol. Spectrosc. **186** (1), 113 (1997).

[25] J. Cernicharo and M. Gue´lin, Astron. Astrophys. **183**, L10 (1987).

[26] E. Hirota, Annu. Rep. Prog. Chem., Sect. C: Phys. Chem. **96** (2000).

[27] L. M. Ziurys, A. J. Apponi, and T. G. Phillips, Astrophys. J. **433** (1994).

[28] J. E. Ross and L. H. Aller, Science **191** (4233) (1976).

[29] L. A. Kaledin, A. L. Kaledin, and M. C. Heaven, Journal of Molecular Spectroscopy **179** (2), 246 (1996).

[30] L. A. Kaledin, J. E. McCord, M. C. Heaven, and R. F. Barrow, Journal of Molecular Spectroscopy **169** (1), 253 (1995).

[31] J. T. Hougen, G. E. Leroi, and T. C. James, Journal of Chemical Physics **34**, 1670 (1961).

[32] G. K. Rothschopf and M. D. Morse, Journal of Physical Chemistry A **109** (50), 11358 (2005).

[33] S. P. Murarka, Ann. Rev. Mater. Sci. **13**, 117 (1983).

[34] S. P. Murarka, *Silicides for VLSI Applications*. (Academic Press, 1983).

[35] E. R. Corey, J. Y. Corey, P. P. Gaspar, and Editors, *Silicon Chemistry*. (Ellis Horwood Ltd., Chichester, UK, 1988).

CHAPTER 2

EXPERIMENTAL METHODS

2.1 Introduction

The Morse group specializes in the spectroscopic investigation of small gas phase transition metal containing molecules. The molecules of interest to this research group typically contain no more than two or three atoms, but systems with as many as nine atoms have been studied. The end result of a spectroscopic investigation is a spectrum that maps the energy levels, eigenstates, for the molecular system of interest. From this spectrum certain other properties, such as bond lengths (r) and rotational constants (B), for the ground and excited state of the molecule can be extracted. To obtain this information, all the spectroscopic techniques must allow for the interaction of electromagnetic radiation with matter, where the absorption of a photon by a single molecule occurs. The various spectroscopic techniques used in this lab allow the absorption of photons to be monitored through either direct or indirect means. Out of the three techniques currently available in the Morse group, the resonant two-photon ionization (R2PI) and laser induced fluorescence (LIF) instruments indirectly monitor the absorption of the probing radiation. The tunable diode laser infrared (IR) spectrometer, on the other hand, directly detects the absorption of light by monitoring the intensity of laser light as it passes through a sample. This chapter discusses the experimental setup of the R2PI and IR spectroscopic techniques.

2.2 Infrared Diode Laser Spectroscopy

The initial project that I was responsible for included designing, building, and writing the data collection program for the tunable diode laser infrared spectrometer. The first set of molecules to be studied with this newly constructed IR spectrometer was the unsaturated transition metal carbonyls. These molecules were created from the vapor pressure of a commercially purchased starting product, such as $Fe(CO)_5$ or $Ni(CO)_4$, which was entrained in argon gas. The molecules of interest were studied by exciting the CO vibration of the molecule. Due to the strong IR absorptions of transition-metal carbonyls, small concentrations of the parent molecule (e.g., $Fe(CO)_5 \approx 40$ torr at room temperature and $Ni(CO)_4 < 13$ torr at -40^0C) were adequate for the experiments.

A schematic of the recently constructed IR spectrometer that was used to study the unsaturated transition metal carbonyls is displayed in Figure 2.1. The IR radiation is produced by a set of lead-salt diode lasers (purchased from Laser Components Instrument Group) and collimated with an off-axis paraboloidal (OAP) mirror. When more than one mode is active, the IR beam can be sent through a monochromator to select the mode of interest. Afterwards, partial reflections from the front and back surfaces of a 2.54 cm thick CaF_2 window are used to collect transmission fringes from a 0.048 cm^{-1} free spectral range germanium étalon and the absorption spectrum of a reference gas, either OCS or allene. Both signals are chopped at 1 kHz and detected using a lock-in detector. These data channels are used for calibration purposes. The electrical diagram for the lock-in detector is provided in Appendix A.

The remainder of the IR beam is directed through a CaF_2 window into a vacuum chamber, where it is sent into an optical multi-pass Perry cell by means of a spherical

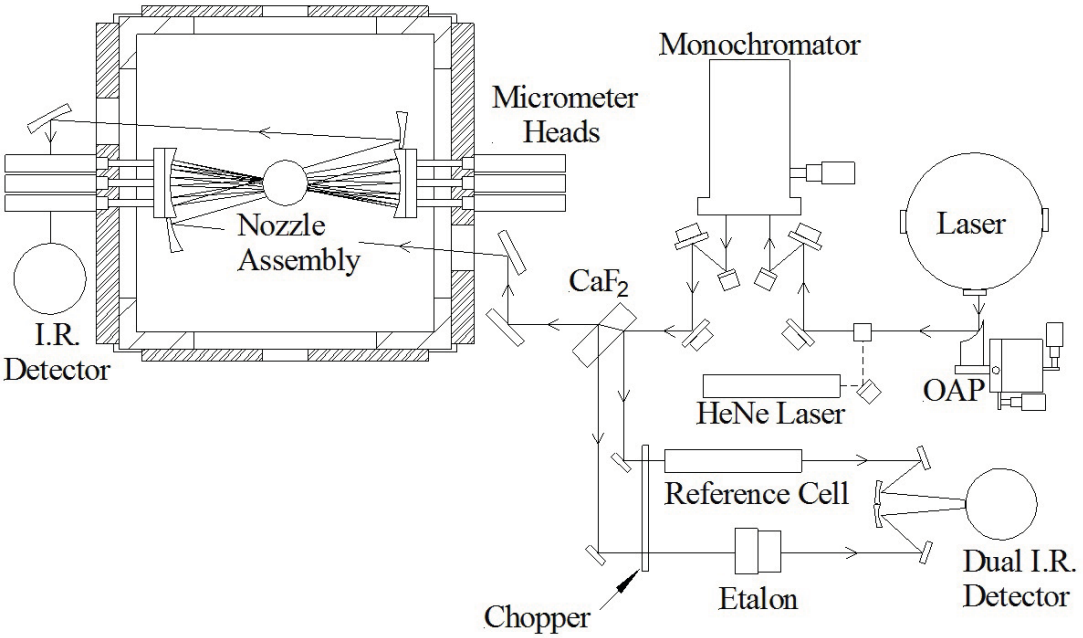

Figure 2.1 A schematic of the infrared (IR) spectrometer showing the path the light travels in an experimental cycle. The dashed lines represent the light from the HeNe laser that runs collinear to and is used to align the IR laser. The second optic that the HeNe laser strikes is a removable laser beam splitter that sends a portion of the laser light to the IR diodes and the remainder of the light to the rest of the experimental setup. The mirrors used to direct the light into the monochromator are also removable, allowing the monochromator to be bypassed.

mirror (300 mm radius of curvature). Two spherical mirrors (150 mm radius of curvature) that are fastened to kinematic mounts and separated by slightly less than twice their radius of curvature form the Perry multipass cell.[1] The nearly concentric alignment of the two mirrors of the Perry cell is achieved using Mitutoyo micrometers that have a round face and 5.08 cm of travel. In the current alignment of the cell, the IR beam is passed through the supersonic expansion 15 times. After each reflection, the IR beam is refocused at the center of the cell and traverses the length of a slit nozzle orifice. The distance between the nozzle orifice and the waist collectively formed by the reflected IR beams is set to approximately 5 mm. As the IR radiation is propagated across the slit nozzle beam, absorption of IR radiation at specific frequencies occurs as the unsaturated transition-metal carbonyls exiting the orifice cross the path of the IR beam. After the IR beam exits the Perry cell, it is collimated and directed out of the vacuum chamber with another spherical mirror (300 mm radius of curvature). Outside the chamber the beam is focused onto a HgCdTe detector, where the transmitted radiation intensity is monitored as a function of frequency. All mirrors used in the instrument are gold coated for high reflectivity (>99.9%) in the infrared. A silicon exit window, antireflection coated for the 3 – 5 μm wavelength range, is used to form the seal between the vacuum chamber and atmosphere. This acts as an IR-transmitting, visible-blocking filter that greatly reduces the amount of discharge-generated plasma radiation that reaches the detector, thereby improving the signal-to-noise ratio of the experiment. All initial alignments were carried out with a HeNe laser propagating collinear with the IR laser beam.

The frequency dependent absorbance of infrared radiation by the unsaturated transition metal carbonyls is described by Beer's law:

$$A(v) = n\ \sigma\ l. \tag{2.1}$$

In this equation n ≡ number density (molecules/cm^3), σ ≡ absorption cross-sectional area (cm^2), and l ≡ path length (cm) the light travels through the sample. A commonly sought goal in the experimental sciences is obtaining a greater signal to noise ratio. This is attainable with this experimental technique by increasing the number density of molecules and the path length, as described by Beer's law, or by decreasing the noise introduced into the signal of interest. In the interest of achieving the greatest signal to noise ratio possible, careful consideration was given to the components used in the experimental setup.

2.2.1 The Vacuum Chamber

The chamber, which has a stainless steel frame that was constructed out of 304-stainless steel and machined flanges, encloses a volume of approximately 36 L. With the use of an Edwards EH500 booster pump backed by an Edwards E2M80 rotary pump the pressure in this system is decreased to less than one millitorr. The mechanical booster pump is attached via the bottom plate of the vacuum chamber.

The remaining five sides of the vacuum chamber are sealed with flanges that were machined from 304-stainless steel, 6061-aluminum, or 7075-aluminum. The top flange of this chamber was machined from 304-stainless steel and contains an MHV feedthrough for the square wave modulated high voltage electrical discharge that is used to create the unsaturated transition metal carbonyls, a 9-pin delta connector that runs the nozzle and an optional heating tape, a VCO connection that supplies the gas to the nozzle, and the nozzle support assembly. Two flanges that lie on opposite walls of the

chamber are constructed out of 6061-aluminum and serve for viewing the interior of the chamber and venting the chamber to atmosphere. The last two flanges were machined out of 7075-aluminum and are 2.54 cm thick. Each flange is equipped with a recessed opening to accommodate the 5.08 cm diameter input and output windows for the infrared light, three ports for the Mitutoyo micrometers, and counter bored openings that can be used to attach bracing posts between these two flanges. These flanges were constructed out of 7075-aluminum and were outfitted to make use of bracing posts because of the sensitivity in the spacing between the mirrors that form the Perry multipass cell. Deflections on these flanges as small as 0.01 cm,[1] which could occur when the chamber is evacuated, have been reported to affect the alignment of the multipass cell.

2.2.2 Supersonic Expansion from a Slit Nozzle

The advent of supersonically expanded molecular beams has benefited the spectroscopist in search of molecules that are electronically, vibrationally, and rotationally cool. A molecule with cold internal degrees of freedom leads to a simplified spectrum and a larger signal-to-noise ratio, which is a result of having more molecules populating a single state. An ideal cooling scenario would place all the molecules in the v = 0 level of the electronic ground state and set the rotational temperature to 30 K or less. Meeting these conditions results in a clean vibrational spectrum and, more importantly, ensures that rotational transitions are visible and assignable. This is needed if a proper assignment of the vibronic symmetry of the two states involved in the transition is to be made.

The cooling of a molecule is accomplished by supersonically expanding it in a gas pulse of an inert monatomic gas. Implementing a slit nozzle of dimensions *L* (length) x

W (width), in which W is much greater than the mean free path (λ_0) of the monatomic gas in the reservoir, results in the gaseous molecules and atoms undergoing many collisions as they travel from the high-pressure reservoir to vacuum.[2] These collisions continue until the gas density cannot sustain further collisions. Assuming the expansion of the gas into vacuum to be adiabatic calls for the sum of the enthalpy and kinetic energy to be conserved,[2]

$$H(x) + \frac{1}{2} mu(x)^2 = \text{constant}. \tag{2.2}$$

In this equation *H* is the enthalpy and *u* is the flow velocity of a molecule at a distance (*x*) from the point of expansion. Conserving the sum of these two properties requires that the enthalpy decrease when the kinetic energy increases. The collisions that the entrained molecules experience with the monatomic gas increase their flow velocity and reduce their enthalpy. This is accomplished by relaxing the higher electronically, vibrationally, and rotationally populated levels to lower energy levels, leaving the excess energy accessible to increase the flow velocity of the molecule. The effectiveness with which each degree of freedom is cooled differs. The electronic and vibrational degrees of freedom require the molecule to undergo more energetic collisions to achieve cooling. The best place for this relaxation to occur is in the immediate vicinity of the expansion orifice, where a high density, high-pressure environment exists. As the separation between rotational levels is much less than those of electronic and vibrational levels, rotational relaxation is the easiest to achieve. The smaller collision energies required for this cooling process allow rotational relaxation to take place further downstream in the expansion, where lower energy collisions occur.

The number of molecules in the gas pulse is very dilute when compared to the concentration of the inert gas, allowing the dynamics of the expansion to be understood in terms of the pure monatomic gas. The maximum velocity the molecules in the gas pulse can reach is expressed as

$$u_{\max} = \sqrt{\frac{2C_pT_0}{m}}, \tag{2.3}$$

where C_p is the constant pressure heat capacity and T_0 is the temperature of the reservoir for the calorically perfect ideal gas.[2] For Ar and He, the monatomic gases typically used in this lab for supersonic expansion, C_p is 5/2 R. At 300 K velocities near 5.59 x 10^4 and 1.77 x 10^5 cm/sec for molecules in Ar and He, respectively, can be achieved.

The expansion of a molecular beam from a high-pressure reservoir to vacuum is said to be supersonic when the Mach number is larger than unity. The Mach number is the ratio of the flow velocity to the speed of sound of the monatomic gas. The speed of sound is given by

$$a(T) = \sqrt{\frac{\gamma RT}{m}}, \tag{2.4}$$

with γ being the ratio of C_p/C_v.[2] The cooling effect that the monatomic gas experiences when its random translational motion in the reservoir is converted to directed mass flow also decreases the speed of sound for the gas, making a supersonic expansion easily achievable.

Another relationship worth mentioning are the temperature, pressure, and density ratios between the conditions in the reservoir (T_0, p_0, ρ_0) and those at some distance from

the expansion orifice ($T(x)$, $p(x)$, $\rho(x)$). For a calorically perfect ideal gas these ratios can be expressed as

$$\frac{T(x)}{T_0} = C_s\left(\frac{x - x_0}{W}\right)^{-(\gamma-1)} \; ; \; \frac{p(x)}{p_0} = F_s\left(\frac{x - x_0}{W}\right)^{-\gamma} \; ; \; \frac{\rho(x)}{\rho_0} = G_s\left(\frac{x - x_0}{W}\right)^{-1}, \qquad (2.5)$$

in the limit of x being greater than the slit width (W).[2] In this equation C_s, F_s, and G_s are constants that are dependent on γ, and x_0 is where the expansion process begins with respect to the nozzle orifice.

A final consideration concerns the characteristics of the expansion as x approaches the length of the slit (L). In this limit the slit expansion will gradually transition to resemble that of a nozzle with a circular orifice.[2] This scenario loses the advantages that expansion from a slit orifice offers, specifically high molecular density and an absence of Doppler broadening along the axis of the slit. It is because of this limitation that the supersonically expanded molecular beam is probed 5 mm from the expansion orifice.

2.2.3 Slit Nozzle Coupled to a Square Wave Modulated Electrical Discharge

Traditionally, the Morse group has solely used nozzles that contain a circular orifice. The decision to use a nozzle with a slit orifice was made because of the advantages it provides over the circular nozzle. The first important advantage is found in the density of molecules as a function of distance from the orifice. With a slit nozzle the density of molecules falls off as $1/x$, in contrast to the $1/x^2$ dependence in a circular nozzle.[2] A second advantage found in using a slit nozzle is the evident increase in path length that is provided by an orifice that is slit-like, as opposed to a circular orifice. A

final advantage to using a slit nozzle as opposed to a circular nozzle lies in the reduction of Doppler broadening in the spectrum. This is a result of more molecules traveling with velocities perpendicular to the slit axis as they exit the nozzle orifice. The narrowing of the lines, which results from the narrowing of the velocity distribution along the slit axis, concentrates more absorbance at the line centers, making the absorption features more readily distinguished from the noise. The greater signal-to-noise ratio that a slit nozzle promises led us to use this design in the construction of our diode laser infrared spectrometer.

The slit nozzle that was implemented in these studies is formed by attaching a circular to slit orifice adapter onto a commercially purchased pulsed nozzle from General Valve Co. The circular side of the adapter was made to conjoin with the orifice of the General Valve nozzle and smoothly convert into a slit of dimensions 0.20 × 15.25 mm. The adapter was precisely machined to prevent any impedance of the gas flow and was made in two halves to ease the machining process. Once the two halves are assembled, the front surface of the attachment is equipped with a 1 mm thick piece of Teflon, which contains a slit of dimensions slightly larger than those of the slit nozzle orifice. The slotted piece of Teflon acts as an insulator between a set of electrodes and the grounded nozzle assembly. When a high negative voltage is applied to the set of electrodes, an electrical discharge is generated between the electrodes and the grounded nozzle assembly, in which electrons flow upstream into the expanding gas pulse. The high voltage is applied synchronously with the firing of the nozzle so that the parent molecule, which is entrained in the gas flow, is fragmented by electron impact excitation, resulting in the formation of the species of interest. Figure 2.2 shows a close up view of the

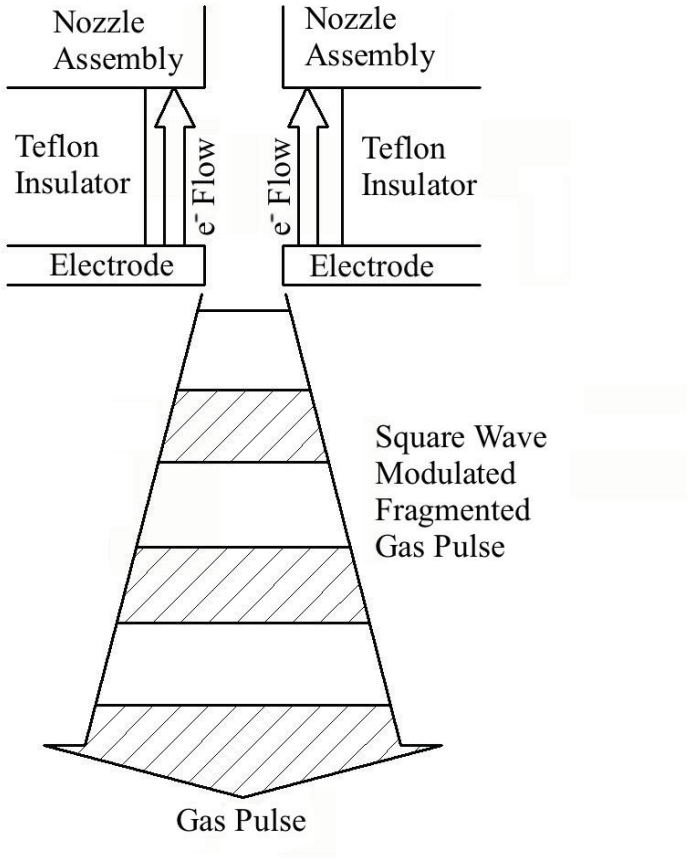

Figure 2.2 A cross-sectional view of the electrical discharge assembly along the width of the slit orifice. When a high voltage is applied to the electrodes during a nozzle pulse an electrical discharge occurs to the grounded nozzle assembly. This electrical discharge fragments the molecules carried in the gas pulse. For the duration of the nozzle pulse the electrical discharge is turned on and off to increase the signal-to-noise ratio through the use of a lock-in detector. The hashed portions of the gas pulse illustrate when the electrical discharge was turned on.

electrical discharge region and the flow direction of the electrons when a high voltage is applied to the electrodes.

Within the period of one nozzle pulse, which is approximately 2 ms in duration but can be varied with the custom-built nozzle driver, the applied high voltage is square wave modulated between on and off. This modulates the concentration of fragment molecules in the expanding gas pulse. Of course, the concentration of parent molecules is also modulated, but in the opposite sense. When the IR diode laser frequency is in resonance with a transition in the molecule of interest, the intensity of the radiation transmitted to the detector is modulated at the same frequency as the electrical discharge. The modulated absorption signal is sent to a lock-in detection system to improve the signal-to-noise ratio. The electrical diagrams of the homemade nozzle driver and lock-in detector are provided in Appendix A. The modulated electrical discharge system, as well as the rest of the instrument, is modeled after a similar apparatus developed by Scott Davis in the David Nesbitt's group at the University of Colorado, Boulder.[3]

2.2.4 Optical Multipass Perry Cell

In this instrument, the greatest increase in path length is attained by the use of a Perry multipass cell.[1] Aside from just reflecting the laser beam multiple times, the Perry cell presents an advantage over other optical multipass cells, such as the White cell.[4] This is the ability of the reflected laser beams to probe a region of gas with a higher density of molecules. Unlike the White Cell, the Perry cell focuses each reflected laser beam at the center of the cavity and as a result forms a small waist that can be placed close to the nozzle orifice, where the gas density is high. At this distance each reflected laser beam probes approximately the same volume of gas. In contrast, the reflected laser

beams in a White cell are spread over a larger area and as a consequence some of the reflected beams probe regions of gas that are not as dense as those probed by other beams,[5] as can be seen in Figure 2.3.

Alignment of the Perry cell was accomplished by determining the distance each mirror had to be placed from their supporting flange so the separation between the minima of their concave faces was twice the radius of curvature. Once this value was obtained, the diameter of a Meyer precision pin was used to set the mirrors separation to the desired distance. As the body of the vacuum chamber and the flanges were machined to be nearly parallel and position the spherical mirrors opposite each other, alignment of the spherical mirrors with the precision pins sets the mirrors extremely close to being concentric. Only small adjustments are required to bring the mirrors to a concentric alignment; at this limit the laser spot pattern on each mirror is linear. To easily couple the laser beam into the multipass cell and distinguish the individual spots on each mirror, the separation between the mirrors is decreased to be slightly less than twice the radius of curvature and a small vertical tilt is applied on one mirror. The final desired spot pattern on each mirror is illustrated in Figure 2.4.

2.2.5 Tunable Diode Infrared Laser

The collection of semiconductor lead-salt diode lasers that was employed is capable of scanning the IR region from 1930 to 2040 cm^{-1} by varying the temperature and current that is applied to the diodes. The application of certain temperatures and currents can result in multiple active longitudinal modes in the diodes; as a consequence a monochromator must be used to select the IR frequency of interest. Due to the low resolution of the monochromator, IR radiation that is within a couple of wavenumbers of

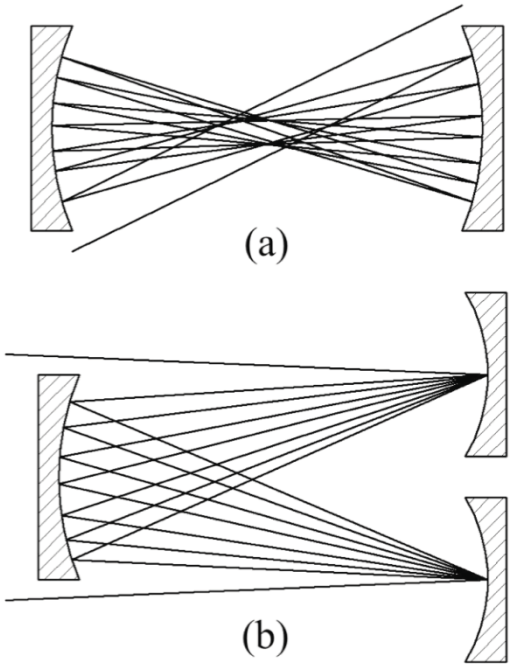

Figure 2.3 Schematics of multipass cells illustrating how the laser light is propagated through a Perry cell (a) and a White cell (b).

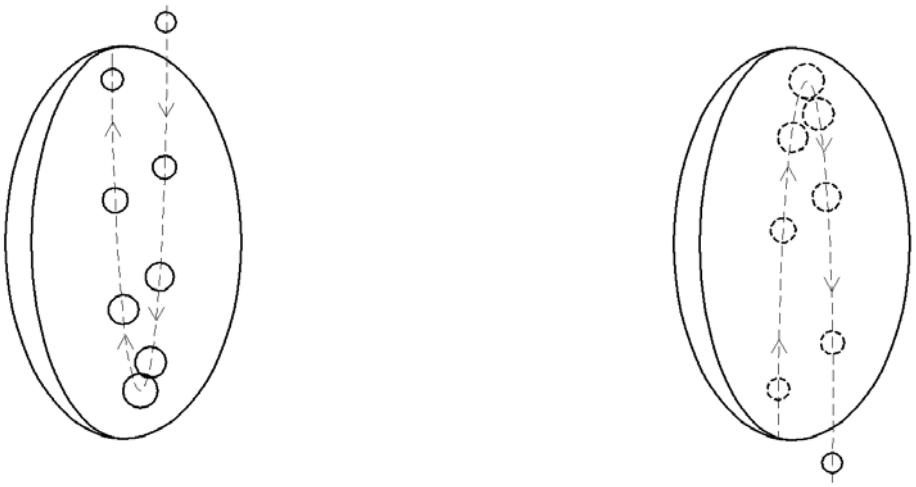

Figure 2.4 Proper alignment of the Perry multipass cell results in the illustrated spot pattern.

the desired frequency will also be allowed to exit the instrument. This ultimately limits the scanning of the laser to no more than a couple of wavenumbers at a time before adjustments must be made to the monochromator. Thus, the spectrum of a molecule of interest is collected in short segments, which are separately calibrated and pasted together to obtain a continuous spectrum.

An important consideration in any experiment using lead-salt diode lasers is the phenomenon of mode-hops. In order to gain an understanding of what a mode-hop is, it is essential to first grasp what a mode is. A continuous wave laser, such as a lead-salt diode laser, can only emit radiation for which the cavity length is a half-integer multiple of the emitted wavelength.[6] Each wavelength that satisfies this condition is said to be a laser mode, and these modes can be labeled by their half-integer multiples. The cavity in a lead-salt diode is the diode itself. As previously mentioned, when a certain temperature and current is applied to a diode it will emit radiation of a certain frequency, assuming only one mode is active. The application of this temperature and current gives rise to a certain cavity length that corresponds to the emitted frequency of IR radiation. This mode can typically be scanned no more than three wavenumbers by varying the current that is being applied to the diode. Once the condition required for oscillation of a given mode fails, the diode will cease to emit radiation on the desired mode, and radiation will be emitted on a different mode. This process is called mode-hopping, and it obviously limits the continuous range that is accessible in a given scan. In order to begin a new scan close to the termination point of the previous scan, a different diode must be used.

2.2.6 Testing the Tunable Diode Laser Infrared Spectrometer

Before any attempts to collect the spectrum for an unstudied transition metal carbonyl were undertaken, the IR spectrometer was first tested by collecting the absorption spectrum for a saturated transition metal carbonyl, a nozzle profile as the electrical discharge was fired, and the spectrum of a previously studied unsaturated transition metal carbonyl. Iron pentacarbonyl was the obvious test candidate. For this molecule, the infrared absorption spectrum collected with this instrument could be compared to the gas phase absorption spectrum of $Fe(CO)_5$ collected by Asselin *et al.*[7] and to the spectra of FeCO and $Fe(CO)_2$ collected by Tanaka *et al.*[8-11]

The first dataset that was collected with the tunable diode laser infrared spectrometer was a portion of the spectrum of the ν_6 parallel band of jet-cooled $Fe(CO)_5$ near 2038 cm^{-1}.[7] This was accomplished by blowing Ar gas over the surface of a $Fe(CO)_5$ reservoir held at room temperature. The $Fe(CO)_5$ entrained in Ar was then supersonically expanded into vacuum, where it absorbed IR radiation that was resonant with a CO vibrational transition as it crossed the path of the multipassed light beam. The resulting absorption spectrum is found in Figure 2.5. Due to the IR laser's inability to produce light that covered the complete spectral range of the ν_6 band, the peaks collected were assigned by comparing the observed peak positions (ν) to those calculated from the constants B', B'', and ν_0 reported by Asselin *et al*. using the equation:

$$\upsilon = \upsilon_0 + B'J'\left(J'+1\right) - B''J''\left(J''+1\right). \tag{2.6}$$

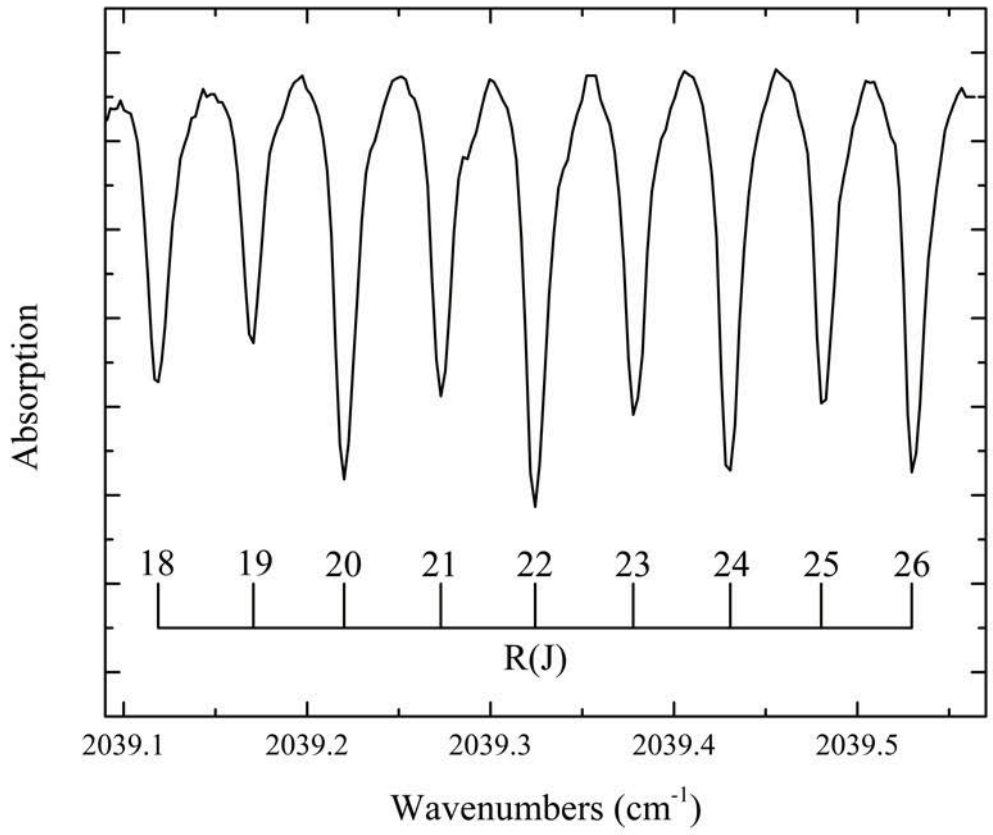

Figure 2.5 A portion of the ν_6 parallel band of $Fe(CO)_5$ that has been rotationally resolved, calibrated, and assigned. The spectrum appears upside-down because the $Fe(CO)_5$ parent molecule is being depleted in the electrical discharge.

The constants *B*' and *B*" are the rotational constants belonging to the excited and ground states of $Fe(CO)_5$, respectively. The constant ν_0 is the band origin for the molecule and *J*' and *J*" are the rotational quantum numbers for the excited and ground state.

The second test conducted on the IR spectrometer was the collection of a profile of the nozzle pulse as the electrical discharge was fired. The nozzle profile, displayed in Figure 2.6, was collected by tuning the frequency of the IR laser to the R(14) transition in the ν_6 band of $Fe(CO)_5$ at 2038.905 cm^{-1}, modulating the electrical discharge, and monitoring the transmitted laser intensity as a function of time. The oscillating reduction in the absorption intensity in Figure 2.6 is due to fragmentation of the parent molecule as the electrical discharge is fired. Subtraction of the dataset acquired when the discharge is off from that acquired when it is on provides positive-going features due to molecules produced in the discharge and negative-going features due to molecules consumed in the discharge.

The first unsaturated transition metal carbonyls detected with this instrument were FeCO and $Fe(CO)_2$. The purpose for collecting the spectra of these molecules was to use the known transitions to further test and refine the IR spectrometer. This was a useful endeavor, as it allowed us to identify and greatly reduce a number of sources of noise in the experiment. The FeCO and $Fe(CO)_2$ lines that were recorded using our instrument are in excellent agreement with Tanaka's published measurements.[8-11]

2.2.7 Molecules of Interest

The first molecular system targeted with the IR spectrometer was nickel monocarbonyl. During the search for this species the spectra for the naturally occuring isotopomers $Ni(CO)_3(^{13}CO)$ and $Ni(CO)_3(C^{18}O)$ were encountered and collected. The

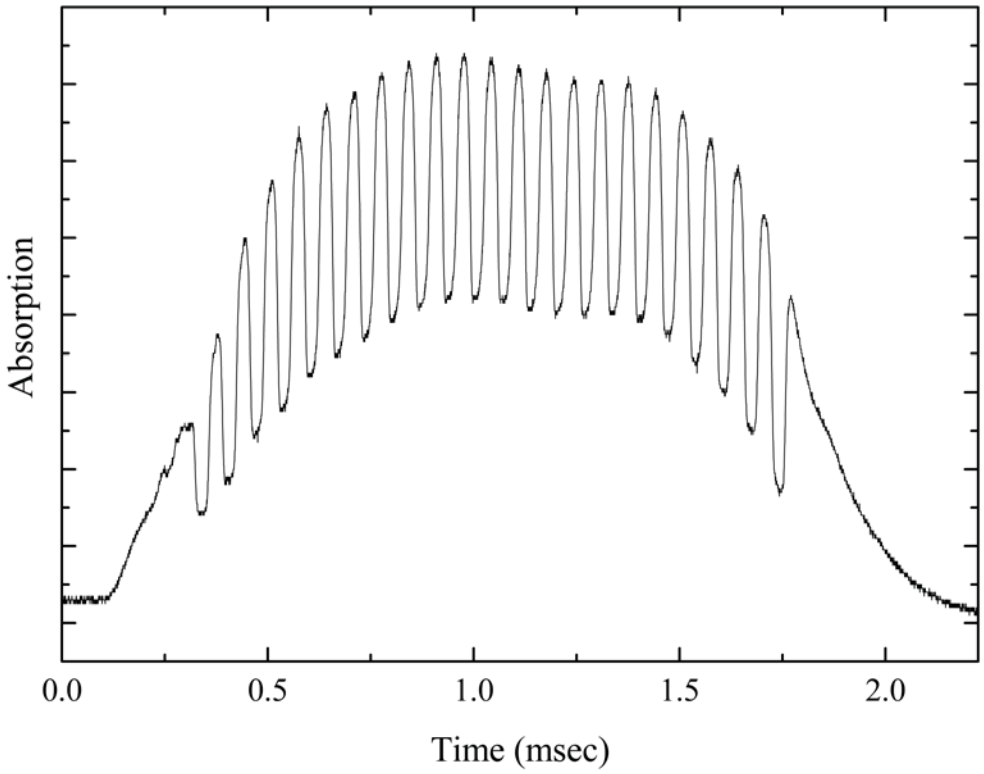

Figure 2.6 A profile of a nozzle pulse showing the modulation of $Fe(CO)_5$ as the discharge is pulsed on and off.

analysis of the data collected for NiCO, $Ni(CO)_3(^{13}CO)$, and $Ni(CO)_3(C^{18}O)$ is found in Chapter 3 of this dissertation.

After the data for NiCO were collected, the search for $Ni(CO)_2$ and $Ni(CO)_3$ commenced. The quickness with which the absorption spectrum of NiCO was detected left us with a false sense of how easily the unsaturated transition metal carbonyls are formed in an electrical discharge. The first attempt at detecting these other unsaturated nickel carbonyl species was carried out under the same conditions used to collect the spectrum of NiCO. After the diode laser was scanned over a large range of frequencies and no absorption of light due to these molecules was detected, the voltage of the electrical discharge was changed and the laser was scanned once again. The electrical discharge voltage was varied over a large range, from just barely visible to a very bright discharge. When this approach failed to produce any spectra, the backing pressure of the nozzle was changed and the discharge was varied for each pressure setting. Although this was a tedious process, it was necessary to confirm that $Ni(CO)_2$ and $Ni(CO)_3$ were not being formed in the discharged.

Other molecules for which spectra were also sought included the unstudied unsaturated iron carbonyls, chromium carbonyls, manganese carbonyls, and cobalt carbonyls. The search for these molecules was carried out in the same manner as $Ni(CO)_2$ and $Ni(CO)_3$. When no absorption due to these species was detected, we became convinced it was because the molecules were not being created and not an instrumentation problem, as the spectrum for the parent molecule could always be collected. Figure 2.7 displays a portion of the R-branch for $Cr(CO)_6$, which is in agreement with the findings of Hansford and Davies.[12] In an effort to cool the chaotic

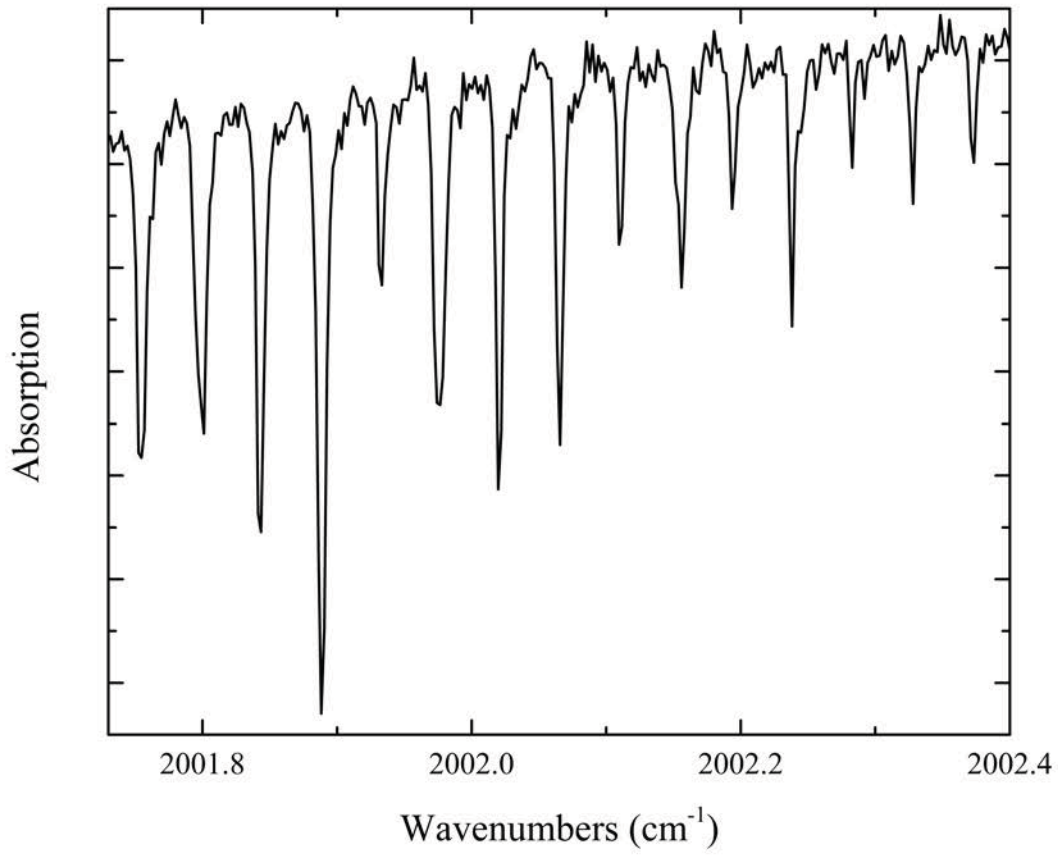

Figure 2.7 Rotationally resolved spectrum of $Cr(CO)_6$. As $Cr(CO)_6$ is a parent molecule the spectrum appears upside-down because it is being consumed in the electrical discharge.

environment created by the electrical discharge, which gives the unsaturated transition metal carbonyls a better chance of forming, a liquid nitrogen cooled copper add-on was implemented downstream of the discharge. The add-on was attached to a liquid nitrogen reservoir equipped on one of the viewing flanges. This, however, also did not prove to be helpful in creating the molecules of interest.

A final attempt at detecting the IR absorption of additional unsaturated transition metal carbonyls was carried out by replacing the electrical discharge with photolysis by the 3rd or 4th harmonics of a Nd:YAG laser. Laser photolysis has been often used to prepare unsaturated transition-metal carbonyls.[11,13-21] The photolysis of the parent molecules did not result in a different outcome; the unsaturated transition metal carbonyls of interest were not detectable. For our purposes, the use of photolysis was a step backwards because the spectra for FeCO, $Fe(CO)_2$, and NiCO were no longer detectable. This could have been because these species were no longer being made or they were being made in such a small quantity, due to the short laser pulse, that the signal was being drowned by noise. As the laser fires at 10 Hz, the use of the lock-in detector to improve the signal to noise ratio was no longer possible.

As time progressed these experiments became increasingly more difficult because the infrared diode laser became less reliable. Toward the end of my time with this instrument there were many days per week when the laser would not run for more than a few minutes before it would randomly shut down and stop emitting light. At other times the laser would stop because of interference with another object, such as the microwave oven in an adjacent room. All attempts to improve the stability of the laser, which included moving interfering objects and building a Faraday cage around the laser

controller, were fruitless. The unreliability of the diode laser and not being able to create or detect the unsaturated transition metal carbonyls of interest led me to abandon this project and do other spectroscopic studies on the R2PI instrument.

2.3 Resonant Two-Photon Ionization Spectroscopy

The first spectroscopic technique used in the Morse group was resonant two-photon ionization spectroscopy. This technique has been successfully used to study a variety of transition metal containing molecules, including metal diatomics,[22-26] metal carbides,[27-32] metal fluorides,[33] and metal silicides[34,35] to name a few. A diagram of the R2PI instrument is provided in Figure 2.8. Unlike the tunable diode laser infrared spectrometer, this instrument does not depend on the direct detection of photon absorption to map out the energy levels of a molecular system. Instead, this method relies on the detection of ions that are produced in an experimental cycle via the sequential absorption of two photons.

2.3.1 The Source Chamber

The R2PI instrument contains two differentially pumped vacuum chambers, the source chamber on the left, in Figure 2.8, and the spectroscopy chamber on the right. The source chamber is where the molecule of interest is formed. The dimensions of this chamber are approximately 71 cm long, 41 cm high, and 46 cm wide, enclosing roughly 110 L. The source chamber is evacuated to 20 millitorr with a Kinney vacuum pump (KDH-130). The pressure in the chamber is brought down to 5 μtorr using a 10-inch Varian (VHS-10) diffusion pump. These pressures are easily achieved when the nozzle is not operating. Typical pressures for the source chamber when experiments are being

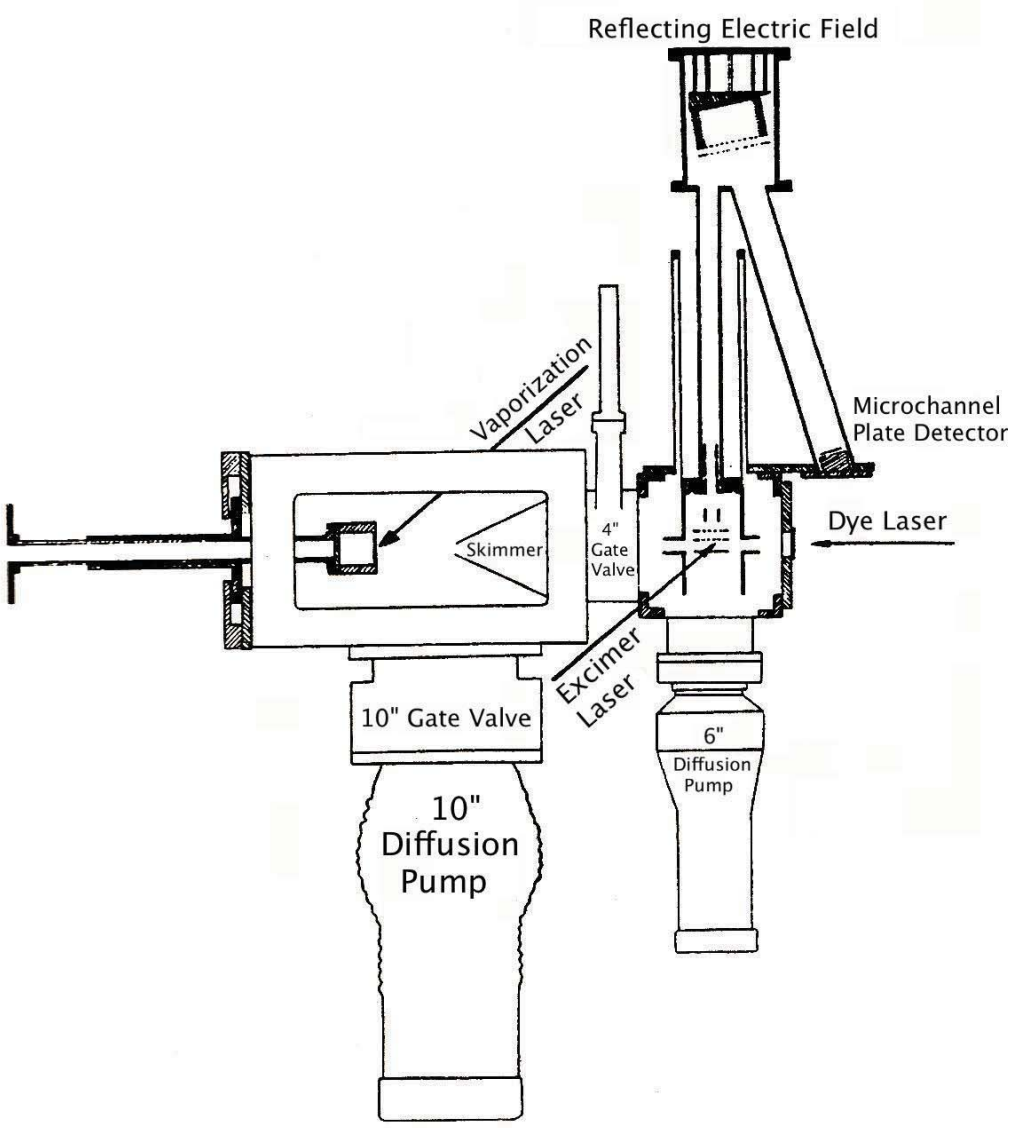

Figure 2.8 Schematic of the resonant two-photon ionization (R2PI) spectrometer. The left chamber, the source chamber, is where a molecular beam is generated through the vaporization of a metal sample in a pulse of He gas, which may be seeded with a reactant gas. The right chamber, the spectroscopy chamber, is where the molecular beam is ionized. Ions are then separated and detected using the Wiley-McLaren time-of-flight mass spectrometer.

carried are in the range of 0.2 millitorr. All pressures reported here are uncorrected for the ionization efficiency of helium, as the gauges are calibrated for air.

The bottom of the source chamber is sealed with a pneumatic gate valve that, when open, allows the 10-inch diffusion pump to evacuate the chamber. The sides of this chamber are sealed with 6061-aluminum flanges. One of these flanges is used for viewing purposes, the other introduces the vaporization laser light into the vacuum chamber and has a motor mounted on it that is responsible for the rotation and translation of the metal sample. The top and rear of the chamber are also sealed with aluminum flanges. The top flange contains an MHV connector that provides a voltage to a set of electrodes housed within the skimmer, while the rear flange supports the nozzle and the vaporization block. The front of the chamber is sealed with a 4-inch pneumatic gate valve that is used to separate the source chamber from the spectroscopy chambers.

2.3.2 Laser Vaporization

Housed in the source chamber is a commercially purchased pulsed valve (General Valve series 9) that is attached to a vaporization block. When the valve is opened, gas flows into a 2 mm diameter channel in the vaporization block. As the gas flows over the vaporization region, the output radiation of a Nd:YAG laser is focused onto a rotating and translating metal sample, entraining the vaporized species. The mount that rotates and translates the metal sample is modeled after the design of O'Brien.[36] Figure 2.9 shows a schematic of the vaporization block assembly. When the focused laser beam strikes the metal sample, the laser energy is deposited onto the metal sample in a small area for a short period of time. The duration of a laser pulse is typically 5 nanoseconds, out of which only the first few nanoseconds actually vaporize the metal sample. During

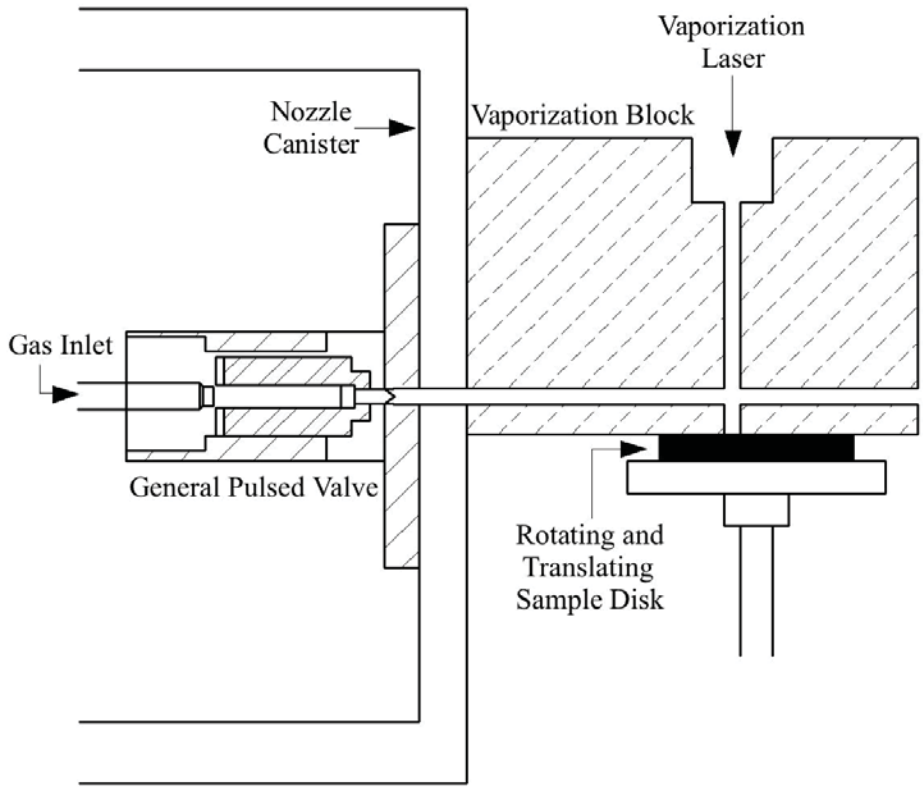

Figure 2.9 A cross-sectional schematic of the nozzle (single hash lines) in its housing (the nozzle canister) and the vaporization block (broken hash lines). When the poppet housing in the nozzle (double hash lines) is pulled back, gas is released into the channel of the vaporization block. At this time the vaporization laser is fired onto the rotating and translating sample disk, entraining the vaporized material in the nozzle gas pulse.

these first few nanoseconds the temperature of the metal sample at the vaporization point is rapidly increased to the range of 10000 K, well past the melting and vaporization points.[37] This forms a hot vapor of metal atoms that absorb the remainder of the vaporizing light pulse, leading to a hot plasma that contain metal atoms, cations, and electrons. The entrainment of the vaporized metal in the gas pulse leads to multi-body collisions between the vaporized metal atoms and the carrier gas that results in the formation of various molecular systems, one of which is the molecule of interest. Only a simplified description of the vaporization process is given here because this technique is simply used as a means to deposit metal atoms into the gas phase.

2.3.3 Supersonic Expansion from a Circular Nozzle

The gas pulse is supersonically expanded into vacuum at the end of the 2mm diameter channel, which cools the molecular beam through the same means described in section 2.2.2. The use of a circular nozzle requires the orifice diameter (D) to be much greater than the mean free path (λ_0) of the monatomic gas if many collisions are to occur during the expansion.[2] The difference between using a circular and a slit nozzle is found in the temperature, pressure, and density the molecular beam reaches at some distance (x) from the expansion orifice. In the limit of x being much greater than the diameter of the orifice, the ratio between the temperature, pressure, and density of the reservoir and the supersonically expanded molecular beam can be described by[2]

$$\frac{T(x)}{T_0} = C_c\left(\frac{x - x_0}{D}\right)^{-2(\gamma-1)}; \quad \frac{p(x)}{p_0} = F_c\left(\frac{x - x_0}{D}\right)^{-2\gamma}; \quad \frac{\rho(x)}{\rho_0} = G_c\left(\frac{x - x_0}{D}\right)^{-2}. \qquad (2.7)$$

The constants C_c, F_c, and G_c are dependent on γ, and x_0 is where the expansion begins with respect to the orifice boundary. As in the corresponding expression for a slit expansion, equation (2.5), γ is the heat capacity ratio of the carrier gas, C_p/C_v, and D is the diameter of the nozzle orifice. Section 2.2.3 describes the advantages that a slit nozzle has over a circular nozzle. However, the use of a nozzle with a circular orifice does not come without a benefit. A comparison of equations (2.5) and (2.7) shows that a circular nozzle reaches a colder temperature than a slit nozzle, for a given downstream position, x.

After the gas pulse is supersonically expanded into vacuum, it is skimmed to allow the molecules traveling with nearly parallel velocities to continue into the spectroscopy chamber. The skimmer assists in keeping the spectroscopy chamber at a lower operating pressure than otherwise would be possible. Additionally, the skimmer is equipped with a set of electrodes that prevent ions produced in the vaporization of the metal sample from entering the probing region of the spectroscopy chamber. Allowing these ions into the probing region results in a lower signal to noise ratio, as they are always present in the molecular beam and a certain fraction of them can always find their way to the detector. The task of deviating the trajectory of these ions is accomplished by generating a 210 V/cm electric field with the electrodes in the skimmer, which are separated by 1.27 cm.

2.3.4 Spectroscopy Chamber and Wiley-McLaren Reflectron Time-of-Flight Mass Spectrometer

The spectroscopy chamber is where the molecule of interest is investigated. This chamber is a 27 cm cube that encloses a volume of 13.5 L. This chamber is evacuated to

0.6 μtorr when the nozzle is not operational, and is kept at a pressure of approximately 2 μtorr when experiments are being conducted. These pressures are achieved with the use of a 6-inch Edwards High Vacuum diffusion pump that is backed by a Welch Scientific mechanical pump, and are uncorrected for the ionization efficiency of helium.

The bottom of the spectroscopy chamber is connected to the 6-inch Edwards diffusion pumps through a pneumatic butterfly valve. The rear of this chamber is attached to the 4-inch pneumatic gate valve that joins this chamber and the source chamber. The front of the chamber is sealed with a flange that is used to send the probing laser light into the source chamber. The two sides of this chamber are sealed with aluminum flanges; one is used for viewing purposes and the other to introduce the ionizing laser radiation into the chamber. The top of the chamber is connected to the Wiley-McLaren reflectron time-of-flight mass spectrometer.[38]

The first leg of the time-of-flight mass spectrometer is constructed from a stainless steel tube that is 5.08 cm in diameter and extends approximately 55.88 cm. The top of this tube meets a cylinder that is 20.32 cm in diameter and 25.53 cm in height. This large cylinder houses a reflectron assembly and connects to a second leg of the time-of-flight mass spectrometer, which extends at 18^{o} and houses the dual microchannel plate (MCP) detector.

The time-of-flight mass spectrometer is equipped with a Dewar capable of holding approximately 4 L of liquid nitrogen. This Dewar is in direct contact with a copper housing located in the spectroscopy chamber. This housing surrounds the electrode assembly responsible for directing ionized molecules into the time-of-flight mass spectrometer. The addition of liquid nitrogen to the Dewar drops the temperature of

the copper housing to approximately -196°C. Decreasing the temperature of this housing is desirable when the signal due to fragmented oil vapor overwhelms the signal of interest in the mass spectrum. Oil fragments are created when the ionization laser encounters oil vapor that rises from the diffusion pump under the spectroscopy chamber. The cooled copper housing reduces the oil fragment signal by condensing the oil vapor onto its surface, removing them from the gas phase and from the ionization region. Although this liquid nitrogen-cooling feature was not implemented in the present studies, the ability to decrease any signal arising from pump oil fragments can be important in some cases.[39]

2.3.5 The Ionization Process

In the spectroscopy chamber, radiation from a Lambda Physik ScanMate Pro dye laser is directed to interact with the molecules in the skimmed gas pulse. The laser radiation can be absorbed if the energy of the photon matches the separation between two eigenstates of a molecule. The absorption of the probing photon excites the molecule, adding anywhere from 1.40 – 2.88 eV of energy to the molecular system. As the energy invested by this photon into the molecule is not sufficient to ionize the molecules typically studied in this lab, an excimer laser (Lambda Physik COMPex) is fired shortly after the excitation laser to ionize the excited molecule. The time difference between the first and second laser firing is typically a few tens of nanoseconds. The excimer laser adds 5.00 (KrF gas mixture), 6.42 (ArF gas mixture), or 7.86 (F_2 gas mixture) eV of energy to the system, allowing the energy in the molecule to exceed the ionization threshold. Careful consideration must be given to the energy that is provided by the second photon, as it is undesirable for the ionization process to occur through the absorption of a single ionizing photon. Placing this restriction on the second photon

allows for an effective method to discriminate whether the probing photon was absorbed. Simply put, neither of the two laser pulses can have enough energy per photon to ionize the molecule of interest when absorbed. It is only through the absorption of the excitation photon that the excimer photon is capable of ionizing the molecule. Thus, the sequential absorption of two photons is required for ionization, leading to the designation of this technique as resonant two-photon ionization spectroscopy. Figure 2.10a schematically illustrates the process used to produce the ions that are subsequently detected.

The previous paragraph describes an idealized resonant two-photon ionization process. In this scheme a zero background signal would be observed unless the probing photon is absorbed. This is, unfortunately, not the only path that leads to the ionization of molecules in the gas pulse. Other processes occur that can lead to background signals that can be difficult to eliminate. The varieties of molecules that are carried within the gas pulse are many, all with varying ionization potentials. Because there are various routes through which the atoms and molecules carried in the gas pulse can be ionized, it is important to distinguish the possible ways ions can be formed. Figure 2.10b-d illustrates several paths that can result in the ionization of a molecule.

The first process that can lead to molecular ionization is through the absorption of a single photon whose energy is greater than the ionization energy. This scheme is represented in Figure 2.10b. Typically, the excitation photon does not contain sufficient energy for a one-photon ionization process. On the other hand, it is often easy to select an ionization wavelength that can ionize the molecule in a one-photon process. Although one-photon ionization can be useful in detecting what is contained within the gas pulse, it

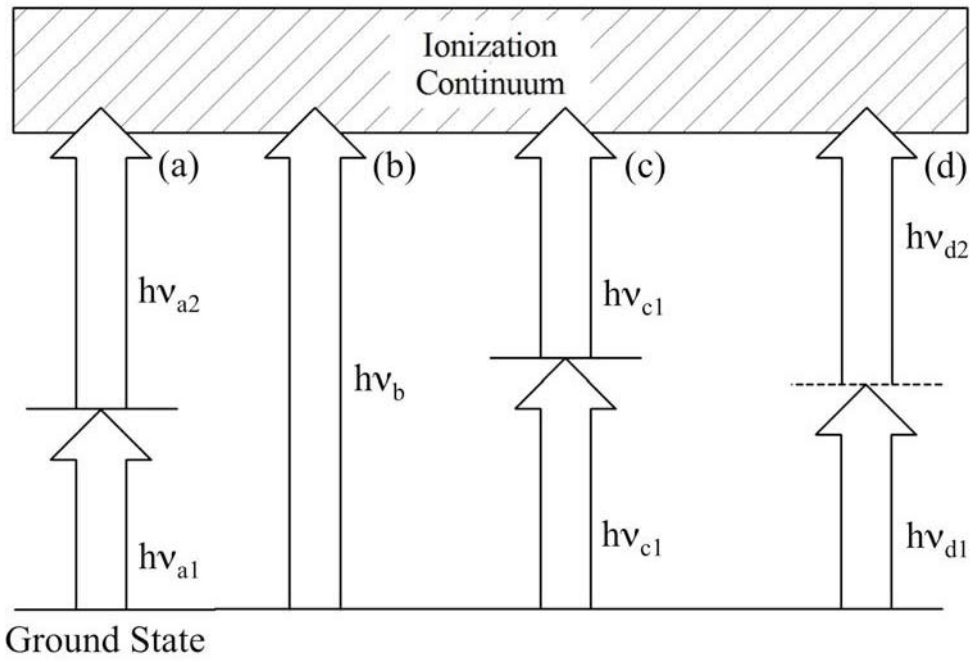

Figure 2.10 The various ionization pathways in a resonant two-photon process are illustrared. Pathway (a) represents the ideal two-photon (two color) ionization process. Pathway (b) illustrates the single photon ionization process. Pathway (c) shows the ionization of a molecule occurring by the absorption of two photons with the same frequency. Lastly, pathway (d) has the ionization of a molecule being reached through a so-called virtual state, which can only occur if the two photons are absorbed in a time that is short enough for the energy broadening of an allowed transition to encompass the laser energy.

can be bothersome when a spectroscopic experiment is conducted. This ionization pathway is undesirable because ions are formed and detected regardless of the frequency of the excitation photon. Forming cations through the absorption of a single photon will not allow the energy levels of the molecule to be mapped because of the high background that is always present. Fortunately, simply selecting an ionization photon with less energy can easily overcome this difficulty.

The remaining ionization pathways that will be discussed proceed through the absorption of two photons. The first of these paths is illustrated in Figure 2.10c. In this scheme, the photons that are absorbed to form the ions are of the same energy. If this single laser technique is to be used to map out the molecular energy levels, it must be conducted with two dye laser photons, as the frequency of the excimer laser cannot be scanned. The result of two excimer photons being absorbed is an enhanced background signal, which is a common problem in the R2PI method, occurring if the excimer laser wavelength happens to be resonant with a molecular transition. When a dye laser supplies the two photons, this scheme is conceptually not very different from that illustrated in Figure 2.10a, but it is more restrictive. The first restriction concerns the energy levels that can be mapped out using this scheme. The only eigenstates that are accessible via this ionization pathway are those that lie at least halfway between the ground state and the ionization energy of the molecule. This scheme also restricts the molecules that can be studied to those that possess an ionization energy less than 5.76 eV, the maximum energy that can be obtained in the Morse laboratory from two dye laser photons. A final restriction that this scheme presents is the inability to measure excited state lifetimes, a technique that is implemented in the R2PI instruments and that is

discussed below. The Morse group implemented this one-color resonant two-photon ionization technique in its study of LiCa, which has a calculated ionization energy of 4.43 eV.[40]

The second two-photon absorption channel that can produce ions is illustrated in Figure 2.10d. In this scheme, the first photon excites the molecule to a virtual state, which is not a real eigenstate of the system but a fictitious state that can be described as a linear combination of real eigenstates that are accessible from the initial state of the molecule. Although this virtual state in not an eigenstate of the molecule it has a non-zero probability of being accessed and can lead to an ion via the absorption of a second photon. Even though the two-photon absorption process is inefficient when the energy of the excitation photon is not in resonance with a molecular transition, this scheme produces a background signal that is sometimes difficult to reduce.

The probability of ionization due to the absorption of two photons, as described in the previous paragraphs, is proportional to the following mathematical expression:[41]

$$\frac{\gamma_{if} I_1 I_2}{\left[\omega_{if} - \omega_1 - \omega_2 - \vec{v}\cdot\left(\vec{k}_1 + \vec{k}_2\right)\right]^2 + \left(\gamma_{if}/2\right)^2} \times \left|\sum_k \frac{\left(\langle i|\hat{\mu}|k\rangle\cdot\vec{e}_1\right)\left(\langle k|\hat{\mu}|f\rangle\cdot\vec{e}_2\right)}{\omega_{ki} - \omega_1 - \vec{v}\cdot\vec{k}_1} + \frac{\left(\langle i|\hat{\mu}|k\rangle\cdot\vec{e}_2\right)\left(\langle k|\hat{\mu}|f\rangle\cdot\vec{e}_1\right)}{\omega_{ki} - \omega_2 - \vec{v}\cdot\vec{k}_2}\right|^2 . \quad (2.8)$$

The first factor of this equation describes the Lorentzian spectral line profile of the transition. I_1 and I_2 are the intensities of the lasers, γ_{if} is the homogeneous linewidth, ω_{if} represents the separation between the initial and final levels in the transition, ω_1 and ω_2 are the frequencies of the lasers, $\vec{v}$ is the velocity of the molecule, and $\vec{k}_1$ and $\vec{k}_2$

correspond to the wave vector of the light waves. The term $\vec{v}\cdot\left(\vec{k}_1+\vec{k}_2\right)$ expresses the Doppler shift in ω_1 and ω_2 that is due to the velocity of the molecule. From this factor, it is important to note that an increase in laser intensity increases the probability of photon absorption in a manner that is linearly proportional to each laser intensity. Saturation effects are not included in equation (2.8).

The second factor in the equation gives the probability of a two-photon transition. Here, $\hat{\mu}$ is the electric dipole operator, $|i\rangle$ represents the initial state of the molecule, $|f\rangle$ is the final state of the molecule, $|k\rangle$ is the intermediate state that is reached by the absorption of a photon, and $\vec{e}_1$ and $\vec{e}_2$ are the polarization vectors of the laser light. The first requirement needed for the absorption of two-photons calls for $\langle i|\hat{\mu}|k\rangle$ and $\langle k|\hat{\mu}|f\rangle$ to be nonzero. This necessitates states $|i\rangle$ and $|f\rangle$ to be connected through $|k\rangle$ by allowed single photon transitions. The upper states that are accessible from a given lower state are dependent of the polarization characteristics of the radiation, $\vec{e}_1$ and $\vec{e}_2$, which restrict ΔM. A beam of light that is right-circularly polarized induces a change in M that is opposite to that of left-circularly polarized light. The polarization of the dye laser used in this experimental setup is linear, meaning is can be considered as the sum of right and left-circularly polarized light, making ΔM = ±1 transitions possible. In the absence of a magnetic field, these transitions are degenerate. The second condition for a two-photon absorption is met when the energy of the first photon matches the separation between states $|i\rangle$ and $|k\rangle$. As the R2PI experiment places $|f\rangle$ in the ionization continuum, the probability of two-photon absorption increases dramatically when $\omega_1 = \omega_{ki}$, which causes the denominator of equation (2.8) to vanish. This is the basis for resonant enhancement

of the two-photon ionization process. In contrast, ionization through a virtual state occurs when the denominator does not precisely vanish. Its importance varies from molecule to molecule, depending on how closely the denominator approaches zero.

2.3.6 Time-of-Flight

After the ions are formed, they are guided through the reflectron time-of-flight mass spectrometer using electrostatic fields, resulting in a separation of the ions that is mass dependent. Figure 2.11 shows the ion optics found in the time-of-flight tube and the motion of the ions in response to the electric field.

The portion of the gas pulse that is ionized experiences a force exerted by the electric field that is generated by the repeller and draw out grid (D.O.G) electrodes. This repulses the ions from the repeller plate and pulls them out of the ionization region. The force experienced by the cations is described as

$$F = m\frac{d^2z}{dt^2} = q_e\frac{V_{rep} - V_{DOG}}{d_1} \quad . \tag{2.9}$$

In this equation, m is the mass of the ion, z is the distance of the ionized molecule from the repeller, d^2z/dt^2 is the acceleration the molecule experiences, q_e is the charge of an electron, V_{rep} and $V_{D.O.G}$ are the voltages applied to the repeller and draw out grid, and d_1 is the separation between the two charged plates. Equation (2.9) shows that for a given set of cations, those closer to the repeller are accelerated for a greater amount of time than those at a greater distance, as these later ions spend less time in this electric field. As a result, ions created closer to the repeller travel with a greater velocity than other cations as they pass the D.O.G border. Additionally, this equation also states that

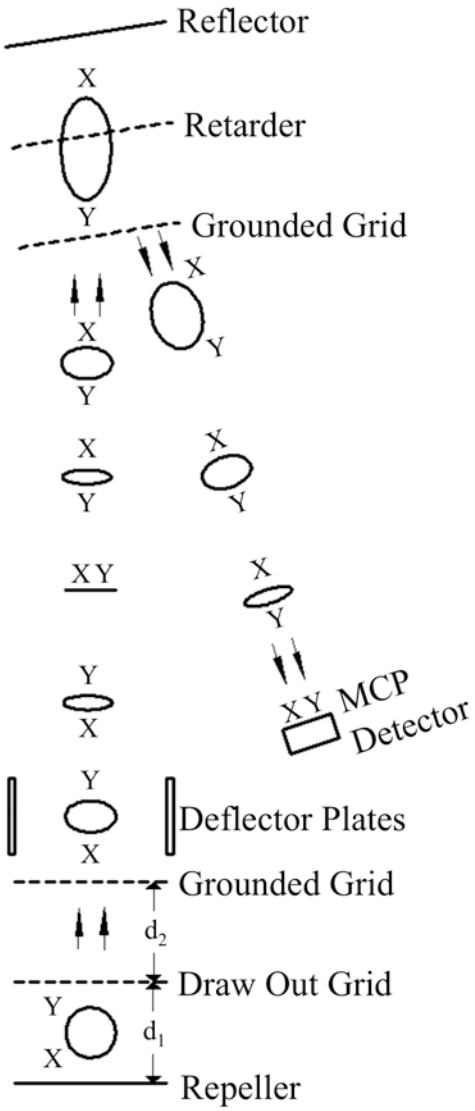

Figure 2.11 A schematic of the Wiley-McLaren time-of-flight mass spectrometer and the trajectory for a packet of ions are depicted; all of the ions are identical in charge and mass. Additionally, the focusing and divergence of the ions that comes about because of where they are generated with respect to the repeller plate is also illustrated.

molecules that vary in masses will be accelerated to different velocities, with lighter molecules reaching higher speeds. This leads to a separation of the ionized molecules by mass as they travel through the flight tube.

After the cations pass the D.O.G they enter another acceleration region that is created by this electrode and a grounded plate. The force imposed on the ions in this region can be described similarly to equation (2.9), the difference coming in the electric field that is produced by the draw out grid and the grounded plate. The electric field for this acceleration region is $V_{D.O.G}/d_2$, where d_2 is the distance between the draw out grid and the grounded plate.

Following the two-stage acceleration region is a set of electrodes that are designed to counteract the forward velocity of the molecular beam. Prior to ionization the molecules are traveling perpendicular to the flight tube. The Wiley-McLauren ion extraction assembly accelerates the ions in a direction perpendicular to the molecular beam, but does nothing to change the component of velocity along the beam. In order to travel through the flight tube and reach the detector, the forward velocity must be halted, particularly for the heavier ions. Heavier cations are likely to crash into the flight tube walls and never make it to the detector if their trajectory is left unchecked. To adjust the path taken by the heavier ions, an electric field that is perpendicular to the axis of the flight tube is generated between the deflector plates. This field is created by positively charging one plate while the other is grounded. The greater the mass of the ion of interest the larger the voltage that must be applied to the charged deflector plate in order to halt the forward velocity.

As a given set of ionized molecules make their way through the first leg of the flight tube, they experience a focusing effect in which the faster moving ions, which are produced closer to the repeller, catch up to the slower ones. This focusing of the ions is illustrated in Figure 2.11, where the faster ions are labeled X and the slower ones Y. Where along the time-of-flight tube the faster and slower ions come to a planar focus is determined by the voltage applied to the draw out grid. Applying a greater voltage to the draw out grid moves the focal plane of the cations further up the time-of-flight tube. To attain the best mass resolution, the MCP detector must be located at the focal point. However, placing the detector at this focal point will not allow the different ions sufficient time to separate well and will prevent the best possible mass resolution from being achieved.

To obtain better mass resolution, a second leg is added to the flight tube. The ion trajectory is altered to travel down the second portion of the flight tube by a set of three electrodes, one of which is grounded; the other two are positively charged. The first set of electrodes the ions encounter are a grounded grid and the charged grid called the retarder. These two grids exert a force on the ionized molecules that slows down their forward momentum. The electric field created by these two grids can be expressed similarly to the field produced by the draw out grid and the grounded grid described earlier. After the cations pass the retarder grid, they enter a second electric field region made up of this grid and another charged plate called the reflector. This second region, which can be described similarly to the field generated by the repeller and draw out grid, imposes a force on the molecules that completely halts the forward motion of the ions and reflects them down the path of the second leg of the time-of-flight mass

spectrometer. Once the cations have come to a stop between the retarder and reflector grids, the electrodes become another two-stage acceleration assembly.

By the point a given set of ions reaches the grounded, retarder, and reflector plates they have passed the focusing point and are diverging. The ions with the greater velocity (X) penetrate deeper into the reflecting electric field region than the slower moving ones (Y). The greater distance these ions travel results in them trailing the slower moving cations when they exit the reflecting electric field region. This once again leads to a focusing of the ionized molecules down the second leg of the flight tube, as the faster ions catch up with the slower ones. By adjusting the voltage on the retarder grid, this focus point may be placed on the MCP detector. The detector is a dual microchannel plate assembly, each plate containing a large number of electron amplification channels that are oriented in a V-like chevron configuration. When an ion strikes the surface of the first MCP, electrons are ejected. As these electrons are accelerated down a channel, they collide with the walls, releasing additional electrons. This process of electron multiplication continues throughout the two plates, with a gain of approximately 1000 per plate. Finally, the current output is collected on a gold plated conical anode and sent out of the MCP detector to be converted into a mass spectrum.

2.3.7 Mass Spectrum

The process for generating a mass spectrum begins with the output of the detector being amplified (approximately 90x) and converted to a voltage using a Pacific Instruments (2-A50) pre-amplifier. The signal is then digitized with a Transiac 2001 transient digitizer at a rate of 100 MHz for 10.24 μsec and is stored in the digitizer's memory. The data is then read and stored on an Intel 386 computer in an array. In order

to obtain a good signal-to-noise ratio, 30 sets of data points are collected and averaged. The averaged array is then plotted as a function of record number, the index of a data point, mapping out the intensity of the ions striking the MCP detector.

To transform this waveform into a mass spectrum, one must consider the kinetic energy with which the ionized molecules travel through the time of flight tube. For a single charged molecule the kinetic energy may be expressed as

$$K.\,E. = \frac{1}{2}mv^2 = e\Phi, \tag{2.10}$$

where m and v are the mass and velocity of the ion, e is the charge of an electron, and Φ is the local potential where the molecule was ionized. The time that it takes an ionized molecule to travel the length of the flight tube can be determined from the equation

$$t = t_D + 0.01R_{\#} - t_I + \Delta. \tag{2.11}$$

Here, t_D is the time when the Transiac 2001 begins to digitize, 0.01 is the digitization rate (in μsec) of the Transiac 2001, $R_{\#}$ is the record number of where the peak appears, t_I is when the fire command is sent to the ionization laser, and Δ is the time delay between when the firing command is sent to the ionization laser and when it actually fires. Combining equations (2.10) and (2.11) and rearranging the resulting formula to solve for m leads to

$$m = K\left(t_D + 0.01R_{\#} - t_I + \Delta\right)^2, \tag{2.12}$$

where K equals the constant $2e\Phi/d^2$. As this equation has a nonlinear dependence in Δ it is difficult to fit a set of known reference masses (m_i, R_i) to obtain K and Δ, as this is a nonlinear least-squares fit. It is more convenient to solve (2.12) for the $R_\#$,

$$R_\# = \frac{1}{0.01\sqrt{K}}\sqrt{m} - \frac{1}{0.01}\left(t_D - t_I + \Delta\right), \tag{2.13}$$

which gives a linear equation that allows sets of (m, $R_\#$) values to be least square fitted to obtain K and Δ, the calibration constants for the mass spectrometer. Pairing a record number to a mass is accomplished by running known species, preferably with multiple isotopes, through the mass spectrometer. As the intensity of a peak is correlated to its concentration in the molecular beam, the natural isotopic pattern of the known species allow $R_\#$ and m to be matched. Knowing values for K and Δ lets equation (2.12) convert any record number dependent waveform into a mass dependent plot.

The R2PI investigation of any species begins with the collection of a mass spectrum, which, at this stage, is typically gathered using only the ionization laser. This allows the user an opportunity to see what species are carried in the molecular beam and adjust experimental conditions to enhance the signal intensity of the molecule of interest. Additionally, collection of a mass spectrum offers a sense of whether the ionization laser is one photon ionizing the molecule of interest or not. This insight can be gained by observing the intensity of the molecules as the laser light is attenuated. A signal intensity that diminishes linearly as the power of the ionization laser is reduced is indicative of a molecule undergoing single photon ionization. This scenario leaves the user with the option to use a different ionization wavelength or to change the molecule to be studied.

2.3.8 Low-Resolution Optical Scans

Once conditions are optimized to make the molecule of interest, the ionization laser is attenuated to minimize the background signal that is generated by ionizing the molecule with two photons of the ionization laser wavelength. While in low-resolution (0.15 cm^{-1} linewidth) the dye laser is directed into the spectroscopy chamber and scanned to collect a vibronic spectrum by monitoring the intensity of the masses of interest. Figure 2.12 compares the peak intensity of PdSi in a mass spectrum while the dye laser is on and off resonance. Laser wavelengths ranging from 400 – 900 nm can be obtained by scanning a motorized diffraction grating over various dyes. A vibronic spectrum of ^{63}CuSi, which was prepared by pasting together scans over several dyes is displayed in Figure 2.13.

Analysis of a vibronic spectrum can be facilitated when it is possible to group bands into a vibrational progression in the excited state. Recognition of the bands that belong to a given vibrational progression is based on the regular separation between sequential bands and the similarities in excited state lifetimes of the bands. Once a vibrational progression is identified, the vibrational quantum number of the excited state can be easily assigned if the origin band is visible. If the origin band is not observed, the excited state vibrational quantum number can be identified by simultaneously collecting a low-resolution optical spectrum for multiple isotopes of the molecule, plotting the isotope shift versus the band position, and comparing the results with theoretically calculated values. Theoretical values for the band positions and isotope shifts can be approximated using the following equations, when the transitions arise from $v'' = 0$ vibrational level:

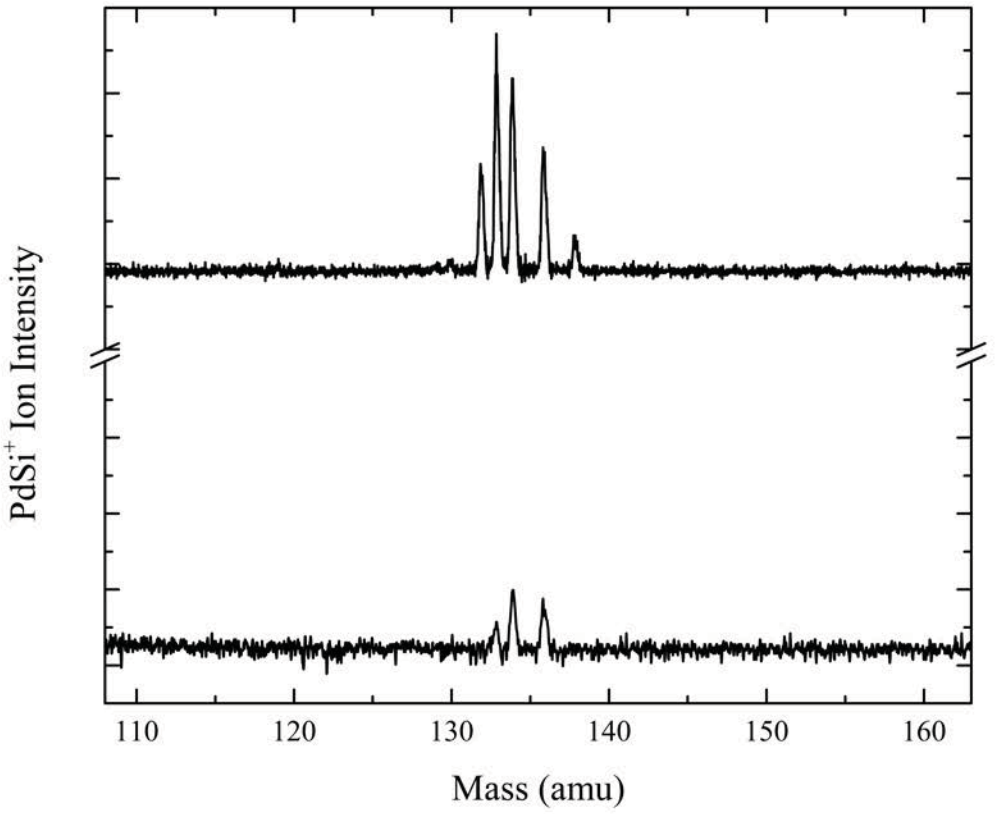

Figure 2.12 A mass spectrum centered around the masses of PdSi. The lower mass spectrum shows the intensities of the three most abundant isotopes of PdSi barely visible above the base line. This mass spectrum was collected with the dye laser off resonance and the ionization laser filtered down to minimize the number of PdSi molecules that are two photon ionized by the ionization laser. The difference between the two mass spectra is that the top plot has the dye laser on resonance with a transition. A comparison between the two spectra show a clear enhancement in the PdSi signal, which would show up in an optical scan as a transition.

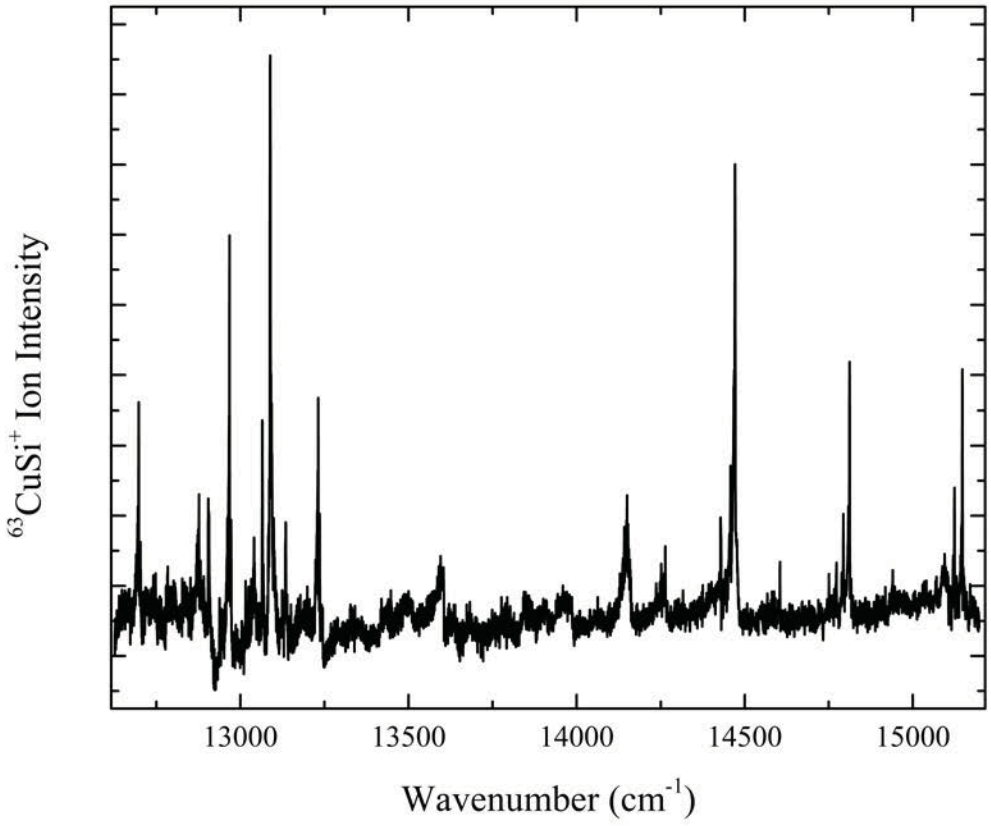

Figure 2.13 A low-resolution optical spectrum of ^{63}CuSi. As none of these bands could be rotationally resolved, no further analysis of these data was carried out.

$$\upsilon_{v'-0}^{(i)} = T_e + \omega_e'^{(i)}(v'+0.5) - \omega_e'\chi_e'^{(i)}(v'+0.5)^2 - 0.5\omega_e''^{(i)} \quad (2.14)$$

$$\Delta\upsilon_{v'-0}^{(i-j)} = \omega_e'^{(i)}(1-\rho)(v'+0.5) - \omega_e'\chi_e'^{(i)}(1-\rho^2)(v'+0.5)^2 - 0.5\omega_e''^{(i)}(1-\rho). \quad (2.15)$$

In these equations T_e is the energy separation between the minima of the excited and ground state potential wells of the molecule, ω_e' and ω_e'' are the vibrational frequencies for the excited and ground states, $\omega_e'\chi_e'$ is the anharmonicity of the excited state, ρ is given by the ratio $(\mu^{(i)}/\mu^{(j)})^{1/2}$ for the i^{th} and j^{th} isotope, and v' is the vibrational quantum number for the excited state.[42] To properly deduce the vibrational numbering, several vibrational assignments must be simulated using the equations (2.14) and (2.15) and plotted on the same graph as the experimental results. The correct vibrational numbering is taken to be that which provides the best match between the experimental and theoretical values. Examples of when this latter method were used in the Morse group can be found in the literature[43,44] and in Chapter 4 of this dissertation.

A vibronic spectrum can also provide insight if the molecule experiences a change in bond length upon excitation, which can be verified with a rotationally resolved scan. Even if a vibronic spectrum cannot be sorted into any progressions or give insight on a bond length change, these scans are extremely useful because they provide the user a window over which to scan the excitation laser in high-resolution (0.04 cm^{-1} linewidth) mode.

2.3.9 High-Resolution Optical Spectrum

A scan over a vibronic band in high-resolution mode will show the rotational structure of the transition. The dye laser is scanned in high-resolution mode by inserting an air-spaced étalon into the oscillator cavity, evacuating the cavity, and slowly

pressurizing it with SF_6. As the cavity is slowly pressurized, the index of refraction in the cavity changes, altering the wavenumber of the light emitted. The spectrum of each rotationally resolved band is calibrated by concurrently collecting the absorption spectrum of I_2 or $^{130}Te_2$ and the transmission fringes of an étalon, whose free spectral range is 0.22 cm^{-1}.[45,46] To improve the signal-to-noise ratio, it is typical to collect multiple scans of each region and average them. The averaged spectrum for each band is assigned and fitted using a least-squares routine, allowing the band origin and ground and excited state rotational constants and bond lengths to be obtained. In conjunction with theoretical work, the assignment of a rotationally resolved spectrum can sometimes lead to a determination of the ground state term symbol for the molecule under investigation. Figure 2.14 shows a rotationally resolved spectrum of ZrF, along with the transmission fringes of an étalon and the absorption spectrum of I_2.

2.3.10 Excited State Lifetimes

As mentioned earlier, the excited state lifetime of each band can help group transitions into the vibrational progression of an electronic state. The lifetime of a band is determined by tuning the excitation laser to a vibronic transition and uniformly varying the time at which it fires, relative to the firing of the ionization laser. The time at which the dye laser is initially set to fire occurs after the excimer has been fired. With this timing setup no molecules are ionized, so the signal emerging from the detector is purely background. The background remains low until the dye laser is fired just before the excimer laser, at which time the ion signal intensity drastically increases. Further increasing the timing separation between the excitation and ionization lasers results in an exponential decay of the signal intensity. This occurs because a larger timing separation

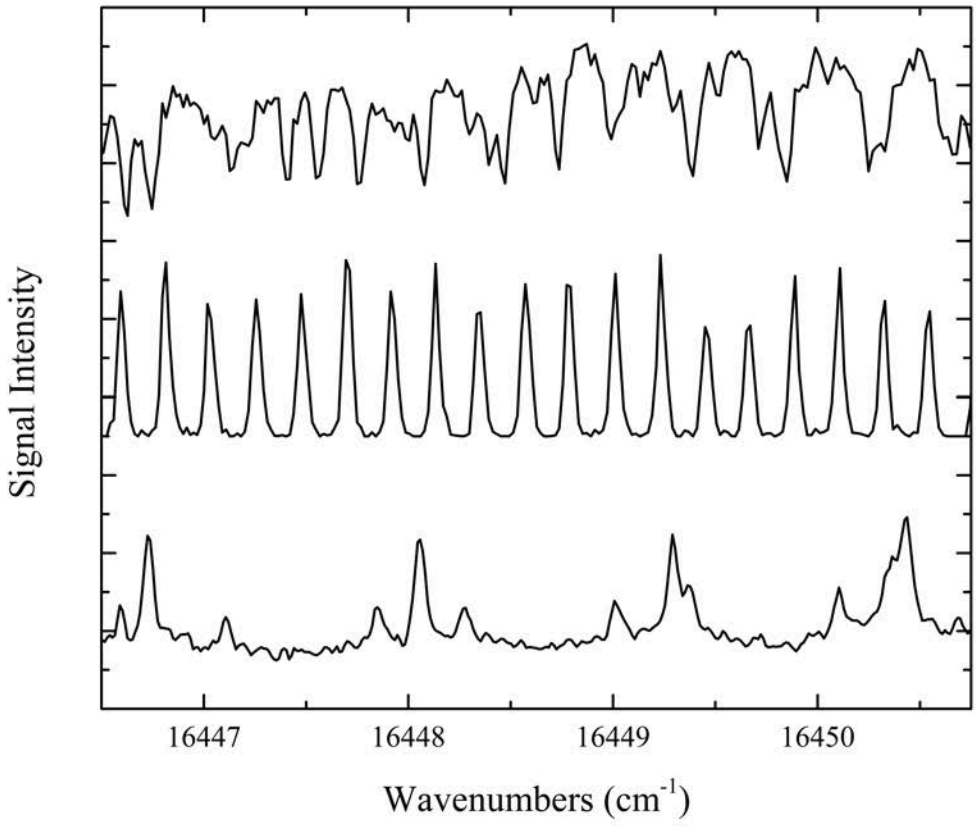

Figure 2.14 To properly calibrate a rotationally resolved spectrum (lowest plot), the transmission fringes of an étalon (middle plot), and absorption spectrum of a well known gas, like I_2 (top plot), must be collected concurrently with the spectrum of interest. The rotationally resolved spectrum shown belongs to the P-branch of ZrF. This ZrF spectrum was calibrated by first using the absolute frequencies of the I_2 line positions to determine the free spectral range (FSR) of the étalon and then using this value to linearize the rotationally resolved spectrum in energy.

allows for a greater number of molecules to relax from the excited state. Figure 2.15 shows the decay curve of an excited state for ZrF at approximately 16965 cm^{-1}. The data points making up this curve are then fit to an exponential decay model to obtain the lifetime of the excited state.

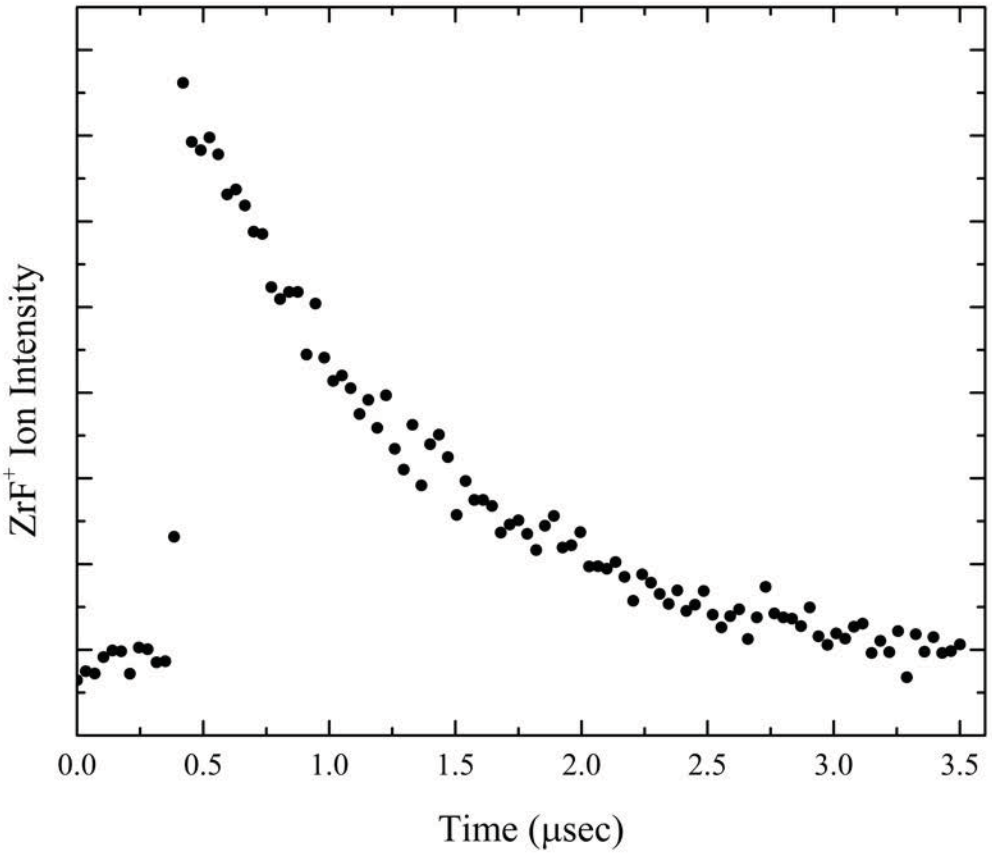

Figure 2.15 This plot shows the exponential decay of an excited state of ZrF at 16965 cm^{-1}. Lifetime plots are generated as a function of the delay between the excitation and ionization laser pulses. This lifetime plot was fitted and found to have a lifetime of 0.97 μsec.

2.4 References

[1] D. Kaur, A. M. De Souza, J. Wanna, S. A. Hammad, L. Mercorelli, and D. S. Perry, Appl. Opt. **29** (1), 119 (1990).

[2] M. D. Morse, in *Methods of Experimental Physics: Atomic, Molecular, and Optical Physics*, edited by F. B. Dunning and R. Hulet (Academic Press, Inc., Orlando, Florida, 1996), Vol. II Atoms and Molecules, pp. 21.

[3] S. Davis, University of Colorado, 1999.

[4] J. U. White, Journal of the Optical Society of America **32**, 285 (1942).

[5] D. S. Perry and G. A. Bethardy, Techniques of Chemistry **23**, 71 (1995).

[6] R. Wolfson and J. M. Pasachoff, *Physiscs: With Modern Physics*. (HarperCollins College, New York, 1995).

[7] P. Asselin, P. Soulard, G. Tarrago, N. Lacome, and L. Manceron, Journal of Chemical Physics **104** (12), 4427 (1996).

[8] K. Tanaka, K. Sakaguchi, and T. Tanaka, Journal of Chemical Physics **106** (6), 2118 (1997).

[9] K. Tanaka, M. Shirasaka, and T. Tanaka, Journal of Chemical Physics **106** (17), 6820 (1997).

[10] K. Tanaka, Y. Tachikawa, K. Sakaguchi, T. Hikida, and T. Tanaka, Journal of Chemical Physics **111** (9), 3970 (1999).

[11] K. Tanaka, Y. Tachikawa, and T. Tanaka, Chem. Phys. Lett. **281** (4,5,6), 285 (1997).

[12] G. M. Hansford and P. B. Davies, J. Mol. Spectrosc. **168** (2), 540 (1994).

[13] G. Nathason, B. Gitlin, A. M. Rosan, and J. T. Yardley, Journal of Chemical Physics **74** (1981).

[14] J. T. Yardley, B. Gitlin, G. Nathason, and A. M. Rosan, Journal of Chemical Physics **74** (1981).

[15] A. B. Callear and R. J. Oldman, Transactions fo the Faraday Society **63** (1967).

[16] Y. Kasai, K. Obi, Y. Ohshima, Y. Endo, and K. Kawaguchi, Journal of Chemical Physics **103** (1), 90 (1995).

[17] A. J. Ouderkirk, P. Wermer, N. L. Schultz, and E. Weitz, J. Am. Chem. Soc. **105** (10), 3354 (1983).

[18] T. R. Fletcher and R. N. Rosenfeld, Journal of the American Chemical Society **105** (20), 6358 (1983).

[19] T. A. Seder, S. P. Church, A. J. Ouderkirk, and E. Weitz, J. Am. Chem. Soc. **107** (5), 1432 (1985).

[20] G. W. Tyndall and R. L. Jackson, Journal of the American Chemical Society **109** (1987).

[21] W. E. Hollingsworth and V. Vaida, Journal of Physical Chemistry **90** (1986).

[22] R. Nagarajan and M. D. Morse, Journal of Chemical Physics **127** (1), 014311/1 (2007).

[23] R. Nagarajan and M. D. Morse, Journal of Chemical Physics **127** (7), 074304/1 (2007).

[24] S. M. Sickafoose, J. D. Langenberg, and M. D. Morse, Journal of Physical Chemistry A **104** (16), 3521 (2000).

[25] E. M. Spain and M. D. Morse, Journal of Chemical Physics **97**, 4605 (1992).

[26] S. Taylor, G. W. Lemire, Y. M. Hamrick, Z. Fu, and M. D. Morse, Journal of Chemical Physics **89**, 5517 (1988).

[27] D. J. Brugh and M. D. Morse, Journal of Chemical Physics **117** (23), 10703 (2002).

[28] D. J. Brugh, T. J. Ronningen, and M. D. Morse, Journal of Chemical Physics **109**, 7851 (1998).

[29] O. Krechkivska and M. D. Morse, J. Chem. Phys. **128** (8), 084314/1 (2008).

[30] O. Krechkivska and M. D. Morse, Journal of Chemical Physics **133**, 054309/1 (2010).

[31] J. D. Langenberg, R. S. DaBell, L. Shao, D. Dreessen, and M. D. Morse, Journal of Chemical Physics **109**, 7863 (1998).

[32] J. D. Langenberg, L. Shao, and M. D. Morse, Journal of Chemical Physics **111**, 4077 (1999).

[33] R. Nagarajan and M. D. Morse, Journal of Chemical Physics **126** (14), 144309/1 (2007).

[34] N. Lindholm and M. D. Morse, Journal of Chemical Physics **127** (8), 084317/1 (2007).

[35] N. F. Lindholm, D. J. Brugh, G. K. Rothschopf, S. M. Sickafoose, and M. D. Morse, Journal of Chemical Physics **118** (5), 2190 (2003).

[36] S. C. O'Brien, Y. Liu, Q. Zhang, J. R. Heath, F. K. Tittel, R. F. Curl, and R. E. Smalley, Journal of Chemical Physics **84** (7), 4074 (1986).

[37] J. F. Ready, *Industrial Applications of Lasers*, 2 ed. (Academic Press, San Diego, 1997).

[38] W. C. Wiley and I. H. McLaren, Review of Scientific Instruments **26** (12), 1150 (1955).

[39] D. Brugh, University of Utah, 1997.

[40] L. M. Russon, G. K. Rothschopf, M. D. Morse, A. I. Boldyrev, and J. Simons, Journal of Chemical Physics **109**, 6655 (1998).

[41] W. Demtroder, *Laser Spectroscopy: Basic Concepts and Instrumentation*, 3 ed. (Springer, New York, 2003).

[42] G. Herzberg, *Molecular Spectra and Molecular Structure I. Spectra of Diatomic Molecules*, 2nd ed. (Van Nostrand Reinhold, New York, 1950).

[43] S. A. Heidecke, Z. Fu, J. R. Colt, and M. D. Morse, Journal of Chemical Physics **97**, 1692 (1992).

[44] L. Shao, S. M. Sickafoose, J. D. Langenberg, D. J. Brugh, and M. D. Morse, Journal of Chemical Physics **112** (9), 4118 (2000).

[45] J. Cariou and P. Luc, *Atlas du Spectre d'Absorption de la Molécule de Tellure entre 18500 - 23800 cm^{-1}*. (CNRS, Paris, 1980).

[46] S. Gerstenkorn and P. Luc, *Atlas du Spectre d'Absorption de la Molécule d'Iode entre 14800-20000 cm^{-1}*. (CNRS, Paris, 1978).

CHAPTER 3

INFRARED DIODE LASER SPECTROSCOPY OF JET-COOLED NiCO, Ni(^{13}CO)(CO)$_3$, AND Ni(C^{18}O)(CO)$_3$

3.1 Introduction

Transition metal carbonyls and their reactive intermediates have received a great deal of attention due to their importance in organometallic synthesis and catalytic processes.[1] Among the unsaturated transition metal carbonyls that have been of particular interest are the monocarbonyls (MCO). These molecules have attracted much attention because they serve as the simplest model for understanding the chemisorption of CO on a metal surface.[2] Thus, much theoretical and spectroscopic work has been undertaken on these species.

One of the most thoroughly computationally investigated of the transition metal monocarbonyls is NiCO. Many calculations on this molecule have predicted its geometry, vibrational frequencies, binding energy, and ground state electronic symmetry.[3] Determination of the ground state electronic symmetry is of particular importance if the nature of the Ni-CO bond is to be understood. Early calculations on this molecule predicted a $^3\Delta$ ground state, which arises from the $^1\Sigma^+$ ground state of CO and the ^{3}D ($4s^13d^9$) term of atomic Ni.[4] However, the subsequent theoretical work of Rives and Fenske predicted a $^1\Sigma^+$ ground state, with a calculated separation between the $^1\Sigma^+$ and $^3\Delta$ states of approximately 1.2 eV.[5] More recent calculations carried out by

Bauschlicher and co-workers confirmed the $^1\Sigma^+$ ground state prediction, and identified that this state arises from *sd* hybridization that results from the mixing of the ^{1}D ($4s^1 3d^9$) and ^{1}S ($3d^{10}$) Ni configurations.[6,7] Additionally, Bauschlicher and co-workers found the most important interaction in the Ni-CO bond to be the π back-donation occurring from the filled $3d\pi$ metal orbitals to the empty $2\pi^*$ CO orbitals; the metal-CO σ donation was found to have a minor or even repulsive bonding contribution.[6] In more recent calculations, Xu *et al*. confirmed that the largest contribution to forming the Ni-CO bond is indeed due to π-back bonding.[8]

Even though the number of theoretical calculations that have been performed on NiCO is extensive, the spectroscopic work has been rather limited. To date, the most commonly used spectroscopic technique for the investigation of NiCO has been matrix isolation spectroscopy. In the earliest matrix isolation study of NiCO, DeKock found the C-O (ν_1) vibrational frequency of this molecule trapped in Ar to be 1996 cm^{-1}.[9] Subsequent work, performed by Liang, *et al*., observed the ν_1 vibrational band of NiCO in a Ne matrix at 2006.6 cm^{-1}.[10] The different C-O vibrational frequencies observed in these studies arise from the interactions between the rare gas solids and NiCO. Typically, the use of heavier, more polarizable inert gases in the matrix results in a stronger interaction with the trapped molecule, thus causing a greater deviation of the vibrational frequency from the gas-phase value.[11]

Another method that was successfully used to study NiCO is mass-selected negative-ion photoelectron spectroscopy. With this technique, Leopold and co-workers found the ν_1 (C-O stretch) and ν_3 (Ni-C stretch) frequencies for the ground state of NiCO to be 2015 ± 10 and 595 ± 10 cm^{-1}, respectively.[12] Additionally, the electron affinity of

NiCO was determined to be 0.766 ± 0.005 eV, a value slightly smaller than the 0.804 ± 0.012 eV previously reported by the Lineberger group.[13] Finally, a broad, vibrationally unresolved, feature was identified as photodetachment of the anion to form the repulsive $^3\Sigma^+$ excited state.[12]

Recently, Yamazaki, Okabayashi, and Tanimoto recorded the rotational spectra of six isotopologues of NiCO using source modulation microwave spectroscopy.[14] The spectrum provided rotational and centrifugal distortion constants, from which Ni-C and C-O bond lengths were obtained using the r_0, r_s, $r_{1\varepsilon}$, $r_m^{(1)}$, and $r_m^{(2)}$ methods.

3.2 Experimental

The rotationally resolved spectra of NiCO, $Ni(CO)_3(^{13}CO)$, and $Ni(CO)_3(C^{18}O)$ collected in these studies were obtained using commercially available $Ni(CO)_4$ (Strem Chemicals). A small amount of $Ni(CO)_4$ was released from a lecture bottle and condensed into a trap cooled to -42°C with an acetonitrile-dry ice mixture. A gas mixture of 3% CO in Ar at a pressure of 60 psi was flushed over the cold $Ni(CO)_4$ sample, allowing the carrier gas mixture to pick up the equilibrium vapor pressure of $Ni(CO)_4$. This is estimated to be less than 13 Torr at this temperature, based on an extrapolation of the equilibrium vapor pressure of liquid $Ni(CO)_4$. As the nickel tetracarbonyl sample is a solid at -42°C, the actual vapor pressure could be much lower than 13 Torr. In initial experiments, pure Ar was used as the carrier gas, but an increase in the NiCO signal intensity was noted when CO was added.

The pulsed electrical discharge was operated at an instantaneous current of approximately 400 mA to fragment the $Ni(CO)_4$ parent molecule. Immediately downstream of the discharge, the carrier gas, the nickel tetracarbonyl, and any

fragmentation products undergo a supersonic expansion from the slit nozzle into vacuum. Supersonic expansion of the gases results in a substantial cooling of the internal degrees of freedom, leading to more readily assigned spectra. The spectra of NiCO, $Ni(CO)_3(^{13}CO)$, and $Ni(CO)_3(C^{18}O)$ were measured by scanning the laser frequency over the C–O, ^{13}C–O, and C–^{18}O stretches of these molecules, respectively, while monitoring the transmitted laser intensity.

3.3 Results

3.3.1 NiCO

Owing to the limited spectral range that could be accessed using the diode lasers only part of the ν_1 band of NiCO could be recorded. The sections that were examined lie in the 2005.1 – 2007.6, 2011.0 – 2012.3, and 2013.1 – 2015.1 cm^{-1} range. As displayed in Figure 3.1, the lowest and highest frequency regions contain the P(10) – P(17) and R(8) – R(14) lines, respectively. The intermediate region is not plotted in this figure, as the laser had a greatly reduced intensity in this region, leading to weaker absorption features. The stronger and weaker features in the NiCO spectrum are due to the more abundant ^{58}NiCO and less abundant ^{60}NiCO isotopologues, respectively. Additionally, the lines observed at 2006.4881 and 2013.2239 cm^{-1}, which are marked with an asterisk, arise from unknown species that are produced in the electrical discharge. These lines remain present when $Ni(CO)_4$ is removed from the carrier gas, but disappear when CO is removed from the gas stream.

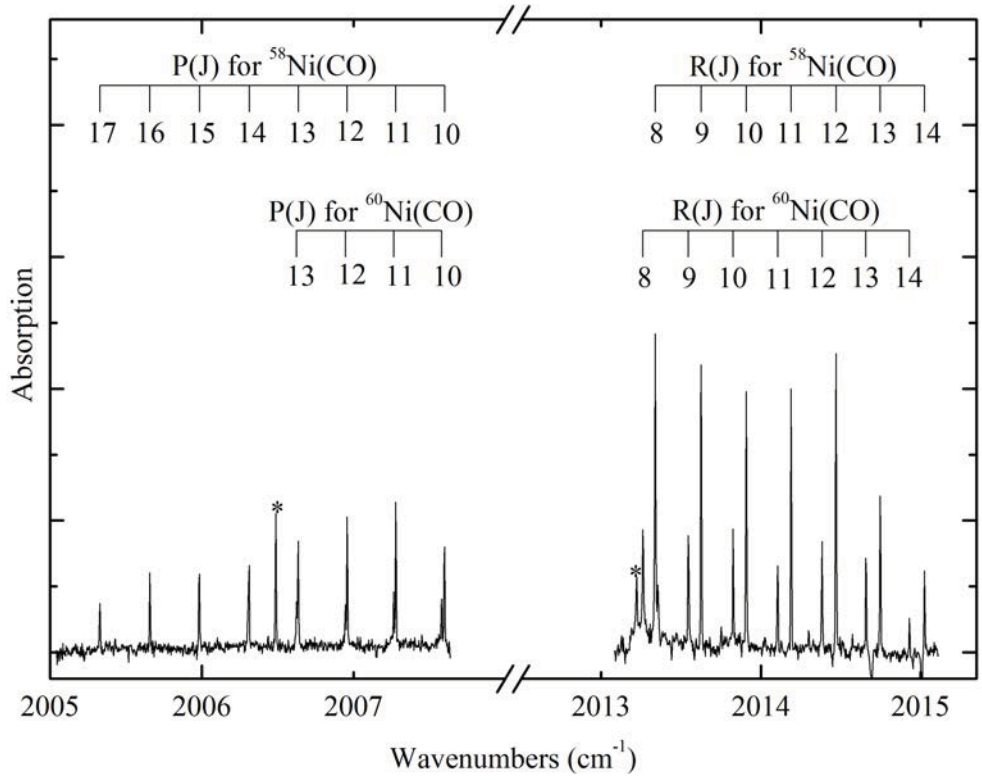

Figure 3.1 A scan of the diode laser over the 2005.1 – 2007.1 and 2013.1 – 2015.1 cm^{-1} range shows portions of the P and R branches of the CO stretching band of $^{58}NiCO$ (more intense features) and of $^{60}NiCO$ (weaker features). The positive going features in this spectrum are a result of the absorption of IR radiation as the molecule is being formed in the electrical discharge.

Calibration of each NiCO spectrum was accomplished with the use of an OCS reference cell and the NIST calibration tables[15] for this molecule. Assignment of each spectrum was achieved by fitting the rotational lines of each species to the formula

$$\nu = \nu_0 + \mathrm{B}'J'(J'+1) - \mathrm{B}''J''(J''+1), \tag{3.1}$$

as is appropriate for a linear molecule. Because the band origin fell within the spectral range which could not be reached with the available diode lasers, the gap between the R(0) and P(1) lines could not be observed. To obtain an unequivocal assignment of the observed lines, it was necessary to adjust the line numbering until a good match to the *B*" value obtained from microwave spectroscopy was achieved.[14] With this requirement, an unambiguous set of assignments was easily obtained. The assigned rotational lines, along with their frequencies and residuals, are listed in Table 3.1. From the least-squares fit, values of ν_0 = 2010.69289(34), *B*' = 0.150244(7), *B*" = 0.151094(7) cm^{-1} and ν_0 = 2010.64529(24), *B*' = 0.148741(6), *B*" = 0.149597(6) cm^{-1} are obtained for ^{58}NiCO and ^{60}NiCO, respectively. With the *B*" values of the two NiCO isotopologues in hand, the moments of inertia are readily deduced, allowing the bond lengths to be determined as r_0(Ni-C) = 1.641(40) Å and r_0(C-O) = 1.193(53) Å. The large relative uncertainty in these values results from the fact that the two isotopologues examined differ only in the mass of the heaviest atom, which is located closest to the center of mass. To achieve greater accuracy, isotopic modification of the C or O atoms would be required. Nevertheless, the resulting bond lengths are in agreement with the more precisely measured values of r_0(Ni-C) = 1.6723(4) Å and r_0(C-O) = 1.1512(5) Å recently obtained using microwave spectroscopy when the 1σ error limits are taken into account.[14]

Table 3.1 Rotational Line Positions for the ν_1 Vibrational Mode of ^{58}NiCO and ^{60}NiCO[a]

	^{58}NiCO			^{60}NiCO	
Line	Measured Wavenumber[b]	Residual[b,c]	Line	Measured Wavenumber[b]	Residual[b,c]
P(17)	2005.3253	-0.0008			
P(16)	2005.6546	-0.0007			
P(15)	2005.9803	0.0013			
P(14)	2006.3074	0.0002			
P(13)	2006.6313	0.0006	P(13)	2006.6218	0.0004
P(12)	2006.9551	-0.0006	P(12)	2006.9425	-0.0005
P(11)	2007.2749	0.0004	P(11)	2007.2603	-0.0003
P(10)	2007.5946	-0.0001	P(10)	2007.5760	0.0004
R(2)	2011.5895	-0.0002	R(2)	2011.5327	0.0001
R(3)	2011.8842	0.0005	R(3)	2011.8251	0.0000
R(4)	2012.1787	-0.0004	R(4)	2012.1158	-0.0001
R(8)	2013.3352	0.0009	R(8)	2013.2602	0.0009
R(9)	2013.6225	-0.0012	R(9)	2013.5432	-0.0001
R(10)	2013.9052	-0.0004	R(10)	2013.8236	-0.0002
R(11)	2014.1865	0.0001	R(11)	2014.1017	0.0003
R(12)	2014.4669	-0.0002	R(12)	2014.3794	-0.0003
R(13)	2014.7447	0.0004	R(13)	2014.6549	0.0006
R(14)	2015.0213	0.0004	R(14)	2014.9276	0.0003

[a]Values for ν_0, B', and B'' of 2010.69289(34), 0.150244(7), and 0.151094(7) cm^{-1} for ^{58}NiCO and 2010.64528(24), 0.148741(6), and 0.149597(6) cm^{-1} for ^{60}NiCO, respectively, were achieved by least-squares fitting the rotational lines to equation 3.1. Values in parentheses represent the 1 σ error limits, in units of the last reported digits.
[b]All numerical values are in units of cm^{-1}.
[c]The residuals are defined as $\nu_{obs} - \nu_{cal}$.

3.3.2 $Ni(CO)_3(^{13}CO)$ and $Ni(CO)_3(C^{18}O)$

While searching for the spectrum of NiCO, two other spectra were found in the range from 2020 – 2024 cm^{-1}. Instead of resulting from molecules that was created in the discharge, these spectra resulted from molecules depleted when the discharge was turned on. Accordingly, the carrier of the transitions were initially thought to be $Ni(CO)_4$. The tetrahedral $Ni(CO)_4$ molecule, however, displays only one IR active mode in the CO stretching region, with a band origin at 2061.3144 cm^{-1}.[16] When a ^{12}C atom is replaced with a ^{13}C atom, however, the C-O stretching frequency is expected to shift to the red, consistent with the spectra observed near 2022 cm^{-1}. Likewise, if a ^{16}O atom were replaced with an ^{18}O atom, a red shift would also be expected. Either the $Ni(CO)_3(^{13}CO)$ or the $Ni(CO)_3(C^{18}O)$ isotopologue could lead to the spectra observed near 2022 cm^{-1}.

Excitation of the normal mode most closely corresponding to the ^{13}CO stretch in the $Ni(CO)_3(^{13}CO)$ molecule (or the $C^{18}O$ stretch in the $Ni(CO)_3(C^{18}O)$ molecule) leads to a parallel band in a symmetric top. This is precisely the structure observed in the band displayed in Figure 3.2, which is a composite of multiple scans collected using two different diode lasers covering the 2020.4 – 2023.9 cm^{-1} spectral range. Figure 3.2 shows two distinct bands, with Q-branch intensities in a ratio of 4.4:1. At first it was believed that these two features corresponded to excitation of the ^{13}CO vibration in $^{58}Ni(CO)_3(^{13}CO)$ and $^{60}Ni(CO)_3(^{13}CO)$, since ^{13}C is a more abundant isotope than ^{18}O. However, the expected abundance ratio of $^{58}Ni(CO)_3(^{13}CO)$ relative to $^{60}Ni(CO)_3(^{13}CO)$ is 2.6:1, which is considerably lower than observed. An alternative possibility is that the two spectra are due to $Ni(CO)_3(^{13}CO)$ and $Ni(CO)_3(C^{18}O)$, with the ^{58}Ni and ^{60}Ni

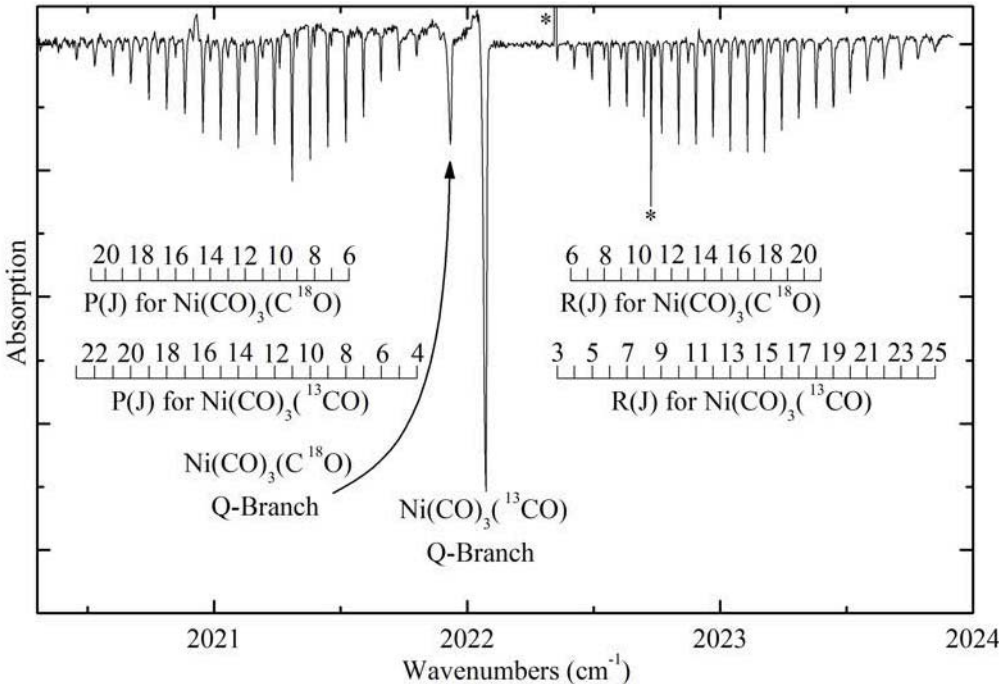

Figure 3.2. The $Ni(CO)_3(^{13}CO)$ and $Ni(CO)_3(C^{18}O)$ spectra were found in the 2020.4 – 2023.9 cm^{-1} spectral range. The more intense features in the spectrum correspond to $Ni(CO)_3(^{13}CO)$, while the weaker lines are due to $Ni(CO)_3(C^{18}O)$. The negative going features in the spectrum are due to the destruction of the parent molecule as a result of the electrical discharge. When the IR frequency is in resonance with a transition and the molecule is destroyed there is a decrease in the absorption intensity, resulting in negative going lines. Both spectra were detected for the isotopologues in their natural abundances of approximately 4.25% and 0.76%, respectively.

isotopologues unresolved. These species are expected to have an abundance ratio of 5.6:1, in much better agreement with the observations.

To verify that the $Ni(CO)_3(^{13}CO)$ and $Ni(CO)_3(C^{18}O)$ isotopologues would have vibrational transitions associated with the motions of the ^{13}CO and $C^{18}O$ subunits lying at nearly identical frequencies, quantum chemical calculations were undertaken to predict the vibrational frequencies using both Hartree-Fock and density functional approaches with Gaussian 03.[17] In all methods, the geometry was optimized, and then harmonic frequencies were calculated for the $^{58}Ni(CO)_4$, $^{60}Ni(CO)_4$, $^{58}Ni(CO)_3(^{13}CO)$, $^{60}Ni(CO)_3(^{13}CO)$, $^{58}Ni(CO)_3(C^{18}O)$, and $^{60}Ni(CO)_3(C^{18}O)$ isotopologues. All vibrational frequencies were then scaled by a multiplicative factor to bring the $^{58}Ni(CO)_4$ frequency into agreement with its known frequency of 2061.3144 cm^{-1}.[16] The specific methods that were employed were a Hartree-Fock calculation using the 6-311+G basis set,[18] and B3LYP density functional calculations using either the 6-311+G basis set[18] or the CEP-121G basis set.[19] The results are listed in Table 3.2.

The calculations provide three major results that support the assignment of the observed bands to the $Ni(CO)_3(^{13}CO)$ and $Ni(CO)_3(C^{18}O)$ species, with the $^{58}Ni/^{60}Ni$ isotopologues unresolved. First, all three methods predict that the vibrational frequencies of these two species lie within 3.5 cm^{-1} of each other, consistent with the 0.14 cm^{-1} separation that is observed. Second, when properly scaled, the calculated vibrational frequencies of the $Ni(CO)_3(^{13}CO)$ and $Ni(CO)_3(C^{18}O)$ species fall within 3 cm^{-1} of the measured bands. This certainly suggests that these isotopologues are the carriers of the spectra. Finally, the isotopic splitting due to the isotopes of nickel is calculated to be

Table 3.2 Calculated Properties of $Ni(CO)_4$ Isotopologues.

Property	HF/6-311+G	B3LYP/6-311+G	B3LYP/CEP-121-G
r(Ni-C) (Å)	1.9005	1.8347	1.8398
r(C-O) (Å)	1.1287	1.1591	1.1774
Vibrational scaling factor	0.944350894	1.047407906	1.062382491
Scaled vibrational frequencies (cm^{-1}):			
$^{58}Ni(CO)_4$	2061.3144	2061.3144	2061.3144
$^{60}Ni(CO)_4$	2061.3135	2061.3126	2061.3103
$^{58}Ni(CO)_3(^{13}CO)$	2022.8376	2021.4177	2021.3169
$^{60}Ni(CO)_3(^{13}CO)$	2022.8366	2021.4161	2021.3134
$^{58}Ni(CO)_3(C^{18}O)$	2019.3421	2021.8069	2022.6628
$^{60}Ni(CO)_3(C^{18}O)$	2019.3414	2021.8044	2022.6578

below 0.005 cm^{-1} in all three methods (much less for some methods), and this is too small to be resolved in these experiments. This casts doubt on the assignment in which the two bands originate from $^{58}Ni(CO)_3(^{13}CO)$ and $^{60}Ni(CO)_3(^{13}CO)$. Based on these results the two bands were assigned as originating from $Ni(CO)_3(^{13}CO)$ and $Ni(CO)_3(C^{18}O)$. These spectra are measured in their natural abundances of 4.25% and 0.76%, respectively.

Calibration of the $Ni(CO)_3(^{13}CO)$ and $Ni(CO)_3(C^{18}O)$ spectra was again accomplished with the use of an OCS reference cell and the NIST calibration tables.[15] Assignment of each spectrum was achieved by fitting the rotational lines of each species to the formula (3.1), which is valid in this case because the K substructure of the parallel transition is not resolved in the spectrum. The rotational line assignments, frequencies, and residuals in the least-squares fit for each isotopologue are listed in Table 3.3. The resulting values of ν_0, B', and B'' from the least-squares fits are 2022.075753(95), 0.034688(2), and 0.034736(2) cm^{-1} for $Ni(CO)_3(^{13}CO)$ and 2021.93684(18), 0.033710(3), and 0.033764(3) cm^{-1} for $Ni(CO)_3(C^{18}O)$, respectively. The 1σ error limits are given in parentheses.

3.4 Discussion

3.4.1 NiCO

As previously mentioned, an important characteristic of the bonding in the transition metal carbonyls is π-back bonding, in which the metal dπ-orbital overlaps with the $2\pi^*$ orbital of the CO molecule, resulting in the transfer of electron density from the metal to the $2\pi^*$ antibonding orbital. The result is a strengthening of the M-C bond and a weakening of the C-O bond. A comparison of the vibrational frequency ($\Delta G_{1/2}$) of the free CO molecule, 2143.27 cm^{-1},[20] to that of the t_2 mode of the saturated $Ni(CO)_4$

Table 3.3 Rotational Line Positions for $Ni(CO)_3(^{13}CO)$ and $Ni(CO)_3(C^{18}O)$[a]

$Ni(CO)_3(^{13}CO)$			$Ni(CO)_3(C^{18}O)$		
Line	Measured Wavenumber[b]	Residual[b,c]	Line	Measured Wavenumber[b]	Residual[b,c]
P(23)	2020.4534	-0.0001			
P(22)	2020.5255	-0.0006			
P(21)	2020.5962	0.0003			
P(20)	2020.6679	0.0000			
P(19)	2020.7394	-0.0002	P(19)	2020.6356	-0.0002
P(18)	2020.8107	-0.0003	P(18)	2020.7044	0.0005
P(17)	2020.8821	-0.0006	P(17)	2020.7743	-0.0001
P(16)	2020.9528	-0.0002	P(16)	2020.8442	-0.0007
P(15)	2021.0235	0.0000	P(15)	2020.9124	0.0002
P(14)	2021.0938	0.0005	P(14)	2020.9826	-0.0009
P(13)	2021.1649	0.0001	P(13)	2021.0511	-0.0005
P(12)	2021.2352	0.0005	P(12)	2021.1186	0.0008
P(11)	2021.3057	0.0005	P(11)	2021.1879	0.0002
P(10)	2021.3763	0.0004	P(10)	2021.2568	0.0000
P(9)	2021.4464	0.0006	P(9)	2021.3249	0.0004
P(8)	2021.5168	0.0005	P(8)	2021.3937	-0.0001
P(7)	2021.5872	0.0002	P(7)	2021.4610	0.0009
P(6)	2021.6570	0.0005	P(6)	2021.5294	0.0007
P(5)	2021.7280	-0.0006			
P(4)	2021.7978	-0.0005			
R(4)	2022.4216	0.0001			
R(5)	2022.4907	-0.0001			
R(6)	2022.5594	-0.0001	R(6)	2022.4063	0.0002
R(7)	2022.6284	-0.0004	R(7)	2022.4736	-0.0004
R(8)	2022.6970	-0.0004	R(8)	2022.5398	0.0000
R(9)	2022.7655	-0.0004	R(9)	2022.6063	-0.0001
R(10)	2022.8340	-0.0005	R(10)	2022.6731	-0.0006
R(11)	2022.9022	-0.0003	R(11)	2022.7393	-0.0005
R(12)	2022.9696	0.0005	R(12)	2022.8052	-0.0003
R(13)	2023.0380	0.0002	R(13)	2022.8712	-0.0003
R(14)	2023.1062	0.0000	R(14)	2022.9370	-0.0002
R(15)	2023.1741	0.0000	R(15)	2023.0022	0.0004
R(16)	2023.2417	0.0002	R(16)	2023.0684	-0.0001
R(17)	2023.3098	-0.0001	R(17)	2023.1338	0.0001
R(18)	2023.3772	0.0001	R(18)	2023.1996	-0.0003
R(19)	2023.4453	-0.0005	R(19)	2023.2639	0.0008
R(20)	2023.5127	-0.0004	R(20)	2023.3295	0.0004
R(21)	2023.5796	0.0000			
R(22)	2023.6464	0.0005			

Table 3.3 Continued

$Ni(CO)_3(^{13}CO)$			$Ni(CO)_3(C^{18}O)$		
Line	Measured Wavenumber[b]	Residual[b,c]	Line	Measured Wavenumber[b]	Residual[b,c]
R(23)	2023.7136	0.0004			
R(24)	2023.7807	0.0003			
R(25)	2023.8481	-0.0001			

[a]The rotational lines of each species were least-squares fitted to equation 3.1, thereby providing values for ν_0 of 2022.075753(95) and 2021.936835(185), *B*' of 0.034688(2) and 0.033710(3), and *B*" of 0.034736(2) and 0.033764(3) cm^{-1} for $Ni(CO)_3(^{13}CO)$ and $Ni(CO)_3(C^{18}O)$, respectively. Values in parentheses represent the 1 σ error limits, in units of the last reported digits.
[b]All numerical values are in units of cm^{-1}.
[c]The residuals are defined as $\nu_{obs} - \nu_{cal}$.

molecule, 2061.3144(45) cm^{-1},[16] demonstrates that this is a significant effect. The lower vibrational frequency of the CO stretching mode in nickel monocarbonyl, 2010.69289(34) cm^{-1} for the ^{58}Ni isotopologue, demonstrates that the π-backbonding interaction is even more substantial in the monocarbonyl.

It is of similar interest to compare the bond length of free CO to the C-O bond distance in NiCO and $Ni(CO)_4$. The free CO molecule bond length has been measured to be r_e = 1.128 Å.[20] This increases to 1.141(2) Å, as measured by electron diffraction,[21] in the tetrahedral $Ni(CO)_4$ molecule, and even further, to 1.1512(5) Å,[14] in NiCO. These changes are consistent with the changes in the CO vibrational frequency noted above. Likewise, if NiCO has a greater degree of 3*d*π backbonding than does $Ni(CO)_4$, one expects to see this borne out by a shorter Ni-C distance in NiCO than in $Ni(CO)_4$. This is indeed the case, with r_0(Ni-C) = 1.6723(4) Å in NiCO[14] and r(Ni-C) = 1.838(2) Å[21] in $Ni(CO)_4$.

A qualitative explanation of this difference is that in the NiCO molecule, four of the nickel 3*d* electrons occupy orbitals that are of the proper symmetry (π) to donate into the empty $2\pi^*$ orbital of CO, while in $Ni(CO)_4$, all ten of the Ni 3*d* electrons occupy orbitals of the appropriate symmetry (t_2 and e) to be donated into the CO antibonding orbital. If all of these electrons were fully donated, the CO ligand in NiCO would receive 4 electrons, while in $Ni(CO)_4$ each CO ligand would only receive 2.5 electrons, on average. Thus, the degree of π-backbonding per CO ligand that is possible in $Ni(CO)_4$ cannot match what is possible in the monocarbonyl. Furthermore, as the single Ni atom transfers electrons to its ligands, it becomes more positively charged, so that further electron transfer becomes increasingly disfavored due to electrostatic effects. This is a

greater limitation in the backbonding interactions in $Ni(CO)_4$ than in NiCO, because donation of one electron (for example) to the CO ligand in the case of NiCO leaves the Ni atom with an effective charge of +1; a corresponding transfer of one electron to each CO ligand in $Ni(CO)_4$ leaves the Ni atom with an effective charge of +4, a situation that is becoming electrostatically untenable. One would expect this effect to operate quite generally, so that the CO vibrational frequencies of a metal-CO complex should decrease as the number of CO ligands is reduced. An examination of the CO vibrational frequencies reported in the review of the unsaturated transition metal carbonyls by Zhou, Andrews, and Bauschlicher shows that this trend is generally followed, although exceptions can be found.[22]

The ν_1 vibrational frequency of NiCO measured in this study (2010.7cm^{-1}) is in good agreement with the value observed in Ne matrix isolation work (2006.6 cm^{-1}).[10] The vibrational frequency of the ν_1 mode measured in an Ar matrix isolation experiment (1996 cm^{-1}),[9] however, is a bit off compared to the gas phase value. The better agreement between the gas phase results and the Ne matrix data is expected, because of the larger polarizability of Ar as compared to Ne. It is well-known that neon, in general, causes smaller matrix shifts than other rare gas matrices, with the possible exception of helium.[23] There is also excellent agreement between the CO vibrational frequency found in this study (2010.7 cm^{-1}) and that reported by photodetachment measurements on $NiCO^-$ (2015 ± 10 cm^{-1}).[12]

3.4.2 $Ni(CO)_3(^{13}CO)$ and $Ni(CO)_3(C^{18}O)$

Only one previous study of the IR spectrum of $Ni(CO)_3(^{13}CO)$ was found in the literature. In that 1967 investigation,[24] IR spectra were reported for $Ni(^{12}CO)_4$ and

$Ni(^{12}CO)_3(^{13}CO)$ in *n*-hexane solution. Taking into account the shift between the gas phase frequency for $Ni(^{12}CO)_4$ (2061.3144 cm^{-1})[16] and the corresponding frequency in *n*-hexane solution (2045.7 cm^{-1}),[24] and applying this same solvent shift to the frequency of $Ni(^{12}CO)_3(^{13}CO)$ in *n*-hexane solution (2007.5 cm^{-1}),[24] one predicts a gas-phase frequency of 2023.1 cm^{-1}. This is in excellent agreement with our measured band origin of 2022.1 cm^{-1} for $Ni(^{12}CO)_3(^{13}CO)$.

Since electron diffraction is the only method that has thus far provided a gas phase measurement of the bond lengths in $Ni(CO)_4$, obtaining the rotationally resolved spectra of $Ni(CO)_3(^{13}CO)$ and $Ni(CO)_3(C^{18}O)$ led to much excitement. These isotopic modifications do not display the complications of vibrational angular momentum that are associated with the spherical top parent molecule, so the measured *B* constants may be directly related to the moment of inertia, I_B, which is a function of the Ni-C and C-O bond lengths. Thus, these quantities may be deduced from our observations. The expression for the moment of inertia, even in the isotopomers $Ni(CO)_3(^{13}CO)$ and $Ni(CO)_3(C^{18}O)$, depends simply on the Ni-C and Ni-O separations squared. Solving for the Ni-C and Ni-O internuclear separations, we obtain values of 1.8387 ± 0.0071 Å and 2.9601 ± 0.0034 Å, respectively. The error limits are obtained by propagating the 1σ errors in the *B* values of the two isotopomers, assuming that the errors in these two measurements are uncorrelated. This may not be completely valid, since they were measured from the same spectrum and both would therefore suffer from the same calibration errors. Of great chemical relevance is the C-O bond length, which is the difference of these two values, readily calculated to be 1.1214 ± 0.0078 Å. Once again, this error limit corresponds to the 1σ uncertainty limit, assuming the errors in the Ni-C

and Ni-O internuclear separations are uncorrelated. A safer error estimate would be to add the errors in the Ni-C and Ni-O internuclear separations, giving a C-O bond length of 1.1214 ± 0.0104 Å.

These values may be compared with the results of the gas phase electron diffraction measurement, r(Ni-C) = 1.838(2) Å and r(C-O)= 1.141(2) Å.[21] The Ni-C bond lengths obtained in both gas phase studies are in superb agreement, but the C-O bond lengths show a significant discrepancy. Both gas phase measurements differ significantly from the X-ray diffraction solid-phase measurement, which provided bond distances of r(Ni-C) = 1.817 Å and r(C-O) = 1.127 Å.[25] Most surprising is the fact that the C-O bond length obtained in the present study (and in the X-ray diffraction study) is actually shorter than the equilibrium bond length of free CO (1.1283 Å).[20] It is likely that the bending motion of the Ni-C-O subunit leads to a decrease in the average Ni-O separation, so that the C-O bond length is not given by the straightforward subtraction of the Ni-C separation from the Ni-O separation. While such a subtraction is valid when the Ni-C-O subunit is linear, it certainly becomes invalid as the Ni-C-O subunit bends. In this connection it is useful to note that all three computational methods employed in the calculations on $Ni(CO)_4$ predict that the molecule has 5 bending motions with harmonic frequencies below 80 cm^{-1}. These loose vibrational motions undoubtedly account for some of the difficulties in extracting a structure from the measured spectroscopic constants.

3.5 Conclusion

The excitation of the CO stretch in NiCO and the ^{13}CO and $C^{18}O$ stretches in $Ni(CO)_3(^{13}CO)$ and $Ni(CO)_3(C^{18}O)$, respectively, yielded rotationally resolved spectra for

these species. These spectra have provided precise vibrational frequencies and ground state and excited state rotational constants. The B" values for ^{58}NiCO and ^{60}NiCO allowed us to determine the bond lengths as r_0 (Ni-C) = 1.641(40) Å and r_0(C-O) = 1.193(53) Å, in agreement with more precise microwave measurements. From the measured vibrational frequencies and the calculated bond lengths for NiCO, it is determined that π-backbonding is more effective in NiCO, as compared to $Ni(CO)_4$. The studies of $Ni(CO)_3(^{13}CO)$ and $Ni(CO)_3(C^{18}O)$ provide vibrationally averaged internuclear separations of 1.8387(71) Å and 2.9601(34) Å, for the Ni-C and Ni-O distances in the ground vibrational level, respectively.

3.6 References

[1] C. M. Luckhart, *Fundamental Transition Metal Organometallic Chemistry*. (Brooks/Cole, Monterey, California, 1985); L. S. Hegedus, *Transition Metals in the Synthesis of Complex Organic Molecules*, 2nd ed. (University Science Books, Sausalito, California, 1999).

[2] P. S. Bagus, C. J. Nelin, and C. W. Bauschlicher, Jr., Phys. Rev. B **28** (10), 5423 (1983); C. W. Bauschlicher, Jr., Chem. Phys. Lett. **115** (6), 535 (1985); C. W. Bauschlicher, Jr., J. Chem. Phys. **101** (4), 3250 (1994); K. Horn, A. M. Bradshaw, K. Hermann, and I. P. Batra, Sol. State Comm. **31** (4), 257 (1979).

[3] R. M. Sosa, P. Gardiol, and G. Beltrame, Int. J. Quantum Chem. **69** (3), 371 (1998); P. V. Madhavan and J. L. Whitten, Chem. Phys. Lett. **127** (4), 354 (1986); V. Barone, Chem. Phys. Lett. **233** (1,2), 129 (1995); M. Sodupe, C. W. Bauschlicher, Jr., and T. J. Lee, Chem. Phys. Lett. **189** (3), 266 (1992); R. Fournier, J. Chem. Phys. **98** (10), 8041 (1993); R. Fournier, J. Chem. Phys. **99** (3), 1801 (1993); C. W. Bauschlicher, Jr., L. A. Barnes, and S. R. Langhoff, Chem. Phys. Lett. **151** (4-5), 391 (1988); M. R. A. Blomberg, U. B. Brandemark, P. E. M. Siegbahn, J. Wennerberg, and C. W. Bauschlicher, Jr., J. Am. Chem. Soc. **110** (20), 6650 (1988); M. R. A. Blomberg, P. E. M. Siegbahn, T. J. Lee, A. P. Rendell, and J. E. Rice, J. Chem. Phys. **95** (8), 5898 (1991).

[4] K. Hermann and P. S. Bagus, Phys. Rev. B **16** (10), 4195 (1977); S. P. Walch and W. A. Goddard, III, J. Am. Chem. Soc. **98** (25), 7908 (1976).

[5] A. B. Rives and R. F. Fenske, J. Chem. Phys. **75** (3), 1293 (1981).

[6] C. W. Bauschlicher, Jr., P. S. Bagus, and B. O. Roos, J. Chem. Phys. **85** (1), 354 (1986).

[7] C. W. Bauschlicher, Jr. and P. S. Bagus, J. Chem. Phys. **81** (12), 5889 (1984); G. L. Gutsev, L. Andrews, and C. W. Bauschlicher, Chem. Phys. **290** (1), 47 (2003).

[8] X. Xu, X. Lu, N. Wang, Q. Zhang, M. Ehara, and H. Nakatsuji, Int. J. Quantum Chem. **72** (3), 221 (1999).

[9] R. L. DeKock, Inorg. Chem. **10** (6), 1205 (1971).

[10] B. Liang, M. Zhou, and L. Andrews, J. Phys. Chem. A **104** (17), 3905 (2000).

[11] S. Cradock and A. J. Hinchcliffe, *Matrix Isolation: A Technique for the Study of Reactive Inorganic Species*. (Cambridge University, Cambridge, 1975).

[12] P. W. Villalta, P. T. Fenn, and D. G. Leopold, Proc. SPIE-The Int. Soc. Opt. Eng. **2124** (Laser Techniques for State-Selected and State-to-State Chemistry II), 325 (1994).

[13] A. E. Stevens, C. S. Feigerle, and W. C. Lineberger, J. Am. Chem. Soc. **104** (19), 5026 (1982).

[14] E. Yamazaki, T. Okabayashi, and M. Tanimoto, J. Am. Chem. Soc. **126** (4), 1028 (2004).

[15] A. G. Maki and J. S. Wells, NIST Special Publication **821**, 660 pp (1991).

[16] P. B. Davies, N. A. Martin, M. D. Nunes, D. A. Pape, and D. K. Russell, J. Chem. Phys. **93** (3), 1576 (1990).

[17] M. J. Frisch, G. W. Trucks, H. B. Schlegel, G. E. Scuseria, M. A. Robb, J. R. Cheeseman, J. A. J. Montgomery, T. Vreven, K. N. Kudin, J. C. Burant, J. M. Millam, S. S. Iyengar, J. Tomasi, V. Barone, B. Mennucci, M. Cossi, G. Scalmani, N. Rega, G. A. Petersson, H. Nakatsuji, M. Hada, M. Ehara, K. Toyota, R. Fukuda, J. Hasegawa, M. Ishida, T. Nakajima, Y. Honda, O. Kitao, H. Nakai, M. Klene, X. Li, J. E. Knox, H. P. Hratchian, J. B. Cross, C. Adamo, J. Jaramillo, R. Gomperts, R. E. Stratmann, O. Yazyev, A. J. Austin, R. Cammi, C. Pomelli, J. W. Ochterski, P. Y. Ayala, K. Morokuma, G. A. Voth, P. Salvador, J. J. Dannenberg, V. G. Zakrzewski, S. Dapprich, A. D. Daniels, M. C. Strain, O. Farkas, D. K. Malick, A. D. Rabuck, K. Raghavachari, J. B. Foresman, J. V. Ortiz, Q. Cui, A. G. Baboul, S. Clifford, J. Cioslowski, B. B. Stefanov, G. Liu, A. Liashenko, P. Piskorz, I. Komaromi, R. L. Martin, D. J. Fox, T. Keith, M. A. Al-Laham, C. Y. Peng, A. Nanayakkara, M. Challacombe, P. M. W. Gill, B. R. Johnson, W. Chen, M. W. Wong, C. Gonzalez, and J. A. Pople, Gaussian 03, Revision B.02 (Gaussian, Inc., Pittsburgh PA, 2003).

[18] A. J. H. Wachters, J. Chem. Phys. **52** (3), 1033 (1970); P. J. Hay, J. Chem. Phys. **66** (10), 4377 (1977); A. D. McLean and G. S. Chandler, J. Chem. Phys. **72** (10), 5639 (1980); R. Krishnan, J. S. Binkley, R. Seeger, and J. A. Pople, J. Chem. Phys. **72** (1), 650 (1980); K. Raghavachari and G. W. Trucks, J. Chem. Phys. **91** (2), 1062 (1989).

[19] W. J. Stevens, M. Krauss, H. Basch, and P. G. Jasien, Can. J. Chem. **70** (2), 612 (1992); W. J. Stevens, H. Basch, and M. Krauss, J. Chem. Phys. **81** (12), 6026 (1984).

[20] K. P. Huber and G. Herzberg, *Constants of Diatomic Molecules*. (Van Nostrand Reinhold, New York, 1979).

[21] L. Hedberg, T. Iijima, and K. Hedberg, J. Chem. Phys. **70** (7), 3224 (1979).

[22] M. Zhou, L. Andrews, and C. W. Bauschlicher, Jr., Chem. Rev. **101** (7), 1931 (2001).

[23] M. E. Jacox, Chem. Phys. **189** (2), 149 (1994).

[24] G. Bor, J. Organomet. Chem. **10**, 343 (1967).

[25] D. Braga, F. Grepioni, and A. G. Orpen, Organomet. **12** (4), 1481 (1993).

CHAPTER 4

RESONANT TWO-PHOTON IONIZATION SPECTROSCOPY OF DIATOMIC ZrF AND ZrCl: 760 – 555 nm

4.1 Introduction

The spectroscopy of the diatomic transition metal halides has been investigated since the early days of molecular spectroscopy. In the past 50 years enormous progress has been made, the ground and at least some of the low-lying electronic states are now known for all of the 3*d* series of transition metal fluorides (MF) and chlorides (MCl) and progress is being made for the 3*d* bromides and iodides. In contrast, the electronic structure of the 4*d* MF and MCl molecules remains poorly known, with experimental spectra available only for YF,[1] YCl,[2] ZrF,[3] ZrCl,[4-7] NbCl,[8] RuF,[9] RhF,[10] RhCl,[11] AgF,[12] and AgCl.[13] While the nature of the halogen (F *vs.* Cl) makes no difference in the ground electronic state for the 3*d* metal halides, there is an interesting dependence of the ground electronic configuration and term on whether the metal atom comes from the 3*d* or 4*d* series. Thus, for example, the ground state of TiF and TiCl ($\sigma^1\delta^1\pi^1$, $^4\Phi_r$)[14,15] differs from that of its isovalent 4*d* congener, ZrF and ZrCl($\sigma^2\delta^1$, $^2\Delta_r$).[3,7] Likewise, the ground states of the group 8 halides FeF ($\sigma^1\delta^3\pi^2\sigma^1$, $^6\Delta_i$)[16] and RuF ($\sigma^1\delta^3\pi^3$, $^4\Phi_i$)[9] differ, as do those of the group 9 halides CoF and CoCl ($\sigma^2\,\delta^3\,\pi^3$, $^3\Phi_i$)[17,18] and RhF and RhCl ($\sigma^1\delta^4\pi^3$, $^3\Pi_i$).[10,11] These differences reflect the variations in n*d* *vs.* (n+1)*s* orbital sizes, energies, and

occupation numbers that occur as one moves down a column within the transition metal series.

Despite the electronic complexity of the diatomic transition metal halides, high quality *ab initio* calculations have been reported on a large number of low-lying electronic states for all of the 3*d* MF molecules.[19-21] Fewer detailed computational investigations of the 4*d* series have been reported, however, with most of the species investigated using density functional methods.[22,23] Generally, these density functional studies only report the lowest energy state of a given spin multiplicity. The ground state of ZrF has been calculated to be a $^2\Delta$ state, deriving from the $3\sigma^2 1\delta^1$ configuration in both density functional theory[23] and in *ab initio*[24] calculations. In a more recent density functional calculation, however, the ground state is predicted to be of quartet multiplicity.[22] In the most recent calculation on ZrF, internally contracted multireference configuration interaction (IC-MRCI) calculations predict a $3\sigma^2 1\delta^1$, $^2\Delta$ ground term, followed by the $3\sigma^1 1\delta^2$, $^4\Sigma^-$ term at T_0 = 2383 cm^{-1}, and the $3\sigma^1 1\delta^1 2\pi^1$, $^4\Phi$ term at T_0 = 4179 cm^{-1}.[3] A complementary computational method that has shown great promise for the study of diatomic metal halides is ligand field theory (LFT),[25,26] which has been used to effectively treat entire manifolds of states in studies of the lanthanide halides[27-29] and oxides,[30-32] the actinide molecules ThO and UO,[33] the alkaline earth halides, oxides, and hydroxides,[34-36] and the transition metal oxides[37,38] and halides.[39-43] Ligand field methods show good promise for systematically understanding the differences between the electronic structures of the 3*d vs.* 4*d* metal halides.

Early reports of the spectra of ZrF[44] were subsequently shown to arise from CuF.[45] After the initial submission of this report, we became aware of a nearly

contemporaneous study of ZrF in the 420 – 470 nm range.[3] That investigation is in agreement with the present study, demonstrating that the ground state of ZrF has Ω = 3/2, arising from the $3\sigma^2 1\delta^1$, $^2\Delta_{3/2}$ term. In one other previous investigation, the bond energy of ZrF, however, has been evaluated through high-temperature mass spectrometric measurements of the gaseous equilibrium

$$BaF(g) + Zr(g) \leftrightarrow Ba(g) + ZrF(g), \qquad (4.1)$$

providing a value of D^0_{298} (Zr − F) = 6.49 ± 0.20 eV.[46] The appearance potential of ZrF^+ from ZrF neutral molecules has been measured as 6.5 ± 0.5 eV in the same study.[46]

Although the spectra of ZrF are not well known, a larger number of studies of ZrCl have been reported.[4,5,7,47] Initial work began in 1961, when Carroll and Daly reported three band systems in the ultraviolet that were suggested to arise from a $^4\Sigma^-$ ground state.[47] A reinvestigation of the band system near 410 nm maintained the assignment as a $^4\Pi \leftarrow X\ ^4\Sigma^-$ transition, although the rotational lines were not resolved.[4] Another band system was identified in the near infrared in 1980, and was rotationally resolved and assigned as a parallel transition. It was thought to be a $^2\Pi - {}^2\Pi$ system, although $^2\Delta - {}^2\Delta$ and $^2\Phi - {}^2\Phi$ transitions were also consistent with the data.[48] More recently, ZrCl has been investigated in a series of Fourier transform emission studies, and additional band systems have been observed.[5-7] The ground state has now been assigned as $X\ ^2\Delta_r$, deriving from a $\sigma^2\delta^1$ configuration of the Zr^+ ion,[7] based largely on the results of *ab initio* calculations.[7,49] The complexity of the electronic structure of ZrCl (or ZrF) arises because of the large number of low-lying states that result from the $5s^2 4d^1$, $5s^1 4d^2$,

and $4d^3$ configurations of the Zr^+ ion. This leads to at least 19 Hund's case (a) $\Lambda - S$ states lying within 15000 cm^{-1} of the ground state.[7]

With the electronic structure of YF having recently been investigated in the Morse group,[50] the intention in this study is to shed some light on the electronic structure of its neighbor, ZrF. In the process, the ground state bond length, vibrational frequency, and Ω value have been determined and several excited states have been identified.

4.2 Experimental

Diatomic ZrF was investigated by resonant two-photon ionization (R2PI) spectroscopy in a jet-cooled molecular beam with time-of-flight mass spectrometric detection, using an instrument that has been previously described in the literature[51] and Chapter 2 of this dissertation. The molecule was produced by pulsed laser ablation (Nd:YAG, 532 nm) of a zirconium sample disk in the throat of a supersonic expansion of helium containing about 0.1% CCl_2F_2. The resulting supersonic beam was roughly collimated with a 1 cm diameter conical skimmer and admitted into the Wiley-McLaren[52] ion source region of a reflectron time-of-flight mass spectrometer.[53] In the ion source region the output of a Nd:YAG-pumped dye laser was counterpropagated along the molecular beam axis and this axis was intersected at right angles with the output of an excimer laser in order to produce ions. Initial experiments were undertaken using ArF excimer radiation (193 nm, 6.42 eV). At high ArF fluences, the isotopes of Zr, ZrN, ZrO, ZrF, ZrCl were readily observed. The alignment of the lasers into the chamber was optimized using a known transition in ZrN.[54] The ZrN signal decayed over time as the surface layers of the zirconium sample were removed.

Initial scans were conducted using ArF radiation for the ionizing photon, but only a few transitions could be observed in ZrF, presumably due to efficient two-photon ionization at 193 nm, leading to a high background signal. This suggests that the ArF wavelength is resonant with a molecular transition, perhaps terminating on a Rydberg level. Nevertheless, the observation of transitions using ArF excimer radiation for ionization places the ionization energy of ZrF above 6.42 eV. When the ionization laser was changed to KrF (248 nm, 5.00 eV), the resonance enhancement was greatly improved. After this was discovered, all subsequent scans were undertaken using KrF excimer radiation as the ionizing photon. Because the molecule used as a source of fluorine was CCl_2F_2, we simultaneously recorded the spectra of ZrCl. In this Chapter, only the results of the vibrationally resolved study of ZrCl are reported, focusing instead on vibrationally and rotationally resolved studies of the ZrF molecule.

Vibronic scans were conducted over the range 12500 – 18000 cm^{-1}, and were calibrated using atomic transitions of zirconium that were observed over this range, many of which originated from metastable Zr atoms.[55] To achieve rotational resolution, selected bands were examined using an intracavity etalon to narrow the linewidth (~0.04 cm^{-1}) of the dye laser radiation. Under these conditions, the laser was pressure-scanned using SF_6. The rotationally resolved scans were calibrated by simultaneously recording the transmission spectrum through a cell filled with I_2 vapor, using the known I_2 absorption lines as tabulated by Gerstenkorn and Luc,[56] corrected for the error in the original measurements[57] and for the Doppler shift of the ZrF molecules as they traveled toward the light source at the beam velocity of helium (1.77×10^5 cm/s). The Doppler correction amounted to +0.10 cm^{-1} or less for all of the bands investigated.

Excited state lifetimes were also measured for many of the observed bands by firing the excimer laser at the time of maximum ZrF density, but varying the timing of the dye laser pulse. By monitoring the ion signal as a function of the delay between the two laser pulses and fitting the resulting decay curve to an exponential model using the Marquardt nonlinear least-squares algorithm,[58] the 1/e decay time, τ, was measured. To obtain an estimate of the error in this quantity, the decay curve was recorded and fitted a minimum of 4 times. The mean of the fitted lifetimes is reported, along with the standard deviation for the set of fitted values.

4.3 Results

4.3.1 Low-Resolution Spectra of ZrF and ZrCl

All together, 93 vibronic transitions were observed in the low-resolution spectrum of $^{90}Zr^{19}F$ over the range 14500 to 18000 cm^{-1}, of which 26 were ultimately arranged into three band systems. A portion of the spectrum covering the 15500 – 16500 cm^{-1} range is displayed in Figure 4.1. In order to determine whether vibrational hot bands were present, the wavenumber difference between all pairs of features was computed, and a Gaussian function of 1 cm^{-1} was assigned to each wavenumber difference. The resulting 4278 Gaussian functions were summed to create a continuous function representing a histogram of the wavenumber differences, with the idea that repeated differences would sum in phase to provide a peak in the plot. The resulting band difference histogram for $^{90}Zr^{19}F$ is displayed in Figure 4.2. Only a single peak is observed, at 691.34 cm^{-1}. The fact that there are multiple occurrences of band differences that match this value strongly suggests that the $v'' = 1$ level of the ground state is

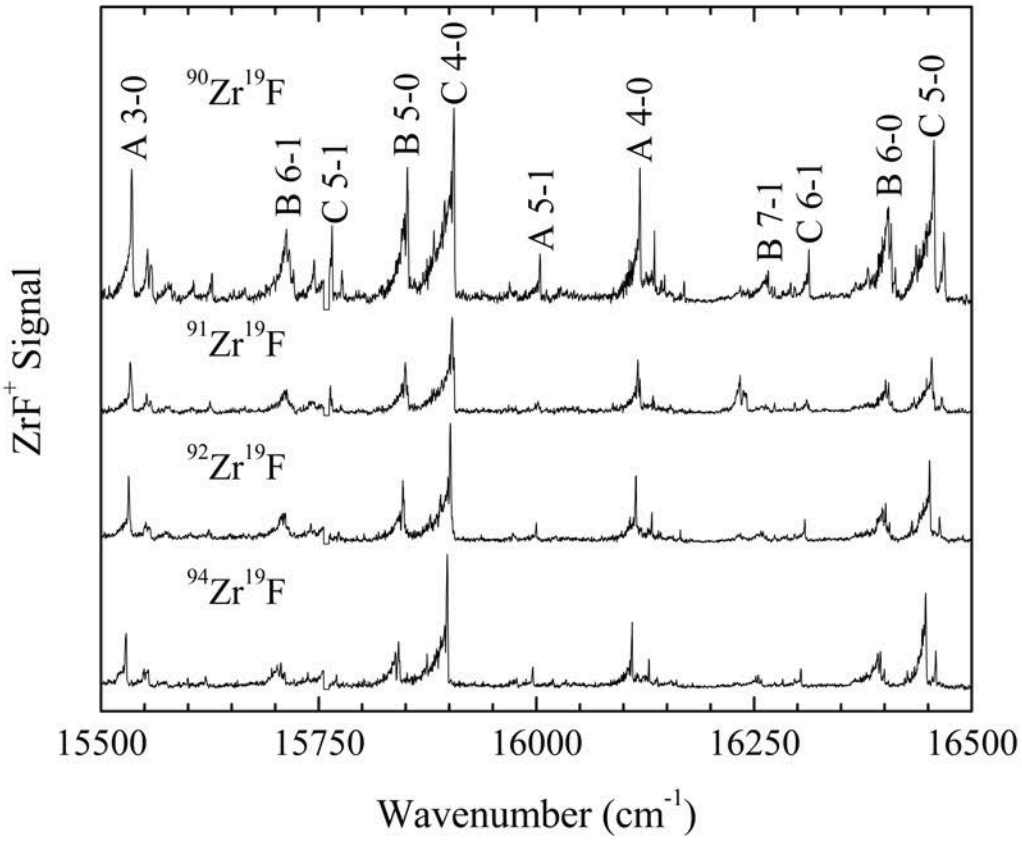

Figure 4.1 A portion of the spectrum recorded for the various isotopomers of ZrF, labeled according to the assigned band systems.

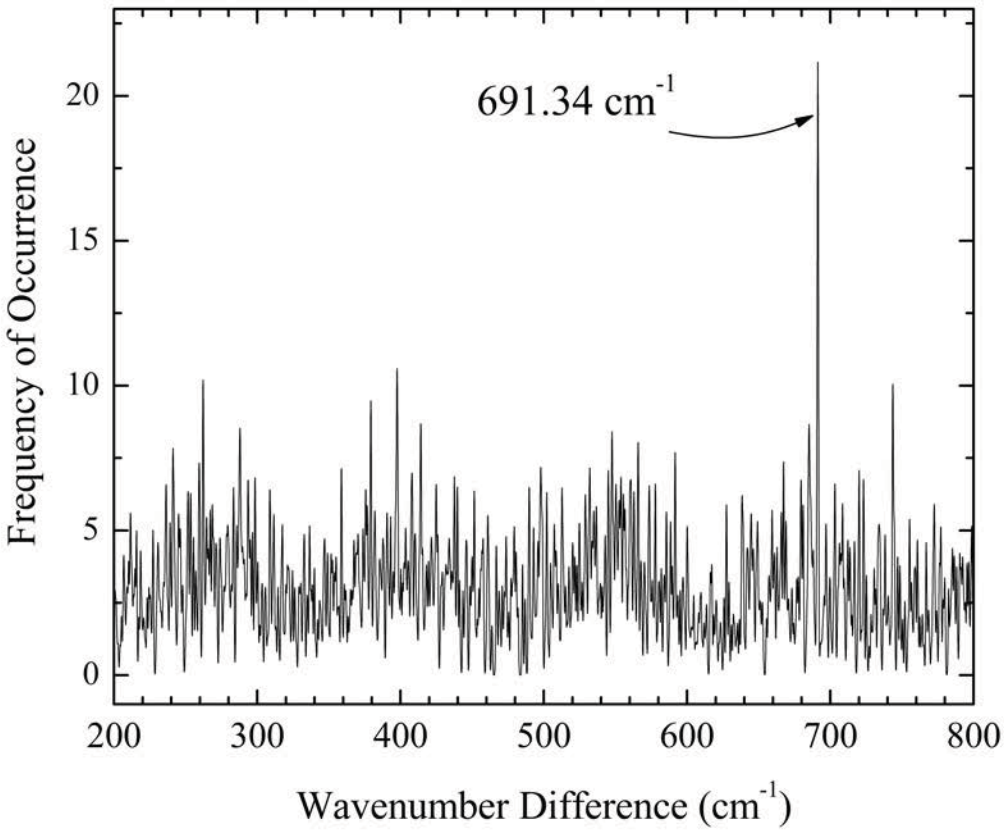

Figure 4.2 Band difference histogram plot for $^{90}Zr^{19}F$, showing a single peak at 691.34 cm^{-1}. This interval is assigned as the $\Delta G_{1/2}''$ value for the ground electronic state of $^{90}Zr^{19}F$.

populated in the molecular beam, and the $\Delta G_{1/2}''$ value for ground state $^{90}Zr^{19}F$ is 691.34 cm^{-1}. Repeating this procedure for the $^{91}Zr^{19}F$, $^{92}Zr^{19}F$, and $^{94}Zr^{19}F$ isotopic modifications also provided peaks shifted to the slightly lower frequencies of 690.56, 689.98, and 688.72 cm^{-1}, in keeping with the larger reduced masses of the heavier isotopic modifications. A more precise value of $\Delta G_{1/2}''$ is provided below from rotationally resolved studies.

Next, bands were sought that could be grouped into band systems, assuming near-constant intervals between successive bands in a progression and isotope shifts, $\nu(^{90}Zr^{19}F) - \nu(^{94}Zr^{19}F)$, that increased with increasing v'. Four progressions were readily assigned, although one of these turned out to be a set of $v'' = 1$ hot bands built on one of the other progressions. Vibrational assignments were established by varying the assignment of v', fitting the measured bands to obtain values of ω_e', $\omega_e'x_e'$, T_0 and $\Delta G_{1/2}''$, and then computing the transition wavenumber as a function of a continuous parameter, v', using the equation

$$\nu = T_0 + v' \omega_e' - (v'^2 + v') \omega_e'x_e'. \qquad (4.2)$$

The corresponding isotope shift was calculated as a function of v', as

$$\nu(^{90}Zr^{19}F) - \nu(^{94}Zr^{19}F) = (1-\rho)[\omega_e'(v'+½)-\omega_e''(½)] - (1-\rho^2)[\omega_e'x_e'(v'+½)^2 - \omega_e''x_e''(½)^2]. \qquad (4.3)$$

Here, the $^{90}Zr^{19}F$ isotope was used as the reference species, and the fitted values of ω_e', $\omega_e'x_e'$, T_0, and $\Delta G_{1/2}''$, which is taken to equal ω_e'', were used in equations (4.2) and (4.3). For purposes of calculating the isotope shift, it was assumed that $\omega_e''x_e''$ is zero. The

parameter ρ is given by $[\mu(^{90}Zr^{19}F)/\mu(^{94}Zr^{19}F)]^{1/2}$.[59] Plots of the resulting isotope shift *vs*. transition wavenumber provided a definite vibrational numbering for all three band systems, as illustrated in Figure 4.3 for the A – X band system. The bands that have been arranged into band systems are listed in Table 4.1, while the remaining band positions, along with band difference histograms, isotope shift plots, band positions and isotope shift plots for ZrCl, and rotational line positions and fits for ZrF, are available through the Electronic Physics Auxiliary Publication Service (EPAPS)[60] of the American Institute of Physics and also in Appendix B of this dissertation. This document also provides figures that display vibrationally (ZrF and ZrCl) and rotationally resolved spectra (ZrF only).

Similarly, 75 bands were observed in $^{90}Zr^{35}Cl$ (38.98% natural abundance), which falls at mass 125. Due to the presence of two naturally occurring isotopes of chlorine, the remaining prominent features in the mass spectrum of ZrCl are mixed isotopomers, with mass 129 being approximately 76% $^{94}Zr^{35}Cl$ and 24% $^{92}Zr^{37}Cl$. Vibronic features for $^{94}Zr^{35}Cl$ in this mass channel have been assigned to the corresponding bands in the pure isotopomer, $^{90}Zr^{35}Cl$. Although not as clean as in the case of ZrF, the measured isotope shifts provide a convincing vibrational assignment for the four band systems identified for ZrCl. These are listed in Table 4.2. Again, a listing of all the measured bands in mass 125 ($^{90}Zr^{35}Cl$) and mass 129 (76% $^{94}Zr^{35}Cl$ + 24% $^{92}Zr^{37}Cl$) are provided in the supplementary document. It is likely that the upper states labeled A and E, with T_0 values of 14363 and 13967 cm^{-1}, respectively, correspond to the calculated 2 $^2\Phi_{5/2}$ and 3 $^2\Pi_{1/2}$ states,[7] which neglecting spin-orbit interaction are calculated to lie at 12315 and 11108 cm^{-1}, respectively. To confirm this conjecture would require rotationally resolved studies to determine the Ω values of the upper states of these transitions.

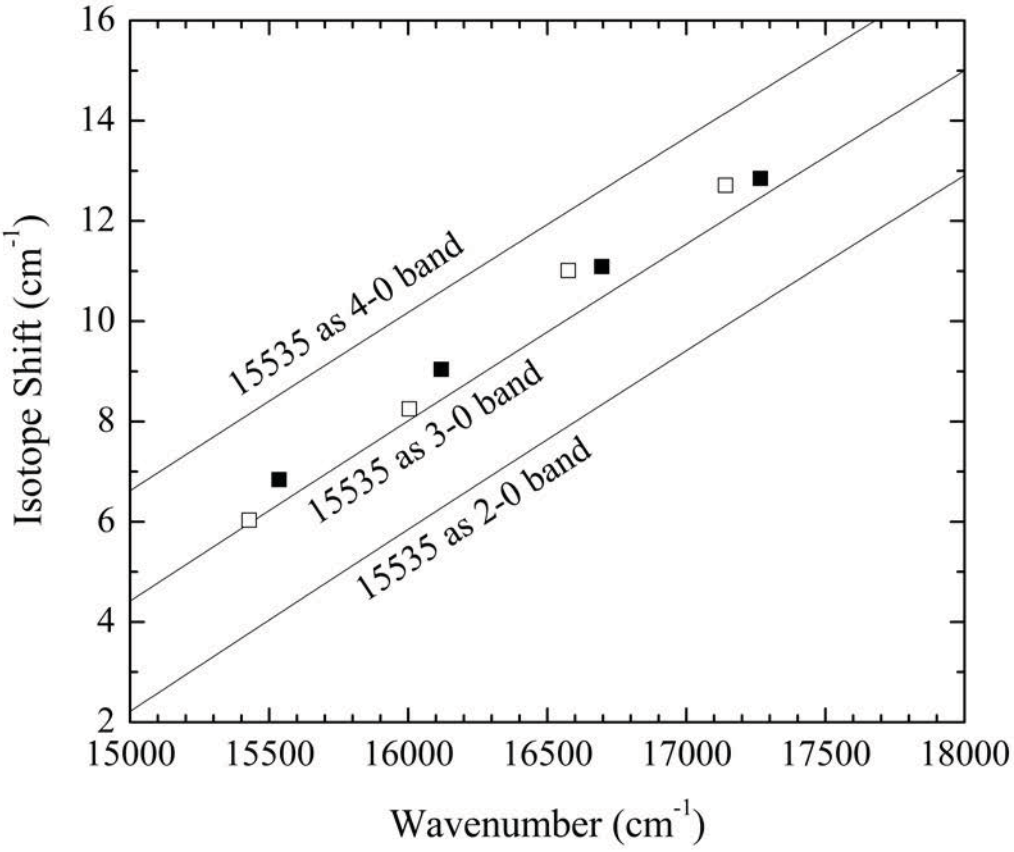

Figure 4.3 Calculated and measured isotope shifts for the A System of ZrF, for various possible vibrational numberings. Cold bands originating from v″ = 0, are indicated by the filled squares, while hot bands originating from v′ = 1 are indicated by open squares. From this plot it is clear that the first band observed in the progression, at 15535 cm^{-1}, is the 3 – 0 band.

Table 4.1 Band Heads and Excited State Lifetimes of Assigned Bands of ZrF.[a]

Band	$^{90}Zr^{19}F$	$^{91}Zr^{19}F$	$^{92}Zr^{19}F$	$^{94}Zr^{19}F$	Isotope Shift $\nu(^{90}Zr^{19}F)-\nu(^{94}Zr^{19}F)$	Lifetime (μs)
A – X 3-0	15535.4(-0.1)	15533.9(0.3)	15531.9(-0.1)	15528.6(0.0)	6.84	
A – X 4-0	16118.9(0.4)	16116.5(-0.2)	16114.3(0.5)	16109.8(0.2)	9.04	2.03(2)
A – X 5-0	16695.6(0.0)	16692.8(-0.1)	16689.9(0.0)	16684.6(0.0)	11.09	
A – X 6-0	17266.4(-0.4)		17259.7(-0.4)	17253.6(-0.2)	12.85	
A – X 3-1	14844.0(-0.3)	14843.0(-0.5)	14841.8(-0.3)	14839.6(-0.3)	4.40	
A – X 4-1	15427.7(0.4)	15427.2(0.8)	15424.3(0.3)	15421.2(0.4)	6.03	
A – X 5-1	16004.2(-0.2)	16002.2(-0.5)	15999.9(-0.1)	15995.9(0.1)	8.25	
A – X 6-1	16575.5(-0.2)	16572.4(0.2)	16569.9(-0.3)	16564.5(-0.5)	11.01	
A – X 7-1	17141.3(0.3)		17135.0(0.4)	17128.6(0.3)	12.71	
B – X 5-0	15851.9(-0.2)	15849.6(-1.0)	15846.7(-1.2)	15841.8(-0.4)	10.15	1.51(8)
B – X 6-0	16407.6(-0.9)	16404.5(1.7)	16401.2(0.7)	16395.0(1.1)	12.53	1.20(5)
B – X 7-0	16957.8(1.1)	16954.2(-0.7)	16950.3(0.6)	16943.2(-0.6)	14.64	0.90(2)
B – X 5-1	15160.5(1.4)	15158.9(0.4)	15157.7(1.2)	15153.1(0.4)	7.39	
B – X 6-1	15712.9(-2.6)	15710.3(-0.4)	15708.4(-0.7)	15703.2(-1.1)	9.75	
B – X 7-1	16266.1(2.4)		16257.7(-0.6)	16254.9(0.6)	11.22	
B – X 8-1	16802.8(-1.1)					

Table 4.1 Continued

Band	$^{90}Zr^{19}F$	$^{91}Zr^{19}F$	$^{92}Zr^{19}F$	$^{94}Zr^{19}F$	Isotope Shift $\nu(^{90}Zr^{19}F)-\nu(^{94}Zr^{19}F)$	Lifetime (μs)
C – X 2-0	14784.9(-0.2)	14782.8(-0.6)	14781.3(-0.6)	14780.0(-0.4)	4.85	
C – X 3-0	15347.3(0.0)	15346.3(0.7)	15344.7(0.8)	15341.9(0.4)	5.41	0.36(1)
C – X 4-0	15905.2(0.6)	15903.1(0.4)	15901.0(0.4)	15897.8(0.5)	7.44	0.49(3)
C – X 5-0	16456.4(-0.5)	16454.0(-0.6)	16451.5(-0.6)	16447.1(-0.6)	9.37	0.42(2)
C – X 6-0	17004.3(0.1)	17001.1(-0.3)	16998.0(-0.3)	16992.4(-0.3)	11.86	0.49(1)
C – X 7-0	17546.5(-0.1)	17543.3(0.3)	17539.5(0.3)	17532.6(0.2)	13.95	0.47(1)
C – X 4-1	15213.8(0.4)	15212.8(0.6)	15211.1(0.1)	15208.8(0.0)	4.96	
C – X 5-1	15765.3(-0.4)	15763.4(-0.7)				0.43(2)
C – X 6-1	16312.8(-0.3)	16310.8(-0.1)	16308.3(-0.3)	16304.0(-0.2)	8.84	
C – X 7-1	16855.8(0.3)	16852.6(0.1)	16849.7(0.2)	16844.0(0.1)	11.83	

Fitted spectroscopic constants

System	Parameter	$^{90}Zr^{19}F$	$^{91}Zr^{19}F$	$^{92}Zr^{19}F$	$^{94}Zr^{19}F$
A – X	T_0	13751.1(1.9)	13744.2(4.7)	13751.6(2.0)	13750.5(1.8)
	ω_e'	606.55(0.91)	610.0(2.5)	605.1(1.0)	604.5(0.9)
	$\omega_e'x_e'$	2.94(0.09)	3.38(0.25)	2.91(0.09)	2.94(0.08)
	$\Delta G_{1/2}$"	691.15(0.27)	690.20(0.50)	689.88(0.29)	688.77(0.26)

Table 4.1 Continued

System	Parameter	$^{90}Zr^{19}F$	$^{91}Zr^{19}F$	$^{92}Zr^{19}F$	$^{94}Zr^{19}F$
B – X	T_0	12949.4(38.9)	13046.1(58.2)	13033.9(46.5)	13058.5(41.7)
	ω_e'	604.8(13.4)	568.6(21.7)	573.0(17.0)	561.9(15.3)
	$\omega_e'x_e'$	4.03(0.97)	1.29(1.69)	1.70(1.31)	0.85(1.17)
	$\Delta G_{1/2}$"	693.0(1.9)	692.4(1.8)	691.5(1.2)	689.6(1.1)
C – X	T_0	13645.83(1.23)	13643.50(1.75)	13641.95(1.70)	13642.03(1.33)
	ω_e'	577.07(0.62)	577.68(0.89)	577.89(0.87)	577.21(0.68)
	$\omega_e'x_e'$	2.48(0.06)	2.58(0.08)	2.64(0.09)	2.68(0.06)
	$\Delta G_{1/2}$"	691.12(0.31)	690.50(0.44)	689.68(0.45)	688.50(0.35)

[a] All entries except the lifetime are given in wavenumbers (cm^{-1}). Following each transition wavenumber listed, the residual in the fit (observed - calculated) is provided in parentheses. Likewise, the 1σ error limits in the fitted constants are provided in parentheses following each entry.

Table 4.2 Band Heads of Assigned Bands of ZrCl.[a]

Band	$^{90}Zr^{35}Cl$	$^{94}Zr^{35}Cl$	Isotope Shift $\nu(^{90}Zr^{35}Cl)-\nu(^{94}Zr^{35}Cl)$
A – X 2-0	15023.1(2.4)	15020.5(3.2)	2.6
A – X 3-0	15347.9(-3.5)	15340.4(-4.7)	7.5
A – X 4-0	15683.4(-0.1)	15675.8(0.6)	7.6
A – X 5-0	16018.1(1.2)	16008.5(0.9)	9.6
A – X 3-1	14936.4(-1.9)	14931.6(-2.7)	4.8
A – X 4-1	15272.1(1.7)	15266.7(2.3)	5.4
A – X 5-1	15605.9(2.1)	15599.3(2.6)	6.6
A – X 6-1	15936.7(-1.9)	15929.0(-2.3)	7.7
B – X 0-0	15648.6(0.0)	15648.7(0.0)	-0.1
B – X 1-0	15973.2(0.0)	15971.4(0.0)	1.8
B – X 2-0	16295.7(0.1)	16292.2(0.2)	3.5
B – X 3-0	16615.8(0.0)	16610.4(-0.3)	5.4
B – X 4-0	16933.8(0.0)	16927.5(0.1)	6.3
B – X 4-1	16521.9(0.0)	16519.0(0.0)	2.9
E – X 0-0	13967.4(0.0)	13968.2(0.0)	-0.8
E – X 1-0	14320.2(-0.4)	14319.2(0.0)	1.0
E – X 2-0	14670.7(0.4)	14667.2(0.0)	3.5
E – X 1-1	13912.6(0.4)	13913.3(0.0)	-0.7
E – X 2-1	14261.4(-0.4)	14261.3(0.0)	0.1
E – X 3-1	14607.9(0.0)		
C – X 0-0	17463.7	17466.0	-2.3
C – X 1-0	17809.2	17807.0	2.2
C – X 0-1	17054.3	17055.9	-1.6
C – X 0-2	16643.8	16650.6	-6.8
Fitted spectroscopic constants			
System	Parameter	$^{90}Zr^{35}Cl$	$^{94}Zr^{35}Cl$
A – X	T_0	14363.2(10.6)	14368.3(13.9)
	ω_e'	326.7(6.3)	321.2(8.2)
	$\omega_e'x_e'$	-0.67(0.69)	-1.12(0.90)
	$\Delta G_{1/2}''$	413.1(2.3)	410.8(3.0)

Table 4.2 Continued

System	Parameter	$^{90}Zr^{35}Cl$	$^{94}Zr^{35}Cl$
B – X	T_0	15648.59(0.05)	15648.75(0.24)
	ω_e'	326.87(0.07)	324.59(0.35)
	$\omega_e'x_e'$	1.11(0.01)	0.98(0.07)
	$\Delta G_{1/2}''$	411.89(0.07)	408.39(0.35)
C – X	T_0	17463.7	17466.0
	$\Delta G_{1/2}'$	345.5	341.0
	ω_e''	408.3	414.9
	$\omega_e''x_e''$	-0.55	2.4
E – X	T_0	13967.4(0.6)	13968.2(0.0)
	ω_e'	356.8(1.1)	354.0(0.0)
	$\omega_e'x_e'$	1.79(0.26)	1.50(0.00)
	$\Delta G_{1/2}''$	408.5(0.6)	405.9(0.0)

[a] All entries are given in wavenumbers (cm^{-1}). Following each transition wavenumber listed, the residual in the fit (observed - calculated) is provided in parentheses. Likewise, the 1σ error limits in the fitted constants are provided in parentheses following each entry.

4.3.2 Rotationally Resolved Spectra of ZrF

In order to measure the ZrF bond length and gain insight into the electronic symmetries of the ground and excited electronic states, experiments were undertaken to rotationally resolve bands belonging to the three band systems. The 3-0 and 4-0 bands of the A – X system were successfully resolved and analyzed, as was the 4-0 band of the C – X system. The remaining bands that were investigated (the 5-0, 6-0, and 7-0 bands of the B – X system, and the 5-0, 5-1, and 6-0 bands of the C – X system) were all perturbed by nearby states. In some cases, line assignments could be made using the ground state rotational constant obtained from the unperturbed bands and combination differences, but this was not always possible. From the fits of the unperturbed 3-0 and 4-0 bands of the A – X system, the fit of the 4-0 band of the C – X system, and one unperturbed *e/f* component of the 6-0 band of the C – X system, a simultaneous fit of the rotational lines provides ground and excited state rotational constants and bond lengths, as listed in Table 4.3.

Using only data from the better-determined isotopic modifications, $^{90}Zr^{19}F$, $^{91}Zr^{19}F$, and $^{92}Zr^{19}F$, this gives a weighted average bond length for the $v'' = 0$ level of the ZrF $\Omega = 3/2$ ground state of r_0 ($X\ ^2\Delta_{3/2}$) = 1.8577(1) Å. In fact, this estimate of the $v'' = 0$ is in error because of S-uncoupling interactions between the $X_1\ ^2\Delta_{3/2}$ and $X_2\ ^2\Delta_{5/2}$ states. A correction for this interaction can be made if the spin-orbit splitting in the $X\ ^2\Delta$ state is assumed to be identical to that found in ZrCl (705 cm^{-1}),[7] using the well-known formula[59]

$$B_{eff}\left(X_1\,^2\Delta_{3/2}\right) = B\left(1 + \frac{2B\Sigma}{A\Lambda}\right). \qquad (4.4)$$

Table 4.3 Fitted Rotational Constants and Bond Lengths of ZrF from Rotationally Resolved Studies. [a]

Level	Spectroscopic Parameter	$^{90}Zr^{19}F$	$^{91}Zr^{19}F$	$^{92}Zr^{19}F$	$^{94}Zr^{19}F$	$^{96}Zr^{19}F$
C1.5	ν_0	17002.6818(45)	16999.6208(27)	16996.6671(37)		
	B_6'	0.26837(7)	0.26813(6)	0.26839(7)		
	r_6'	2.0013(3)	2.0002(2)	1.9973(3)		
C1.5	ν_0	16455.1229(81)	16452.6216(42)	16450.1862(39)	16445.5015(69)	16441.0486(69)
	B_5'	0.26441(16)	0.26414(7)	0.26393(10)	0.26348(26)	0.26373(19)
	r_5'	2.0162(6)	2.0153(3)	2.0142(4)	2.0122(10)	2.0077(7)
C1.5	ν_0	15902.5668(34)	15900.6393(24)	15898.6757(28)	15895.1678(19)	15891.6721(77)
	B_4'	0.28098(5)	0.28020(3)	0.27956(8)	0.27782(8)	0.27652(21)
	r_4'	1.9558(2)	1.9567(1)	1.9571(3)	1.9596(3)	1.9607(7)
	$p_\Delta' + 4q_\Delta'$	0.000264(2)	0.000252(2)	0.000226(6)	0.000176(2)	
A1.5	ν_0	15532.8748(22)	15531.1305(12)	15529.4125(17)	15526.0971(20)	15522.9294(22)
	B_3'	0.27998(5)	0.27954(3)	0.27916(6)	0.27792(8)	0.27752(14)
	r_3'	1.9593(2)	1.9590(1)	1.9585(2)	1.9592(3)	1.9572(5)
A1.5	ν_0	16116.5304(20)	16114.2296(15)	16111.9705(18)	16107.6036(30)	
	B_4'	0.27859(8)	0.27816(3)	0.27778(7)	0.27655(7)	
	r_4'	1.9642(3)	1.9638(1)	1.9633(2)	1.9641(2)	

Table 4.3 Continued

Level	Spectroscopic Parameter	$^{90}Zr^{19}F$	$^{91}Zr^{19}F$	$^{92}Zr^{19}F$	$^{94}Zr^{19}F$	$^{96}Zr^{19}F$
X1.5	B_0''	0.31139(6)	0.31086(6)	0.31036(8)	0.30889(10)	0.30842(24)
	r_0''	1.8579(2)	1.8577(2)	1.8574(2)	1.8584(3)	1.8566(7)
	B_1''	0.30870(40)	0.30963(105)	0.30893(32)		
	r_1''	1.8660(12)	1.8639(18)	1.8617(10)		
	$\Delta G_{1/2}''$	691.45(2)	690.80(3)	690.12(1)		

[a] Owing to perturbations, only one component of the C1.5 – X1.5 6 – 0 band could be fitted. Similarly, perturbations become apparent at higher values of J in the C1.5 – X1.5 5 – 0 band. Only the low-J transitions were included in the fit reported here. The measured line positions of the A – X 3 – 0, A – X 4 – 0, C – X 4 – 0, and one component of the C – X 6 – 0 band were simultaneously fitted to extract the ground state constant, B_0''. The C – X 5 – 1 band was used to extract B_1'' and $\Delta G_{1/2}''$ as described in the text.

Using this formula with $\Sigma = -1/2$ and $A\Lambda = 705$ cm^{-1}, we obtained a revised value of r_0 (X $^2\Delta$) = 1.8573(1) Å. Finally, combining the corrected B_0 value with a similarly corrected B_1 value obtained from a vibrational hot band, we obtained our best estimate for r_e (X $^2\Delta$) of 1.854(1) Å. Unfortunately, the poor quality of the data for the vibrational hot band increases the error in this value significantly compared to the r_0 value. Here and throughout this Chapter, 1σ error limits are provided in parentheses, in units of the last quoted digit.

4.3.2.1 Rotationally Resolved Spectra of the A1.5 – X1.5 System

Figure 4.4 displays a rotationally resolved scan over the 3-0 band of the A – X system, as recorded for the most abundant isotopic modification, $^{90}Zr^{19}F$. The spectrum shows a head in the R-branch, with a large number of P lines marching off to lower wavenumbers. A weak Q-branch with rapidly diminishing intensity indicates that the transition has $\Delta\Omega = 0$, as do all of the bands that were investigated in this study. The assigned lines fit very well to the simple formula

$$\nu = \nu_0 + B'J'(J' + 1) - B''J''(J'' + 1), \qquad (4.5)$$

indicating that there is no observable lambda doubling for either the upper or lower state in this band. Further, the first lines of P(2.5), Q(1.5), and R(1.5) demonstrate that $\Omega' = \Omega'' = 3/2$. A scan over the 4-0 band shows a very similar spectrum as that displayed in Figure 4.4.

Simulation of this spectrum requires a surprisingly high temperature, roughly 100 K. This is unusual for our supersonic expansion source. The point of vaporization in the source is about 1 cm upstream of the final expansion orifice, so normally the molecules

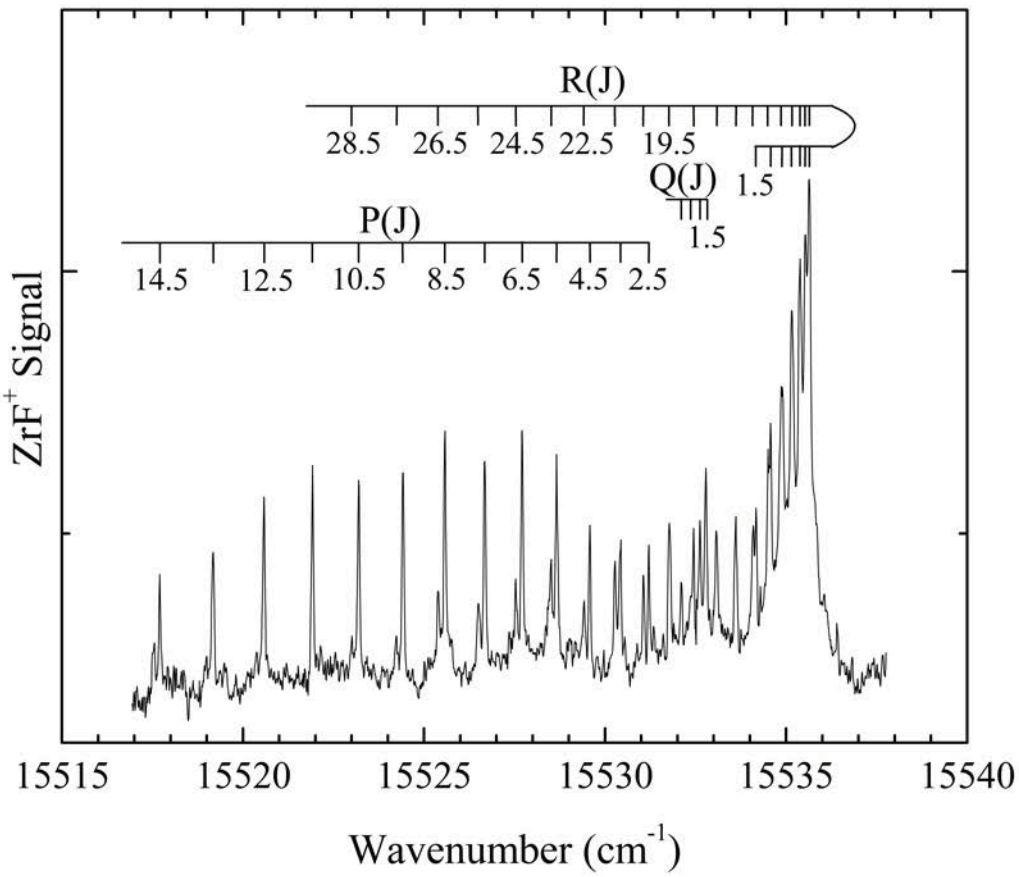

Figure 4.4 Rotationally resolved spectrum of the 3 – 0 band of the A – X system of $^{90}Zr^{19}F$.

produced in the source are exposed to a large number of collisions prior to and during expansion, resulting in cold molecules (10-20 K). The high rotational temperature observed in this case suggests that ZrF molecules that form close to the point of ablation go on to react further, producing larger species such as ZrF_2, which is also detected in the mass spectrum in significant quantities. The ZrF molecules that we detect are likely formed just as the gases are expanding into vacuum, limiting the amount of cooling that they experience, leading to the high rotational temperatures that are observed. This possibility also accounts for the significant population in $v'' = 1$ as well.

4.3.2.2. Rotationally Resolved Spectra of the B – X System

Rotationally resolved studies of the B – X system have been frustrating due to the fact that all of the bands investigated are strongly perturbed. Although it has been possible to assign rotational lines in the B – X 5-0 band, the $v' = 5$ level shows a large lambda doubling that leads to two R-branch band heads, and a pronounced curvature in the reduced term energy plot. It is simply not possible to extract any meaningful upper state rotational constants from this band. Likewise, the B – X 6-0 band is severely perturbed and could not be analyzed. Finally, the B – X 7-0 band was examined, and two distinct bands were found for $^{90}Zr^{19}F$, separated by only 2.5 cm^{-1}. Although these could both be assigned and fitted, it is doubtful that useful information can be obtained from this analysis. It appears that the B state of ZrF has $\Omega' = 3/2$, although overlapping lines in this perturbed band system makes this conclusion rather tentative. In contrast, the A and C states of ZrF definitely possess $\Omega' = 3/2$.

4.3.2.3 Rotationally Resolved Spectra of the C 3/2 – X 3/2 System

Rotationally resolved studies of the C – X system were partially successful. The 4-0 band, displayed in Figure 4.5 for the $^{90}Zr^{19}F$ isotopic modification, is apparently unperturbed except for remote perturbations that lead to lambda doubling, which is evident in the P-branch. The spectrum is readily fitted to the form

$$\nu = \nu_0 + B'J'(J' + 1) \pm [-1/2(p_\Delta' + 4\, q_\Delta')] \times (J' - 1/2)\,(J' + 1/2)\,(J' + 3/2) - B''J''(J'' + 1) \qquad (4.6)$$

for $^{90}Zr^{19}F$, $^{91}Zr^{19}F$, $^{92}Zr^{19}F$, and $^{94}Zr^{19}F$ and displays a smooth, monotonic decrease in the magnitude of the lambda doubling ($p_\Delta' + 4\, q_\Delta'$) with reduced mass. The form of the lambda doubling employed in equation (4.6) is valid for a $^2\Delta_{3/2}$ upper state,[61] but requires a redefinition of the constant ($p_\Delta' + 4\, q_\Delta'$) if the upper state is a $^2\Pi_{3/2}$, $^4\Pi_{3/2}$, or $^4\Delta_{3/2}$ state.[61,62] Regardless of the nature of the upper state, however, the first nonvanishing correction due to lambda doubling in an $\Omega = 3/2$ state exhibits the J-dependence given in equation (4.6),[61,62] which fits the spectrum well.

The 5-0 and 5-1 bands of the C 3/2 – X 3/2 system were also investigated, leading to an improved value of $\Delta G_{1/2}''$. These bands exhibit perturbations that prevent them from being fitted to the form of equation (4.6). Nevertheless, lines have been identified and the differences between corresponding lines allow $\Delta G_{1/2}''$ to be determined via the equation

$$\nu(C\ 5 - 0, J' \leftarrow J'') - \nu(C5 - 1, J' \leftarrow J'') = \Delta G_{½}'' + (B_1'' - B_0'')\, J''(J'' + 1). \qquad (4.7)$$

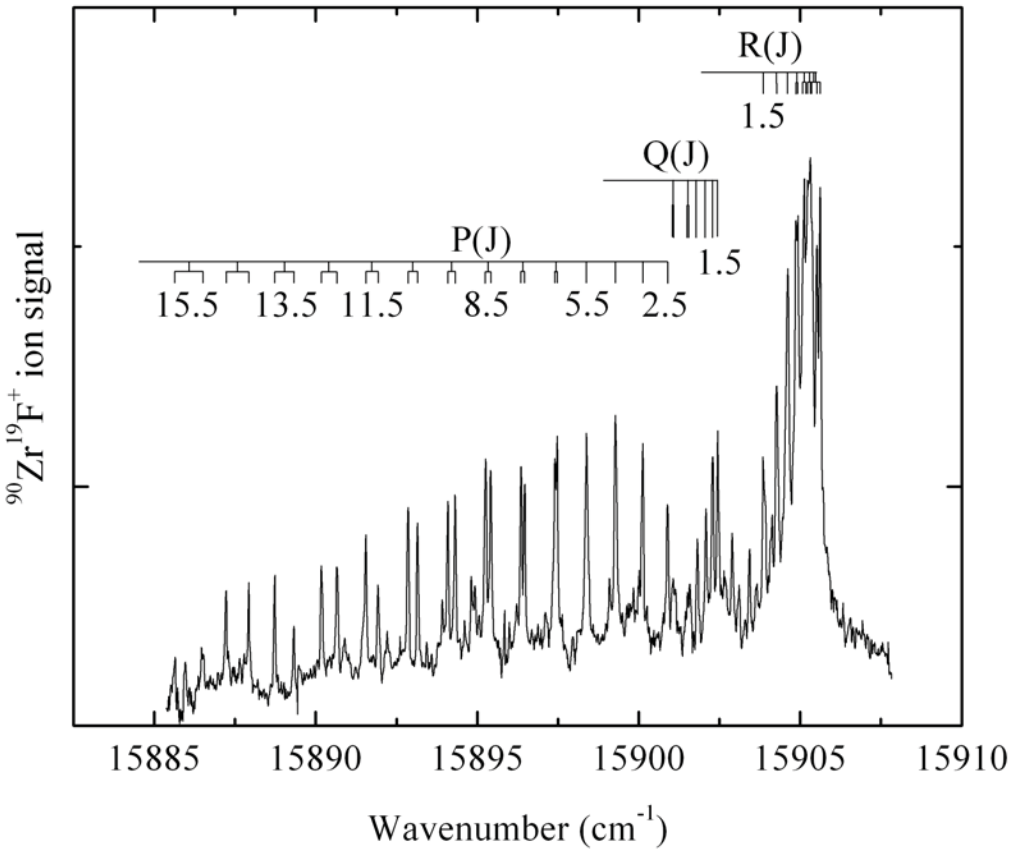

Figure 4.5 Rotationally resolved spectrum of the 4 – 0 band of the C – X system of $^{90}Zr^{19}F$. Lambda doubling is evident in the P-branch, but less obvious in the R-branch.

Using equation (4.7), the measured differences between corresponding rotational lines were fitted as a linear function of J″(J″ + 1), allowing values of $\Delta G_{1/2}''$ and (B_1'' - B_0'') to be extracted from the data. The resulting values of $\Delta G_{1/2}''$ for $^{90}Zr^{19}F$, $^{91}Zr^{19}F$, and $^{92}Zr^{19}F$ are 691.45(2), 690.83(1), and 690.12(1) cm^{-1}, respectively. These are slightly larger than the values estimated from the measured band heads using the band difference histogram method. The derived values of B_1'' and r_1'' are provided in Table 4.3.

4.4 Discussion

While it is satisfying that this investigation has successfully determined the bond length and vibrational frequency of the ZrF ground state, it is unfortunate that the ground electronic configuration and term cannot be clearly identified by the spectroscopic measurements alone. Owing to the high electron affinity of fluorine (3.399 eV)[63] and the low ionization energy of zirconium (6.634 eV),[64] the molecule is certainly ionic in its low energy states, arising from a combination of $Zr^+ + F^-$. While the F^- anion is a closed-shell, $2p^6$, ^1S_g species, the Zr^+ ion has low-lying states arising from the $4d^3$, $4d^25s^1$, and $4d^15s^2$ configurations. The lowest energy levels in each of these configurations are $^4F_{3/2g}$, $^4F_{3/2g}$, and $^2D_{3/2g}$, lying at 2572, 0, and 14299 cm^{-1}, respectively.[55] Further, the $4d^3$, $4d^25s^1$, and $4d^15s^2$ configurations lead to 29, 21, and 3 molecular terms described by S and Λ, respectively, which in turn generate 60, 45, and 5 distinct doubly-degenerate spin-orbit levels labeled by S, Λ, and Ω. Thus, the electronic structure of ZrF is rather complicated.

In the isovalent TiF, TiCl, and TiBr molecules, it is now clear that the ground state is the $3\sigma^1 1\delta^1 2\pi^1$, $^4\Phi_{3/2}$ level that correlates to the $3d^24s^1$, ^4F_g ground term of the Ti^+ ion.[14,15,49,65-70] In the 5*d* analogs, HfF and HfCl, on the other hand, the ground state is the

$3\sigma^2 1\delta^1$, $^2\Delta_{3/2}$ level that correlates to the $5d^1 6s^2$, ^2D_g ground term of Hf^+, with a significant contribution from the $5d^2 6s^1$ configuration.[7,71,72] The zirconium halides, however, lie in an intermediate position between these two clear-cut cases. In ZrCl, careful *ab initio* calculations place the $^2\Delta$ term only 330 – 760 cm^{-1} below the $^4\Phi$ term.[7,49] This separation is expected to narrow when spin-orbit interaction is taken into account, because the $^2\Delta_{3/2}$ level has a first order spin-orbit correction, calculated using numerical Hartree-Fock methods to evaluate ζ_{4d} for the $4d^1 5s^2$, ^2D_g term of Zr^+,[73] of $-\zeta_{4d}$ (Zr^+, $4d^1 5s^2$, ^2D) ≈ -460 cm^{-1}, while the $^4\Phi_{3/2}$ level has a first-order spin-orbit energy correction of – 3/2 ζ_{4d} (Zr^+, $4d^2 5s^1$, ^4F) ≈ -598 cm^{-1}. Thus, the spin-orbit interaction may be expected to reduce the separation between these two states by roughly 138 cm^{-1}. Although it is now thought that the ZrCl ground state is of $^2\Delta_{3/2}$ symmetry,[7] this is a very close call. Further complicating matters is the fact that both candidates for the ground state of ZrCl, $3\sigma^1 1\delta^1 2\pi^1$, $^4\Phi_{3/2}$ and $3\sigma^2 1\delta^1$, $^2\Delta_{3/2}$ have $\Omega = 3/2$, making them difficult to distinguish unless the higher lying spin components are populated and resolved. Indeed, if the $^2\Delta_{3/2}$ and $^4\Phi_{3/2}$ states are sufficiently close in energy, spin-orbit mixing of these levels may render the S and Λ labels meaningless.

A similar pattern of low-lying states is expected in ZrF, with a close competition between the $3\sigma^1 1\delta^1 2\pi^1$, $^4\Phi_{3/2}$ and $3\sigma^2 1\delta^1$, $^2\Delta_{3/2}$ states as to which emerges as the ground state. Although these two states are quite close in energy in ZrCl, it is reasonable to expect the $^2\Delta_{3/2}$ level to emerge clearly as the ground state in ZrF. As has been pointed out by Field, the transition metal halides can be well-understood by a ligand field model in which the metal-centered orbitals undergo an energy shift given by[25]

$$\Delta E(n\ell\lambda) = B^0_0(n\ell) + B^2_0(n\ell)\, C^2_0(n\ell\lambda) + B^4_0(n\ell)\, C^4_0(n\ell\lambda), \qquad (4.8)$$

where the B-factors are radial integrals given by

$$B^{k}_{0}(n\ell) = Z_L e^2 \left[r_e^{-(k+1)} \int_0^{r_e} R_{n\ell} R_{n\ell} r^{(k+2)} dr + \int_{r_e}^{\infty} R_{n\ell} R_{n\ell} r^{(-k+1)} dr \right] \quad (4.9)$$

and the C-factors are angular integrals that are readily expressed in terms of 3-j symbols:

$$C^{k}_{0}(n\ell\lambda) = (-1)^{\lambda}(2\ell + 1) \begin{pmatrix} l & k & l \\ -\lambda & 0 & \lambda \end{pmatrix} \begin{pmatrix} l & k & l \\ 0 & 0 & 0 \end{pmatrix}. \quad (4.10)$$

In expression (4.9), Z_L is the magnitude of the negative charge on the ligand (+1 for the case of ZrF or ZrCl) and r_e is the bond length of the molecule. In this simplified discussion, off-diagonal portions of the ligand-field Hamiltonian are ignored, as they are irrelevant to the main point. In expression (4.8), the $B^{0}_{0}(n\ell)$ term causes a destabilization of all of the metal-based orbitals as the F^- ion is brought in from infinity, while the remaining terms involving $B^{2}_{0}(n\ell)$ and $B^{4}_{0}(n\ell)$ cause a splitting of the orbitals on the basis of λ. Further, the $B^{0}_{0}(n\ell)$ term increases the energy of the 4*d* orbitals more than it does the 5*s* orbital, effectively because the 5*s* orbital extends further beyond the location of the ligand. Thus, placement of electrons in the 5*s* orbital allows the negatively charged fluoride ion to feel more of the underlying charge of the Zr^+ ion, thereby reducing the net upward shift of the energy of the 5*s* orbital. More generally, diffuse orbitals are destabilized less severely than are compact orbitals; thus, occupation of the more diffuse 5*s* orbital is favored as the negatively charged ligand is brought up to the Zr^+ ion.

As is evident in equation (4.9), the ligand field parameters, B^{k}_{0}, depend on the bond length, r_e, becoming smaller as the ligand is pulled out to longer distances. Thus,

the increase in bond length that occurs as one moves from F^- to Cl^-, Br^-, and I^- causes the ligand field interactions to decrease, a fact that is well-known in inorganic chemistry and has been nicely documented in the YF, YCl, YBr, YI series.[74,75] To attempt to quantify this effect, numerical Hartree-Fock methods have been used to calculate the radial wavefunctions, $R_{4d}(r)$ and $R_{5s}(r)$, for the Zr^+ ion in its $4d^15s^2$, ^2D_g and $4d^25s^1$, ^4F_g configurations.[73] With these wavefunctions in hand, it is straightforward to compute the values of the ligand-field parameters $B^k_0(4d)$ and $B^k_0(5s)$. To a first order approximation, the effect of the ligand on the energies of these configurations can be estimated by combining the $B^k_0(n\ell)$ terms for the three relevant electrons, weighted by the values of the $C^k_0(n\ell\lambda)$ coefficients as indicated in equation (4.8). The result for ZrF, using a value of r_e in equation (4.9) given by the measured bond length of 1.858 Å, is a predicted stabilization of the $4d^15s^2$, $3\sigma^21\delta^1$, $^2\Delta$ term over the $4d^25s^1$, $3\sigma^11\delta^12\pi^1$, $^4\Phi$ term by 4533 cm^{-1}. When the same calculation is performed for ZrCl using the measured bond length of 2.284 Å, the predicted relative stabilization of the $4d^15s^2$, $3\sigma^21\delta^1$, $^2\Delta$ term is only 1699 cm^{-1}. Subtracting these values, the $3\sigma^21\delta^1$, $^2\Delta_{3/2}$ state is calculated to be approximately 2834 cm^{-1} further below the $3\sigma^11\delta^12\pi^1$, $^4\Phi_{3/2}$ state in ZrF than it is in ZrCl. On this basis it seems likely that the ground state of ZrF is the $3\sigma^21\delta^1$, $^2\Delta_{3/2}$ state that is already assigned as the ground state in ZrCl.[7]

While the ligand field calculation outlined above provides some insight into the electronic structure of ZrF, it is difficult to carry this further into a full calculation of the expected electronic states of the molecule. To properly treat this system using ligand field methods, it would be necessary to include the effects of the off-diagonal $B^2_0(4d, 5s)$ term, which is quite large (15000 cm^{-1} in ZrCl; 22000 cm^{-1} in ZrF). This term causes

mixing of the 4*d*σ and 5*s*σ orbitals, and is quite important due to the near-degeneracy of these orbitals. Secondly, a proper LFT calculation of the expected state ordering in ZrF would require adjustment of the asymptotic energies of the various states to reproduce the measured Zr^+ energy levels.[55,76] This is straightforward in principle, but is complicated by the strong configuration interaction that is known to occur between terms belonging to the $4d^3$, $4d^25s^1$, and $4d^15s^2$ configurations.[77] The strong configurational mixing that occurs in the isolated Zr^+ ion complicates the use of ligand-field methods to predict the electronic structure of the ZrF and ZrCl molecules, because a detailed understanding of the atomic states is required before this method can be applied. Indeed, the advantage of the ligand field method is that it is based on already well-understood atomic energy levels; if these levels are poorly understood or not easily described, application of ligand field methods becomes more problematic.

The very recent IC-MRCI investigation of ZrF is in agreement with these ideas, placing the X $^2\Delta$ ground term 2383 cm^{-1} below the a $^4\Sigma^-$ term and 4179 cm^{-1} below the b $^4\Phi$ term.[3] These separations are significantly greater than those obtained in a similar calculation on ZrCl, 963 cm^{-1} and 616 cm^{-1}, respectively.[7] Thus, the combination of experimental data and computational investigations has clearly determined the ground state of ZrF to be $3\sigma^21\delta^1$, $^2\Delta$. The IC-MRCI study of ZrF also predicts the first and second excited $^2\Delta$ terms to lie in the 14000 – 18000 cm^{-1} range. As these are the only possible Hund's case (a) terms that can provide a source of oscillator strength for a parallel transition from a $^2\Delta$ ground term, and this is the region probed in the present study, it is likely that these two $^2\Delta$ terms account for two of the observed band systems. The remaining band system is likely a spin-forbidden transition that is made observable

by spin-orbit mixing with the 2 $^2\Delta$ and 3 $^2\Delta$ terms that lie in this region. Given that the A 3/2 and C 3/2 states lie quite close in energy ($\Delta T_0 \approx 106$ cm^{-1}) and have similar bond lengths ($\Delta r_4 \approx 0.008$ Å), and that the spin orbit parameter for Zr 4*d* orbitals is larger than their separation (ζ_{Zr} (4*d*) ≈ 430 cm^{-1}), it seems likely that these states are strong mixtures of an electronically bright $^2\Delta$ state and a dark state, probably quartet in character. If so, these states should exhibit fluorescence to both doublet and quartet states in good yield.

4.5 Conclusion

Resonant two-photon ionization spectroscopy has been applied to jet-cooled ZrF, providing spectroscopic data in the 760 – 555 nm range that compliments a previous investigation in the 420 – 470 nm range. The ground state of the most abundant isotopic modification, $^{90}Zr^{19}F$, has been shown to have $\Omega = 3/2$, $\Delta G_{1/2}'' = 691.45(2)$ cm^{-1}, and $r_e'' = 1.854(1)$ Å. Three band systems have been identified in the 760 – 555 nm wavelength range, along with a large number of unassigned bands. All three of the band systems appear to have upper states with $\Omega = 3/2$, and many of the bands that have been rotationally resolved show evidence of perturbations. Based on a comparison to ZrCl and a consideration of ligand field effects, it is argued that the ground state of the molecule is $3\sigma^2 1\delta^1$, $^2\Delta_{3/2}$.

Vibrationally resolved spectra of ZrCl are also reported over the range 760 – 555 nm, and four new band systems are reported for this molecule, along with a large number of unassigned bands.

4.6 References

[1] L. A. Kaledin, J. E. McCord, M. C. Heaven, and R. F. Barrow, Journal of Molecular Spectroscopy **169** (1), 253 (1995).

[2] J. W. H. Leung, J. Dai, and A. S. C. Cheung, Journal of Molecular Spectroscopy **207** (1), 124 (2001).

[3] S. Soorkia, N. Shafizadeh, M. A. Gaveau, C. Pothier, J. M. Mastdagh, B. Soep, J. Lievin, and R. W. Fields, Journal of Physical Chemistry A **115** (34), 9620 (2011).

[4] K. J. Jordan, R. H. Lipson, N. A. McDonald, and D. S. Yang, Chem. Phys. Lett. **193** (6), 499 (1992).

[5] R. S. Ram and P. F. Bernath, J. Mol. Spectrosc. **186** (2), 335 (1997).

[6] R. S. Ram and P. F. Bernath, Journal of Molecular Spectroscopy **196** (2), 235 (1999).

[7] R. S. Ram, A. G. Adam, W. Sha, A. Tsouli, J. Lievin, and P. F. Bernath, J. Chem. Phys. **114** (9), 3977 (2001).

[8] R. S. Ram, N. Rinskopf, J. Lievin, and P. F. Bernath, Journal of Molecular Spectroscopy **228** (2), 544 (2004).

[9] T. C. Steimle, W. L. Virgo, and T. Ma, Journal of Chemical Physics **124** (2), 024309/1 (2006).

[10] R. Li, R. H. Jensen, W. J. Balfour, S. A. Shepard, and A. G. Adam, Journal of Chemical Physics **121** (6), 2591 (2004).

[11] S. A. Shepard, A. G. Adam, R. Li, and W. J. Balfour, Journal of Molecular Spectroscopy **234** (2), 204 (2005).

[12] R. M. Clements and R. F. Barrow, Chem. Commun. (1), 27 (1968).

[13] G. J. Stueber, M. Foltin, and E. R. Bernstein, Journal of Chemical Physics **109** (22), 9831 (1998).

[14] R. S. Ram, J. R. D. Peers, Y. Teng, A. G. Adam, A. Muntianu, P. F. Bernath, and S. P. Davis, J. Mol. Spectrosc. **184** (1), 186 (1997).

[15] R. S. Ram and P. F. Bernath, J. Mol. Spectrosc. **186** (1), 113 (1997).

[16] S. M. Kermode and J. M. Brown, Journal of Molecular Spectroscopy **207** (2), 161 (2001).

[17] R. S. Ram, P. F. Bernath, and S. P. Davis, J. Mol. Spectrosc. **173** (1), 158 (1995).

[18] T. Hirao, B. Pinchemel, and P. F. Bernath, Journal of Molecular Spectroscopy **219** (1), 119 (2003).

[19] J. F. Harrison, Chem. Rev. **100** (2), 679 (2000).

[20] C. Koukounas and A. Mavridis, Journal of Physical Chemistry A **112** (44), 11235 (2008).

[21] C. Koukounas, S. Kardahakis, and A. Mavridis, Journal of Chemical Physics **120** (24), 11500 (2004).

[22] B. Kharat, S. B. Deshmukh, and A. Chaudhari, International Journal of Quantum Chemistry **109** (5), 1103 (2009).

[23] L. Cheng, M. Y. Wang, Z. J. Wu, and Z. M. Su, J. Comput. Chem. **28** (13), 2190 (2007).

[24] P. E. M. Siegbahn, Theoretica Chimica Acta **86** (3), 219 (1993).

[25] R. W. Field, Ber. Bunsenges. Phys. Chem. **86** (9), 771 (1982).

[26] P. Carette, C. Dufour, and B. Pinchemel, Journal of Molecular Spectroscopy **161** (2), 323 (1993).

[27] A. L. Kaledin, M. C. Heaven, R. W. Field, and L. A. Kaledin, J. Mol. Spectrosc. **179** (2), 310 (1996).

[28] L. A. Kaledin, A. L. Kaledin, and M. C. Heaven, Journal of Molecular Spectroscopy **179** (2), 246 (1996).

[29] J. Ren, M. H. Whangbo, D. Dai, and L. Li, J. Chem. Phys. **108** (20), 8479 (1998).

[30] J. Schamps, M. Bencheikh, J.-C. Barthelat, and R. W. Field, J. Chem. Phys. **103** (18), 8004 (1995).

[31] L. A. Kaledin, M. G. Erickson, and M. C. Heaven, Journal of Molecular Spectroscopy **165**, 323 (1994).

[32] L. A. Kaledin, J. E. McCord, and M. C. Heaven, Journal of Molecular Spectroscopy **170** (1), 166 (1995).

[33] L. A. Kaledin, J. E. McCord, and M. C. Heaven, Journal of Molecular Spectroscopy **164**, 27 (1994).

[34] S. F. Rice, H. Martin, and R. W. Field, J. Chem. Phys. **82** (11), 5023 (1985).

[35] D. P. Baldwin, E. J. Hill, and R. W. Field, J. Am. Chem. Soc. **112** (25), 9156 (1990).

[36] Z. J. Jakubek and R. W. Field, J. Chem. Phys. **98** (8), 6574 (1993).

[37] L. A. Kaledin, J. E. McCord, and M. C. Heaven, Journal of Molecular Spectroscopy **173** (2), 499 (1995).

[38] L. A. Kaledin, J. E. McCord, and M. C. Heaven, Journal of Molecular Spectroscopy **173** (1), 37 (1995).

[39] L. A. Kaledin and M. C. Heaven, Journal of Chemical Physics **107** (18), 7020 (1997).

[40] C. Focsa, M. Bencheikh, and L. G. M. Pettersson, J. Phys. B At., Mol. Opt. Phys. **31** (13), 2857 (1998).

[41] M. Bencheikh, R. Koivisto, O. Launila, and J. P. Flament, Journal of Chemical Physics **106** (15), 6231 (1997).

[42] M. Bencheikh, J. Phys. B At., Mol. Opt. Phys. **30** (5), L137 (1997).

[43] M. Bencheikh, Journal of Molecular Spectroscopy **183** (2), 419 (1997).

[44] M. Afaf, Proc. Phys. Soc., London **63A**, 544 (1950).

[45] P. K. Carroll and P. J. Daly, Proc. Phys. Soc., London **70A**, 549 (1957).

[46] D. L. Hildenbrand and K. H. Lau, J. Chem. Phys. **107** (16), 6349 (1997).

[47] P. K. Carroll and P. J. Daly, Proc. R. Ir. Acad., Sect. A **61A** (No. 11), 101 (1961).

[48] J. G. Phillips, S. P. Davis, and D. C. Galehouse, Astrophys. J., Suppl. Ser. **43** (3), 417 (1980).

[49] Y. Sakai, K. Mogi, and E. Miyoshi, Journal of Chemical Physics **111** (9), 3989 (1999).

[50] R. Nagarajan and M. D. Morse, Journal of Chemical Physics **126** (14), 144309/1 (2007).

[51] D. J. Brugh and M. D. Morse, Journal of Chemical Physics **107** (23), 9772 (1997).

[52] W. C. Wiley and I. H. McLaren, Review of Scientific Instruments **26** (12), 1150 (1955).

[53] B. A. Mamyrin, V. I. Karataev, D. V. Shmikk, and V. A. Zagulin, Zh. Eksp. Teor. Fiz. **64** (1), 82 (1973).

[54] J. K. Bates and T. M. Dunn, Canadian Journal of Physics **54** (12), 1216 (1976).

[55] C. E. Moore, *Atomic Energy Levels*, Natl. Bur. Stand. U.S. Circ. No. 467 ed. (U. S. Government Printing Office, Washington, D. C., 1971).

[56] S. Gerstenkorn and P. Luc, *Atlas du Spectre d'Absorption de la Molécule d'Iode entre 14800-20000 cm^{-1}*. (CNRS, Paris, 1978).

[57] S. Gerstenkorn and P. Luc, Revue de Physique Appliquee **14**, 791 (1979).

[58] P. R. Bevington, *Data Reduction and Error Analysis for the Physical Sciences*. (McGraw-Hill, New York, 1969).

[59] G. Herzberg, *Molecular Spectra and Molecular Structure I. Spectra of Diatomic Molecules*, 2nd ed. (Van Nostrand Reinhold, New York, 1950).

[60] EPAPS, See EPAPS Document No. E-JCPSAx-xxx-xxxxx for 18 pages of line positions, rotational fits, and rotationally resolved spectra of OsC. A direct link to this document may be found in the online article's HTML reference section. The document may also be reached via the EPAPS homepage (http://www.aip.org/pubservs/epaps.html) or from ftp.aip.org in the directory /epaps. See the EPAPS homepage for more information.

[61] J. M. Brown, A. S.-C. Cheung, and A. J. Merer, Journal of Molecular Spectroscopy **124**, 464 (1987).

[62] J. M. Brown and A. J. Merer, Journal of Molecular Spectroscopy **74**, 488 (1979).

[63] H. Hotop and W. C. Lineberger, Journal of Physical and Chemical Reference Data **14** (3), 731 (1985).

[64] P. A. Hackett, M. R. Humphries, S. A. Mitchell, and D. M. Rayner, J. Chem. Phys. **85** (6), 3194 (1986).

[65] T. Imajo, Y. Kobayashi, Y. Nakashima, K. Tanaka, and T. Tanaka, Journal of Molecular Spectroscopy **230** (2), 139 (2005).

[66] R. S. Ram and P. F. Bernath, Journal of Molecular Spectroscopy **231** (2), 165 (2005).

[67] T. Imajo, D. Wang, K. Tanaka, and T. Tanaka, Journal of Molecular Spectroscopy **203** (2), 216 (2000).

[68] A. Maeda, T. Hirao, P. F. Bernath, and T. Amano, Journal of Molecular Spectroscopy **210** (2), 250 (2001).

[69] A. I. Boldyrev and J. Simons, Journal of Molecular Spectroscopy **188**, 138 (1998).

[70] A. G. Adam, W. S. Hopkins, W. Sha, and D. W. Tokaryk, Journal of Molecular Spectroscopy **236** (1), 42 (2006).

[71] A. G. Adam, W. S. Hopkins, and D. W. Tokaryk, Journal of Molecular Spectroscopy **225** (1), 1 (2004).

[72] R. S. Ram, A. G. Adam, A. Tsouli, J. Lievin, and P. F. Bernath, J. Mol. Spectrosc. **202** (1), 116 (2000).

[73] C. F. Fischer, *The Hartree-Fock Method for Atoms*. (John Wiley & Sons, New York, 1977).

[74] J. E. Huheey, *Inorganic Chemistry*. (Harper & Row, New York, 1983).

[75] J. Ye, H. F. Pang, and A. S. C. Cheung, Chemical Physics Letters **442** (4-6), 251 (2007).

[76] C. C. Kiess, Journal of the Optical Society of America **43**, 1024 (1953).

[77] L. Young, C. A. Kurtz, D. R. Beck, and D. Datta, Physical Review A **48** (1), 173 (1993).

CHAPTER 5

RESONANT TWO-PHOTON IONIZATION SPECTROSCOPY OF JET-COOLED PdSi

5.1 Introduction

The various practical applications of transition metal silicides, particularly in the electronics industry, have brought attention to these species over the last few decades. Among the physical properties that make transition metal silicides desirable to industry are low resistivity, high melting points, low density, and resistance to oxidation.[1-3] Transition metal silicides have been successfully implemented in Schottky barrier devices,[1,3] where compounds such as NiSi and PtSi have found use in infrared imaging arrays,[4-5] and in low-power microwave circuitry.[6] More recently, transition metal silicide nanowires have been synthesized and their properties are under investigation.[7-8]

To learn more about the chemical bonding between transition metal atoms and silicon, a number of investigations of the diatomic metal silicide molecules have been performed. Gas phase spectroscopic studies of the coinage metal silicides CuSi,[9-11] AgSi,[12] and AuSi,[13] of the nickel group molecules NiSi[14] and PtSi,[15-16] and of the open 4*d*-subshell molecules RuSi[17] and RhSi[18] have been conducted. Matrix isolation ESR investigations of VSi and NbSi have also been reported.[19] In addition, Knudsen effusion mass spectrometry has been employed to measure the bond energies of a number of transition metal silicides, including ScSi,[20] FeSi,[21] CoSi,[21] NiSi,[21] YSi,[22]RuSi,[23] RhSi,[23]

PdSi, [23-24] IrSi,[23] PtSi,[23] and AuSi.[23,25-26] A number of computational studies have also been performed on the diatomic transition metal silicides. The computational literature for all of the transition metal silicides prior to 2006 has been summarized in a comprehensive density functional study of all of these species by Wu and Su.[27]

In this chapter the spectroscopic results on diatomic PdSi are presented, a molecule that has received limited attention to date. The two earliest calculations on PdSi predicted different ground states. The local spin density calculations of Russo, *et al.* found PdSi to have a $^1\Sigma^+$ ground state and $^3\Pi$ and $^3\Sigma^-$ excited states, with the $^3\Pi$ state 6186 cm^{-1} and the $^3\Sigma^-$ state 18190 cm^{-1} above the ground state.[28] In contrast, in an all-electron Hartree-Fock plus configuration interaction calculation, Shim found the ground state to be the $^3\Pi$ state, with the $^3\Sigma^-$ state lying 1530 cm^{-1} higher and the $^1\Sigma^+$ state lying at 4275 cm^{-1}.[24] The more recent density functional investigation by Wu and Su is in agreement with the early work of Russo, *et al.*, predicting the ground state to be $^1\Sigma^+$, with the lowest triplet state lying 3200 cm^{-1} above.[27]

In a 1969 Knudsen effusion mass spectrometric investigation, the high-temperature equilibrium

$$Pd(g) + Si_2(g) \leftrightarrow PdSi(g) + Si(g) \qquad (5.1)$$

was measured and a value of $D_0(PdSi) = 3.21 \pm 0.15$ eV was deduced using the third law method.[23] This method uses estimates of the bond length, vibrational frequency, and electronic degeneracy of the diatomic molecule to calculate its absolute entropy and other thermodynamic properties. In this study, it was assumed that the PdSi molecule exists in a nondegenerate $^1\Sigma$ ground state, with $\omega_e = 400$ cm^{-1} and $r_e = 2.35$ Å. Of course, if these

values or the bond energy of Si_2, which was taken to be 3.16 eV, are in error, the bond energy of PdSi will be in error as well. In a subsequent Knudsen effusion study of the equilibrium

$$PdSi(g) \leftrightarrow Pd(g) + Si(g), \qquad (5.2)$$

the measured equilibrium constant was combined with *ab initio* calculations on PdSi to determine the PdSi bond energy to be 2.66 ± 0.12 eV, again using the third law method.[24] A major difference between the two studies was that in the latter investigation, PdSi was taken to have a $^3\Pi$ ground state with ω_e = 324 cm^{-1} and r_e = 2.29 Å. While these two studies give very different values of the bond energy, the sixfold degeneracy of the assumed $^3\Pi$ ground state decreases the calculated value of D_0 by kT ln6, which at the high temperatures employed (2200 – 2400 K) amounts to roughly 0.36 eV. Thus, if the ground state of the molecule were of $^1\Sigma^+$ symmetry and the $^3\Pi$ state were sufficiently high in energy to be unpopulated at these temperatures, the value of D_0 = 2.66 eV would require revision to approximately 3.02 eV.

It is also pertinent to review the isovalent molecules NiSi, PtSi, and PdC to gain a better appreciation of the electronic structure and chemical bonding in PdSi. Diatomic PtSi was first studied via cavity ringdown spectroscopy by Paul, *et al*., who found nine bands in the UV region that were assigned as $^1\Sigma^+ \leftarrow {}^1\Sigma^+$ transitions due to the lack of a Q-branch in the rotationally resolved spectra.[15] The Morse group later confirmed the $^1\Sigma^+$ ground state with their investigation of PtSi in the visible.[16] Subsequently, PtSi was examined by Fourier transform microwave spectroscopy, allowing rotational constants, B_v, to be determined for the v = 0 - 3 vibrational levels.[29] The shorter bond length (r_0'' =

2.0629 *vs.* 2.3414 Å),[15-16,30] higher vibrational frequency (ω_e'' = 549 *vs.* 333 cm^{-1}),[15,30] and higher bond energy (D_0 = 5.15 ± 0.19 *vs.* 3.34 ± 0.07 eV) of PtSi[23,31] as compared to the isoelectronic molecule AlAu,[30-31] is due to π bonding in PtSi that is absent in AlAu. The highly electropositive character of aluminum, combined with the stable closed subshell character of the d^{10} configuration of gold, prevents significant $d\pi$ - $p\pi$ bonding from occurring in AlAu. An *ab initio* relativistic calculation carried out by Barysz and Pyykkö confirms the presence of $5d\pi_{Pt}$ - $3p\pi_{Si}$ bonding in PtSi.[32]

A number of computational studies have found the ground state of NiSi to be $^1\Sigma^+$,[33-35] a fact that was confirmed in a resonant two-photon ionization (R2PI) spectroscopic and dispersed fluorescence study that found the molecule to have a bond length of r_0'' = 2.0316 Å and a vibrational frequency of ω_e'' = 467 cm^{-1}.[14] A Knudsen effusion study has also determined the Ni-Si bond energy to be 3.26 ± 0.18 eV.[21] Again, the shorter bond length (r_0'' = 2.0316 Å *vs.* 2.3389 Å),[14,36] higher vibrational frequency (ω_e'' = 467 cm^{-1} *vs.* $\Delta G_{1/2}$ = 294 cm^{-1}),[14,36] and greater bond energy (D_0 = 3.26 eV *vs.* 2.32 eV) [21,36] of NiSi, as compared to AlCu demonstrates that the chemical bond in NiSi is enhanced by $3d\pi_{Ni}$ - $3p\pi_{Si}$ bonding.

The dispersed fluorescence work that was carried out by DaBell and coworkers on PdC established the ground state of the molecule to be $^1\Sigma^+$, with the $^3\Pi_{0^+,0^-,1,2}$ levels lying 2157 – 2818 cm^{-1} higher in energy.[37] This study of PdC complemented the previous work of Langenberg, *et al*., who found the molecule to have $\Omega'' = 0$ and r_0'' = 1.712 Å.[38] Prior to these studies, theoretical calculations predicted a $^1\Sigma^+$ ground state, but the possibility of a $^3\Pi$ ground state was not completely ruled out.[28,39]

5.2 Experimental

The resonant two-photon ionization instrument employed in this study has been previously described in detailed in the literature[40] and Chapter 2 of this dissertation, so only a brief overview is provided here. The PdSi molecule was created by ablating a palladium disc sample with approximately 8 mJ/pulse of third harmonic (355 nm) Nd:YAG laser radiation. The vaporization process was timed to coincide with the firing of a He gas pulse (80 psi) that was seeded with 0.25% SiH_4. During the experiment the palladium sample was rotated and translated to avoid drilling holes and to achieve uniform ablation. The plasma produced during the vaporization process was entrained in the gas pulse and flowed through a 2 mm diameter channel, allowing the metal atoms to undergo multiple collisions with SiH_4 and He to produce a variety of molecules, one of which was PdSi. The molecules entrained in the gas pulse were accelerated to the helium beam velocity (1.77×10^5 cm/s) during the expansion into vacuum,[41] converting their internal energy into translational energy and cooling the internal degrees of freedom to low temperatures. This simplifies the spectra greatly. Following the supersonic expansion into vacuum, the molecular beam was roughly collimated by a 1 cm diameter skimmer prior to entering the spectroscopy chamber.

In the spectroscopy chamber the molecular beam was probed with the radiation produced by a Nd:YAG pumped tunable dye laser, which counterpropagated along the molecular beam axis. When the dye laser was in resonance with a transition, the molecule was excited and subsequently ionized by absorbing a KrF (248 nm, 5.00 eV) excimer laser photon, which was directed across the molecular beam at right angles and fired approximately 20 ns after the pulsed dye laser. Transitions were initially observed

using ArF (193 nm, 6.42 eV) radiation for the ionization step, but the signal-to-noise ratio was much better when KrF radiation was employed. The ionized molecules were extracted using a Wiley-McLaren extraction assembly into a reflectron time-of-flight mass spectrometer.[42,43] After reflection, the ions were directed onto a microchannel plate detector. The resulting ion signal was preamplified, digitized, and stored on a computer.

The dye laser used in these studies was scanned from 17857 – 23148 cm^{-1} to collect low resolution (0.15 cm^{-1}) survey scans of the vibronic bands of $^{104}Pd^{28}Si$ (10.3% natural abundance), $^{105}Pd^{28}Si$ (20.6%), $^{106}Pd^{28}Si$ (25.2%), $^{108}Pd^{28}Si$ (24.4%), and $^{110}Pd^{28}Si$ (10.8%). Higher resolution scans were obtained by the insertion of an air-spaced intracavity etalon, which narrowed the dye laser output to a linewidth of approximately 0.04 cm^{-1}, allowing the observed vibronic bands to be rotationally resolved. By slowly pressurizing the laser cavity from roughly 20 Torr to atmospheric pressure with sulfur hexafluoride (SF_6), the dye laser could be scanned in high-resolution mode. A portion of the output radiation was passed through a high-temperature cell containing ^{130}Te, and the transmission spectrum of $^{130}Te_2$ was recorded simultaneously with the spectra of the PdSi isotopomers. Comparison of the $^{130}Te_2$ spectrum to the tellurium atlas[44] provided an absolute calibration of the rotationally resolved spectra. The spectra were also corrected for the Doppler shift experienced by the PdSi molecules as they travel toward the radiation source at the beam velocity of helium (1.77×10^5 cm/sec). This minor correction shifted the spectra by approximately +0.126 cm^{-1} for the bands reported in this study.

Excited state lifetimes were measured for some of the observed transitions by monitoring the ion signal as a function of the delay between the excitation and ionization

laser pulses. In this process, the ionization laser was fired at the time of maximum PdSi concentration in the molecular beam, and the excitation laser pulse was varied in time. The resulting decay curve was fitted to an exponential function using the Levenberg-Marquardt nonlinear least-squares algorithm.[45] Each decay curve was measured and fitted three times, and the mean and standard deviation of the fitted 1/e lifetimes are reported here.

5.3 Results

5.3.1 Low-Resolution Spectrum of PdSi

Although survey scans were conducted over the 17857 – 23148 cm^{-1} range, PdSi transitions were only observed within the 20400 – 22000 cm^{-1} range. The transitions observed for the most abundant isotopomer, $^{106}Pd^{28}Si$, are displayed in Figure 5.1; band heads are listed in Table 5.1. The band heads near 21392 and 21761 cm^{-1} are tentatively assigned as the 0-0 and 1-0 bands of a vibrational progression. The 369.5 cm^{-1} separation between these two bands is consistent with the 382 cm^{-1} separation between the 0-0 and 1-0 transitions of the [18.0]1 ← X $^1\Sigma^+$ band system of the isovalent NiSi,[14] which is calculated to have vibrational frequencies similar to those of PdSi.[27] Additionally, the excited state lifetimes of the two PdSi states agree within the error of the measurement. The isotope shift, $\nu_0(^{105}Pd^{28}Si) - \nu_0(^{108}Pd^{28}Si)$, is small (0.03 cm^{-1}) for the proposed 0-0 band, and significantly larger (1.77 cm^{-1}) for the proposed 1-0 band, as is expected. Unfortunately, both bands are perturbed by interactions with nearby states, making the isotope shift much larger than reasonable (~0.9 cm^{-1}) for the suspected 1-0 band. The proposed 1-0 band also has a smaller upper state rotational constant than that found for

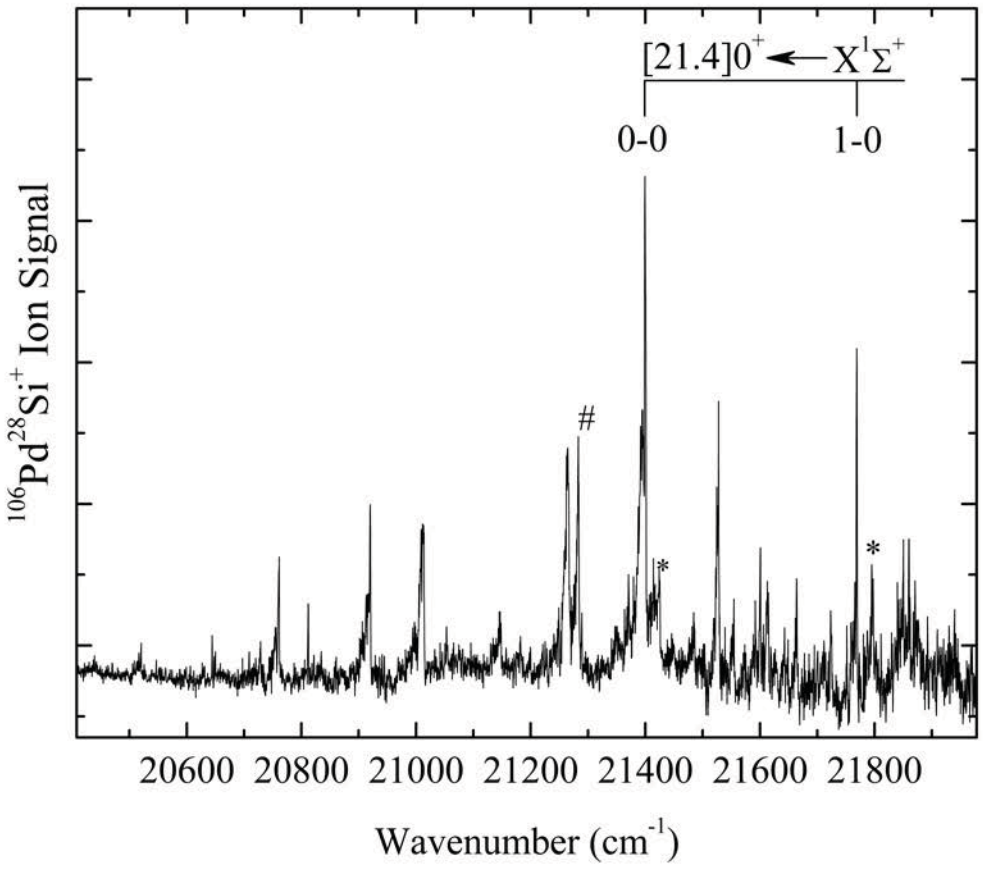

Figure 5.1 Low-resolution spectrum of ^{106}PdSi recorded in the 20400 – 22000 cm^{-1} spectral range. The two bands assigned as the 0-0 and 1-0 bands of the $[21.4]0^+ \leftarrow X\ ^1\Sigma^+$ system are identified. Asterisks indicate the transitions to the states that perturb these states. The transition marked by # has been rotationally resolved (see Figure 5.2) and appears to be unperturbed.

Table 5.1 Band Head Positions and Excited State Lifetimes of PdSi Transitions.[a]

Band System	Band (v′-v″)	^{106}PdSi Band Head Position[b]	Isotope Shift ν(^{105}PdSi) - ν(^{108}PdSi)[c]	Intensity	τ (μsec)
$[21.4]0^+ \leftarrow X^1\Sigma^+$	0 – 0	21392	0.0303(72)*	vs	0.494(58)
	1 – 0	21761	1.7717(45)*	s	0.612(75)
Unclassified Bands		21790	3.75	w	
		21717	5.86	w	
		21657	1.64	w	
		21592	6.24	w	
		21547	7.47	vw	
		21520	4.86	s	
		21418	0.71	m	
		21281	0.38	vw	
		21276	6.8518(32)*	s	
		21258	0.73	s	
		21140	6.52	w	
		21006	5.53	m	
		20912	-1.11	m	

Table 5.1 Continued

Band System	Band (v′-v″)	^{106}PdSi Band Head Position[b]	Isotope Shift ν(^{105}PdSi) - ν(^{108}PdSi)[c]	Intensity	τ (μsec)
Unclassified Bands		20808	-0.91	w	
		20753	6.88	w	
		20721	5.32	vw	
		20636	0.02	vw	
		20513	4.65	vw	

[a] All numerical values are given in the units of cm^{-1}, unless otherwise specified. Values in parenthesis are the 1σ error limits, in units of the last reported digits. Intensity designations are relative: vs (very strong), s (strong), m (medium), w (weak), vw (very weak).

[b] The band heads of the calibrated, rotationally resolved scans over the 21276, 21392, and 21761 bands were used to calibrate the low-resolution scans. As a result, it is thought that these band head positions are accurate to ± 1 cm^{-1}.

[c] The accuracy of the isotope shift measurements is expected to be approximately ± 0.5 cm^{-1}, although it could be larger for the weaker features. Values marked by an asterisk are isotope shifts of band origins, measured in high resolution.

the proposed 0-0 band, again as expected. All of these facts suggest, but do not prove, that the two bands are members of the same band system, which is designated as the [21.4]0 ← X 0 system.

The observation of the 20513 cm^{-1} band using KrF radiation (5.00 eV) implies that the ionization energy of PdSi is less than 7.54 eV, which is the sum of the energies of the excitation and ionization photons. Likewise, the fact that any transitions are visible using ArF radiation (6.42 eV) for ionization implies that this wavelength is insufficient to ionize the molecule in a one-photon process. Together, these two observations place the ionization energy of PdSi in the range 6.42 eV < IE(PdSi) < 7.54 eV.

Higher quality figures of the vibronically resolved spectra and rotationally resolved spectra, along with tables of vibronic band positions and rotational line positions and fits for the various isotopomers are available through the Electronic Physics Auxiliary Publication Service (EPAPS)[46] of the American Institute of Physics and Appendix C of this dissertation.

5.3.2 Rotationally Resolved Spectra of PdSi

Three vibronic bands were investigated in high-resolution mode. These included the two bands of the [21.4] 0 ← X 0 system near 21392 and 21761 cm^{-1} and a band near 21276 cm^{-1}. Rotationally resolved spectra for the transition near 21276 cm^{-1} for $^{104}Pd^{28}Si$ and near 21392 cm^{-1} (the proposed 0-0 band) for $^{108}Pd^{28}Si$ are displayed in Figures 5.2 and 5.3, respectively. The spectrum of the proposed 1-0 band near 21761 cm^{-1} is similar to the 0-0 band shown in Figure 5.3. None of the bands display Q-branches, demonstrating that all three are $\Omega' = 0 \leftarrow \Omega'' = 0$ transitions.

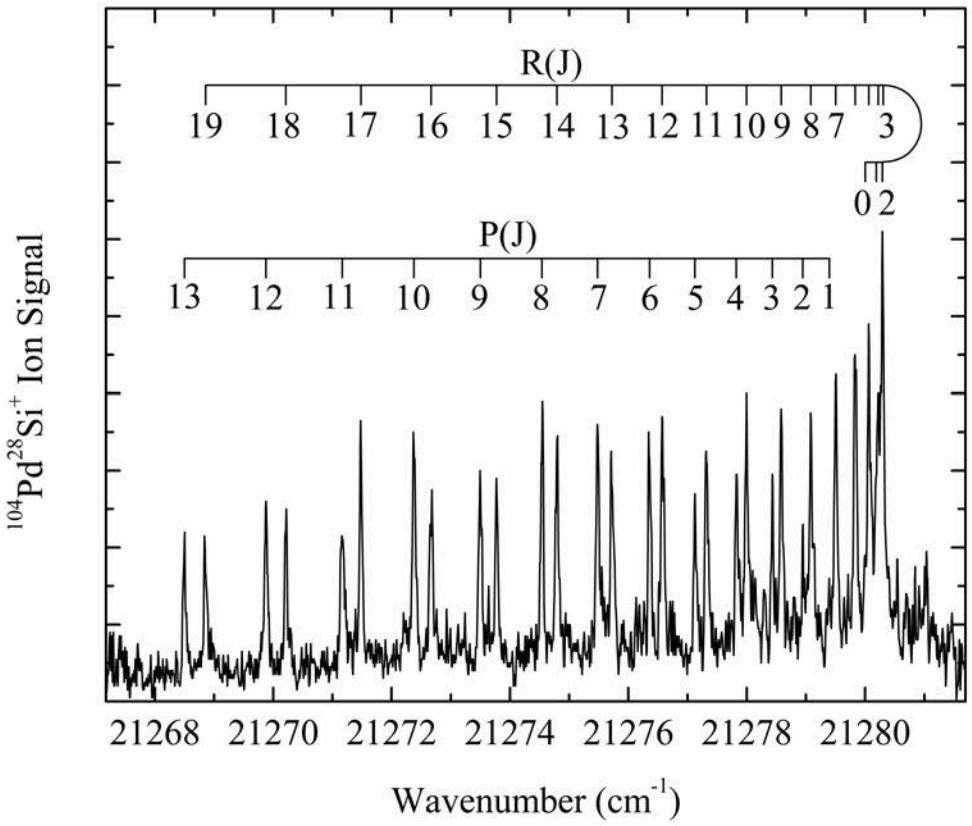

Figure 5.2 Rotationally resolved spectrum of ^{104}PdSi corresponding to the band near 21276 cm^{-1}. The lack of a Q-branch demonstrates that this is a $\Omega' = 0 \leftarrow \Omega'' = 0$ transition.

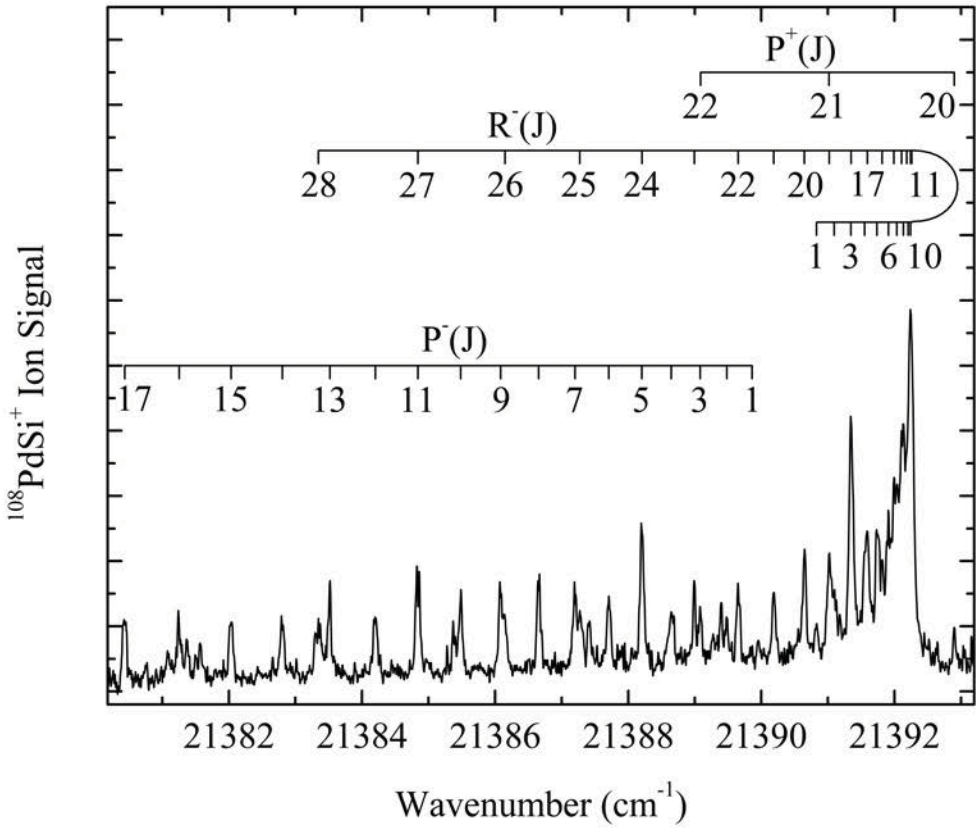

Figure 5.3 Rotationally resolved spectrum of ^{108}PdSi for the 0-0 band belonging to the $[21.4]0^+ \leftarrow X^1\Sigma^+$ system. This band is perturbed by a state at higher energies, with which is undergoes an avoided crossing as J′ increases. The $P^-(J)$ and $R^-(J)$ lines terminate on the lower of the two interacting states. The $P^+(J)$ lines terminate on the upper of the two interacting states.

The spectrum for the feature near 21276 cm^{-1} (Figure 5.2) was assigned by least-square fitting the rotational lines to the equation

$$\nu = \nu_0 + B' J' (J' + 1) - B'' J'' (J'' + 1), \quad (5.3)$$

which gave an excellent fit of the data and provided accurate values of the band origin, ν_0, ground state rotational constant, B'', and excited state rotational constant, B', for $^{104}Pd^{28}Si$, $^{105}Pd^{28}Si$, $^{106}Pd^{28}Si$, and $^{108}Pd^{28}Si$. Ground and excited state bond lengths, r_0'' and r', were determined from the corresponding rotational constants. These spectroscopic parameters are listed in Table 5.2. A weighted average of the r_0'' values for the various isotopomers provides our best estimate of the r_0'' bond length of the molecule, 2.0824 ± 0.0003 Å (1σ error limit). The large increase in bond length that accompanies the electronic excitation causes an abrupt band head to form in the R-branch at R(3).

In contrast to the 21276 cm^{-1} band, the rotationally resolved spectra of the 0-0 and 1-0 bands of the [21.4]0 ← X 0 system cannot be accurately reproduced using line positions that follow equation (5.3). Although the low-J lines can be readily fitted to the form of equation (5.3), perturbations destroy the quality of the fit if higher-J lines are included. Despite the presence of perturbations, it has proven possible to assign many of the lines using combination differences involving the now well-determined ground state rotational constant, B_0'', through the combination difference relationship

$$R(J - 1) - P(J + 1) = (4J + 2) B_0''. \quad (5.4)$$

Using the known B_0'' value, a search for lines separated by $(4J + 2)B_0''$ allowed the R(J-1) and P(J+1) lines to be unambiguously identified.

Table 5.2 Fitted Spectroscopic Parameters of PdSi.[a]

Spectroscopic fitted parameters for transition near 21,276 cm^{-1}							
Molecule	ν_0	B″	B′	r″	r′		
^{104}PdSi	21279.7484(16)	0.176401(74)	0.133681(66)	2.0822(4)	2.3919(6)		
^{105}PdSi	21277.3858(13)	0.176033(64)	0.133381(57)	2.0823(4)	2.3921(5)		
^{106}PdSi	21275.0619(23)	0.175582(134)	0.133049(116)	2.0829(8)	2.3927(10)		
^{108}PdSi	21270.5340(29)	0.174402(353)	0.132098(292)	2.0858(21)	2.3967(26)		
Deperturbation fitting parameters of ^{108}PdSi							
Band Position	T^+	T^-	B^+	B^-	H_{12}	r^+	r^-
21400	21414.09	21391.36	0.1318	0.1627	5.24	2.399	2.160
21769	21780.63	21764.14	0.144	0.1612	11.09	2.293	2.170

[a] All numerical values are given in units of cm^{-1} with the exception of bond lengths, which are given in units of Å. Values given in parentheses represent the 1σ error limits of the fitted parameter, in units of the last reported digits.

The perturbations in the 0-0 and 1-0 bands become evident when the energy of the upper state is computed by adding the energy of the lower level to the measured line position, according to:

$$E(J') = \nu(J' \leftarrow J'') + B_0''J''(J'' + 1). \quad (5.5)$$

For an unperturbed state, the E(J′) values should follow the form

$$E(J') = T_0 + B'J'(J' + 1) . \quad (5.6)$$

Using the value of B' obtained by fitting the low-J R(J) and P(J) lines, the reduced term energy, defined by $E(J') - B'J'(J' + 1)$, should be linear when plotted *vs.* J′(J′+1), and should have zero slope. Here, the subtraction of $B'J'(J'+1)$ allows the deviations from the straight line to be more readily observed. Figure 5.4 provides plots of the reduced term energy for all three bands that have been rotationally resolved. Although the range of observed J values is not as large for the 21276 cm^{-1} band, there is no evidence of curvature in the plot. In contrast, a downward curvature is evident in the data for the 21761 cm^{-1} band and is very clear in the data for the 21392 cm^{-1} band. The downward curvature indicates that the perturbing state lies above the state that is observed. It is also evident that the interaction between the states becomes more important at higher J values. This could result from either of two causes: (1) The interacting states could approach one another as J increases, leading to a stronger interaction at higher J, as would be the case if the higher of the two states had a smaller rotational constant than the lower of the states, or (2) the interaction matrix element could increase as a function of J, as would be the case if the higher of the states had Ω=1, leading to an interaction matrix element that is

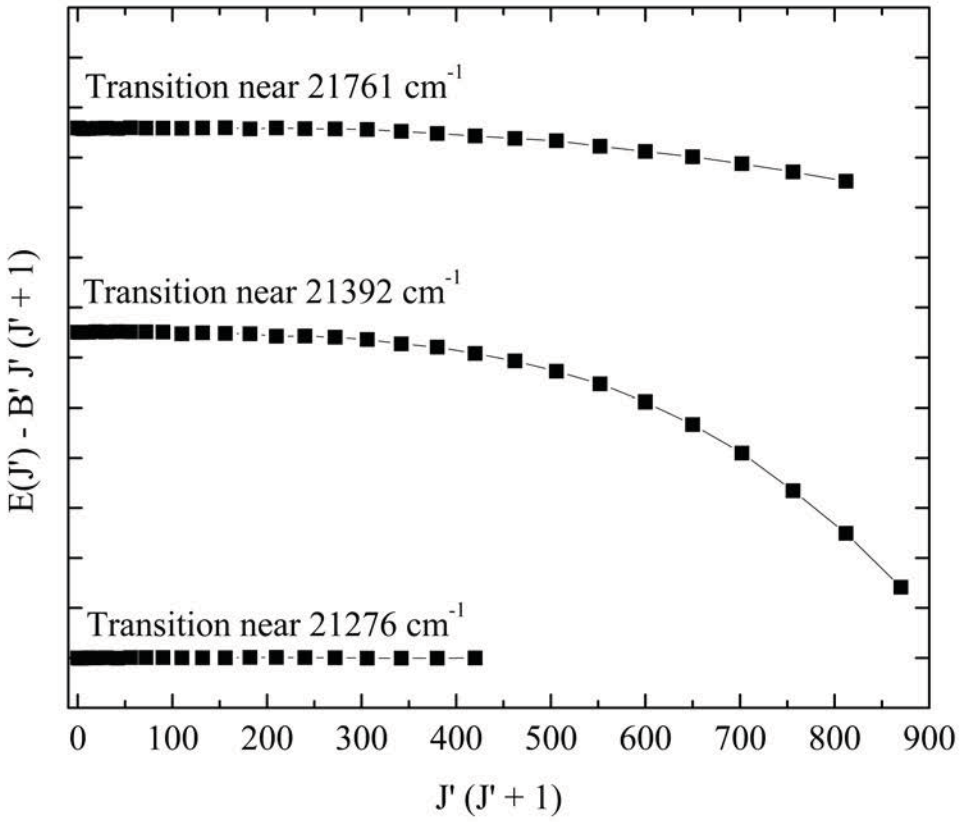

Figure 5.4 Reduced term energy plot, showing the curvature in the reduced term energy for the 21392 and 21761 cm^{-1} bands. For these plots, a constant was added to the reduced term energy to put all three plots on the same axis system. The data plotted are E(J′) – 0.13368 J′(J′+1) + 468.25 for the 21276 cm^{-1} band; E(J′) – 0.1610 J′(J′+1) + 364.29 for the 21392 cm^{-1} band; and E(J′) – 0.1575 J′(J′+1) for the 21761 cm^{-1} band. Tic marks on the vertical axis are spaced 1 cm^{-1} apart.

proportional to J(J+1).[47] These cases are not exclusive; both effects could be present at the same time.

Ideally, in order to deperturb a pair of interacting states, one would like to measure the energies of rotational levels belonging to both of the states, and then fit both sets of levels to a model. Only a few lines were observed for the state perturbing the upper state of the 0-0 band, however; no levels of the state that perturbs the upper state of the 1-0 band were observed. Nevertheless, deperturbation analyses of the upper states of both the 0-0 and 1-0 bands were attempted. To do so, the system was modeled as a homogeneous perturbation in which the two interacting states both have $\Omega = 0$ and have energies given by

$$T^{+} + B^{+}\,J(J+1) \tag{5.7}$$

and

$$T^{-} + B^{-}\,J(J+1) \tag{5.8}$$

in the absence of the perturbation. Here, the + superscript refers to the higher of the two interacting states, the − superscript to the lower. For a homogeneous perturbation ($\Delta\Omega = 0$), the perturbation matrix element should be independent of J, and may be taken to be a constant, H_{12}. Within this model, the energies of the resulting mixed energy levels are the eigenvalues of the matrix Hamiltonian

$$H = \begin{pmatrix} T^{+} + B^{+}J(J+1) & H_{12} \\ H_{12} & T^{-} + B^{-}J(J+1) \end{pmatrix}. \tag{5.9}$$

The eigenvalues that result from this Hamiltonian are given by

$$E^{\pm}(J) = \frac{1}{2}\left[\left(T^{+} + T^{-}\right) + (B^{+} + B^{-})J(J+1) \pm \sqrt{\left[\left(T^{+} + T^{-}\right) + \left(T^{+} + T^{-}\right)J(J+1)\right]^{2} + 4H_{12}{}^{2}}\right] \qquad (5.10)$$

The measured energy levels of the upper state, as deduced using equation (5.6), were then fitted to the expression for $E^{-}(J)$. The lower root was chosen for the fitting procedure, because the downward curvature observed in Figure 5.4 shows that the levels are perturbed from above. In the case of the 0-0 band near 21392 cm^{-1}, three extra lines were observed in the spectrum that were ultimately assigned as the $P^{+}(20)$, $P^{+}(21)$, and $P^{+}(22)$ lines for the upper of the two interacting states. These are labeled in Figure 5.3, where the most obvious of the three lines is the $P^{+}(20)$ line found near 21392.9 cm^{-1}. These three lines were included in the fitting procedure, using the expression for $E^{+}(J)$, which is why the + symbol in the $P^{+}(J)$ designation is included. Their rotational numbering was varied to obtain the best fit in the nonlinear least-squares fitting procedure.

The fitting routine allowed T^{+}, T^{-}, B^{+}, B^{-}, and H_{12} to vary to achieve the best fit. The values of these parameters are listed in Table 5.2 for ^{108}PdSi, the only isotope that was deperturbed. From these parameters it was possible to predict the energies and P- and R-line positions of the higher of the two interacting states, designated as $P^{+}(J)$ and $R^{+}(J)$. This was particularly useful for the 1-0 band because the fit was carried out only using data for the lower of the two interacting states. The fitted parameters could be tested by comparing the predicted $R^{+}(J)$ band head location to what is observed in the low-resolution spectrum. The difference between the calculated and observed $R^{+}(J)$ band head positions was less than 0.07 cm^{-1}. As the resolution of the dye laser in low-resolution is 0.15 cm^{-1}, this must be considered a validation of the fit.

The results of the deperturbation analysis of the 0-0 band are displayed in Figure 5.5, which provides a reduced term energy plot of $E(J') - 0.161\ J'(J'+1)$ as a function of $J'(J'+1)$. The solid points represent the measured energy levels for the upper (circles) and lower (squares) interacting states. The solid curves represent the fitted curves for $E^{+}(J')$ and $E^{-}(J')$, as given in equation (5.10) and plotted as a continuous function of $J'(J' + 1)$. The dashed curves represent the energies of the interacting states prior to their interaction, as given by equations (5.7 and 5.8). Figure 5.6 provides a similar set of plots for the 1-0 band. The fit of the 0-0 band was constrained by the observation of three levels belonging to the upper of the two interacting states, lending credence to the parameters derived from that analysis. The lack of observed levels of the upper of the interacting states in the case of the 1-0 band makes the deperturbation analysis in that case somewhat less secure. The fact that the predicted $R^{+}(J)$ band head falls where it is observed, however, argues for the validity of the analysis.

Although this analysis shows that the data can be fit quite well by assuming a homogeneous interaction with another $\Omega = 0$ state, we have not investigated whether a heterogeneous interaction with a $\Omega = 1$ state could also fit the data. With so little information available about the upper of the two interacting levels for either the 0-0 or the 1-0 bands, it is likely that fits assuming a perturber state with $\Omega = 1$ could also be achieved. In any case, the rotational constants, B_0^{-} and B_1^{-}, deduced for the two bands are consistent with the assignment of the features as the 0-0 and 1-0 bands of a band system.

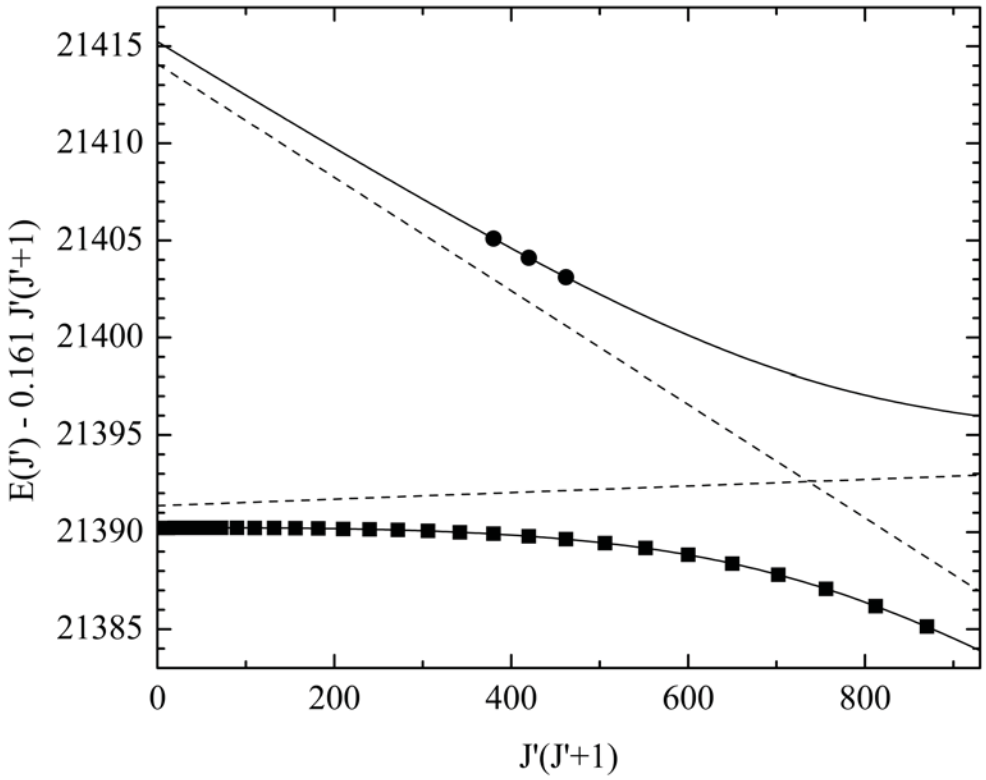

Figure 5.5 Deperturbation of the 0-0 band near 21392 cm^{-1} and the upper interacting state located near 21414 cm^{-1}. The solid squares and circles correspond to the measured energy levels of the lower and upper interacting states. The solid lines are the fits to the data obtained using the two-state perturbation model; the dashed lines correspond to the deperturbed energy levels.

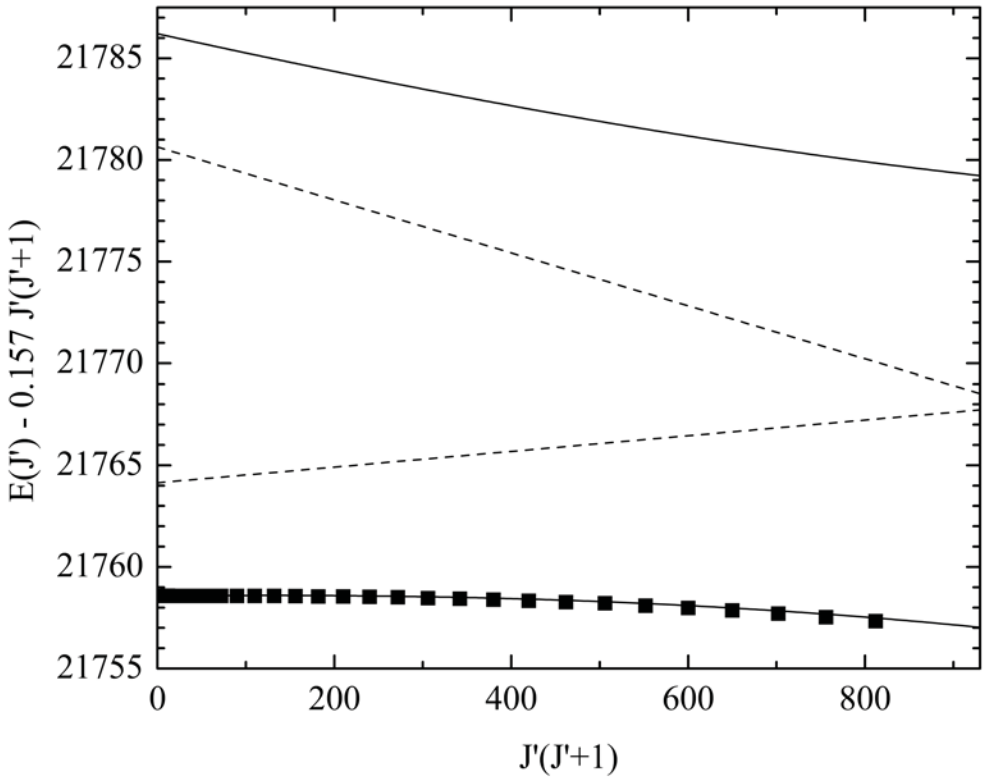

Figure 5.6 Deperturbation of the band near 21761 cm^{-1} using only the $E^{-}(J')$ eigenvalues. The solid squares correspond to the measured energy levels of the lower of the two interacting states, the solid lines provide the fit obtained using the two-state perturbation model, and the dashed lines correspond to the deperturbed energy levels.

5.4 Discussion

Considering the valence orbitals of PdSi to be those that derive from the $4d_{Pd}$, $5s_{Pd}$, $3s_{Si}$, and $3p_{Si}$ atomic orbitals, these atomic orbitals combine to form the core-like 1σ orbital, which is primarily $3s_{Si}$ in character, the bonding 2σ and 1π orbitals, which are primarily bonding combinations of the $4d_{Pd}$ and $3p_{Si}$ orbitals, the nonbonding 1δ and 3σ orbitals, which are primarily $4d\delta_{Pd}$ and $5s_{Pd}$ in character, respectively, and the antibonding 2π and 4σ orbitals, which are primarily antibonding combinations of the $4d_{Pd}$ and $3p_{Si}$ orbitals. Previous theoretical work has identified the strongest candidates for the ground electronic state to be the $1\sigma^2 2\sigma^2 1\pi^4 1\delta^4 3\sigma^2$, $^1\Sigma^+$ state and the $1\sigma^2 2\sigma^2 1\pi^4 1\delta^4 3\sigma^1 2\pi^1$, $^3\Pi$ state.[24,27-28] The $1\sigma^2 2\sigma^2 1\pi^4 1\delta^4 2\pi^2$, $^3\Sigma^-$ state was also calculated to lie low in energy in an early Hartree-Fock plus configuration interaction calculation.[24]

Unfortunately, in all three cases the expected ground level will have Ω = 0. For the $^1\Sigma^+$ state, the only level present has $\Omega=0^+$; for the $^3\Pi$ state, which is regular, the ground level will be either $\Omega=0^+$ or 0^-, depending on the second order spin-orbit interactions that dictate the splitting between these levels; for the $^3\Sigma^-$ state, the $\Omega=0^+$ level is expected to lie lowest in energy because of second order spin-orbit interactions with the higher lying $^1\Sigma^+$ state that arises from the same configuration. Thus, in all cases, the ground level will have Ω = 0, consistent with our experimental data. Based on the experimental data alone, it is impossible to identify the ground configuration and term of PdSi.

By comparing the measured r_0 bond lengths of the closely related molecules, NiSi, RhSi, RuSi, and PtSi, to the r_e bond lengths computed in the most recent density functional (DFT) calculation,[27] we can establish the expected error in the calculation.

This provides justification for assigning a ground configuration and term in PdSi. For NiSi, which is accepted as having the $^1\Sigma^+$ ground state, the DFT calculation of r_e underestimates the measured value of r_0 by 0.017 Å.[14,27] For the $^2\Sigma^+$ ground state of RhSi, the DFT calculation of r_e overestimates the value of r_0 by 0.016 Å.[18,27] For the $^3\Delta$ ground term of RuSi, the calculation overestimates the bond length by 0.016 Å,[17,27] while for PtSi ($^1\Sigma^+$) the bond length is overestimated by 0.025 Å.[16,27] For these related molecules, the DFT value of r_e never differs from the measured value of r_0 by more than 0.03 Å, and the DFT calculation overestimates the bond length in all cases except for NiSi. For PdSi, the calculated r_e bond length for the $^1\Sigma^+$ is 2.117 Å, which is larger than the measured value by 0.035 Å. In contrast, the calculated r_e value for the unidentified triplet state is 2.175 Å, which is larger than the measured value by 0.093 Å. Because the same methodology was used for the calculation of all of the transition metal silicides, one would expect errors of similar magnitude in all cases. On this basis, we conclude that the ground configuration and term of PdSi is probably $1\sigma^2 2\sigma^2 1\pi^4 1\delta^4 3\sigma^2$, $^1\Sigma^+$.

In the Introduction it was noted that a comparison of the bond length, vibrational frequency, and bond dissociation energy of NiSi to AlCu and of PtSi to AlAu demonstrates the existence of strong π bonding in the nickel group silicides. In this context, it is of interest to compare PdSi to its isovalent coinage group counterpart, AlAg. The bond length of PdSi obtained in this investigation, r_0 = 2.082 Å, is 0.392 Å shorter than the r_0 = 2.474 Å value that has been measured for AlAg.[48] Further, the bond energy of PdSi measured by Knudsen effusion methods, 2.66(12) or 3.21(15) eV,[23-24] is much greater than that found using the same method for AlAg, 1.86(9) eV.[49] These comparisons demonstrate that π bonding remains important in the 4*d* molecule, PdSi, just

as in the NiSi and PtSi species. Although the vibrational frequency of PdSi has not yet been measured, these results suggest that it will be significantly larger than the value of ω_e = 256 cm^{-1} that has been measured for AlAg.[48] The enormous contraction in bond length that occurs in moving from AlAg to PdSi also provides strong support for the assignment of the ground configuration and term as $1\sigma^2 2\sigma^2 1\pi^4 1\delta^4 3\sigma^2$, $^1\Sigma^+$. The alternative $^3\Pi$ and $^3\Sigma^-$ states place one or two electrons in the antibonding 2π orbital, and would be expected to have longer bond lengths.

5.5 Conclusion

The spectra of diatomic PdSi have been investigated using the resonant two-photon ionization technique. Numerous bands have been observed, three of which have been rotationally resolved and analyzed. The data demonstrate that the ground state of PdSi has a bond length of 2.082 Å, and has $\Omega = 0$. Based on a comparison to theoretical work, the ground state is assigned as a $^1\Sigma^+$ term deriving from the $1\sigma^2 2\sigma^2 1\pi^4 1\delta^4 3\sigma^2$ configuration. Two of the observed bands are assigned as the 0-0 and 1-0 bands of the $[21.4]0^+ \leftarrow X\ ^1\Sigma^+$ system. Unfortunately, both upper states are perturbed. A deperturbation analysis provides $\Delta G_{1/2}$ = 372.8 cm^{-1}, B_e = 0.16345 cm^{-1}, and r_e = 2.155 Å for the [21.4]0 state. The bond length and bond dissociation energy of the ground state of PdSi demonstrate the existence of strong $5d\pi - 3p\pi$ bonding in this molecule.

5.6 References

[1]S. P. Murarka, Ann. Rev. Mater. Sci. **13,** 117-37 (1983).

[2]B. J. Aylett, B. A. Scott, R. D. Estes, and D. B. Beach, in *Silicon Chemistry*, edited by J. Y. Corey, E. R. Corey, and P. P. Gaspar (Ellis Horwood, 1987), pp. 357-64.

[3]S. P. Murarka, *Silicides for VLSI Applications* (Academic Press, 1983).

[4]J. Kurianski, J. Van Damme, J. Vermeiren, K. Maex, and C. Claeys, Proc. SPIE-Int. Soc. Opt. Eng. **1308,** 27-35 (1990).

[5]J. L. Gates, W. G. Connelly, T. D. Franklin, R. E. Mills, F. W. Price, and T. Y. Wittwer, Proceedings of SPIE - International Society of Optical Engineering **1540,** 262-73 (1991).

[6]J. Chen, J. P. Colinge, D. Flandre, R. Gillon, J. P. Raskin, and D. Vanhoenacker, J. Electrochem. Soc. **144,** 2437-42 (1997).

[7]Y. Song and S. Jin, Appl. Phys. Lett. **90,** 173122/1-/3 (2007).

[8]Y. Song, A. L. Schmitt, and S. Jin, Nano Lett. **7,** 965-9 (2007).

[9]J. J. Scherer, J. B. Paul, C. P. Collier, and R. J. Saykally, J. Chem. Phys. **102,** 5190-9 (1995).

[10]A. I. Boldyrev, J. Simons, J. J. Scherer, J. B. Paul, C. P. Collier, and R. J. Saykally, J. Chem. Phys. **108,** 5728-32 (1998).

[11]Y. Lefebvre and J. Schamps, J. Mol. Spectrosc. **201,** 128-33 (2000).

[12]J. J. Scherer, J. B. Paul, C. P. Collier, and R. J. Saykally, J. Chem. Phys. **103,** 113-20 (1995).

[13]J. J. Scherer, J. B. Paul, C. P. Collier, A. O'Keefe, and R. J. Saykally, J. Chem. Phys. **103,** 9187-92 (1995).

[14]N. F. Lindholm, D. J. Brugh, G. K. Rothschopf, S. M. Sickafoose, and M. D. Morse, J. Chem. Phys. **118,** 2190-6 (2003).

[15]J. B. Paul, J. J. Scherer, C. P. Collier, and R. J. Saykally, J. Chem. Phys. **104,** 2782-8 (1996).

[16]L. Shao, S. M. Sickafoose, J. D. Langenberg, D. J. Brugh, and M. D. Morse, J. Chem. Phys. **112,** 4118-23 (2000).

[17]N. Lindholm and M. D. Morse, J. Chem. Phys. **127,** 084317/1-/5 (2007).

[18]A. G. Adam, A. D. Granger, W. J. Balfour, and R. Li, J. Mol. Spectrosc. **258,** 35-41 (2009).

[19]Y. M. Hamrick and W. Weltner, Jr., J. Chem. Phys. **94,** 3371-80 (1991).

[20]J. E. Kingcade, Jr. and K. A. Gingerich, J. Chem. Soc. Faraday Trans. 2 **85,** 195-200 (1989).

[21]A. Vander Auwera-Mahieu, N. S. McIntyre, and J. Drowart, Chem. Phys. Lett. **4,** 198-200 (1969).

[22]J. E. Kingcade, Jr. and K. A. Gingerich, J. Chem. Phys. **84,** 4574-8 (1986).

[23]A. Vander Auwera-Mahieu, R. Peeters, N. S. McIntyre, and J. Drowart, Trans. Faraday Soc. **66,** 809-16 (1970).

[24]I. Shim, J. E. Kingcade, and K. A. Gingerich, Z. Phys. D: At., Mol. Clusters **7,** 261-9 (1987).

[25]K. A. Gingerich, J. Chem. Phys. **50,** 5426-8 (1969).

[26]K. A. Gingerich, R. Haque, and J. E. Kingcade, Jr., Thermochim. Acta **30,** 61-71 (1979).

[27]Z. J. Wu and Z. M. Su, J. Chem. Phys. **124,** 184306/1-/15 (2006).

[28]N. Russo, J. Andzelm, and D. R. Salahub, Chem. Phys. **114,** 331-8 (1987).

[29]S. A. Cooke, M. C. L. Gerry, D. J. Brugh, and R. D. Suenram, J. Mol. Spectrosc. **223,** 185-94 (2004).

[30]R. F. Barrow and D. N. Travis, Proc. Roy. Soc. (Lond.) A **273,** 133-44 (1963).

[31]K. A. Gingerich and G. D. Blue, J. Chem. Phys. **59,** 185-9 (1973).

[32]M. Barysz and P. Pyykko, Chem. Phys. Lett. **368,** 538-41 (2003).

[33]A. N. Andriotis, M. Menon, G. E. Froudakis, Z. Fthenakis, and J. E. Lowther, Chem. Phys. Lett. **292,** 487-92 (1998).

[34]H. Haberlandt, Chem. Phys. **138,** 315-25 (1989).

[35]I. Shim and K. A. Gingerich, Z. Phys. D: At., Mol. Clusters **16,** 141-8 (1990).

[36]J. M. Behm, C. A. Arrington, J. D. Langenberg, and M. D. Morse, J. Chem. Phys. **99,** 6394-408 (1993).

[37]R. S. DaBell, R. G. Meyer, and M. D. Morse, J. Chem. Phys. **114,** 2938-54 (2001).

[38]J. D. Langenberg, L. Shao, and M. D. Morse, J. Chem. Phys. **111,** 4077-86 (1999).

[39]H. Tan, D. Dai, and K. Balasubramanian, Chem. Phys. Lett. **286,** 375-81 (1998).

[40]Z. Fu, G. W. Lemire, Y. M. Hamrick, S. Taylor, J.-C. Shui, and M. D. Morse, J. Chem. Phys. **88,** 3524-31 (1988).

[41]M. D. Morse, in *Methods of Experimental Physics: Atomic, Molecular, and Optical Physics*, Vol. II Atoms and Molecules, edited by F. B. Dunning and R. Hulet (Academic Press, Inc., Orlando, Florida, 1996), pp. 21-47.

[42]W. C. Wiley and I. H. McLaren, Rev. Sci. Instrum. **26,** 1150 - 7 (1955).

[43]B. A. Mamyrin, V. I. Karataev, D. V. Shmikk, and V. A. Zagulin, Zh. Eksp. Teor. Fiz. **64,** 82-9 (1973).

[44]J. Cariou and P. Luc, *Atlas du Spectre d'Absorption de la Molécule de Tellure entre 18500 - 23800 cm^{-1}* (CNRS, Paris, 1980).

[45]P. R. Bevington, *Data Reduction and Error Analysis for the Physical Sciences* (McGraw-Hill, New York, 1969).

[46]EPAPS, See EPAPS Document No. E-JCPSAx-xxx-xxxxx for 12 pages of vibronically resolved spectra, rotationally resolved spectra, line positions, and rotational fits of PdSi. A direct link to this document may be found in the online article's HTML reference section. The document may also be reached via the EPAPS homepage (http://www.aip.org/pubservs/epaps.html) or from ftp.aip.org in the directory /epaps. See the EPAPS homepage for more information.

[47]H. Lefebvre-Brion and R. W. Field, *The Spectra and Dynamics of Diatomic Molecules* (Elsevier, Amsterdam, 2004).

[48]D. L. Robbins, C. S. Yeh, J. S. Pilgrim, G. L. Lang, and M. A. Duncan, J. Chem. Phys. **100,** 4775-83 (1994).

[49]A. M. Cuthill, D. J. Fabian, and S. Shu-Shou-Shen, J. Phys. Chem. **77,** 2008-11 (1973).

APPENDIX A

ELECTRICAL DIAGRAMS FOR VARIOUS COMPONENTS USED IN THE INFRARED SPECTROMETER

A.1 Electrical Diagrams for the Master Oscillator

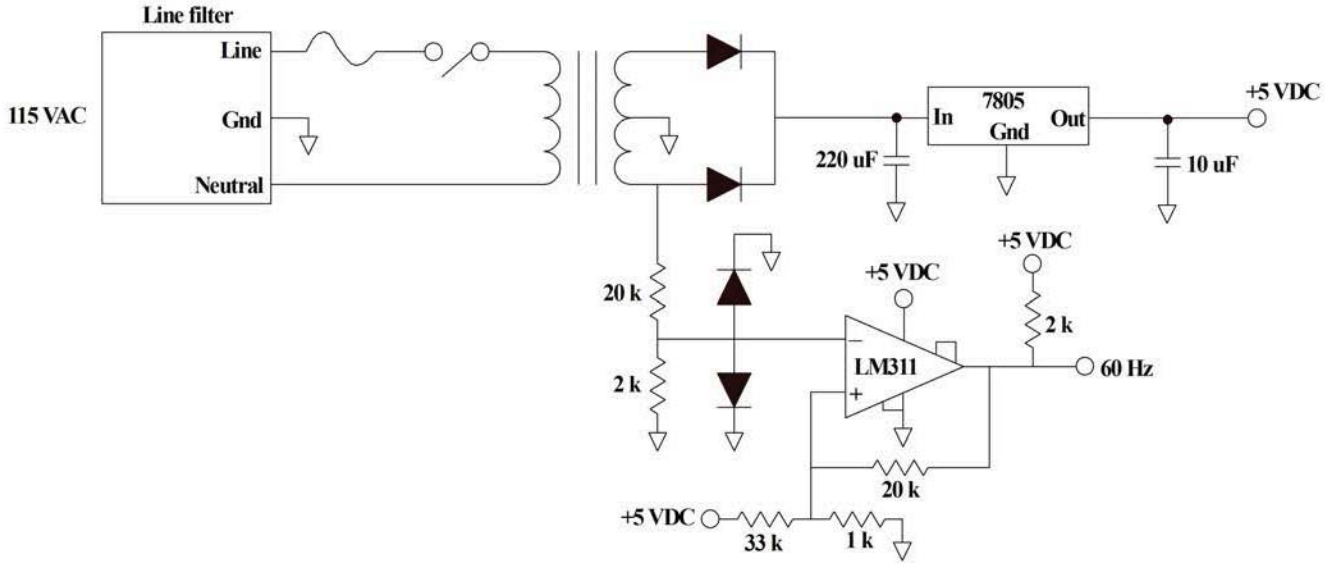

Figure A.1 An electrical diagram showing the power supply and 60 Hz generator used in the master oscillator. The LM311 component is responsible for producing a 60Hz 50% duty cycle square wave waveform from the 60Hz sinusoidal AC voltage input. All resistors have units of Ohms (Ω).

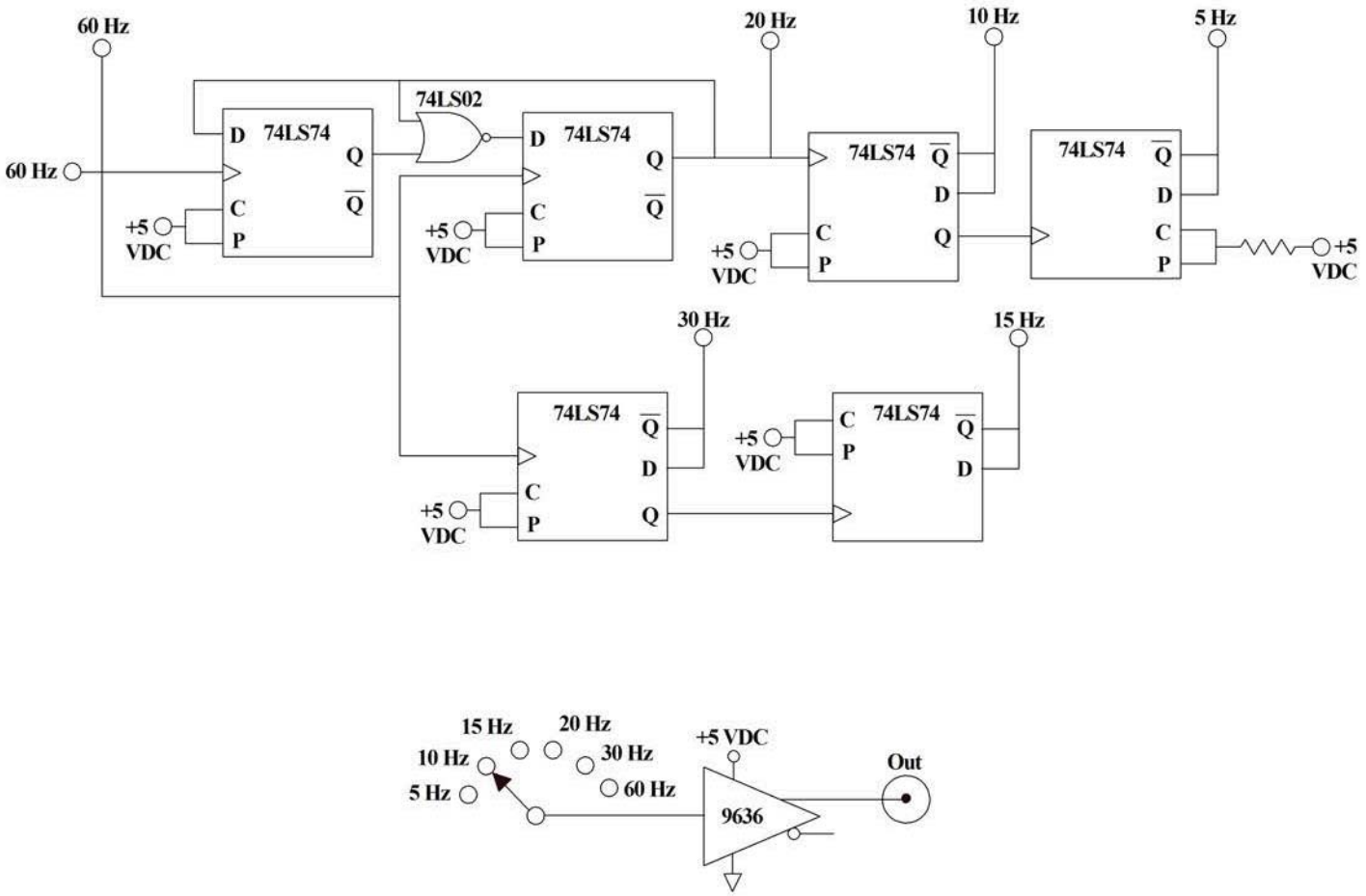

Figure A.2 Circuit diagram showing the components needed to divide the 60 Hz square wave generated in Figure A.1 to 5, 10, 15, 20, or 30 Hz. The desired frequency is selected with a multi-position switch and sent out through a BNC bulkhead.

A.2 Electrical Diagrams for the Nozzle Driver

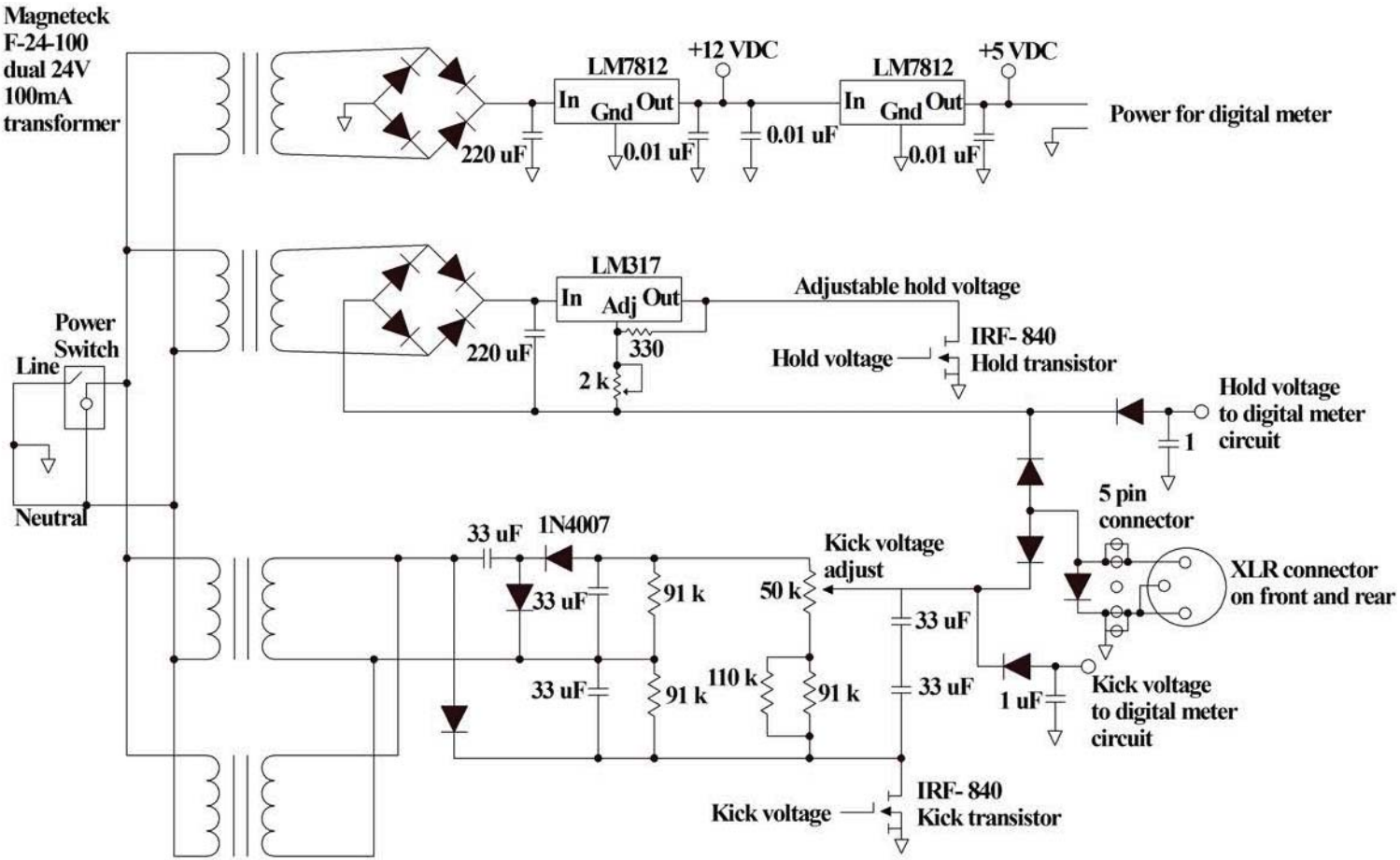

Figure A.3 This electrical diagram shows the circuits used to produce DC voltages in the nozzle driver, as well as the circuits used to generate the kick and hold voltages needed to run the nozzle. All resistors have units of Ohms (Ω).

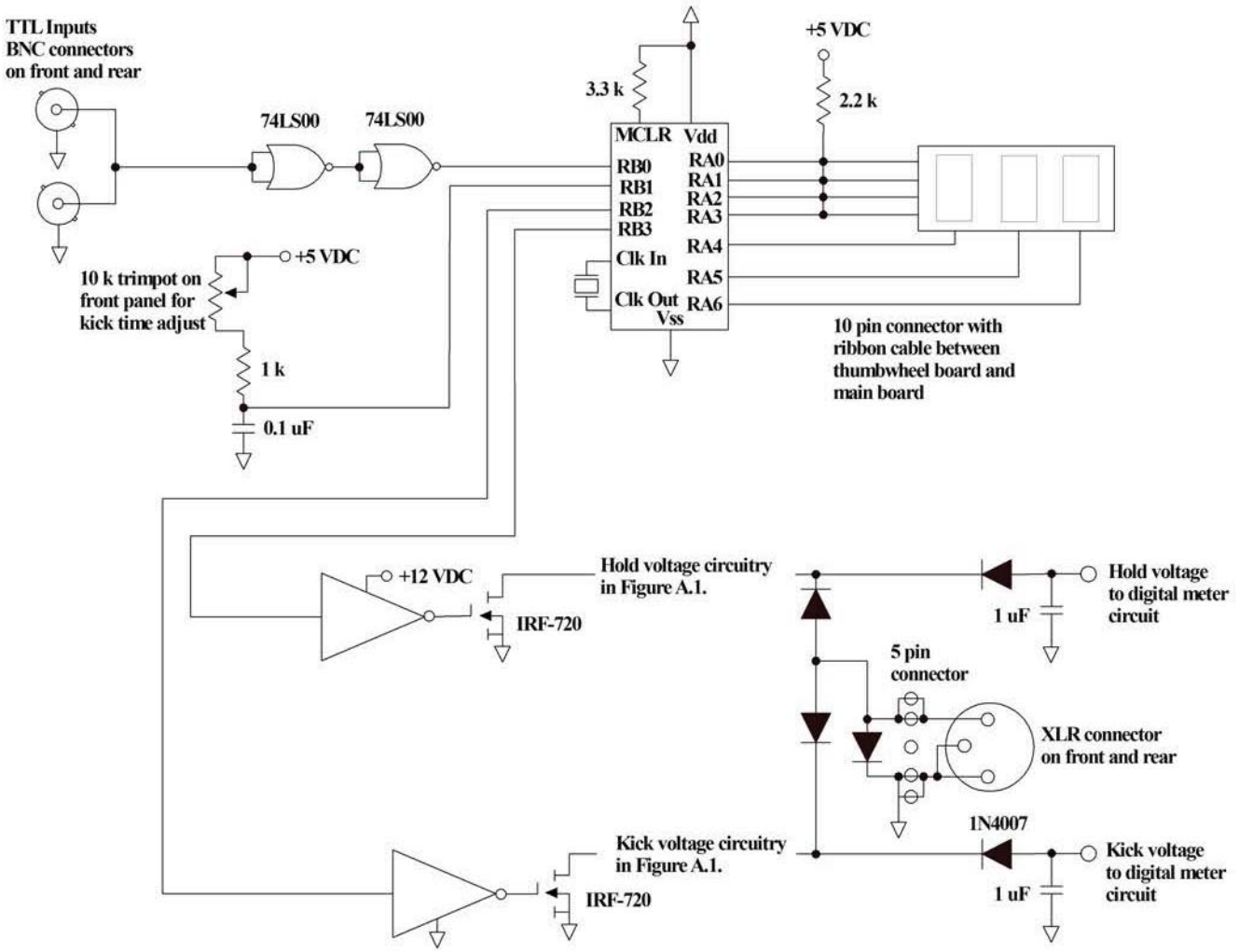

Figure A.4 Circuit diagram showing the components needed to set the hold and kick times (in units of μs) of the nozzle. All resistors have units of Ohms (Ω).

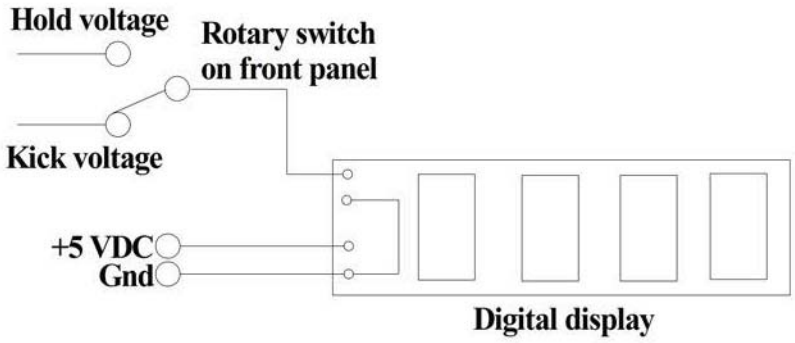

Figure A.5 Schematic of the digital display on the nozzle driver, showing the two voltages that can be displayed and the power source needed to drive the display.

A.3 Electrical Diagrams for the High Voltage Pulser

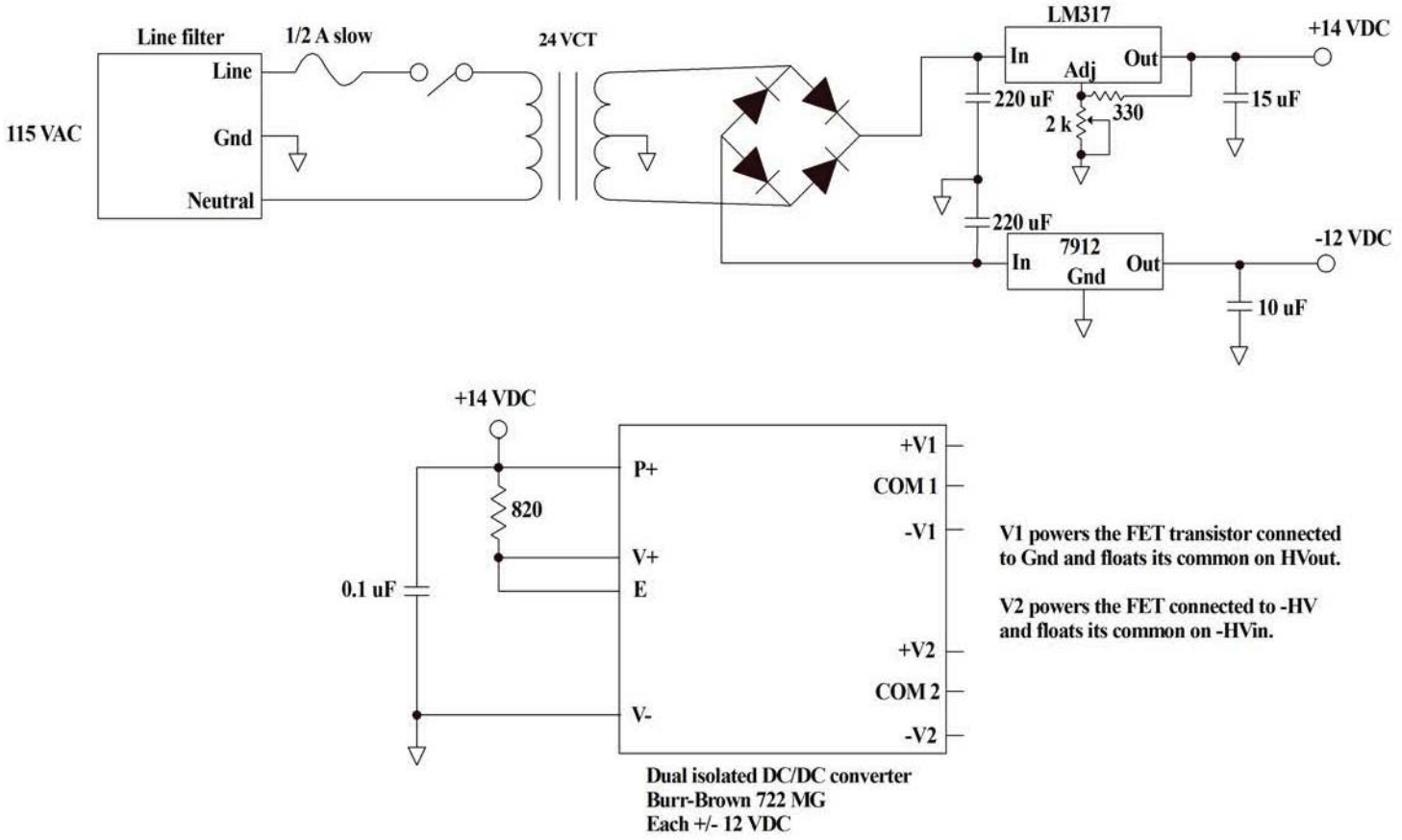

Figure A.6 An electrical diagram showing how the various voltages required by the high voltage pulser are generated. All resistors have units of Ohms (Ω).

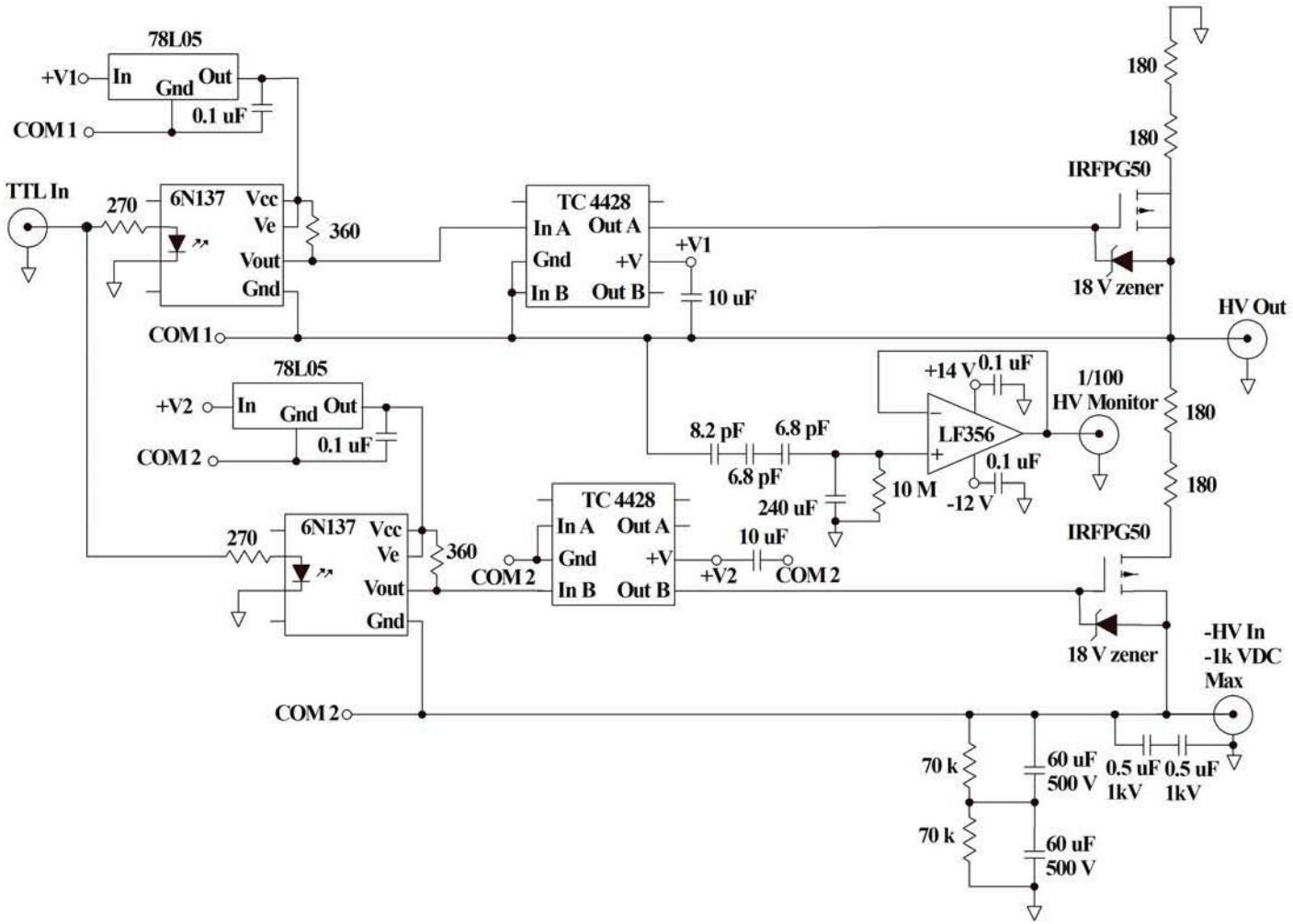

Figure A.7 This diagram shows the components needed to produce a high voltage output that follows the TTL In signal. The TTL In signal is generated from a National Instruments 6602 timer/counter card and is typically a finite pulse train of 15kHz. All resistors have units of Ohms (Ω).

A.4 Electrical Diagram for the High Frequency Lock-In Detector

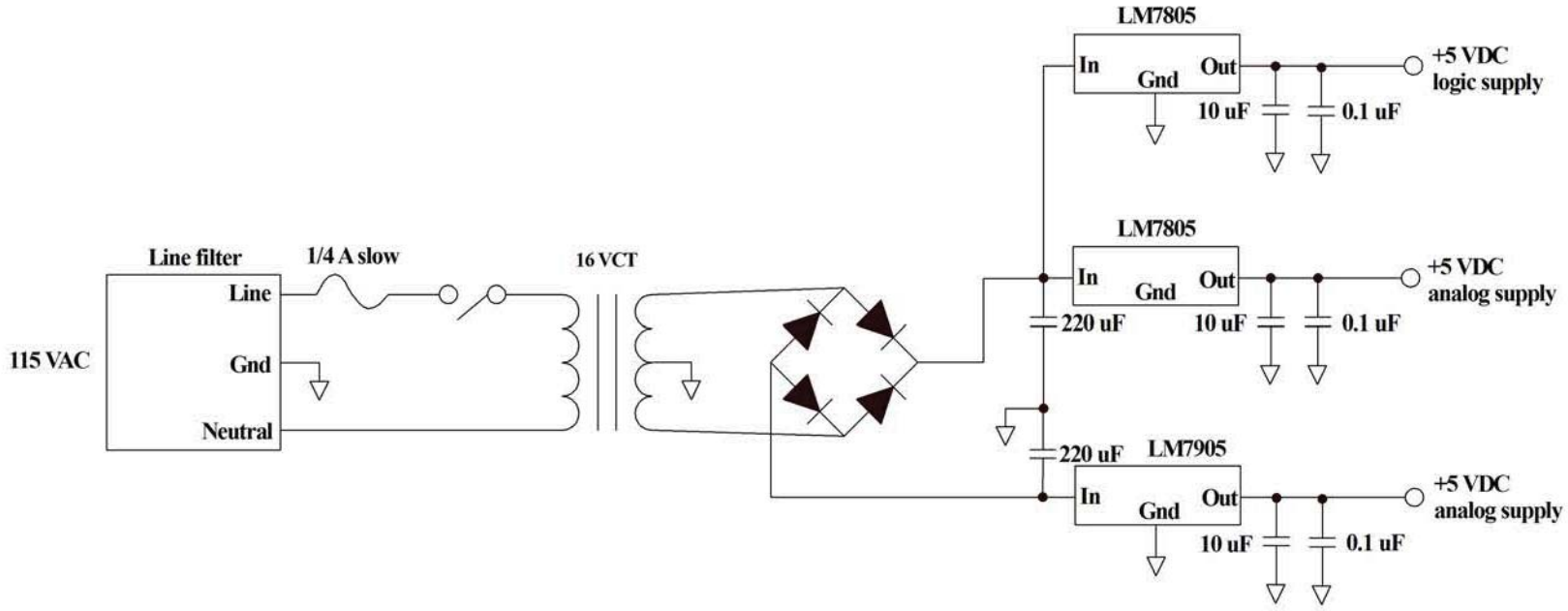

Figure A.8 An electrical diagram showing how the three power supplies used in the high frequency lock-in detector are generated.

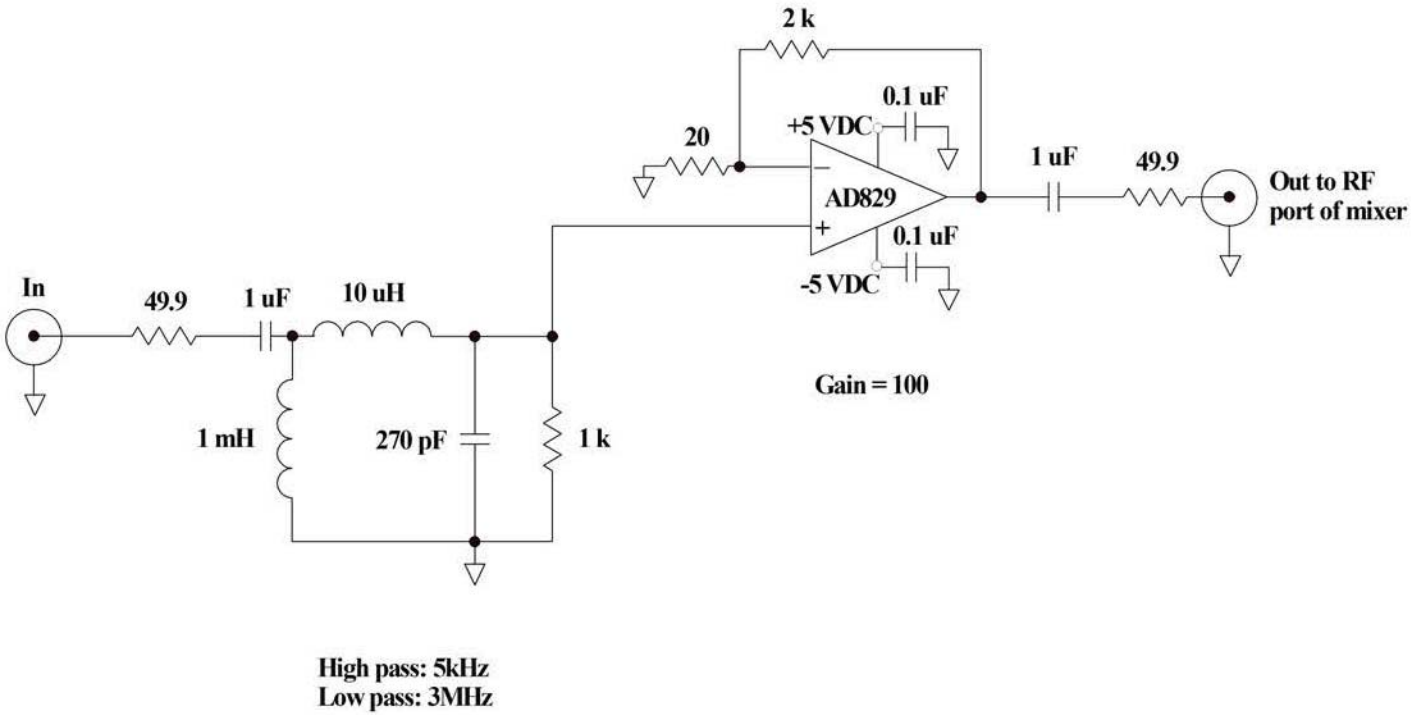

Figure A.9 Electronic circuit that filters the absorption signal from the infrared detector (only allowing signal between 5kHz and 3MHz to pass) and amplifies it by 100x. This signal is then fed to the RF pin on the mixer (Figure A.11). All resistors have units of Ohms (Ω).

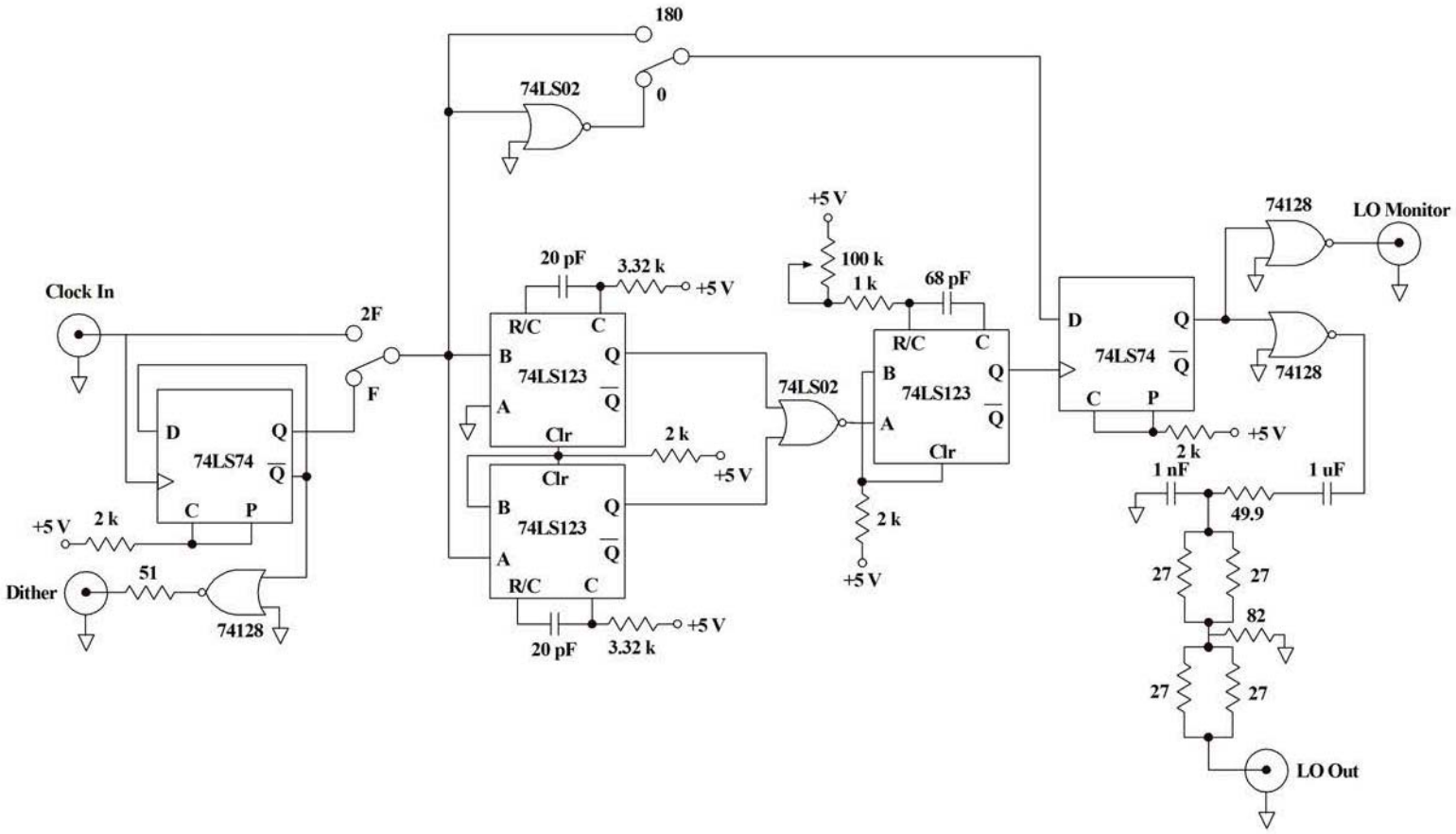

Figure A.10 Electrical diagram showing how the Clock In signal is transformed into a square wave of proper amplitude for the mixer in Figure A.11. The Clock In signal is generated from a National Instruments 6602 timer/counter card. All resistors have units of Ohms (Ω).

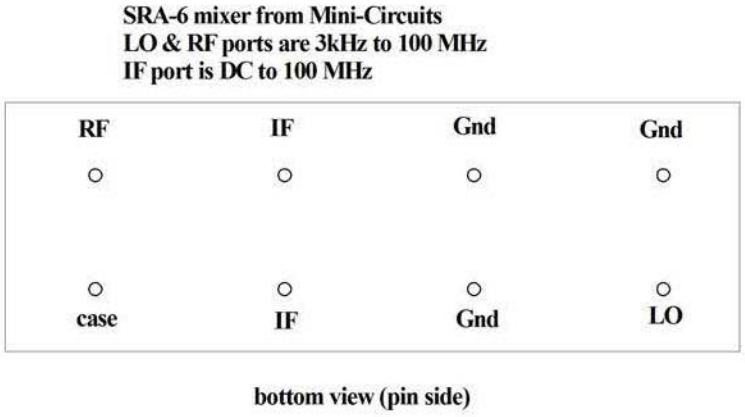

Figure A.11 The mixer is housed in its own enclosure, with the local oscillator (LO), radio frequency (RF), and intermediate frequency (IF) signals all delivered to BNC bulkhead receptacles. The RF signal is obtained from the Preamp/Input filter module in Figure A.9. The LO pin connects to the module in Figure A.10. The IF signal, the sum and difference of the RF and LO signals, connects to the Output Filter module in Figure A.12.

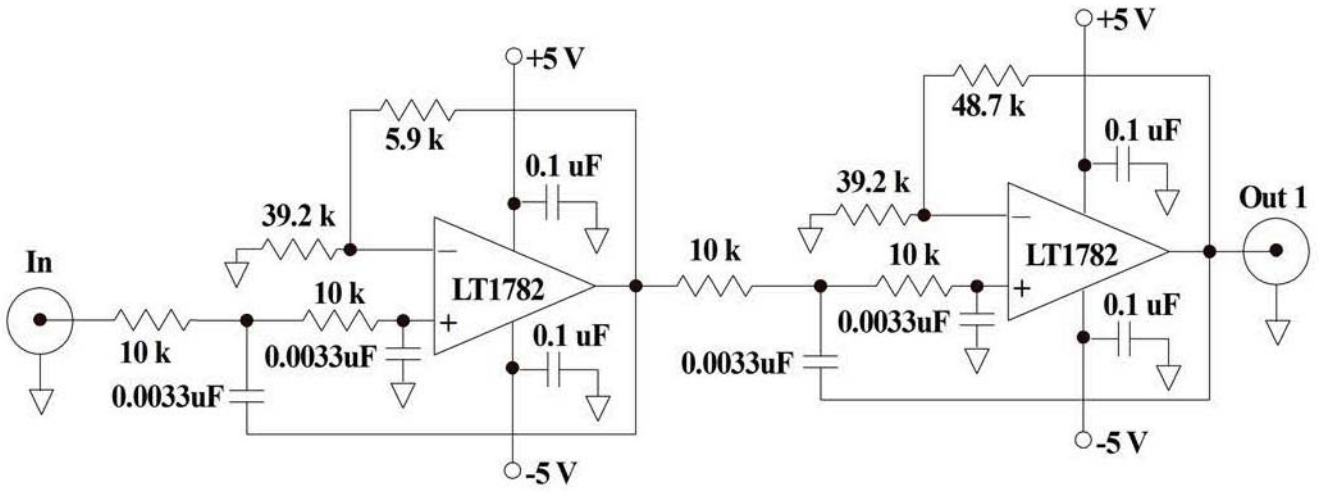

Figure A.12 Electronic circuit that takes the sum and difference signals from the IF terminal (Figure A.11) and only allows the difference in the signals to pass. This signal is then digitized and stored on a computer for analysis. All resistors have units of Ohms (Ω).

A.5 Electrical Diagrams for the Low Frequency Lock-In Detector

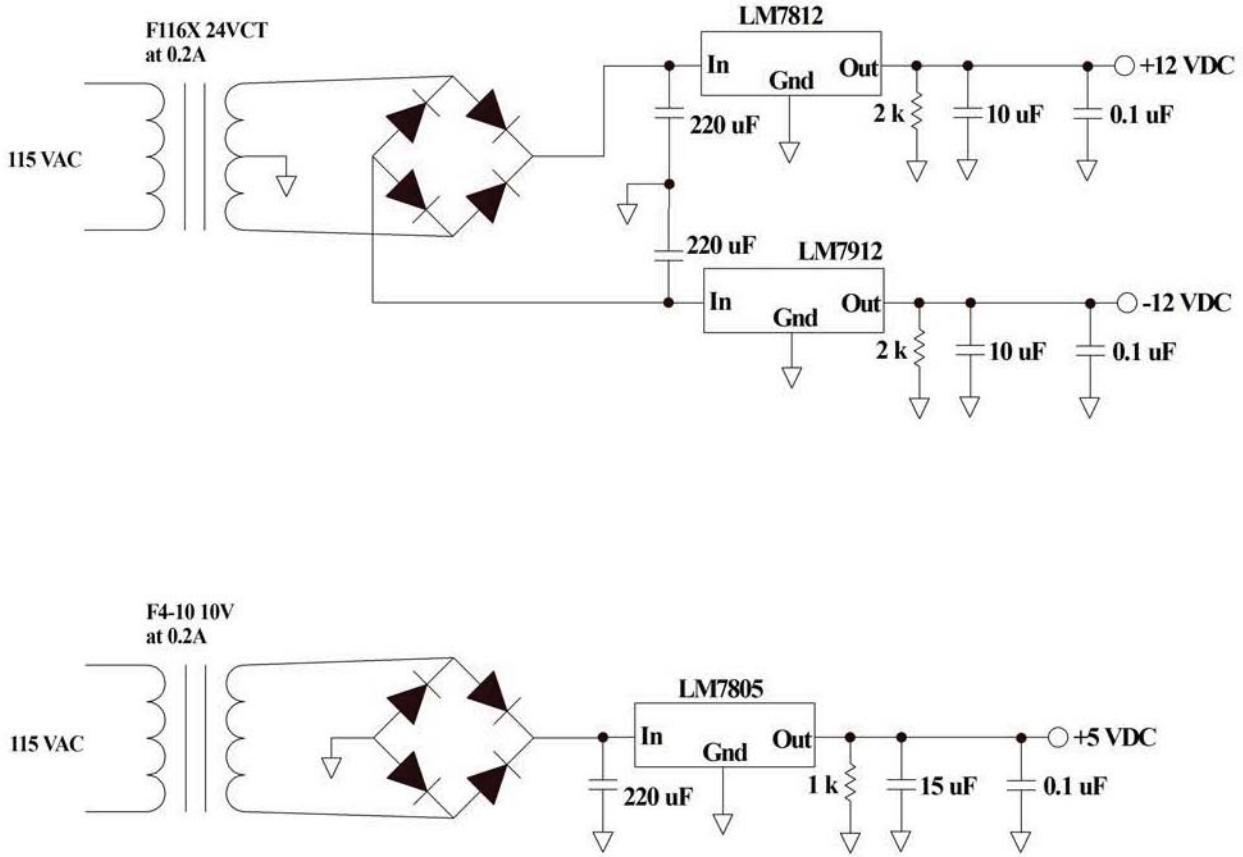

Figure A.13 An electrical diagram showing the power supplies used in the low frequency lock-in detector. All resistors have units of Ohms (Ω).

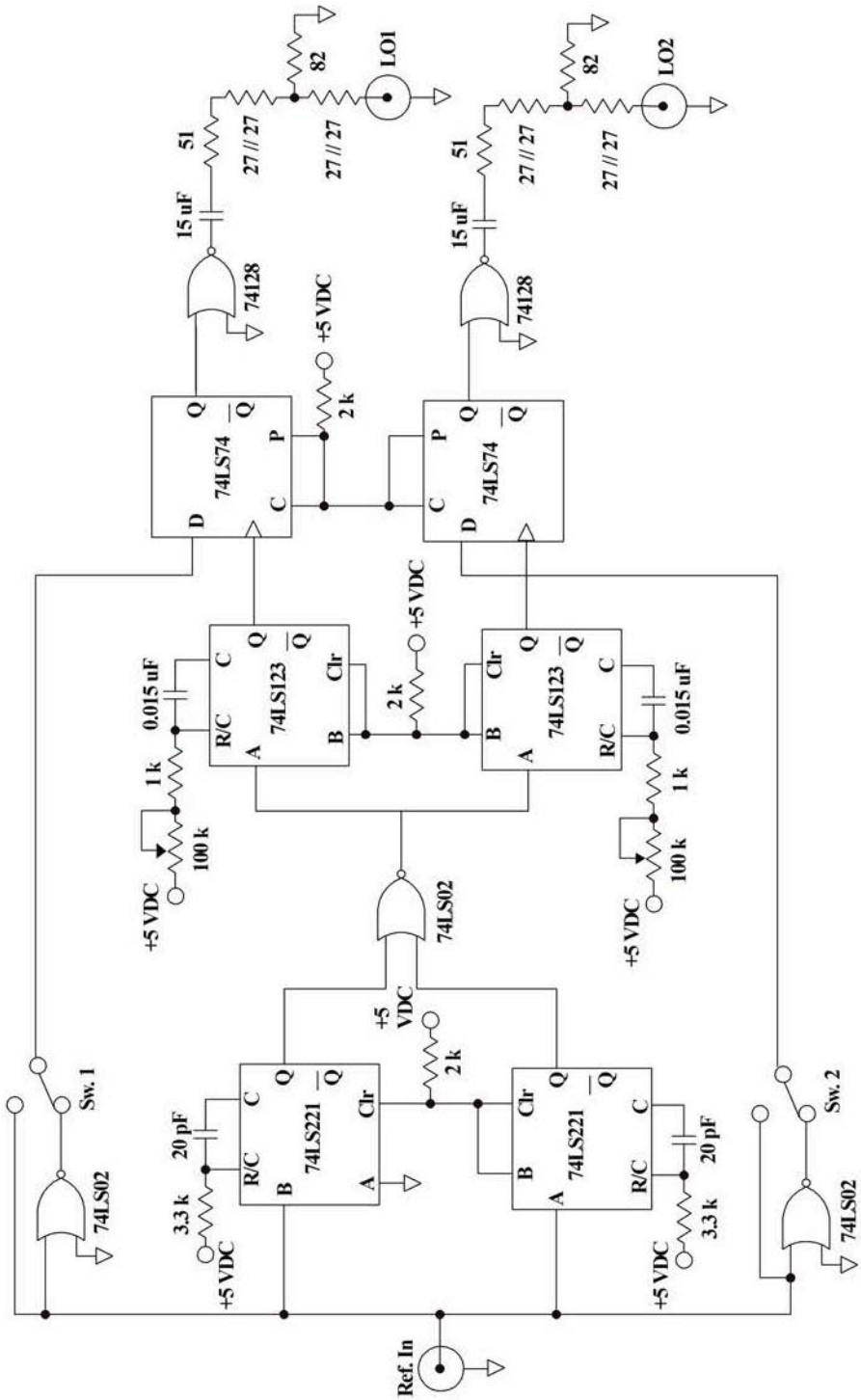

Figure A.14 Electrical diagram showing how the Ref. In signal, which comes from a 1kHz chopper, is transformed into a square wave of proper amplitude for the mixers in Figure A.15. All resistors have units of Ohms (Ω).

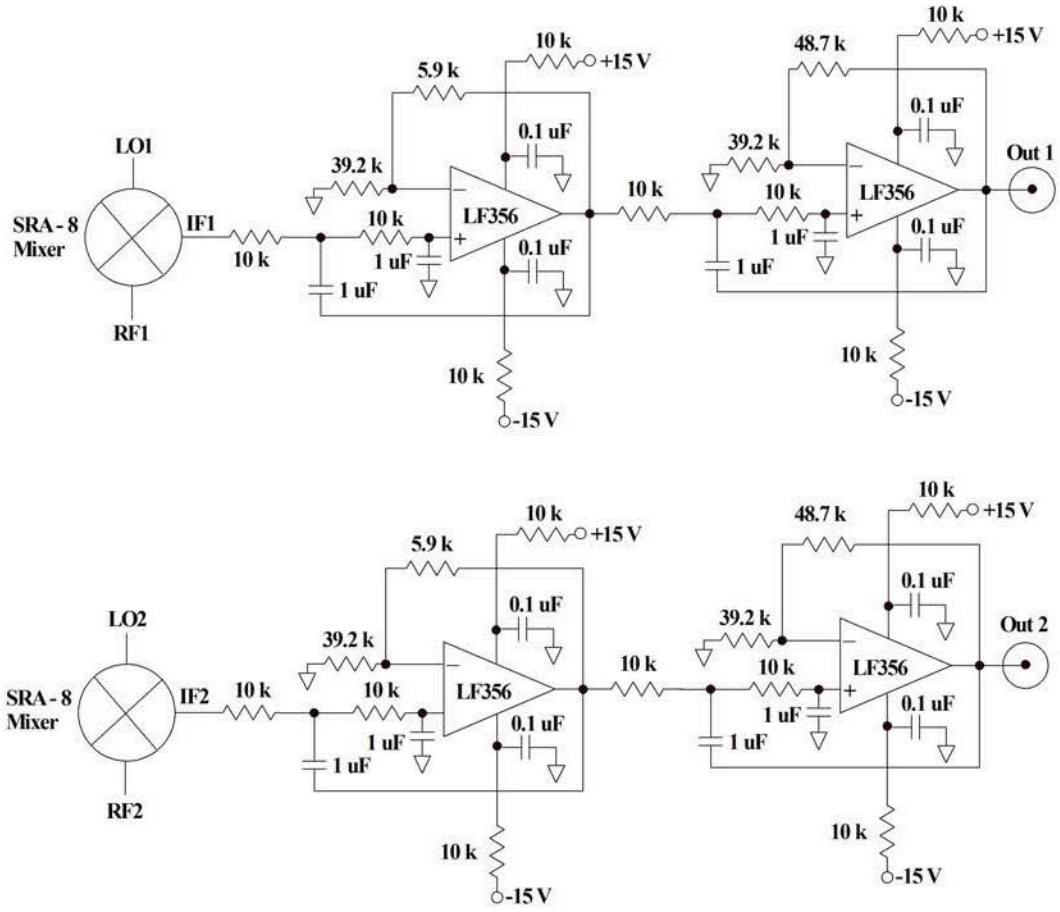

Figure A.15 The LO signals for each mixer are obtained from the circuit in Figure A.14. The RF signals are obtained from a dual infrared detector. The mixer sums and subtracts these two signals and the results are passed through the IF line. The rest of the electrical diagram is used to filter out the difference of the LO and RF signals and send out that signal to be digitized and stored on a computer for analysis. All resistors have units of Ohms (Ω).

APPENDIX B

ZrF AND ZrCl SPECTRA, LINE POSITIONS, AND SPECTROSCOPIC CONSTANTS

B.1 Vibronically Resolved Spectra of ZrF and ZrCl

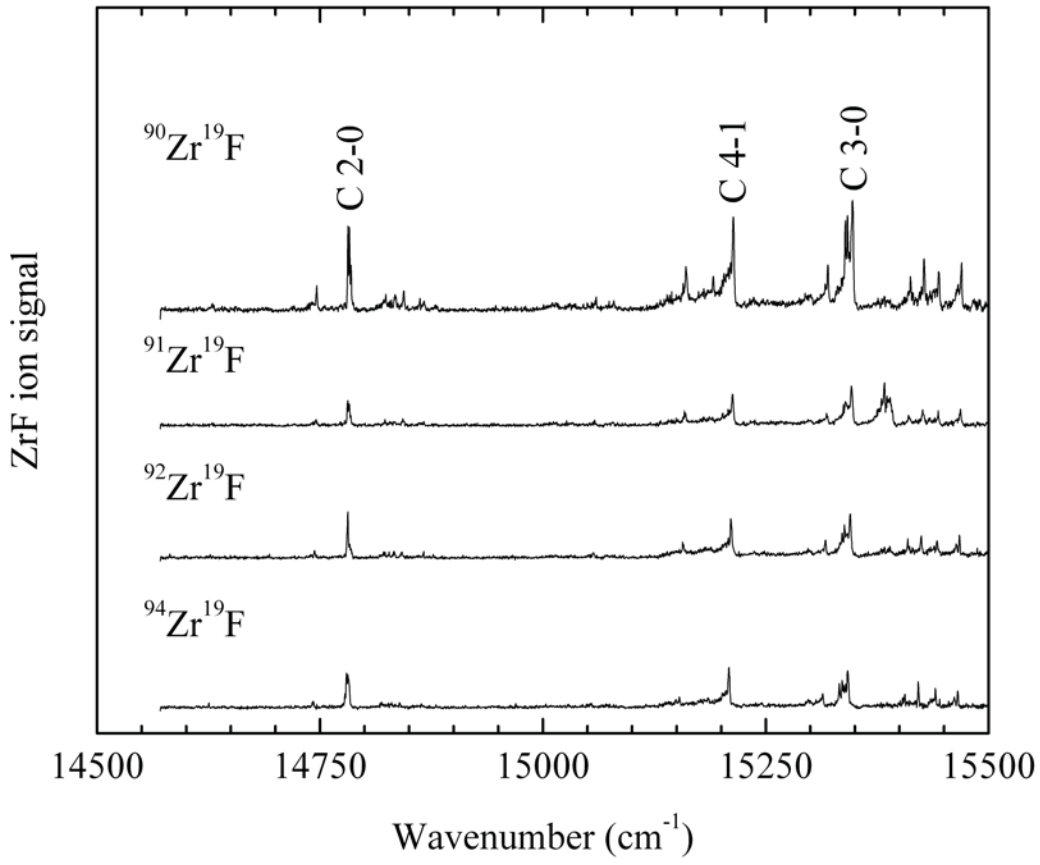

Figure B.1 Spectra of the various isotopomers of ZrF in the 14500 – 15500 cm^{-1} range.

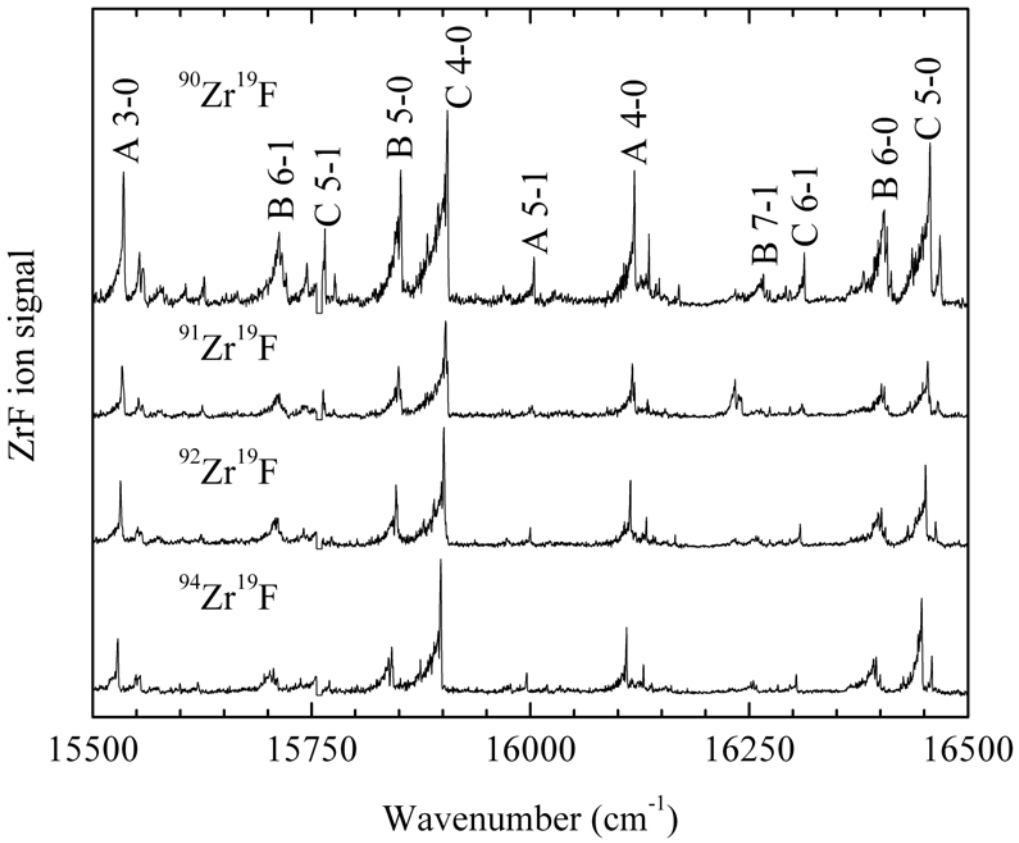

Figure B.2 Spectra of the various isotopomers of ZrF in the 15500 – 16500 cm^{-1} range.

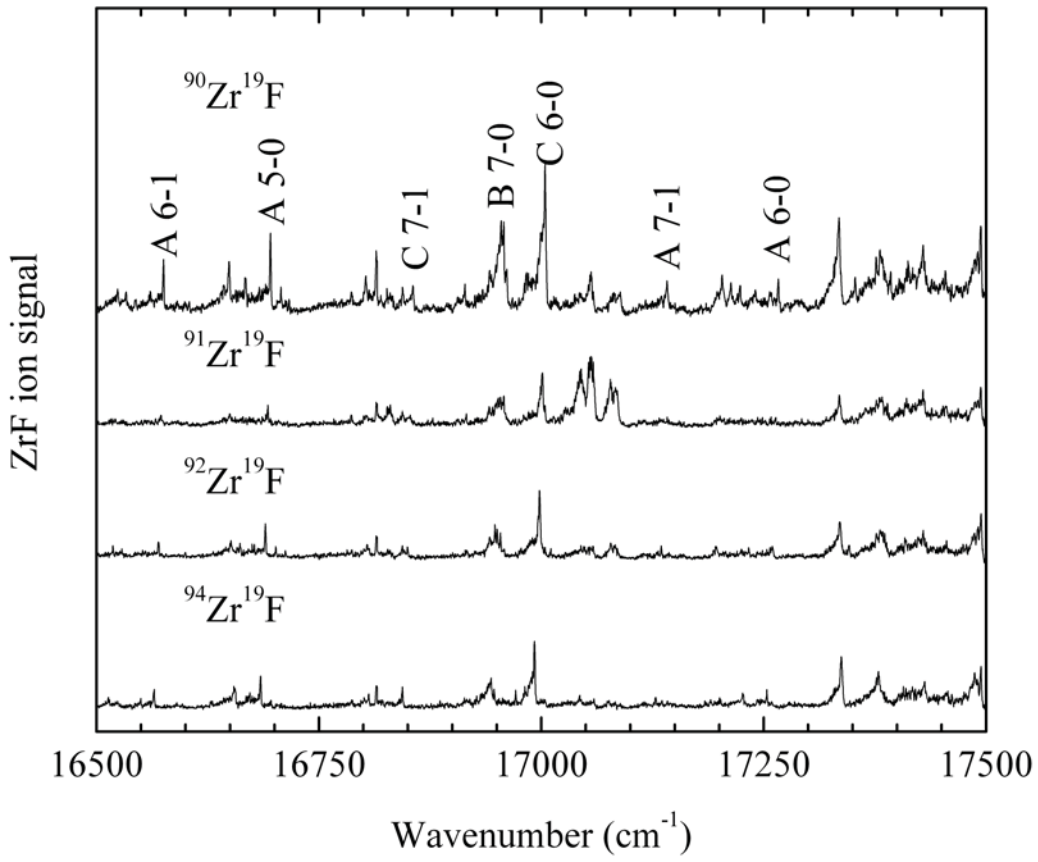

Figure B.3 Spectra of the various isotopomers of ZrF in the 16500 – 17500 cm^{-1} range.

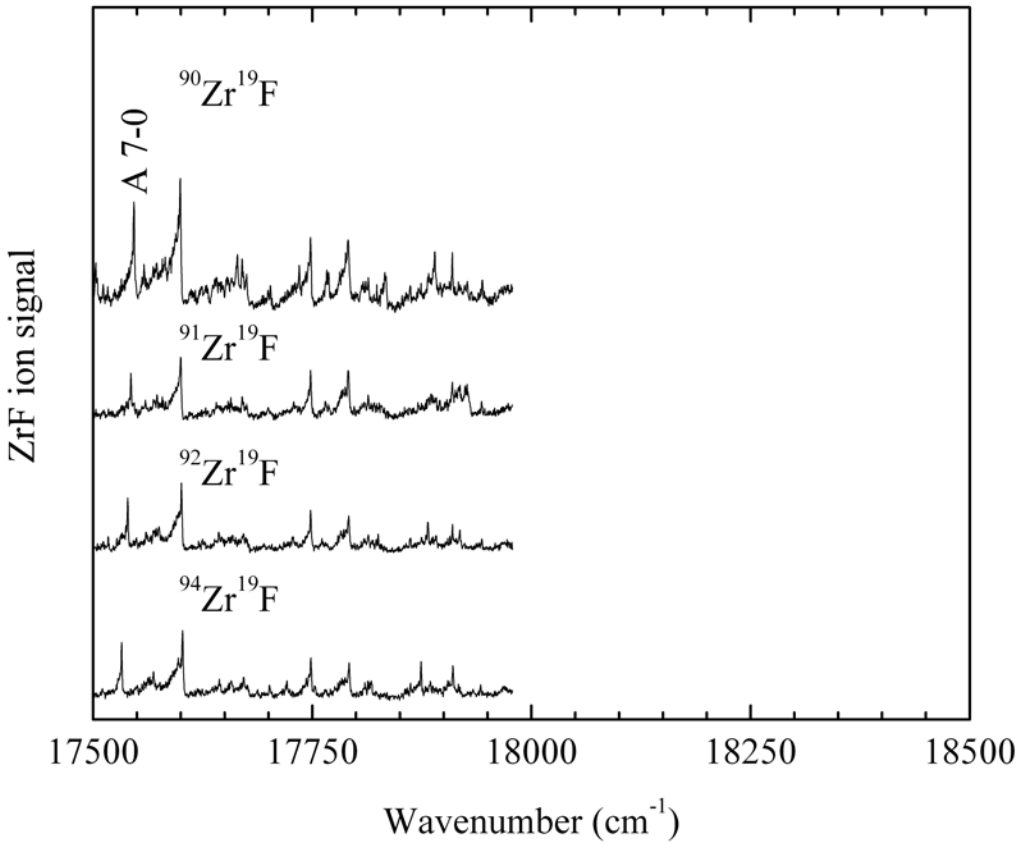

Figure B.4 Spectra of the various isotopomers of ZrF in the 17500 – 18000 cm^{-1} range.

Table B.1 Band Heads of the Various ZrF Isotopomers.

Assignment	$^{90}Zr^{19}F$	$^{91}Zr^{19}F$	$^{92}Zr^{19}F$	$^{94}Zr^{19}F$	Lifetime (μs)
	17943.9	17943.3	17943.6	17942.1	
	17909.8	17909.6	17909.9	17910.6	
	17889.9	17885.7	17882.0	17874.2	
	17861.8		17861.8	17862.1	
	17814.1	17814.0	17814.3	17817.6	
	17790.7	17791.0	17791.4	17792.1	
	17768.6				
	17748.0	17748.1	17748.3	17748.3	
	17735.1		17728.0	17721.0	
	17675.0			17687.3	
	17670.0	17670.2	17671.6	17671.7	
	17664.6			17657.7	
	17599.4	17599.9	17600.7	17602.1	0.213(14)
C 7-0 band	17546.5	17543.3	17539.5	17532.6	0.465(7)
	17502.8		17517.3		
	17494.1	17494.0	17494.4	17494.1	
	17454.2		17455.5	17487.3	
	17428.8	17429.2	17429.5	17431.0	
	17392.7	17389.2	17386.0	17378.8	
	17380.9				
	17376.4	17376.9	17376.9	17379.3	
	17353.0		17346.1		
	17334.9	17335.0	17335.7	17337.3	
A 6-0	17266.4		17259.7	17253.6	
	17223.5		17225.0		
	17213.2				
	17203.2	17200.8	17196.8	17190.4	
A 7-1	17141.3		17135.0	17128.6	
	17088.9	17085.1	17083.2	17059.2	
		17077.8	17078.3		
		17058.4	17058.2		
	17056.3	17056.3	17052.8		
		17044.8	17044.7	17043.1	
C 6-0	17004.3	17001.1	16998.0	16992.4	0.487(11)
B 7-0	16957.8	16954.2	16950.3	16943.2	
C 7-1	16855.8	16852.6	16849.7	16844.0	
B 8-1	16802.8				
	16786.8	16786.4			
	16707.4		16701.7	16696.2	

Table B.1 Continued

Assignment	$^{90}Zr^{19}F$	$^{91}Zr^{19}F$	$^{92}Zr^{19}F$	$^{94}Zr^{19}F$	Lifetime (μs)
A 5-0	16695.6	16692.8	16689.9	16684.6	0.902(19)
	16667.7		16661.5	16655.8	
	16649.2				
A 6-1	16575.5	16572.4	16569.9	16564.5	
	16560.6	16466.0		16549.8	
	16543.8			16513.3	
	16533.2				
	16523.9		16518.6		
	16468.2	16466.0	16463.1	16458.7	
	16464.8				
C 5-0	16456.4	16454.0	16451.5	16447.1	0.424(14)
	16436.3	16434.1	16431.4	16426.0	
	16412.1	16408.6	16405.4	16399.6	
B 6-0	16407.6	16404.5	16401.2	16395.0	1.201(49)
	16404.4	16401.1	16398.0	16392.1	
C 6-1	16312.8	16310.8	16308.3	16304.0	
	16292.0		16287.8	16282.9	
B 7-1	16266.1		16257.7	16254.9	
	16169.7		16165.5	16161.0	
	16147.2		16142.8	16138.6	
	16135.6	16133.9	16132.6	16129.3	
A 4-0	16118.9	16116.5	16114.3	16109.8	2.030(24)
A 5-1	16004.2	16002.2	15999.9	15995.9	
C 4-0	15905.2	15903.1	15901.0	15897.8	0.491(27)
	15882.4		15878.4	15874.5	
B 5-0	15851.9	15849.6	15846.7	15841.8	1.512(78)
	15776.7	15775.4	15772.8	15770.3	
C 5-1	15765.3	15763.4			0.433(16)
	15744.8		15741.0	15737.5	
	15716.2	15713.4	15711.6	15710.8	
B 6-1	15712.9	15710.3	15708.4	15703.2	
	15627.4	15625.2	15623.8	15620.1	
	15580.5	15578.7		15575.5	
	15557.6	15557.2	15555.9	15554.1	
	15553.6	15552.3	15551.5	15549.4	
A 3-0	15535.4	15533.9	15531.9	15528.6	2.076(55)
	15469.6	15468.4	15467.3	15465.4	
	15444.2	15443.4	15442.1	15440.4	
A 4-1	15427.7	15427.2	15424.3	15421.2	
	15412.5	15411.0	15409.3	15406.1	

Table B.1 Continued

Assignment	$^{90}Zr^{19}F$	$^{91}Zr^{19}F$	$^{92}Zr^{19}F$	$^{94}Zr^{19}F$	Lifetime (μs)
C 3-0	15347.3	15346.3	15344.7	15341.9	0.363(6)
	15341.8	15339.7	15338.5	15335.9	
	15339.2	15337.2	15335.7	15332.5	
	15319.6	15319.2	15316.8	15313.8	
C 4-1	15213.8	15212.8	15211.1	15208.8	
	15191.2		15188.5		
B 5-1	15160.5	15158.9	15157.7	15153.1	
	15059.8	15058.0	15056.5	15054.7	
	14866.8		14866.0		
	14862.1				
A 3-1	14844.0	14843.0	14841.8	14839.6	
	14834.6		14833.6		
	14823.9	14823.1	14821.4	14819.2	
C 2-0	14784.9	14782.8	14781.3	14780.0	
	14783.0	14781.1			
	14746.5	14745.8	14744.0	14742.5	
	14631.0	14630.2	14627.0	14625.5	

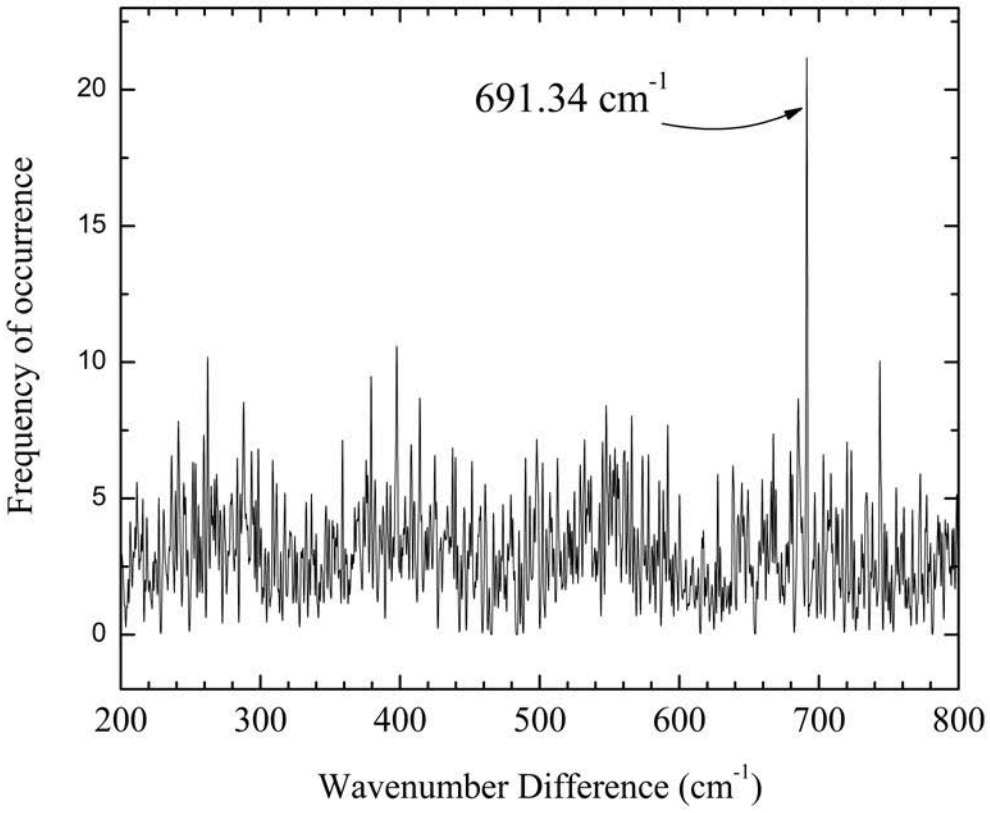

Figure B.5 Band difference histogram plot for $^{90}Zr^{19}F$, showing the peak at 691.34 cm^{-1} that corresponds to the ground state value of $\Delta G_{1/2}''$.

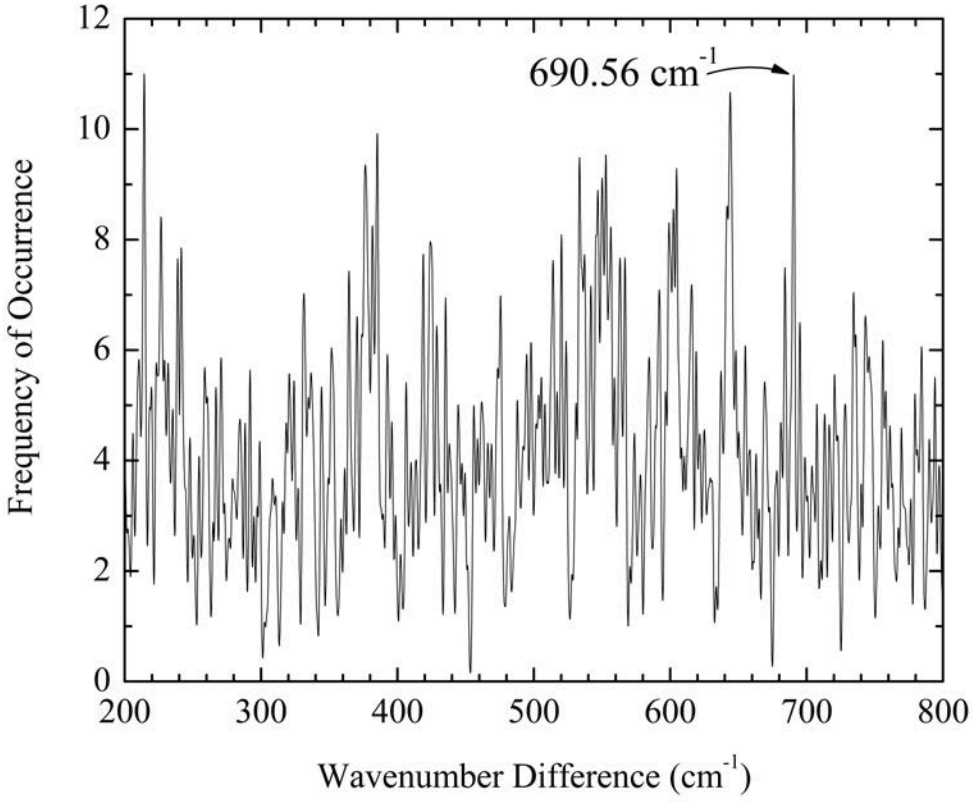

Figure B.6 Band difference histogram plot for $^{91}Zr^{19}F$, showing the peak at 690.56 cm^{-1} that corresponds to the ground state value of $\Delta G_{1/2}''$. In this case, the low natural abundance of $^{91}Zr^{19}F$ (11.22%) has prevented us from identifying the weaker features in the spectrum. Unfortunately, the hot bands arising from $v'' = 1$ and among the weaker features. Nevertheless, a peak can be identified at 690.56 cm^{-1}, based on the corresponding feature in the more abundant isotopomers.

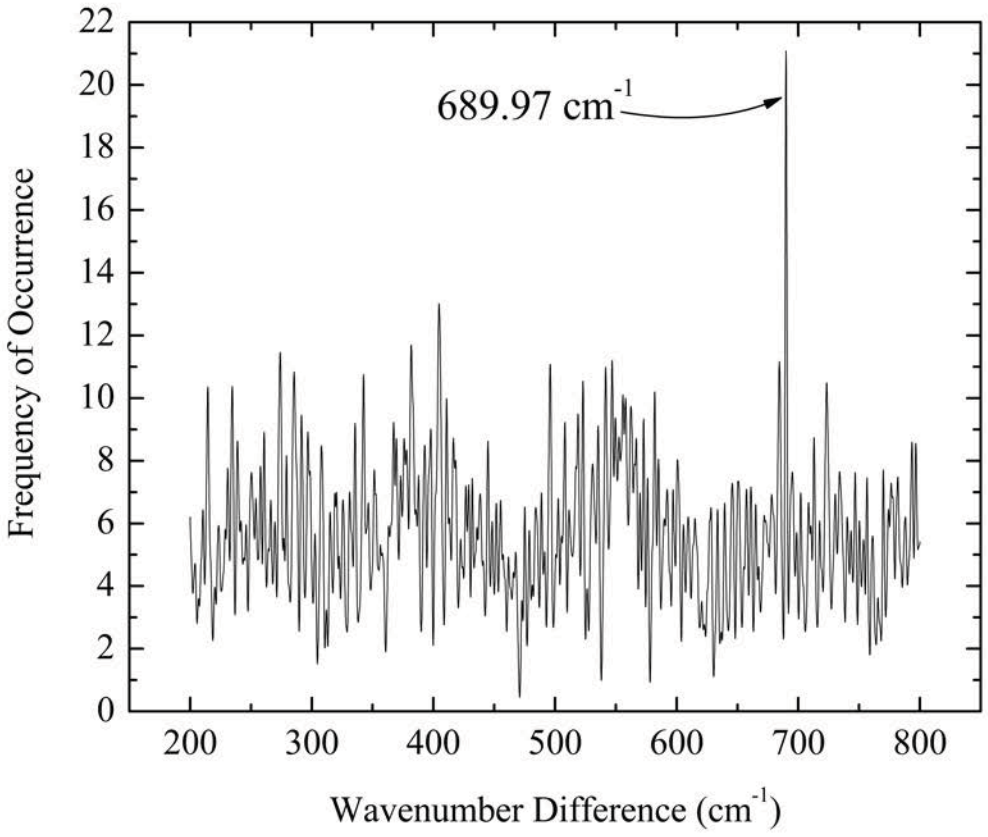

Figure B.7 Band difference histogram plot for $^{92}Zr^{19}F$, showing the peak at 689.97 cm^{-1} that corresponds to the ground state value of $\Delta G_{1/2}''$.

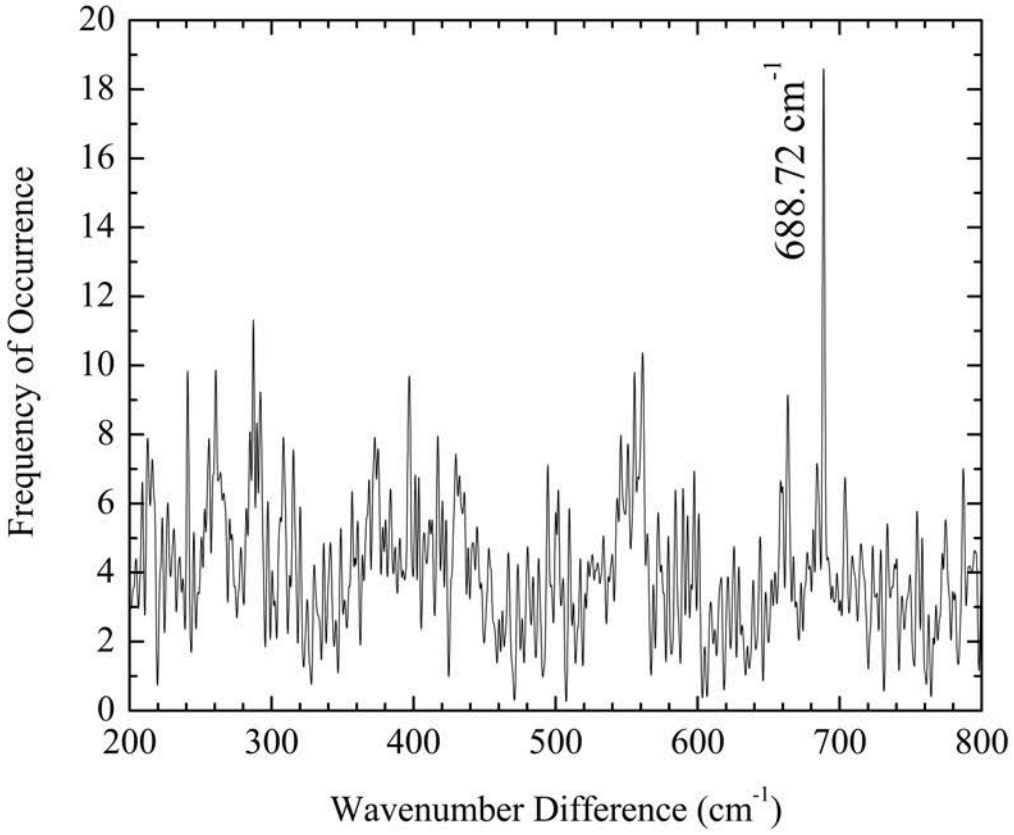

Figure B.8 Band difference histogram plot for $^{94}Zr^{19}F$, showing the peak at 688.72 cm^{-1} that corresponds to the ground state value of $\Delta G_{1/2}''$.

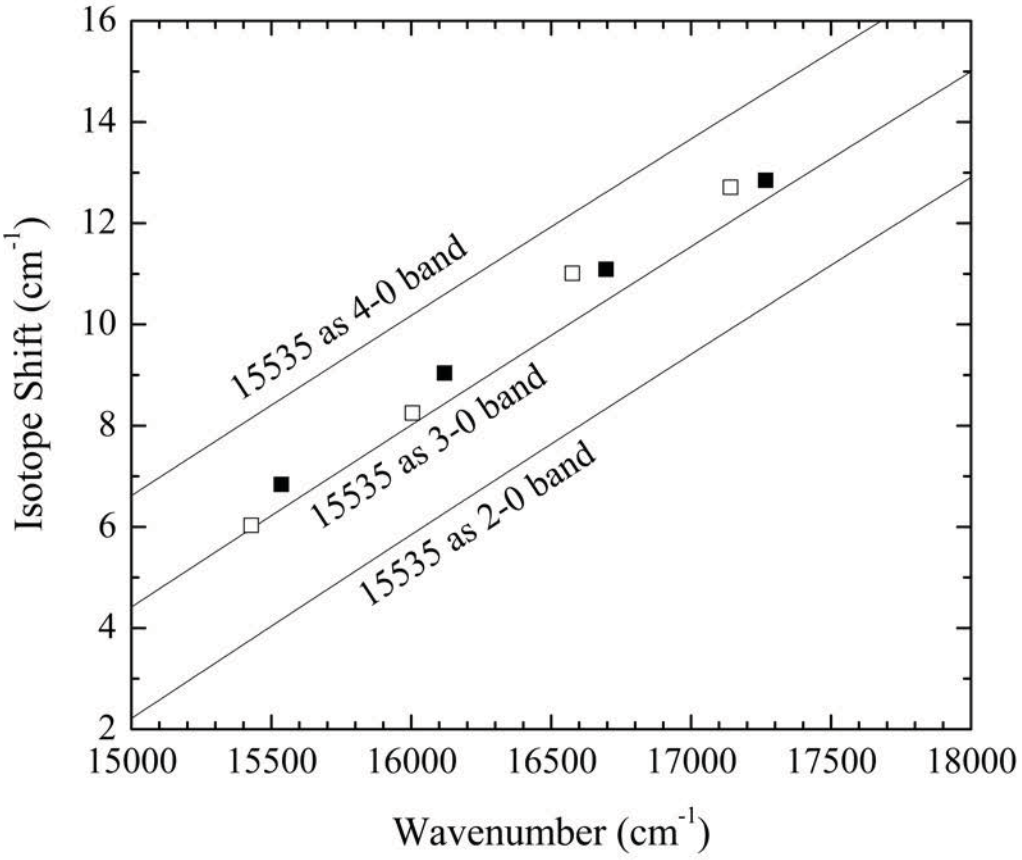

Figure B.9 Measured (symbols) *vs.* calculated (lines) isotope shifts, $\nu(^{90}Zr^{19}F) - \nu(^{94}Zr^{19}F)$, for bands belonging to the A system of ZrF. Filled symbols correspond to v′ – 0 bands, while open symbols correspond to v′– 1 hot bands. From these plots, the assignment of the 15535 cm^{-1} band as the 3-0 band seems secure.

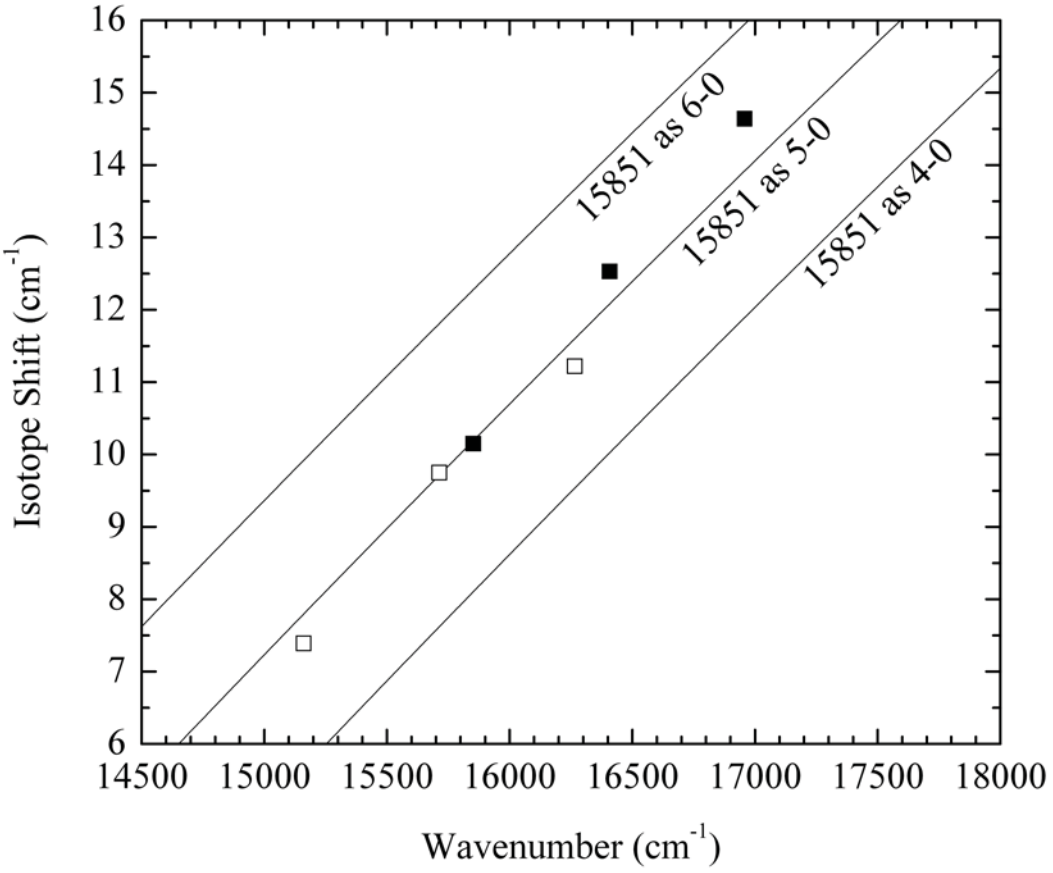

Figure B.10 Measured (symbols) *vs.* calculated (lines) isotope shifts, $\nu(^{90}Zr^{19}F) - \nu(^{94}Zr^{19}F)$, for bands belonging to the B system of ZrF. Filled symbols correspond to $v' - 0$ bands, while open symbols correspond to $v' - 1$ hot bands. From these plots, the assignment of the 15851 cm^{-1} band as the 5-0 band seems secure.

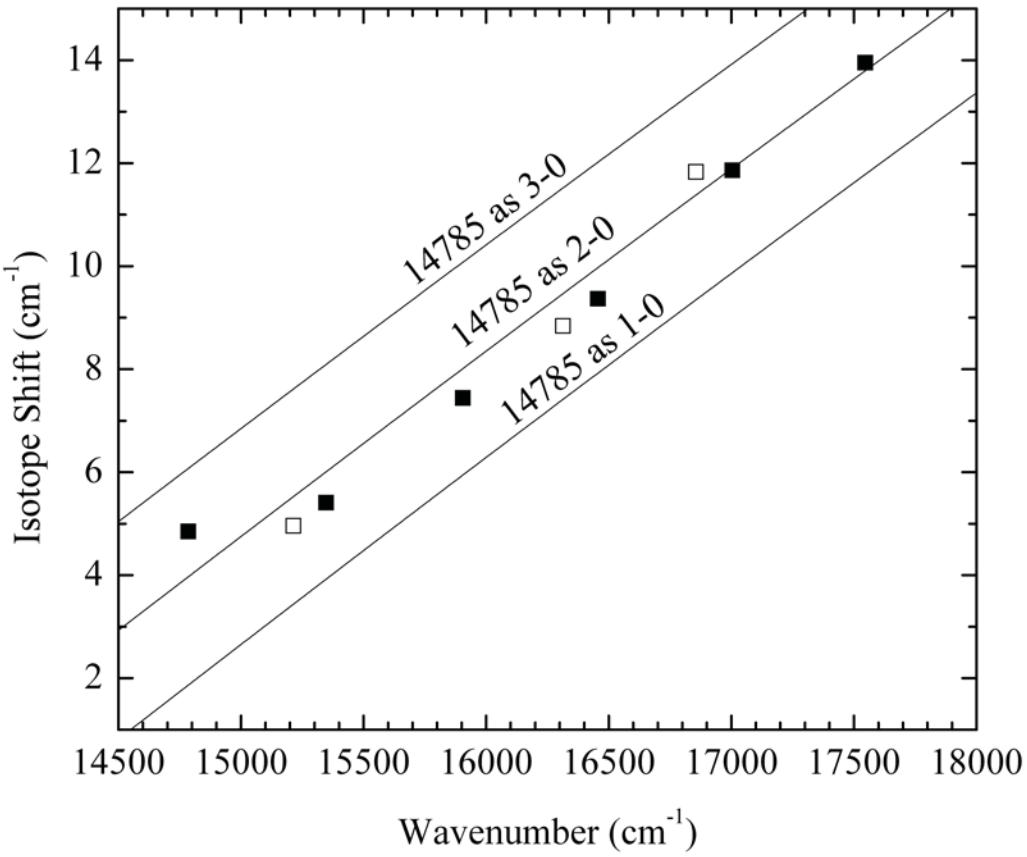

Figure B.11 Measured (symbols) *vs.* calculated (lines) isotope shifts, $\nu(^{90}Zr^{19}F) - \nu(^{94}Zr^{19}F)$, for bands belonging to the C system of ZrF. Filled symbols correspond to $v' - 0$ bands, while open symbols correspond to $v' - 1$ hot bands. From these plots, the assignment of the 14785 cm^{-1} band as the 2-0 band seems secure.

Table B.2 Vibrational Fit of System A for the ZrF Isotopomers, Based on Band Heads.[a]

Band	$^{90}Zr^{19}F$	$^{91}Zr^{19}F$	$^{92}Zr^{19}F$	$^{94}Zr^{19}F$
A 3-0	15535.4(-0.1)	15533.9(0.3)	15531.9(-0.1)	15528.6(0.0)
A 4-0	16118.9(0.4)	16116.5(-0.2)	16114.3(0.5)	16109.8(0.2)
A 5-0	16695.6(0.0)	16692.8(-0.1)	16689.9(0.0)	16684.6(0.0)
A 6-0	17266.4(-0.4)		17259.7(-0.4)	17253.6(-0.2)
A 3-1	14844.0(-0.3)	14843.0(-0.5)	14841.8(-0.3)	14839.6(-0.3)
A 4-1	15427.7(0.4)	15427.2(0.8)	15424.3(0.3)	15421.2(0.4)
A 5-1	16004.2(-0.2)	16002.2(-0.5)	15999.9(-0.1)	15995.9(0.1)
A 6-1	16575.5(-0.2)	16572.4(0.2)	16569.9(-0.3)	16564.5(-0.5)
A 7-1	17141.3(0.3)		17135.0(0.4)	17128.6(0.3)
Fitted constants				
T_0	13751.14(1.94)	13744.15(4.67)	13751.56(2.02)	13750.53(1.82)
ω_e'	606.55(0.91)	610.00(2.45)	605.10(0.95)	604.48(0.86)
$\omega_e'x_e'$	2.94(0.09)	3.38(0.25)	2.91(0.09)	2.94(0.08)
$\Delta G_{1/2}''$	691.15(0.27)	690.20(0.50)	689.88(0.29)	688.77(0.26)

[a] Following each transition wavenumber listed, the residual in the fit (observed - calculated) is provided in parentheses. Likewise, the 1σ error limits in the fitted constants are provided in parentheses following each entry. All quantities are provided in wavenumber (cm^{-1}) units.

Table B.3 Vibrational Fit of System B for the ZrF Isotopomers, Based on Band Heads.[a]

Band	$^{90}Zr^{19}F$	$^{91}Zr^{19}F$	$^{92}Zr^{19}F$	$^{94}Zr^{19}F$
B 5-0	15851.9(-0.2)	15849.6(-1.0)	15846.7(-1.2)	15841.8(-0.4)
B 6-0	16407.6(-0.9)	16404.5(1.7)	16401.2(0.7)	16395.0(1.1)
B 7-0	16957.8(1.1)	16954.2(-0.7)	16950.3(0.6)	16943.2(-0.6)
B 5-1	15160.5(1.4)	15158.9(0.4)	15157.7(1.2)	15153.1(0.4)
B 6-1	15712.9(-2.6)	15710.3(-0.4)	15708.4(-0.7)	15703.2(-1.1)
B 7-1	16266.1(2.4)		16257.7(-0.6)	16254.9(0.6)
B 8-1	16802.8(-1.1)			
Fitted constants				
T_0	12949.40(38.93)	13090.05(5.96)	13033.93(46.50)	13058.50(41.66)
ω_e'	604.75(13.36)	552.12(0.98)	573.00(17.04)	561.85(15.27)
$\omega_e'x_e'$	4.03(0.97)	---	1.70(1.31)	0.85(1.17)
$\Delta G_{1/2}''$	695.98(1.94)	692.11(1.50)	691.47(1.23)	689.6(1.1)

[a] Following each transition wavenumber listed, the residual in the fit (observed - calculated) is provided in parentheses. Likewise, the 1σ error limits in the fitted constants are provided in parentheses following each entry. All quantities are provided in wavenumber (cm^{-1}) units.

Table B.4 Vibrational Fit of System C for the ZrF Isotopomers, Based on Band Heads.[a]

Band	$^{90}Zr^{19}F$	$^{91}Zr^{19}F$	$^{92}Zr^{19}F$	$^{94}Zr^{19}F$
C 2-0	14784.9(-0.2)	14782.8(-0.6)	14781.3(-0.6)	14780.0(-0.4)
C 3-0	15347.3(0.0)	15346.3(0.7)	15344.7(0.8)	15341.9(0.4)
C 4-0	15905.2(0.6)	15903.1(0.4)	15901.0(0.4)	15897.8(0.5)
C 5-0	16456.4(-0.5)	16454.0(-0.6)	16451.5(-0.6)	16447.1(-0.6)
C 6-0	17004.3(0.1)	17001.1(-0.3)	16998.0(-0.3)	16992.4(-0.3)
C 7-0	17546.5(-0.1)	17543.3(0.3)	17539.5(0.3)	17532.6(0.2)
C 4-1	15213.8(0.4)	15212.8(0.6)	15211.1(0.1)	15208.8(0.0)
C 5-1	15765.3(-0.4)	15763.4(-0.7)		
C 6-1	16312.8(-0.3)	16310.8(-0.1)	16308.3(-0.3)	16304.0(-0.2)
C 7-1	16855.8(0.3)	16852.6(0.1)	16849.7(0.2)	16844.0(0.1)
Fitted constants				
T_0	13645.83(1.23)	13643.50(1.75)	13641.95(1.70)	13642.03(1.33)
ω_e'	577.07(0.62)	577.68(0.89)	577.89(0.87)	577.21(0.68)
$\omega_e'x_e'$	2.48(0.06)	2.58(0.08)	2.64(0.09)	2.68(0.06)
$\Delta G_{1/2}''$	691.12(0.31)	690.50(0.44)	689.68(0.45)	688.50(0.35)

[a] Following each transition wavenumber listed, the residual in the fit (observed - calculated) is provided in parentheses. Likewise, the 1σ error limits in the fitted constants are provided in parentheses following each entry. All quantities are provided in wavenumber (cm^{-1}) units.

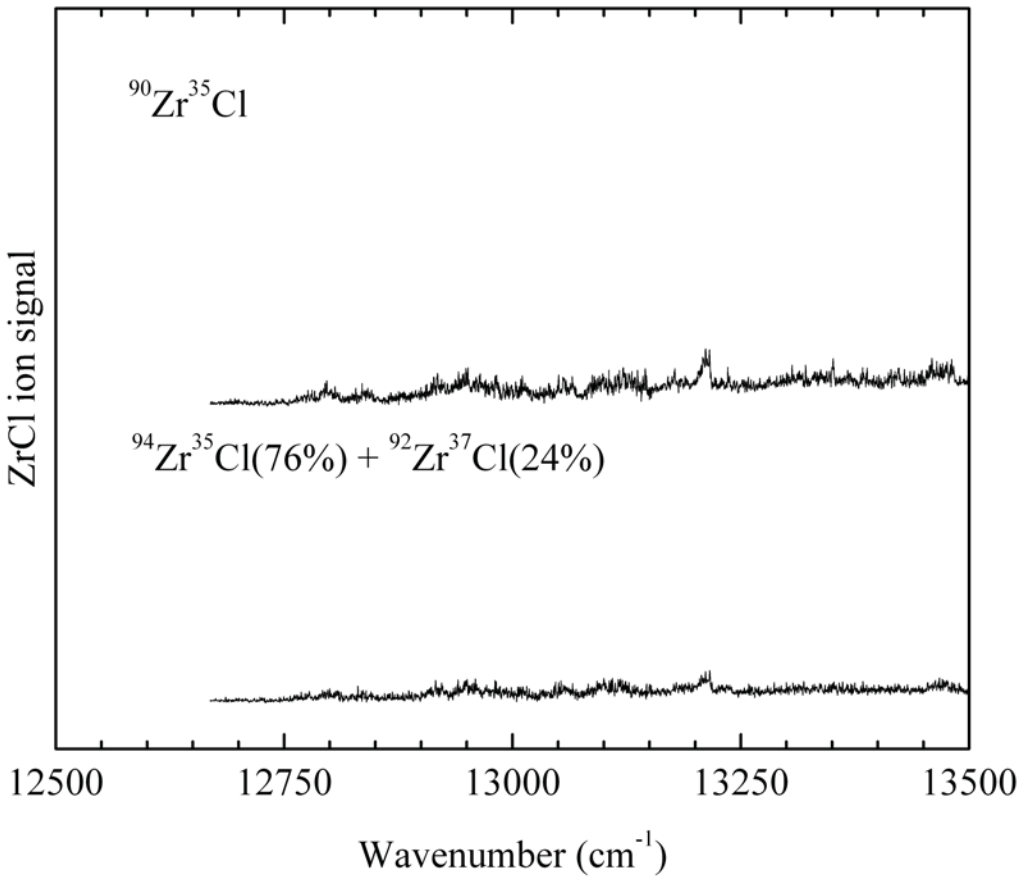

Figure B.12 Spectra of two isotopomers of ZrCl in the 12500 – 13500 cm^{-1} range.

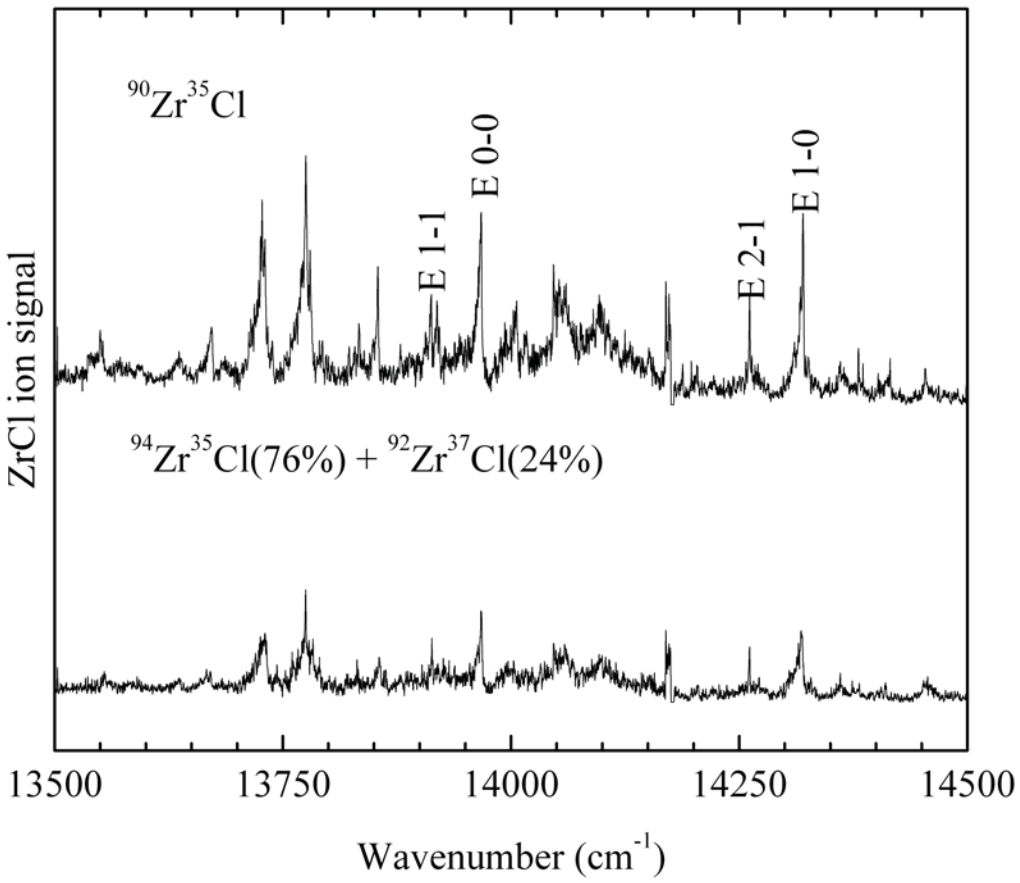

Figure B.13 Spectra of two isotopomers of ZrCl in the 13500 – 14500 cm^{-1} range.

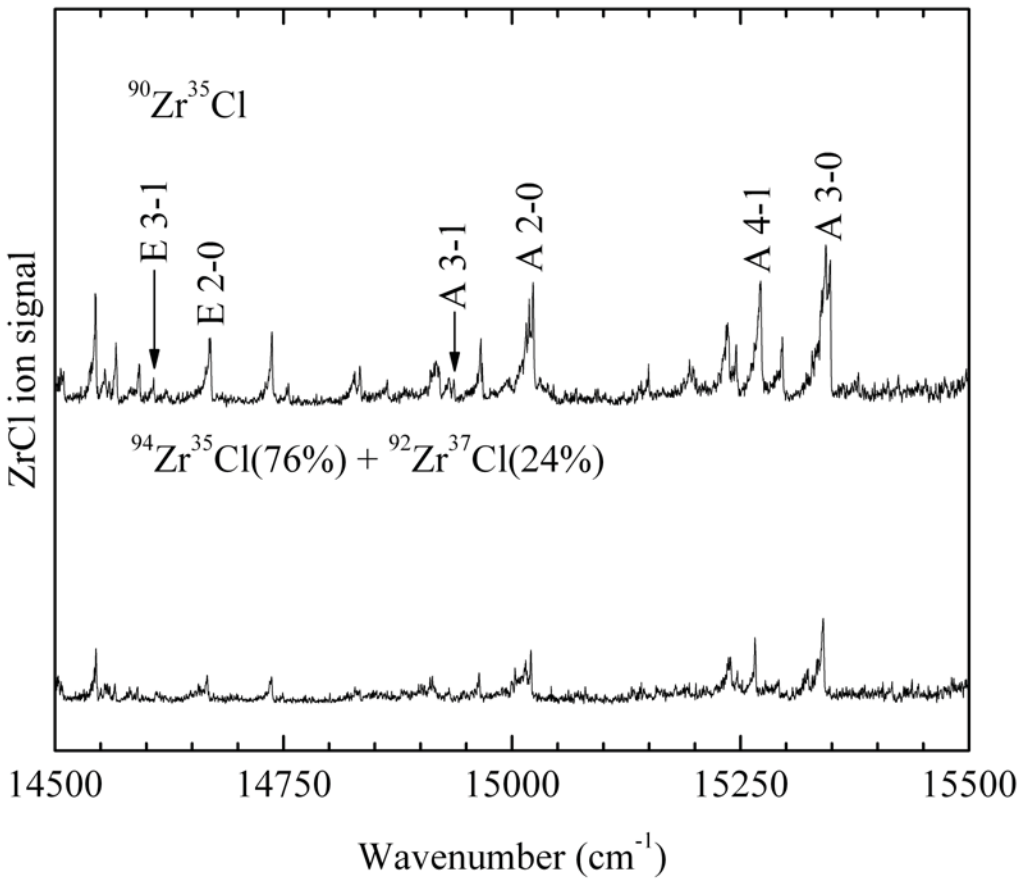

Figure B.14 Spectra of two isotopomers of ZrCl in the 14500 – 15500 cm^{-1} range.

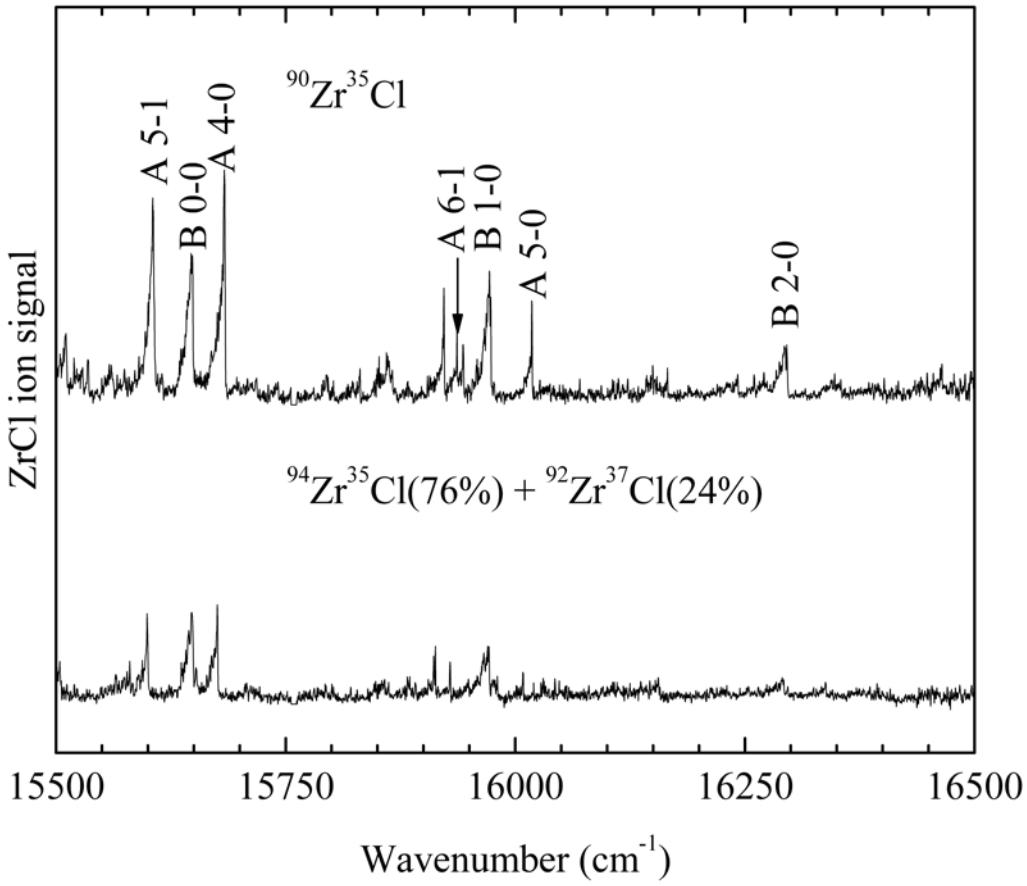

Figure B.15 Spectra of two isotopomers of ZrCl in the 15500 – 16500 cm^{-1} range.

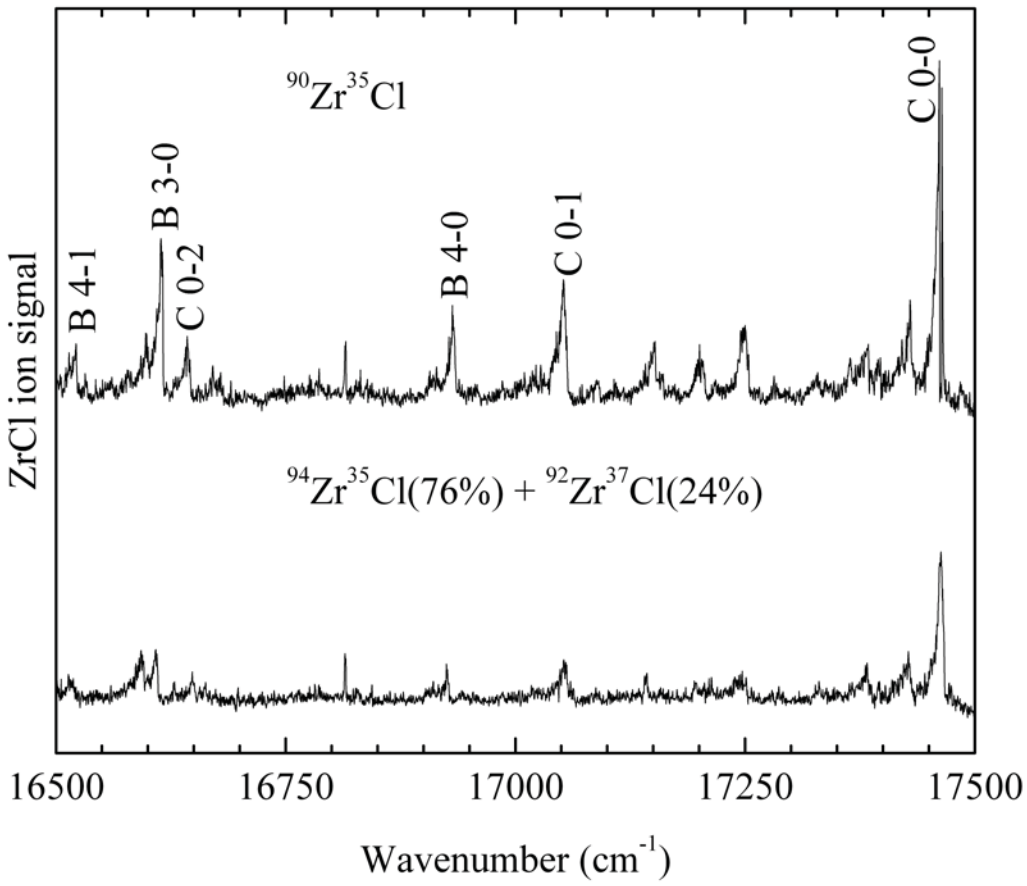

Figure B.16 Spectra of two isotopomers of ZrCl in the 16500 – 17500 cm^{-1} range.

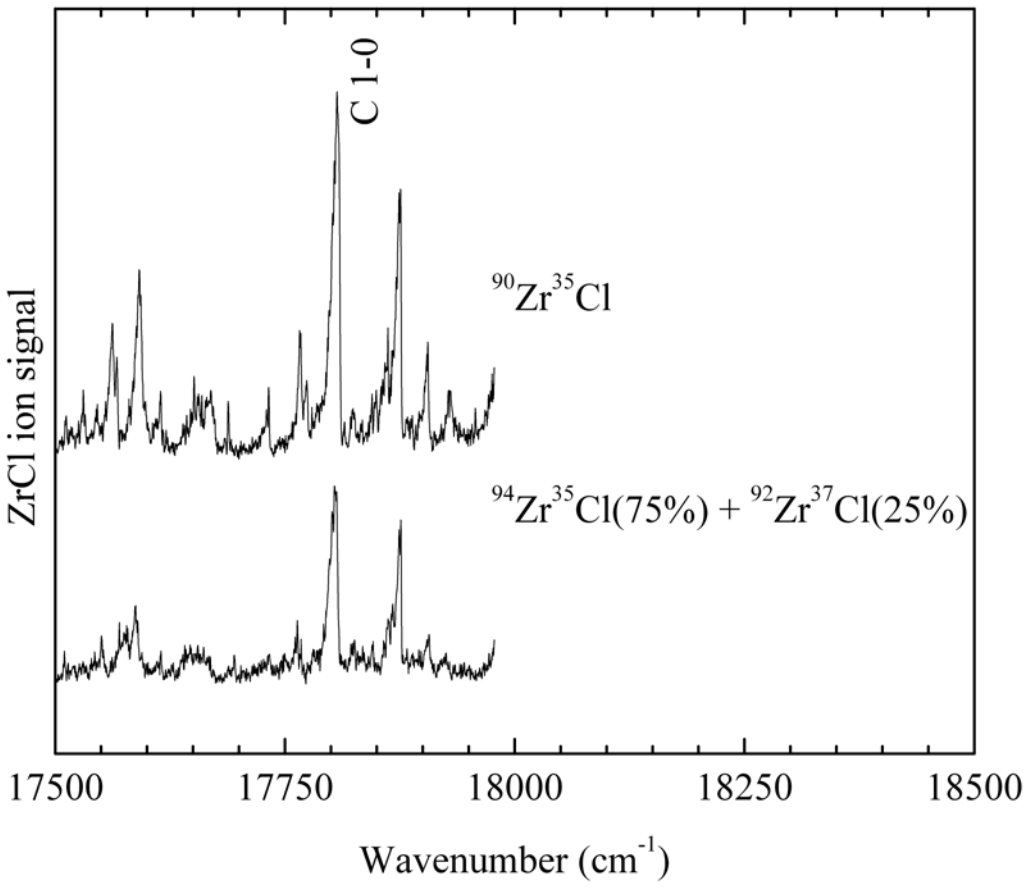

Figure B.17 Spectra of two isotopomers of ZrCl in the 17500 – 18500 cm^{-1} range.

Table B.5 Band Heads of $^{90}Zr^{35}Cl$ (Mass 125) and $^{94}Zr^{35}Cl$ (Mass 129).

Assignment	$^{90}Zr^{35}Cl$	$^{94}Zr^{35}Cl$	Isotope Shift $\nu(^{90}Zr^{35}Cl) - \nu(^{94}Zr^{35}Cl)$
	17905.90	17906.90	-1.00
	17876.20	17876.50	-0.30
C 1-0	17809.20	17807.00	2.20
	17774.30	17767.70	6.60
	17767.70	17763.70	4.00
	17732.40		
	17688.40		
	17614.90	17615.20	-0.30
	17594.20	17590.00	4.20
	17567.50	17552.60	14.90
	17532.70		
C 0-0	17463.70	17466.00	-2.30
	17429.80	17429.00	0.80
	17253.70		
	17151.90	17143.20	8.70
C 0-1	17054.30	17055.90	-1.60
B 4-0	16933.80	16927.50	6.30
C 0-2	16643.80	16650.60	-6.80
B 3-0	16615.80	16610.40	5.40
		16595.40	
B 4-1	16521.90	16519.00	2.90
		16337.80	
B 2-0	16295.70	16292.20	3.50
	16260.00		
A 5-0	16018.10	16008.50	9.60
		15980.50	
B 1-0	15973.20	15971.40	1.80
		15949.05	
	15943.30		
A 6-1	15936.70	15929.00	7.70
	15922.40	15913.00	9.40
	15830.80		
A 4-0	15683.40	15675.80	7.60
B 0-0	15648.60	15648.70	-0.10
A 5-1	15605.90	15599.30	6.60
	15535.30		
	15510.90	15504.10	6.80
A 3-0	15347.90	15340.40	7.50
	15343.40		
	15295.90	15292.00	3.90

Table B.5 Continued

Assignment	$^{90}Zr^{35}Cl$	$^{94}Zr^{35}Cl$	Isotope Shift $\nu(^{90}Zr^{35}Cl) - \nu(^{94}Zr^{35}Cl)$
A 4-1	15272.10	15266.70	5.40
	15245.50	15246.90	-1.40
	15237.10	15240.00	-2.90
	15149.00		
A 2-0	15023.10	15020.50	2.60
	14967.50	14964.20	3.30
A 3-1	14936.40	14931.60	4.80
	14918.30		
	14863.70		
	14834.00	14830.70	3.30
	14755.70	14749.80	5.90
	14737.50	14737.30	0.20
E 2-0	14670.70	14667.20	3.50
E 3-1	14607.90		
	14592.50	14590.50	2.00
	14566.90	14565.60	1.30
	14544.60	14544.90	-0.30
	14509.70	14508.10	1.60
	14453.90	14456.40	-2.50
	14415.40	14411.00	4.40
	14380.60	14381.50	-0.90
E 1-0	14320.20	14319.20	1.00
E 2-1	14261.40	14261.30	0.10
	14188.10		
	14046.70	14046.80	-0.10
	14006.30		
E 0-0	13967.40	13968.20	-0.80
	13921.60		
	13919.10		
E 1-1	13912.60	13913.30	-0.70
	13854.10	13855.80	-1.70
	13833.60	13831.30	2.30
	13779.90	13783.10	-3.20
	13775.20	13775.00	0.20
	13730.30	13732.10	-1.80
	13672.70	13671.10	1.60
	13550.90	13554.20	-3.30
	13215.74	13216.18	-0.45
	13211.62	13211.50	0.12

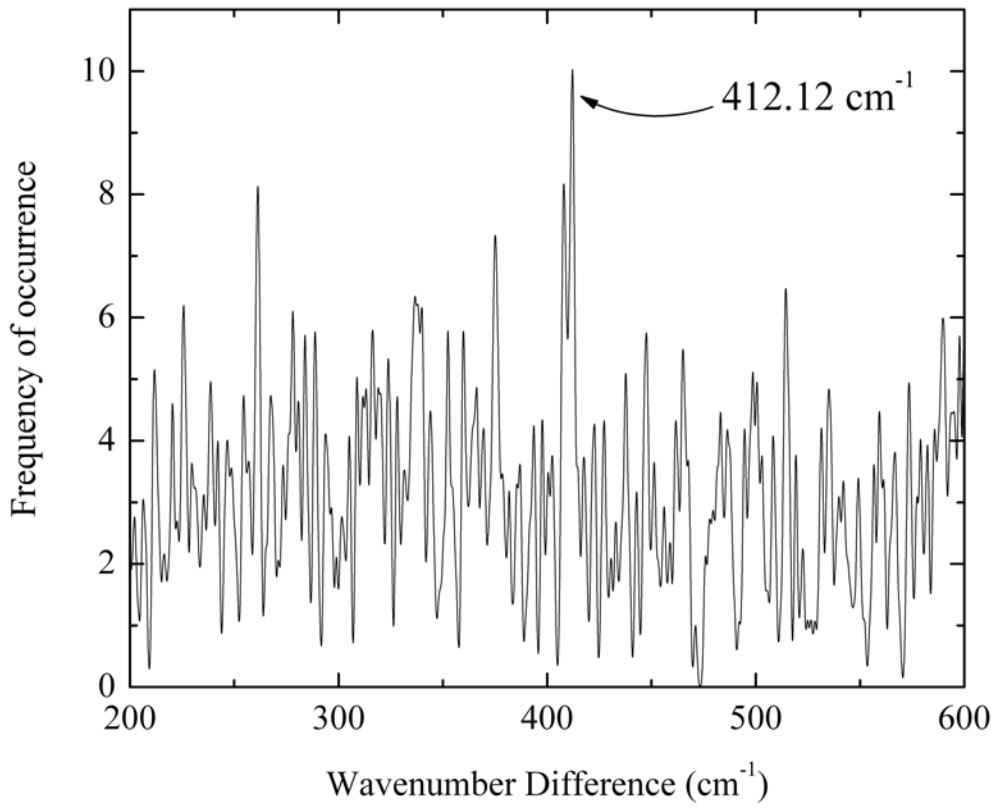

Figure B.18 Band difference histogram plot for $^{90}Zr^{35}Cl$, showing the peak at 412.12 cm^{-1} that corresponds to the ground state value of $\Delta G_{1/2}''$. The neighboring features at 408.00 cm^{-1} probably corresponds to the second hot band, giving $\Delta G_{3/2}'' = 408.00$ cm^{-1}. These values compare to published values of $\Delta G_{1/2}'' = 411.3$ cm^{-1} and $\Delta G_{3/2}'' = 408.4$ cm^{-1} for an isotopically mixed or unidentified sample of ZrCl. [R. S. Ram, A. G. Adam, W. Sha, A. Tsouli, J. Lievin, and P. F. Bernath, J. Chem. Phys. **114**, 3977-87 (2001)]

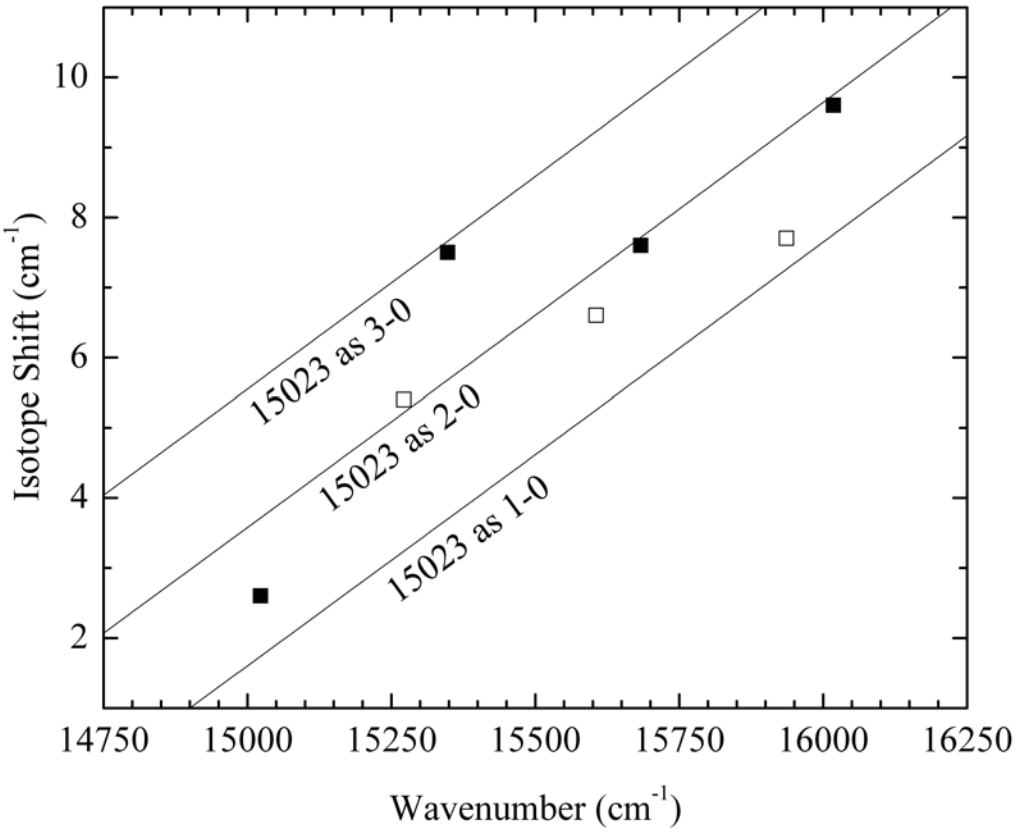

Figure B.19 Measured (symbols) *vs.* calculated (lines) isotope shifts, $\nu(^{90}Zr^{35}Cl) - \nu(^{94}Zr^{35}Cl)$, for bands belonging to the A system of ZrCl. Filled symbols correspond to $v' - 0$ bands, while open symbols correspond to $v' - 1$ hot bands. From these plots, the assignment of the 15023 cm^{-1} band as the 2-0 band seems secure.

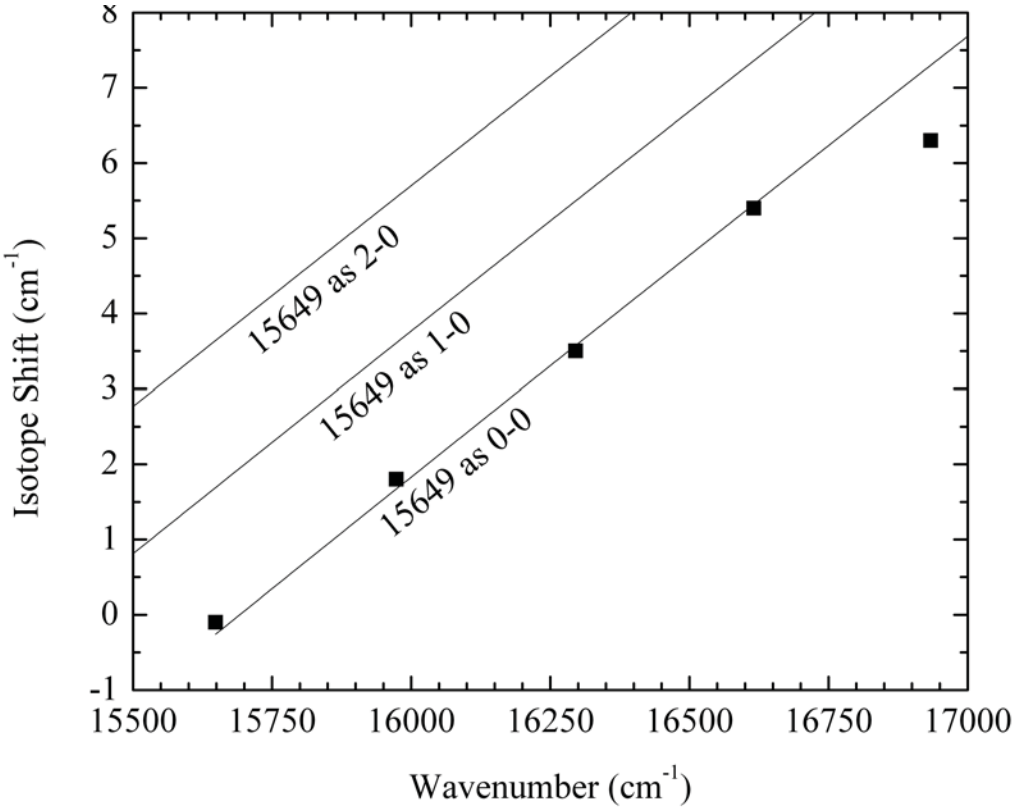

Figure B.20 Measured (symbols) *vs.* calculated (lines) isotope shifts, $\nu(^{90}Zr^{35}Cl) - \nu(^{94}Zr^{35}Cl)$, for bands belonging to the B system of ZrCl. Filled symbols correspond to v′ – 0 bands. From these plots, the assignment of the 15649 cm^{-1} band as the 0-0 band seems secure.

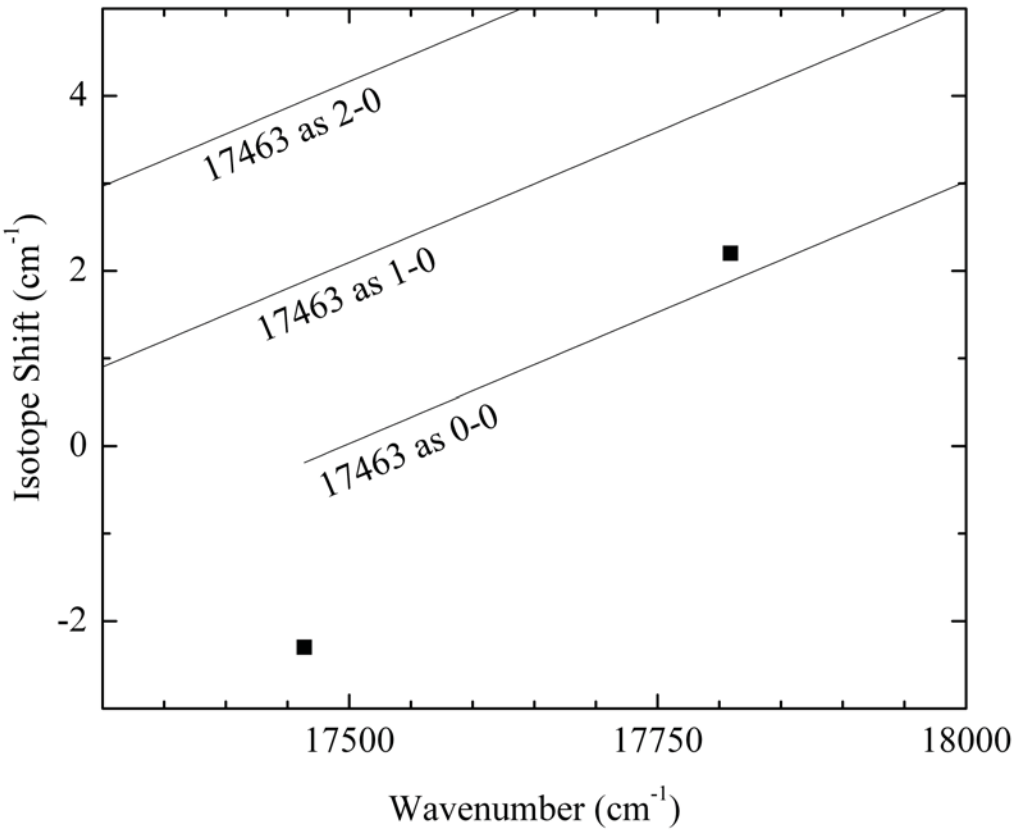

Figure B.21 Measured (symbols) *vs.* calculated (lines) isotope shifts, $\nu(^{90}Zr^{35}Cl) - \nu(^{94}Zr^{35}Cl)$, for bands belonging to the C system of ZrCl. Filled symbols correspond to v′ – 0 bands. Although there is an anomalous isotope shift in the 17463 cm^{-1} band, the assignment of this feature as the 0-0 band is likely correct.

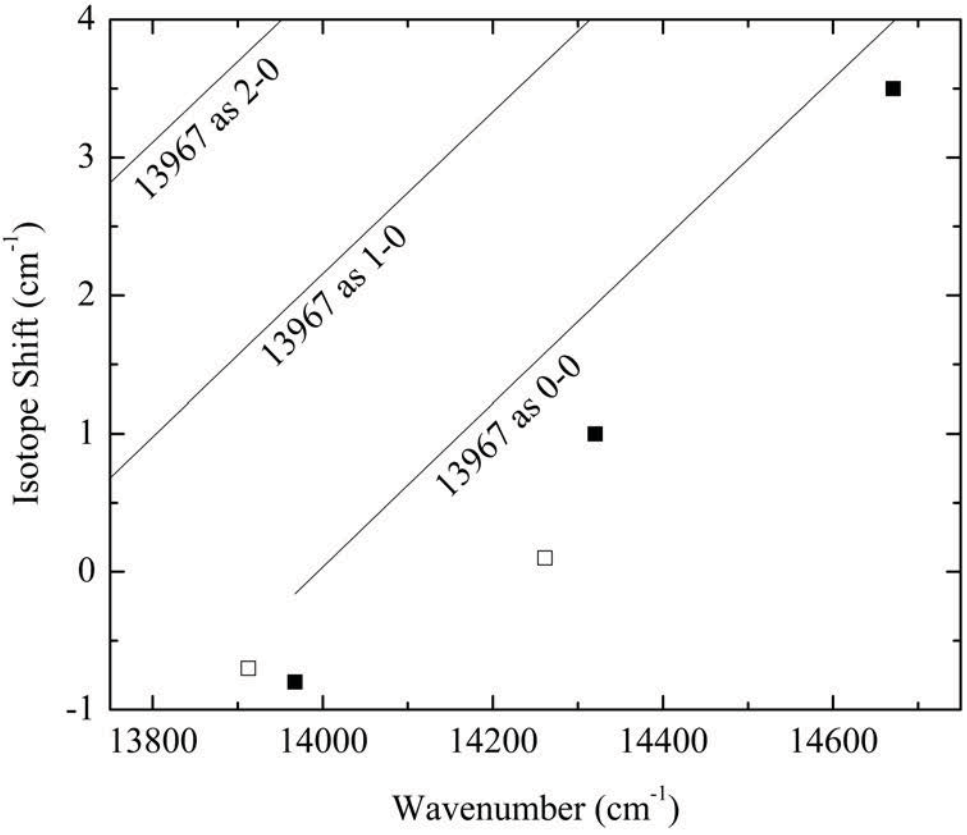

Figure B.22 Measured (symbols) *vs.* calculated (lines) isotope shifts, $\nu(^{90}Zr^{35}Cl) - \nu(^{94}Zr^{35}Cl)$, for bands belonging to the E system of ZrCl. Filled symbols correspond to $v' - 0$ bands, open symbols to $v' - 1$ bands. Although the measured isotope shifts lie somewhat below the line resulting from the assignment of the 13967 cm^{-1} band as a 0-0 band, there is no other obvious assignment. The bands belonging to this progression are not hot bands, which would be the most likely reason for the discrepancy, because no bands are found shifted to the blue by the known ground state interval, $\Delta G_{1/2}''$. Thus, from these plots, the assignment of the 13967 cm^{-1} band as the 0-0 band seems secure.

Table B.6 Vibrational Fit of System A for the ZrCl Isotopomers, Based on Band Heads.[a]

Band	$^{90}Zr^{35}Cl$	$^{94}Zr^{35}Cl$
A 2-0	15023.1(2.4)	15020.5(3.2)
A 3-0	15347.9(-3.5)	15340.4(-4.7)
A 4-0	15683.4(-0.1)	15675.8(0.6)
A 5-0	16018.1(1.2)	16008.5(0.9)
A 3-1	14936.4(-1.9)	14931.6(-2.7)
A 4-1	15272.1(1.7)	15266.7(2.3)
A 5-1	15605.9(2.1)	15599.3(2.6)
A 6-1	15936.7(-1.9)	15929.0(-2.3)
Fitted constants		
T_0	14363.2(10.6)	14368.3(13.9)
ω_e'	326.7(6.3)	321.2(8.2)
$\omega_e'x_e'$	-0.67(0.69)	-1.12(0.90)
$\Delta G_{1/2}''$	413.1(2.3)	410.8(3.0)

[a] Following each transition wavenumber listed, the residual in the fit (observed - calculated) is provided in parentheses. Likewise, the 1σ error limits in the fitted constants are provided in parentheses following each entry. All quantities are provided in wavenumber (cm^{-1}) units.

Table B.7 Vibrational Fit of System B for the ZrCl Isotopomers, Based on Band Heads.[a]

Band	$^{90}Zr^{35}Cl$	$^{94}Zr^{35}Cl$
B 0-0	15648.6(0.0)	15648.7(0.0)
B 1-0	15973.2(0.0)	15971.4(0.0)
B 2-0	16295.7(0.1)	16292.2(0.2)
B 3-0	16615.8(0.0)	16610.4(-0.3)
B 4-0	16933.8(0.0)	16927.5(0.1)
B 4-1	16521.9(0.0)	16519.0(0.0)
Fitted constants		
T_0	15648.59(0.05)	15648.75(0.24)
ω_e'	326.87(0.07)	324.59(0.35)
$\omega_e'x_e'$	1.11(0.01)	0.98(0.07)
$\Delta G_{1/2}''$	411.89(0.07)	408.39(0.35)

[a] Following each transition wavenumber listed, the residual in the fit (observed - calculated) is provided in parentheses. Likewise, the 1σ error limits in the fitted constants are provided in parentheses following each entry. All quantities are provided in wavenumber (cm^{-1}) units.

Table B.8 Vibrational Fit of System C for the ZrCl Isotopomers, Based on Band Heads.[a]

Band	$^{90}Zr^{35}Cl$	$^{94}Zr^{35}Cl$
C 0-0	17463.7	17466.0
C 1-0	17809.2	17807.0
C 0-1	17054.3	17055.9
C 0-2	16643.8	16650.6
Fitted constants		
T_0	17463.7	17466.0
$\Delta G_{1/2}'$	345.5	341.0
ω_e''	408.3	414.9
$\omega_e''x_e''$	-0.55	2.4

[a] For this band system, four bands were observed, from which four constants were extracted. These reproduce the data exactly. As a result, it is impossible to provide any error estimates. All quantities are provided in wavenumber (cm^{-1}) units.

Table B.9 Vibrational Fit of System E for the ZrCl Isotopomers, Based on Band Heads.[a]

Band	$^{90}Zr^{35}Cl$	$^{94}Zr^{35}Cl$
E 0-0	13967.4(0.0)	13968.2(0.0)
E 1-0	14320.2(-0.4)	14319.2(0.0)
E 2-0	14670.7(0.4)	14667.2(0.0)
E 1-1	13912.6(0.4)	13913.3(0.0)
E 2-1	14261.4(-0.4)	14261.3(0.0)
E 3-1	14607.9(0.0)	
Fitted constants		
T_0	13967.4(0.6)	13968.2(0.0)
ω_e'	356.8(1.1)	354.0(0.0)
$\omega_e'x_e'$	1.79(0.26)	1.50(0.00)
$\Delta G_{1/2}''$	408.5(0.6)	405.9(0.0)

[a] Following each transition wavenumber listed, the residual in the fit (observed - calculated) is provided in parentheses. Likewise, the 1σ error limits in the fitted constants are provided in parentheses following each entry. All quantities are provided in wavenumber (cm^{-1}) units.

B.2 Rotationally Resolved Spectra of ZrF

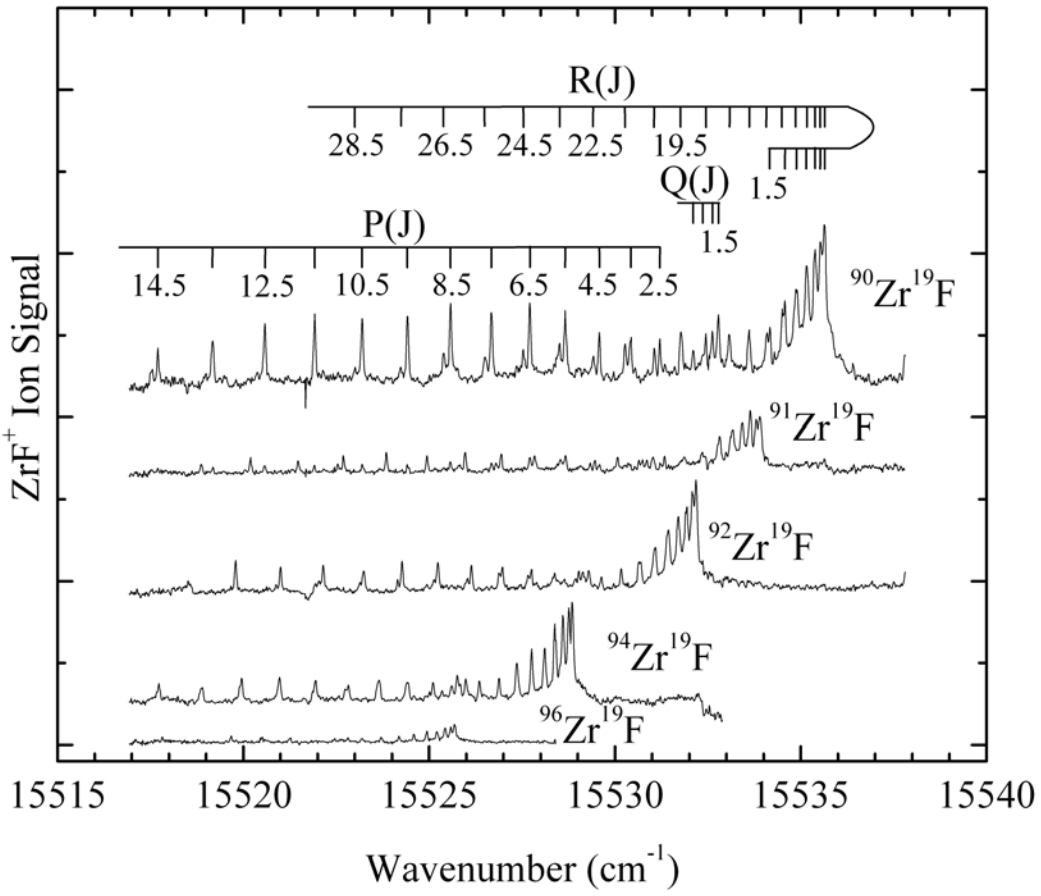

Figure B.23 Rotationally resolved spectra of the various ZrF isotopic modifications for the 3-0 band of the A – X system. Line assignments are provided for the $^{90}Zr^{19}F$ isotopic modification, which is the most abundant isotopomer.

Table B.10 Fitted Rotational Lines of the 3-0 Band of the A – X System of ZrF.[a]

Line	$^{90}Zr^{19}F$	$^{91}Zr^{19}F$	$^{92}Zr^{19}F$	$^{94}Zr^{19}F$	$^{96}Zr^{19}F$
P(2.5)	15531.207(-7)	15529.452(7)	15527.755(-11)	15524.433(4)	15521.259(12)
P(3.5)	15530.421(-1)	15528.671(10)	15526.973(-6)	15523.658(6)	15520.505(-5)
P(4.5)	15529.577(0)	15527.838(2)	15526.137(-10)	15522.827(2)	15519.672(-5)
P(5.5)	15528.665(7)	15526.940(-4)	15525.235(-9)	15521.939(-6)	15518.783(-11)
P(6.5)	15527.707(-3)	15525.970(0)	15524.270(-8)	15520.980(-5)	15517.814(2)
P(7.5)	15526.675(-2)	15524.943(-2)	15523.238(-1)	15519.958(-4)	
P(8.5)	15525.576(3)	15523.848(1)	15522.149(-1)		
P(9.5)	15524.419(4)	15522.695(0)	15521.002(-5)		
P(10.5)	15523.203(0)	15521.476(2)	15519.791(-8)		
P(11.5)	15521.918(3)	15520.194(5)			
P(12.5)	15520.581(-5)				
P(13.5)	15519.172(-5)				
P(14.5)	15517.704(-7)				
Q(1.5)	15532.780(-23)	15531.014(0)	15529.295(0)	15525.987(-6)	15522.816(-2)
Q(2.5)	15532.622(-22)	15530.858(-1)	15529.133(7)	15525.836(-10)	15522.668(-9)

Table B.10 Continued

Line	$^{90}Zr^{19}F$	$^{91}Zr^{19}F$	$^{92}Zr^{19}F$	$^{94}Zr^{19}F$	$^{96}Zr^{19}F$
Q(3.5)	15532.367(13)	15530.643(-5)	15528.924(-3)	15525.609(0)	15522.453(-10)
Q(4.5)	15532.106(-8)	15530.359(-3)	15528.639(1)	15525.349(-18)	
R(1.5)	15534.170(-14)	15532.411(0)	15530.693(-2)	15527.364(7)	15524.188(13)
R(2.5)	15534.574(-14)	15532.815(-2)	15531.089(5)	15527.758(14)	15524.589(13)
R(3.5)	15534.900(0)	15533.154(-1)	15531.437(-3)	15528.107(4)	15524.939(2)
R(4.5)	15535.163(14)	15533.428(3)	15531.705(7)	15528.381(7)	15525.209(9)
R(5.5)	15535.384(8)	15533.639(6)	15531.934(-8)	15528.604(-1)	15525.431(1)
R(6.5)	15535.529(15)	15533.798(-1)	15532.080(-1)	15528.755(1)	15525.581(5)
R(7.5)	15535.636(-3)	15533.894(-8)	15532.163(7)	15528.850(-3)	15525.686(-8)
R(8.5)	15535.657(2)	15533.924(-11)	15532.182(15)	15528.874(3)	
R(9.5)	15535.612(10)		15532.163(0)	15528.834(11)	
R(10.5)	15535.529(-7)			15528.739(11)	15525.581(0)
R(11.5)	15535.359(1)	15533.613(4)	15531.898(9)		15525.431(-6)
R(12.5)	15535.126(9)	15533.387(6)		15528.371(4)	15525.209(0)
R(13.5)	15534.838(9)	15533.108(-1)	15531.397(4)	15528.107(-12)	15524.939(-10)

Table B.10 Continued

Line	$^{90}Zr^{19}F$	$^{91}Zr^{19}F$	$^{92}Zr^{19}F$	$^{94}Zr^{19}F$	$^{96}Zr^{19}F$
R(14.5)	15534.501(-5)	15532.767(-9)	15531.065(-10)	15527.758(-5)	15524.589(-1)
R(15.5)	15534.081(1)	15532.349(-4)	15530.643(4)	15527.364(-15)	15524.188(-3)
R(16.5)	15533.607(-1)	15531.866(5)	15530.168(7)	15526.883(-1)	15523.712(9)
R(17.5)	15533.073(-7)	15531.334(0)	15529.635(7)	15526.353(2)	15523.190(4)
R(18.5)	15532.440(24)	15530.739(-4)	15529.028(19)	15525.758(7)	
R(19.5)	15531.776(23)	15530.067(5)	15528.378(10)	15525.107(5)	
R(20.5)	15531.061(11)		15527.663(4)		
R(21.5)	15530.275(6)		15526.885(-1)		
R(22.5)	15529.415(13)		15526.030(9)		
R(23.5)	15528.504(8)		15525.133(-2)		
R(24.5)	15527.532(1)		15524.154(7)		
R(25.5)	15526.507(-16)		15523.139(-12)		
R(26.5)	15525.390(-4)		15522.034(-2)		
R(27.5)	15524.235(-16)		15520.884(-8)		
R(28.5)	15523.004(-15)		15519.667(-12)		

Table B.10 Continued

Fitted spectroscopic constants[b]					
Constant	$^{90}Zr^{19}F$	$^{91}Zr^{19}F$	$^{92}Zr^{19}F$	$^{94}Zr^{19}F$	$^{96}Zr^{19}F$
ν_0 (cm^{-1})	15532.8748(22)	15531.1306(12)	15529.4125(17)	15526.0971(20)	15522.9294(22)
B_3' (cm^{-1})	0.27998(5)	0.27954(3)	0.27916(6)	0.27792(8)	0.27752(14)
r_3' (Å)	1.9593(2)	1.9590(1)	1.9585(2)	1.9592(3)	1.9572(5)
B_0'' (cm^{-1})	0.31139(6)	0.31086(6)	0.31036(8)	0.30889(10)	0.30842(24)
r_0'' (Å)	1.8579(2)	1.8577(2)	1.8574(2)	1.8584(3)	1.8566(7)

[a] Residuals (ν(calculated) – ν(measured)) are given in parentheses following each line position, in units of 0.001 cm^{-1}.
[b] Error limits (1σ) are provided for each fitted spectroscopic constant, in units of the last digit quoted. B_0'' was constrained to take the same value in all fitted bands originating from the ground vibronic level, namely the A – X 3-0 and 4-0 bands, the C – X 4-0 band, and one (*e/f*) component of the C – X 6-0 band.

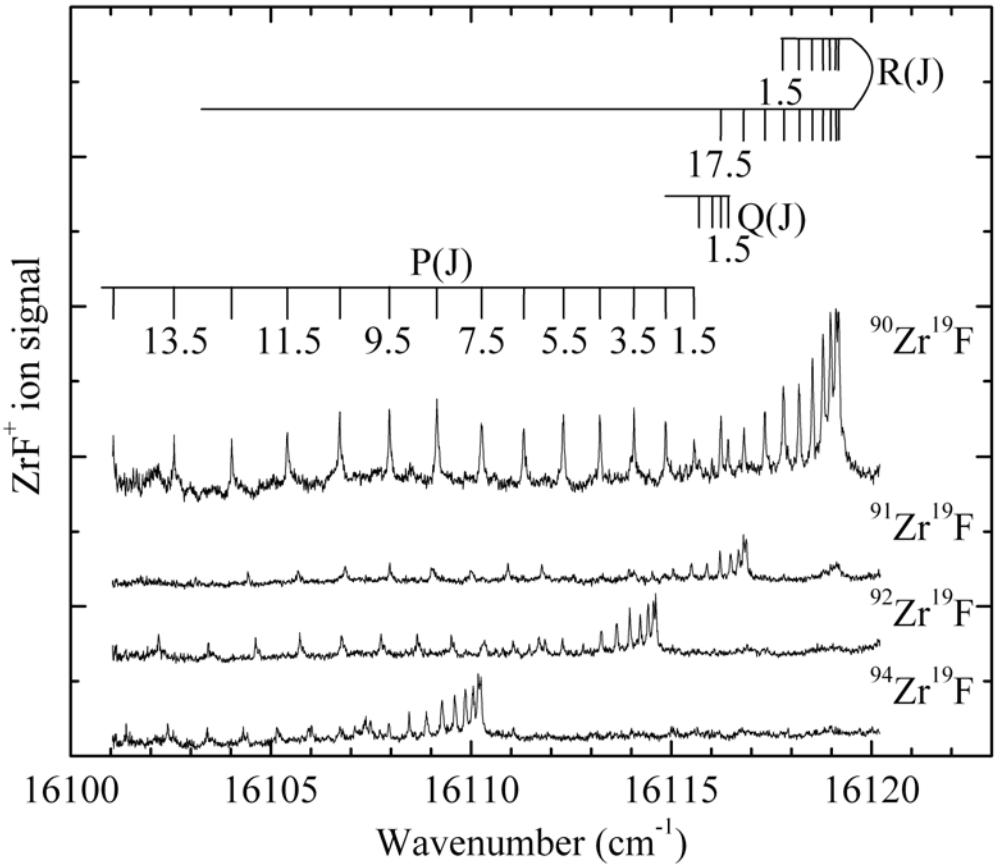

Figure B.24 Rotationally resolved spectra of the various ZrF isotopic modifications for the 4-0 band of the A – X system. Line assignments are provided for the $^{90}Zr^{19}F$ isotopic modification, which is the most abundant isotopomer.

Table B.11 Fitted Rotational Lines of the 4-0 Band of the A – X System of ZrF.[a]

Line	$^{90}Zr^{19}F$	$^{91}Zr^{19}F$	$^{92}Zr^{19}F$	$^{94}Zr^{19}F$
P(2.5)	16114.858(-8)			16105.941(-3)
P(3.5)	16114.069(-6)	16111.767(1)	16109.507(6)	16105.151(7)
P(4.5)	16113.219(-8)	16110.922(-6)	16108.653(11)	16104.313(2)
P(5.5)	16112.296(-3)	16110.002(-1)	16107.749(1)	16103.410(-4)
P(6.5)	16111.314(-5)	16109.027(-8)	16106.769(2)	16102.425(7)
P(7.5)	16110.265(-4)	16107.965(7)	16105.721(6)	16101.386(8)
P(8.5)	16109.145(1)	16106.857(3)	16104.618(-1)	
P(9.5)	16107.960(6)	16105.683(-1)	16103.437(5)	
P(10.5)	16106.718(2)	16104.431(8)	16102.197(6)	
P(11.5)	16105.404(5)	16103.119(12)		
P(12.5)	16104.021(11)			
P(13.5)	16102.583(6)			
P(14.5)	16101.060(22)			
Q(1.5)	16116.417(-10)		16111.844(5)	16107.491(-9)
Q(2.5)	16116.237(6)		16111.691(-5)	16107.097(-2)
Q(3.5)	16116.012(1)		16111.452(6)	
Q(4.5)	16115.700(18)			
Q(5.5)	16115.361(-4)			
R(1.5)	16117.803(-3)	16115.499(-2)	16113.253(-16)	16108.886(-20)
R(2.5)	16118.194(-1)	16115.891(-1)	16113.638(-8)	16109.273(-17)
R(3.5)	16118.526(-5)	16116.219(-1)	16113.963(-6)	16109.592(-9)
R(4.5)	16118.789(-6)	16116.484(-4)	16114.225(-5)	16109.860(-15)
R(5.5)	16118.979(1)	16116.683(-7)	16114.421(-4)	16110.056(-13)
R(6.5)	16119.114(-4)	16116.809(-1)	16114.555(-6)	16110.179(-4)
R(7.5)	16119.167(9)	16116.868(6)	16114.610(6)	16110.226(18)
R(8.5)		16116.86(6)	16114.627(-10)	16110.245(1)
R(9.5)		16116.809(-1)	16114.555(-2)	16110.179(6)
R(10.5)		16116.683(-5)	16114.421(4)	16110.056(4)
R(11.5)		16116.484(-2)		16109.860(8)
R(12.5)		16116.219(2)		16109.592(21)
R(13.5)		16115.891(3)		16109.273(20)
R(14.5)		16115.499(3)		16108.886(23)
R(15.5)	16117.335(3)	16115.045(-1)	16112.797(6)	16108.453(6)
R(16.5)	16116.817(-3)	16114.527(-6)	16112.280(4)	16107.948(-3)
R(17.5)	16116.237(-14)	16113.939(-6)	16111.691(8)	16107.373(-7)
R(18.5)	16115.575(-8)	16113.290(-11)	16111.046(3)	16106.725(-2)
R(19.5)		16112.558(2)	16110.335(-1)	16106.016(-1)
R(20.5)		16111.767(9)	16109.567(-14)	16105.232(10)
R(21.5)				16104.412(-8)
R(22.5)				
R(23.5)				16102.559(-24)

Table B.11 Continued

Fitted spectroscopic constants[b]				
Constant	$^{90}Zr^{19}F$	$^{91}Zr^{19}F$	$^{92}Zr^{19}F$	$^{94}Zr^{19}F$
ν_0 (cm^{-1})	16116.5297(20)	16114.2296(15)	16111.9705(18)	16107.6036(30)
B_4' (cm^{-1})	0.27860(7)	0.27816(6)	0.27777(7)	0.27655(7)
r_4' (Å)	1.9642(2)	1.9638(2)	1.9634(2)	1.9641(2)
B_0'' (cm^{-1})	0.31139(6)	0.31086(6)	0.31036(8)	0.30889(10)
r_0'' (Å)	1.8579(2)	1.8577(2)	1.8574(2)	1.8584(3)

[a] Residuals (ν(calculated) – ν(measured)) are given in parentheses following each line position, in units of 0.001 cm^{-1}.

[b] Error limits (1σ) are provided for each fitted spectroscopic constant, in units of the last digit quoted. All quantities are given in cm^{-1} units, except for the bond lengths, which are given in Å. B_0'' was constrained to take the same value in all fitted bands originating from the ground vibronic level, namely the A – X 3-0 and 4-0 bands, the C – X 4-0 band, and one (*e/f*) component of the C – X 6-0 band.

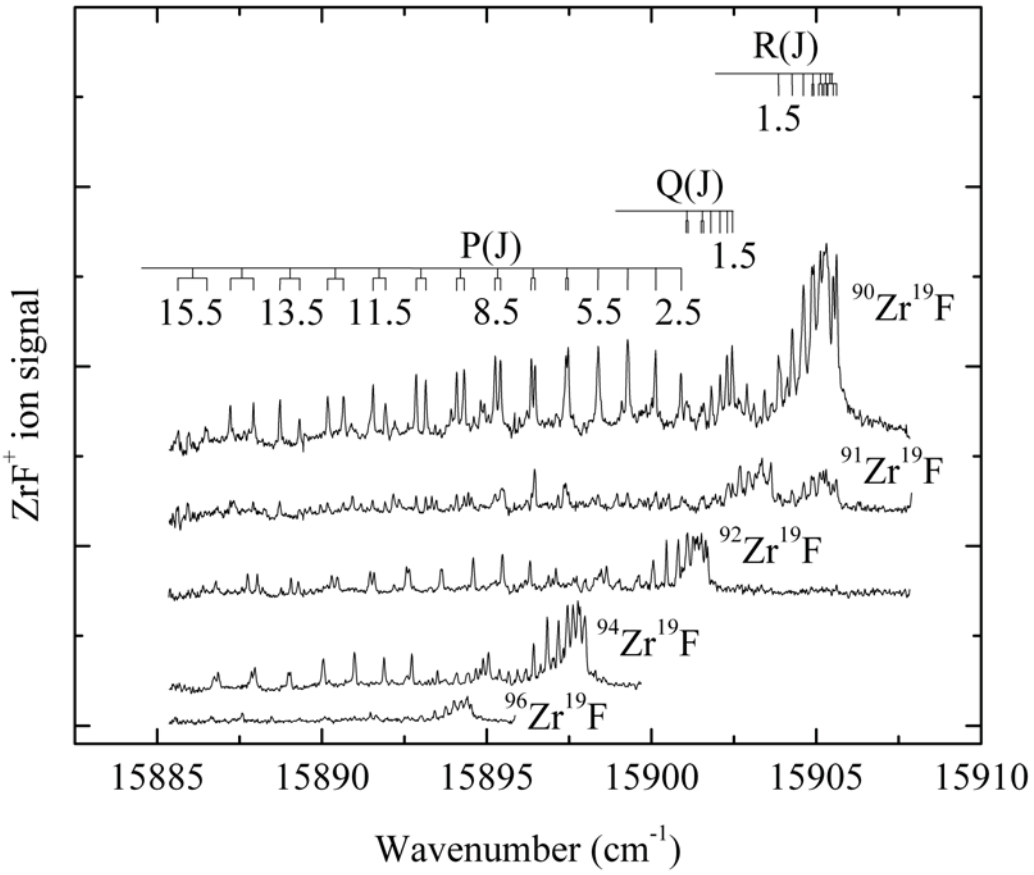

Figure B.25 Rotationally resolved spectra of the various ZrF isotopic modifications for the 4-0 band of the C – X system. Line assignments are provided for the $^{90}Zr^{19}F$ isotopic modification, which is the most abundant isotopomer. Unlike the 3-0 and 4-0 bands of the A – X system, this system clearly shows the effects of lambda doubling. When this band was scanned, the mass channels used to collect the spectrum of $^{91}Zr^{19}F$ (mass 110) were imperfectly selected, and some signal due to $^{90}Zr^{19}F$ leaked into the spectrum of $^{91}Zr^{19}F$. This accounts for the presence of a second R branch head in this spectrum, as well as some of the additional lines. Nevertheless, it has been possible to identify lines originating from $^{91}Zr^{19}F$ for the rotational fit.

Table B.12 Fitted Rotational Lines of the 4-0 Band of the C – X System of ZrF.[a]

Line	$^{90}Zr^{19}F$	$^{91}Zr^{19}F$	$^{92}Zr^{19}F$	$^{94}Zr^{19}F$	$^{96}Zr^{19}F$
P(2.5)	15900.896(0)			15893.512(-6)	15890.001(9)
P(3.5)	15900.125(-4)	15898.199(-4)	15896.229(5)	15892.730(4)	15889.241(-7)
P(4.5)	15899.278(7)	15897.346(13)	15895.388(9)	15891.891(8)	15888.384(10)
P(5.5)	15898.387(2)	15896.454(7)	15894.503(-4)	15890.997(4)	15887.500(-10)
P(6.5)					15886.548(-26)
P(7.5)					15885.456(35)
P_f(6.5)	15897.406(-2)	15895.469(7)	15893.523(-7)	15890.025(-2)	
P_e(6.5)	15897.466(-7)	15895.521(8)	15893.559(4)	15890.046(14)	
P_f(7.5)	15896.354(15)	15894.440(0)	15892.480(0)	15888.988(3)	
P_e(7.5)	15896.467(-9)	15894.537(-13)	15892.561(-4)	15889.046(3)	
P_f(8.5)	15895.258(10)	15893.335(2)	15891.378(1)	15887.873(19)	
P_e(8.5)	15895.418(-17)	15893.474(-10)	15891.492(1)	15887.968(12)	
P_f(9.5)	15894.092(8)	15892.164(3)	15890.209(1)	15886.740(-12)	
P_e(9.5)	15894.317(-27)	15892.345(3)	15890.380(-7)	15886.861(-8)	
P_f(10.5)	15892.859(5)	15890.926(3)	15888.973(1)		

Table B.12 Continued

Line	$^{90}Zr^{19}F$	$^{91}Zr^{19}F$	$^{92}Zr^{19}F$	$^{94}Zr^{19}F$	$^{96}Zr^{19}F$
$P_e(10.5)$	15893.149(-24)	15891.185(-7)	15889.195(3)		
$P_f(11.5)$	15891.549(10)	15889.638(-17)	15887.659(10)		
$P_e(11.5)$	15891.927(-20)	15889.956(-2)	15887.951(17)		
$P_f(12.5)$	15890.177(7)	15888.241(3)			
$P_e(12.5)$	15890.662(-24)	15888.688(-10)			
$P_f(13.5)$	15888.728(11)				
$P_e(13.5)$	15889.319(-3)				
$P_f(14.5)$	15887.219(5)				
$P_e(14.5)$	15887.922(23)				
$P_f(15.5)$	15885.633(3)				
$P_e(15.5)$	15886.514(9)				
Q(1.5)	15902.447(6)	15900.525(-1)	15898.548(12)	15895.058(-7)	15891.551(1)
Q(2.5)	15902.291(10)		15898.389(18)	15894.900(-4)	15891.386(7)
Q(3.5)	15902.083(5)		15898.181(10)	15894.680(-1)	
Q(4.5)	15901.819(-4)				15890.899(-17)

Table B.12 Continued

Line	$^{90}Zr^{19}F$	$^{91}Zr^{19}F$	$^{92}Zr^{19}F$	$^{94}Zr^{19}F$	$^{96}Zr^{19}F$
$Q_{fe}(2.5)$		15900.389(-15)			
$Q_{ef}(2.5)$		15900.352(16)			
$Q_{fe}(3.5)$					
$Q_{ef}(3.5)$		15900.145(4)			
$Q_{fe}(4.5)$		15899.896(-1)	15897.918(9)	15894.417(-7)	
$Q_{ef}(4.5)$			15897.883(16)	15894.397(-9)	
$Q_{fe}(5.5)$	15901.510(-3)	15899.582(-13)			
$Q_{ef}(6.5)$	15901.056(-16)	15899.093(10)			
R(1.5)	15903.857(1)	15901.944(-18)	15899.968(-10)	15896.430(11)	15892.918(17)
R(2.5)	15904.271(-3)	15902.324(9)	15900.367(-4)	15896.844(-3)	15893.335(-6)
R(3.5)	15904.612(4)	15902.686(-7)			15893.672(-14)
R(4.5)					15893.923(2)
R(5.5)					15894.128(-1)
$R_f(3.5)$			15900.703(-10)	15897.165(4)	
$R_e(3.5)$			15900.733(-13)	15897.188(2)	

Table B.12 Continued

Line	$^{90}Zr^{19}F$	$^{91}Zr^{19}F$	$^{92}Zr^{19}F$	$^{94}Zr^{19}F$	$^{96}Zr^{19}F$
$R_f(4.5)$	15904.873(4)	15902.936(0)	15900.970(-5)	15897.445(-9)	
$R_e(4.5)$	15904.927(5)		15901.025(-13)	15897.476(-3)	
$R_f(5.5)$	15905.079(10)	15903.149(-6)	15901.178(-7)	15897.640(0)	
$R_e(5.5)$	15905.174(3)	15903.242(-14)	15901.253(-6)		
$R_f(6.5)$	15905.233(0)	15903.295(-10)	15901.317(-6)	15897.779(-2)	
$R_e(6.5)$	15905.362(3)	15903.415(-4)	15901.429(-5)		
$R_f(7.5)$	15905.313(-3)	15903.357(1)	15901.388(-5)	15897.844(3)	
$R_e(7.5)$	15905.514(-14)	15903.547(-7)	15901.553(-7)	15897.985(-11)	
$R_f(8.5)$	15905.313(7)	15903.357(6)		15897.859(-8)	
$R_e(8.5)$	15905.617(-36)		15901.616(-4)	15898.017(8)	
$R_f(9.5)$	15905.233(27)	15903.622(10)		15897.793(-6)	
$R_e(9.5)$	15905.617(-8)				
$R_f(10.5)$	15905.124(7)				
$R_e(10.5)$	15905.617(-32)				
$R_f(11.5)$	15904.927(5)			15897.456(0)	

Table B.12 Continued

Line	$^{90}Zr^{19}F$	$^{91}Zr^{19}F$	$^{92}Zr^{19}F$	$^{94}Zr^{19}F$	$^{96}Zr^{19}F$
$R_e(11.5)$	15905.514(-6)	15903.496(18)		15897.840(-1)	
$R_f(12.5)$	15904.612(49)	15902.686(1)		15897.188(0)	
$R_e(12.5)$	15905.362(20)			15897.666(0)	
$R_f(13.5)$	15904.318(2)			15896.844(5)	
$R_e(13.5)$	15905.179(28)				
$R_f(14.5)$	15903.909(-4)				
$R_e(14.5)$				15897.155(0)	
$R_f(15.5)$	15903.428(-12)				
$R_f(16.5)$	15902.894(-40)				
$R_e(18.5)$		15901.520(-5)			
$R_e(19.5)$		15901.028(11)			
$R_e(20.5)$		15900.525(-7)			
Fitted spectroscopic constants[b]					
Constant	$^{90}Zr^{19}F$	$^{91}Zr^{19}F$	$^{92}Zr^{19}F$	$^{94}Zr^{19}F$	$^{96}Zr^{19}F$
ν_0 (cm^{-1})	15902.5668(34)	15900.6393(25)	15898.6757(28)	15895.1678(19)	15891.6721(77)

Table B.12 Continued

Constant	$^{90}Zr^{19}F$	$^{91}Zr^{19}F$	$^{92}Zr^{19}F$	$^{94}Zr^{19}F$	$^{96}Zr^{19}F$
B_4' (cm^{-1})	0.28098(5)	0.28020(3)	0.27956(8)	0.27782(8)	0.27652(21)
r_4' (Å)	1.9558(2)	1.9567(1)	1.9571(3)	1.9596(3)	1.9607(7)
$p_\Delta' + 4q_\Delta'$ (cm^{-1})	0.000264(2)	0.000252(2)	0.000226(6)	0.000176(2)	…
B_0'' (cm^{-1})	0.31139(6)	0.31086(6)	0.31036(8)	0.30889(10)	0.30842(24)
r_0'' (Å)	1.8579(2)	1.8577(2)	1.8574(2)	1.8584(3)	1.8566(7)

[a] Residuals (ν(calculated) – ν(measured)) are given in parentheses following each line position, in units of 0.001 cm^{-1}.
[b] Error limits (1σ) are provided for spectroscopic constants, in units of the last digit quoted. All quantities are given in cm^{-1} units, except for the bond lengths, which are given in Å. B_0'' was constrained to take the same value in all fitted bands originating from the ground vibronic level, namely the A – X 3-0 and 4-0 bands, the C – X 4-0 band, and one (*e/f*) component of the C – X 6-0 band. The entry labeled $p_\Delta' + 4q_\Delta'$ is the lambda doubling parameter for the upper state, which shifts the energy of the (*e/f*) levels by $\pm(-1/2)(p_\Delta' + 4q_\Delta')(J-0.5)(J+0.5)(J+1.5)$ for a $^2\Delta_{3/2}$ state. Similar expressions are valid for $^2\Pi_{3/2}$, $^4\Pi_{3/2}$, or $^4\Delta_{3/2}$ states. Note that the actual (*e/f*) parity of the observed levels could be reversed; the absolute parity is unknown.

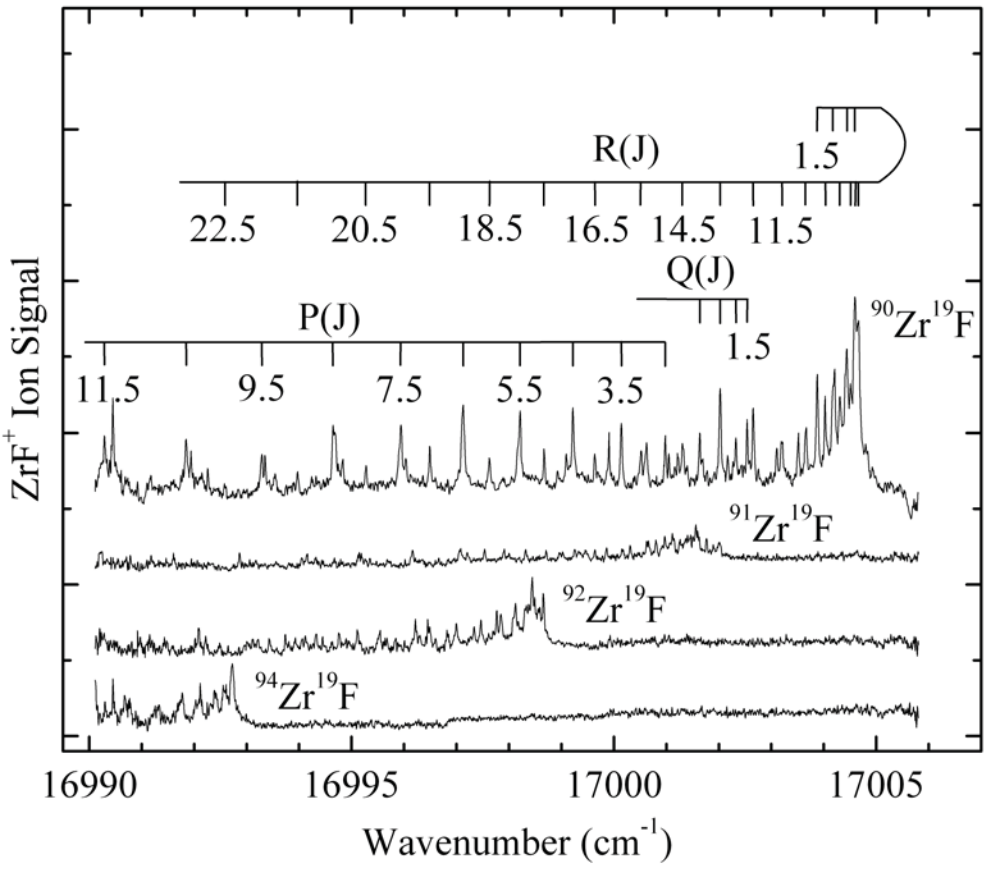

Figure B.26 Rotationally resolved spectra of the various ZrF isotopic modifications for the 6-0 band of the C – X system. Line assignments are provided for the unperturbed *e/f* component of the $^{90}Zr^{19}F$ isotopic modification, which is the most abundant isotopomer.

Table B.13 Fitted Rotational Lines of One Parity Component of the 6-0 Band of the C – X System of ZrF.[a]

Line	$^{90}Zr^{19}F$	$^{91}Zr^{19}F$	$^{92}Zr^{19}F$
P(2.5)	17000.978(-14)	16997.906(0)	16994.955(3)
P(3.5)	17000.139(-13)	16997.075(-4)	16994.118(10)
P(4.5)	16999.214(-12)	16996.164(-13)	16993.214(-1)
P(5.5)	16998.207(-15)	16995.147(-3)	16992.220(-5)
P(6.5)	16997.119(-23)	16994.053(-1)	16991.152(-2)
P(7.5)	16995.905(9)	16992.866(9)	
P(8.5)	16994.647(-1)	16991.606(6)	
P(9.5)	16993.283(8)		
P(10.5)	16991.845(6)		
P(11.5)	16990.290(35)		
Q(1.5)		16999.464(-3)	
Q(2.5)		16999.255(-8)	16996.301(-1)
Q(3.5)		16998.965(-17)	16996.008(-2)
R(1.5)		17000.804(-3)	16997.845(7)
R(2.5)	17004.174(10)	17001.116(8)	16998.177(2)
R(3.5)	17004.436(-17)	17001.367(-6)	16998.443(-21)
R(4.5)	17004.596(-27)	17001.503(10)	16998.587(-6)
R(5.5)	17004.653(-21)	17001.598(-19)	16998.654(2)
R(6.5)	17004.596(14)	17001.564(-4)	16998.654(-7)
R(7.5)	17004.506(-4)	17001.458(-3)	16998.554(0)
R(8.5)	17004.307(-1)	17001.260(5)	16998.380(-3)
R(9.5)	17004.021(5)	17000.972(17)	16998.122(-6)
R(10.5)	17003.654(5)	17000.624(5)	16997.766(6)
R(11.5)	17003.198(8)	17000.164(18)	16997.336(8)
R(12.5)	17002.650(18)	16999.639(11)	16996.821(10)
R(13.5)	17002.024(19)	16999.022(11)	16996.215(20)
R(14.5)	17001.307(25)	16998.318(12)	16995.536(19)
R(15.5)	17000.518(18)	16997.535(7)	16994.767(23)
R(16.5)	16999.633(19)	16996.662(6)	16993.927(15)
R(17.5)	16998.668(16)	16995.719(-10)	16993.011(-1)
R(18.5)	16997.626(2)	16994.672(-8)	16992.017(-23)
R(19.5)	16996.488(-1)	16993.558(-2)	16990.923(-29)
R(20.5)	16995.273(-13)		
R(21.5)	16993.969(-23)		
R(22.5)	16992.580(-32)		
Spectroscopic constants			
Constant	$^{90}Zr^{19}F$	$^{91}Zr^{19}F$	$^{92}Zr^{19}F$
ν_0 (cm^{-1})	17002.6818(45)	16999.6208(27)	16996.6671(37)
B_6' (cm^{-1})	0.26837(7)	0.26813(6)	0.26839(7)

Table B.13 Continued

Constant	$^{90}Zr^{19}F$	$^{91}Zr^{19}F$	$^{92}Zr^{19}F$
r_6' (Å)	2.0013(3)	2.0002(2)	1.9974(3)
B_0'' (cm^{-1})	0.31139(6)	0.31086(6)	0.31036(8)
r_0'' (Å)	1.8579(2)	1.8577(2)	1.8574(2)

[a] Residuals (ν(calculated) – ν(measured)) are given in parentheses following each line position, in units of 0.001 cm^{-1}. For this band, a perturbation seriously affects one of the (*e/f*) components. Only the unaffected component is listed and fitted here.

[b] Error limits (1σ) are provided for spectroscopic constants, in units of the last digit quoted. B_0'' was constrained to take the same value in all fitted bands originating from the ground vibronic level, namely the A – X 3-0 and 4-0 bands, the C – X 4-0 band, and one (*e/f*) component of the C – X 6-0 band.

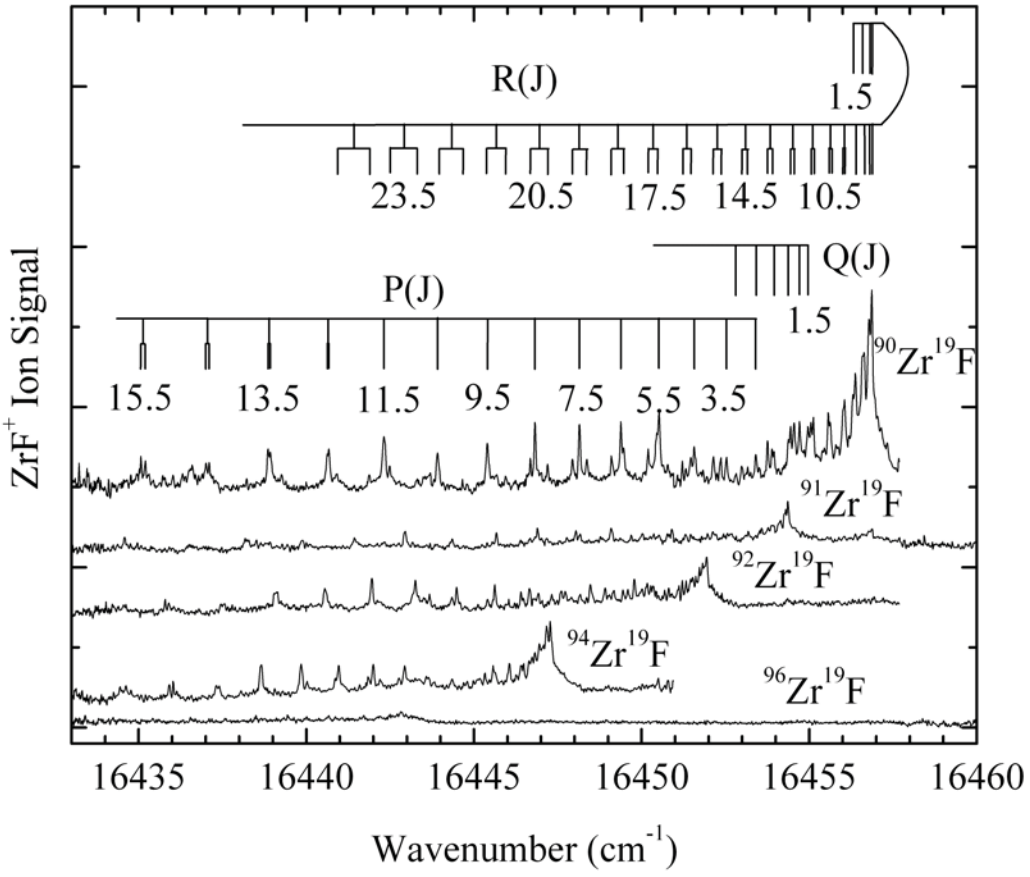

Figure B.27 Rotationally resolved spectra of the various ZrF isotopic modifications for the 5-0 band of the C – X system. Line assignments are provided for the *e/f* components of the $^{90}Zr^{19}F$ isotopic modification, which is the most abundant isotopomer.

Table B.14 Assigned Rotational Lines of the 5-0 Band of the C – X System of ZrF.[a]

Line	$^{90}Zr^{19}F$	$^{91}Zr^{19}F$	$^{92}Zr^{19}F$	$^{94}Zr^{19}F$	$^{96}Zr^{19}F$
P(2.5)	16453.317	16450.904	16448.475	16443.716	16439.336
P(3.5)	16452.442	16450.029	16447.603	16442.842	16438.503
P(4.5)	16451.473	16449.095	16446.660	16441.906	16437.586
P(5.5)	16450.432	16448.043	16445.620	16440.876	16436.545
P(6.5)	16449.292	16446.894	16444.488	16439.757	16435.425
P(7.5)	16448.056	16445.669	16443.258	16438.558	16434.238
P(8.5)	16446.729	16444.356	16441.960		
P_e(8.5)				16437.224	
P_f(8.5)				16437.315	
P(9.5)	16445.309	16442.943			
P_e(9.5)			16440.592	16435.823	
P_f(9.5)			16440.541	16435.942	
P(10.5)		16441.440			
P_e(10.5)	16443.834		16439.123	16434.529	
P_f(10.5)	16443.814		16439.059	16434.354	

Table B.14 Continued

Line	$^{90}Zr^{19}F$	$^{91}Zr^{19}F$	$^{92}Zr^{19}F$	$^{94}Zr^{19}F$	$^{96}Zr^{19}F$
$P_e(11.5)$	16442.252	16439.899	16437.547		
$P_f(11.5)$	16442.219	16439.848	16437.455		
$P_e(12.5)$	16440.580	16438.289	16435.903		
$P_f(12.5)$	16440.533	16438.174	16435.789		
$P_e(13.5)$	16438.836				
$P_f(13.5)$	16438.770				
$P_e(14.5)$	16437.009				
$P_f(14.5)$	16436.918				
$P_e(15.5)$	16435.106				
$P_f(15.5)$	16434.977				
$P_e(16.5)$	16433.134				
Q(1.5)	16454.870	16452.445	16450.020	16445.237	16440.866
Q(2.5)	16454.622	16452.222	16449.789	16445.013	16440.670
Q(3.5)	16454.284	16451.873	16449.445	16444.710	16440.378
Q(4.5)	16453.857	16451.468	16449.042	16444.255	

Table B.14 Continued

Line	$^{90}Zr^{19}F$	$^{91}Zr^{19}F$	$^{92}Zr^{19}F$	$^{94}Zr^{19}F$	$^{96}Zr^{19}F$
Q(5.5)	16453.317		16448.546		
Q(6.5)	16452.725		16447.911		
Q(7.5)	16452.049				
R(1.5)	16456.206	16453.774	16451.332	16446.552	16442.204
R(2.5)	16456.493	16454.087	16451.614	16446.864	16442.520
R(3.5)	16456.693	16454.259	16451.824	16447.087	16442.713
R(4.5)	16456.772	16454.363	16451.941	16447.187	16442.827
R(5.5)	16456.772	16454.363	16451.941	16447.228	16442.873
R(6.5)	16456.693	16454.299	16451.881		
R_e(6.5)				16447.087	
R_f(6.5)				16447.187	
R(7.5)	16456.539	16454.143	16451.725		
R_e(7.5)				16446.984	
R_f(7.5)				16447.087	
R(8.5)	16456.285	16453.867			

Table B.14 Continued

Line	$^{90}Zr^{19}F$	$^{91}Zr^{19}F$	$^{92}Zr^{19}F$	$^{94}Zr^{19}F$	$^{96}Zr^{19}F$
$R_e(8.5)$			16451.523	16446.864	
$R_f(8.5)$			16451.464	16446.728	
$R_e(9.5)$	16455.967	16453.582	16451.217		
$R_f(9.5)$	16455.915	16453.523	16451.119		
$R_e(10.5)$	16455.536	16453.184	16450.809		
$R_f(10.5)$	16455.476	16453.106	16450.692		
$R_e(11.5)$	16455.032	16452.669	16450.276		
$R_f(11.5)$	16454.960	16452.561	16450.169		
$R_e(12.5)$	16454.458	16452.125	16449.789		
$R_f(12.5)$	16454.354	16451.971	16449.587		
$R_e(13.5)$	16453.801	16451.468	16449.176		
$R_f(13.5)$	16453.671	16451.311	16448.913		
$R_e(14.5)$	16453.074	16450.772	16448.475		
$R_f(14.5)$	16452.895	16450.513	16448.168		
$R_e(15.5)$	16452.262	16450.029	16447.724		

Table B.14 Continued

Line	$^{90}Zr^{19}F$	$^{91}Zr^{19}F$	$^{92}Zr^{19}F$	$^{94}Zr^{19}F$	$^{96}Zr^{19}F$
$R_f(15.5)$	16452.049	16449.695	16447.323		
$R_e(16.5)$	16451.376		16446.921		
$R_f(16.5)$	16451.129	16448.774	16446.477		
$R_e(17.5)$	16450.356	16448.151	16446.041		
$R_f(17.5)$	16450.105	16447.772	16445.408		
$R_e(18.5)$	16449.374		16445.121		
$R_f(18.5)$	16449.017		16444.346		
$R_e(19.5)$	16448.278				
$R_f(19.5)$	16447.850				
$R_e(20.5)$	16447.108				
$R_f(20.5)$	16446.595				
$R_e(21.5)$	16445.860				
$R_e(22.5)$	16444.567				
$R_e(23.5)$	16443.200				
$R_e(24.5)$	16441.789				

Table B.14 Continued

Line	$^{90}Zr^{19}F$	$^{91}Zr^{19}F$	$^{92}Zr^{19}F$	$^{94}Zr^{19}F$	$^{96}Zr^{19}F$
$R_f(24.5)$	16440.820				
$R_f(25.5)$	16439.175				
Fitted spectroscopic constants[b]					
Constant	$^{90}Zr^{19}F$	$^{91}Zr^{19}F$	$^{92}Zr^{19}F$	$^{94}Zr^{19}F$	$^{96}Zr^{19}F$
ν_0 (cm^{-1})	16455.1229(81)	16452.6216(42)	16450.1862(39)	16445.5015(69)	16441.0486(69)
B_5' (cm^{-1})	0.26441(16)	0.26414(7)	0.26393(10)	0.26348(26)	0.26373(19)
r_5' (Å)	2.0162(6)	2.0153(3)	2.0142(4)	2.0122(10)	2.0077(7)
B_0'' (cm^{-1})	0.31139(6)	0.31086(6)	0.31036(8)	0.30889(10)	0.30842(24)
r_0'' (Å)	1.8579(2)	1.8577(2)	1.8574(2)	1.8584(3)	1.8566(7)

[a] Note that the actual (*e/f*) parity of the observed levels could be reversed; the absolute parity is unknown.
[b] Fitted constants have been obtained only by fitting lines with low values of J (typically less than 10.5), before lambda doubling is apparent. Because of the perturbation in this band, the lower state constant was held fixed at the value determined from the other bands. The variation in apparent upper state bond length illustrates the perturbations found in the C1.5, v = 5 level.

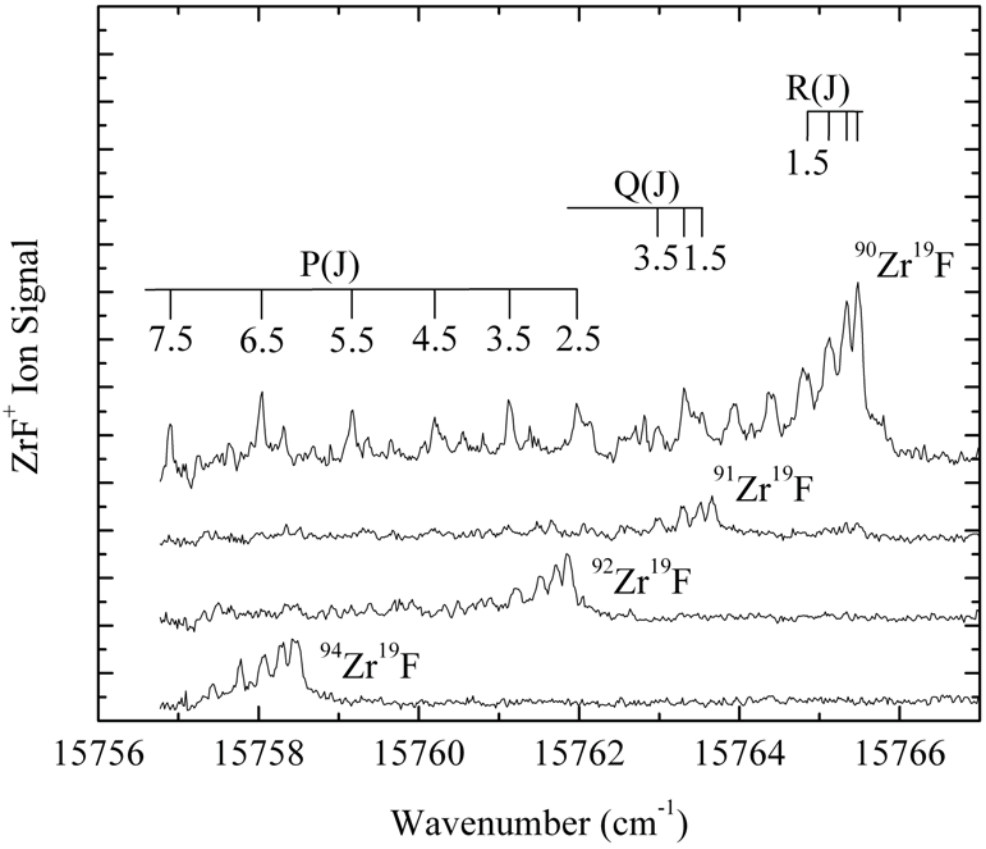

Figure B.28 Rotationally resolved spectra of the various ZrF isotopic modifications for the 5-1 band of the C – X system. Line assignments are provided for the $^{90}Zr^{19}F$ isotopic modification, which is the most abundant isotopomer.

Table B.15 Assigned Rotational Lines of the 5-1 Band of the C – X System of ZrF.[a]

Line	$^{90}Zr^{19}F$	$^{91}Zr^{19}F$	$^{92}Zr^{19}F$	$^{94}Zr^{19}F$
P(2.5)	15761.976(7)	15760.160(-24)	15758.348(4)	
P(3.5)	15761.130(9)	15759.305(-10)	15757.499(8)	
P(4.5)	15760.197(7)	15758.347(17)		
P(5.5)	15759.169(10)	15757.348(-4)		
P(6.5)	15758.030(33)			
P(7.5)	15756.895(-39)			
Q(1.5)	15763.534(-9)	15761.655(25)	15759.903(-5)	
Q(2.5)	15763.315(-16)	15761.476(-19)	15759.693(-22)	
Q(3.5)	15762.987(-6)	15761.123(21)		
R(1.5)	15764.863(-22)	15763.003(-2)	15761.210(7)	15757.771
R(2.5)	15765.125(16)	15763.310(-4)	15761.516(2)	15758.069
R(3.5)	15765.343(6)	15763.509(13)	15761.714(14)	15758.289
R(4.5)	15765.480(-12)	15763.662(-14)	15761.856(-9)	15758.432
R(5.5)	15765.480(15)			15758.487
Fitted spectroscopic constants[b]				
Constant	$^{90}Zr^{19}F$	$^{91}Zr^{19}F$	$^{92}Zr^{19}F$	$^{94}Zr^{19}F$
ν_0 (cm^{-1})	15763.6957(89)	15761.8482(106)	15760.0685(86)	
B_5' (cm^{-1})	0.26315(66)	0.26415(81)	0.26382(76)	
r_5' (Å)	2.0210(25)	2.0152(31)	2.0146(29)	
B_1'' (cm^{-1})	0.30852(58)	0.30887(81)	0.30920(120)	
r_1'' (Å)	1.8665(18)	1.8636(24)	1.8609(36)	

[a] Residuals (ν(calculated) – ν(measured)) are given in parentheses following each line position, in units of 0.001 cm^{-1}.

[b] Error limits (1σ) are provided for spectroscopic constants, in units of the last digit quoted.

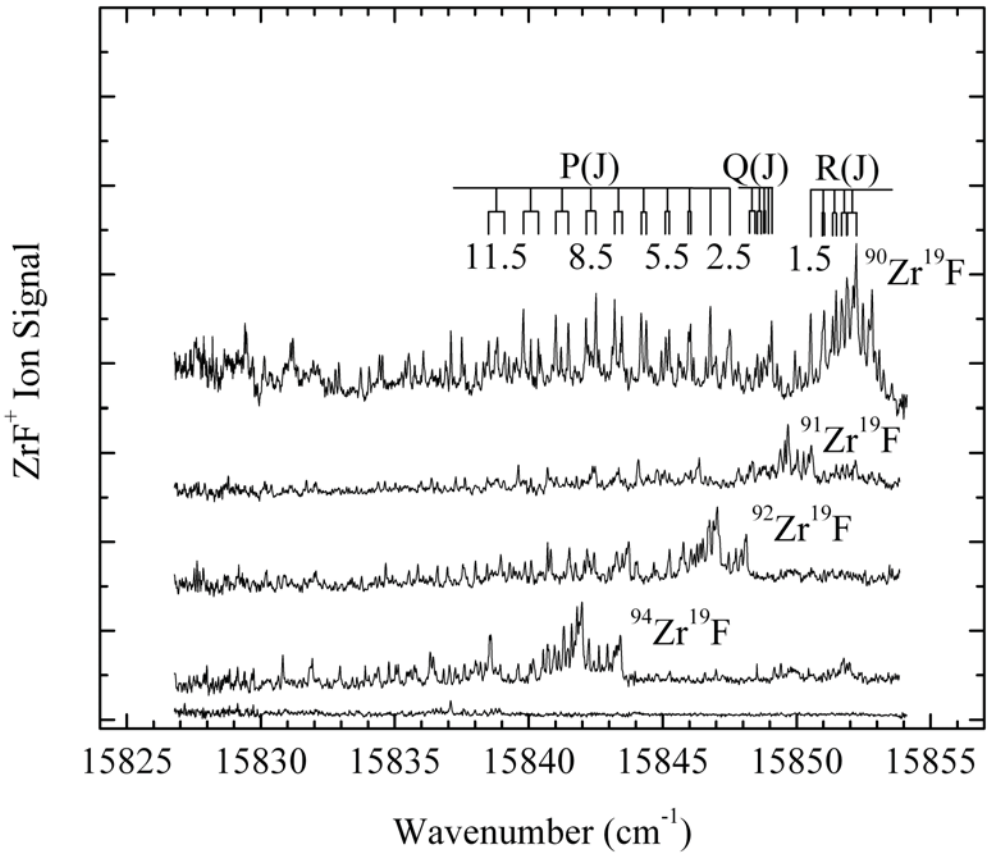

Figure B.29 Rotationally resolved spectra of the various ZrF isotopic modifications for the 5-0 band of the B – X system. Line assignments are provided for the *e/f* components of the $^{90}Zr^{19}F$ isotopic modification, which is the most abundant isotopomer.

Table B.16 Assigned Rotational Lines of the 5-0 Band of the B – X System of ZrF.[a]

Line	$^{90}Zr^{19}F$	$^{91}Zr^{19}F$	$^{92}Zr^{19}F$	$^{94}Zr^{19}F$
P(2.5)	15847.510	15844.796	15842.179	15837.038
P(3.5)	15846.777	15844.091	15841.518	
P_e(3.5)				15836.438
P_f(3.5)				15836.325
P_e(4.5)	15846.039	15843.362	15840.827	15835.737
P_f(4.5)	15845.974	15843.289	15840.707	15835.595
P_e(5.5)	15845.241	15842.476	15840.094	15835.133
P_f(5.5)	15845.118	15842.389	15839.864	15834.783
P_e(6.5)	15844.392	15841.400	15839.295	15834.608
P_f(6.5)	15844.201		15838.958	15833.903
P_e(7.5)	15843.477		15838.447	15834.036
P_f(7.5)	15843.208		15838.015	15832.957
P_e(8.5)	15842.513		15837.545	15832.740
P_f(8.5)	15842.138		15836.967	15831.928
P_e(9.5)	15841.480		15836.598	15831.845
P_f(9.5)	15841.012		15835.864	15830.822
P_e(10.5)	15840.362		15835.537	15830.822
P_f(10.5)	15839.801		15834.661	
P_e(11.5)	15839.109		15834.429	
P_f(11.5)	15838.505		15833.405	
P_e(12.5)			15833.255	
P_f(12.5)	15837.099		15832.056	
P_e(13.5)			15831.997	
P_f(13.5)			15830.656	
P_f(14.5)			15829.176	
Q(1.5)	15849.069	15846.363	15843.733	15838.584
Q(2.5)	15848.963	15846.292	15843.698	
Q_{ef}(2.5)				15838.584
Q_{fe}(2.5)				15838.509
Q_{ef}(3.5)	15848.850	15846.155	15843.645	15838.541
Q_{fe}(3.5)	15848.783	15846.043	15843.494	15838.386
Q_{ef}(4.5)	15848.669		15843.494	
Q_{fe}(4.5)	15848.533		15843.283	15838.200
Q_{ef}(5.5)	15848.452		15843.283	
Q_{fe}(5.5)	15848.245		15842.996	15837.908
Q_{ef}(6.5)	15848.147		15843.126	
Q_{fe}(6.5)			15842.735	
Q_{ef}(7.5)			15842.805	
R(1.5)	15850.525	15847.834	15845.255	
R_e(1.5)				15840.166
R_f(1.5)				15840.059
R_e(2.5)	15851.026	15848.346	15845.777	15840.706

Table B.16 Continued

Line	$^{90}Zr^{19}F$	$^{91}Zr^{19}F$	$^{92}Zr^{19}F$	$^{94}Zr^{19}F$
$R_f(2.5)$	15850.971	15848.249	15845.673	15840.542
$R_e(3.5)$	15851.477	15848.716	15846.286	15841.310
$R_f(3.5)$	15851.349	15848.617	15846.060	15840.964
$R_e(4.5)$	15851.883	15848.850	15846.752	15841.985
$R_f(4.5)$	15851.676		15846.409	15841.310
$R_e(5.5)$	15852.221		15847.118	15842.624
$R_f(5.5)$	15851.918		15846.702	15841.606
$R_e(6.5)$	15852.478		15847.463	
$R_f(6.5)$	15852.113		15846.892	15841.806
$R_e(7.5)$	15852.690		15847.733	
$R_f(7.5)$	15852.221		15847.040	15841.985
$R_e(8.5)$	15852.818		15847.940	15843.180
$R_f(8.5)$	15852.221		15847.118	
$R_e(9.5)$	15852.818		15848.080	
$R_f(9.5)$	15852.221		15847.040	
$R_e(10.5)$			15848.122	
$R_f(10.5)$	15852.066		15846.938	
$R_e(11.5)$			15848.080	
$R_f(11.5)$	15851.676		15846.752	
$R_f(12.5)$	15851.263		15846.503	
$R_f(13.5)$	15850.724		15846.179	

[a] For this band, perturbations are too severe to attempt a fit. It has only been possible to identify the observed lines using combination differences, using the known values of B″, which have been obtained from the analysis of other bands.

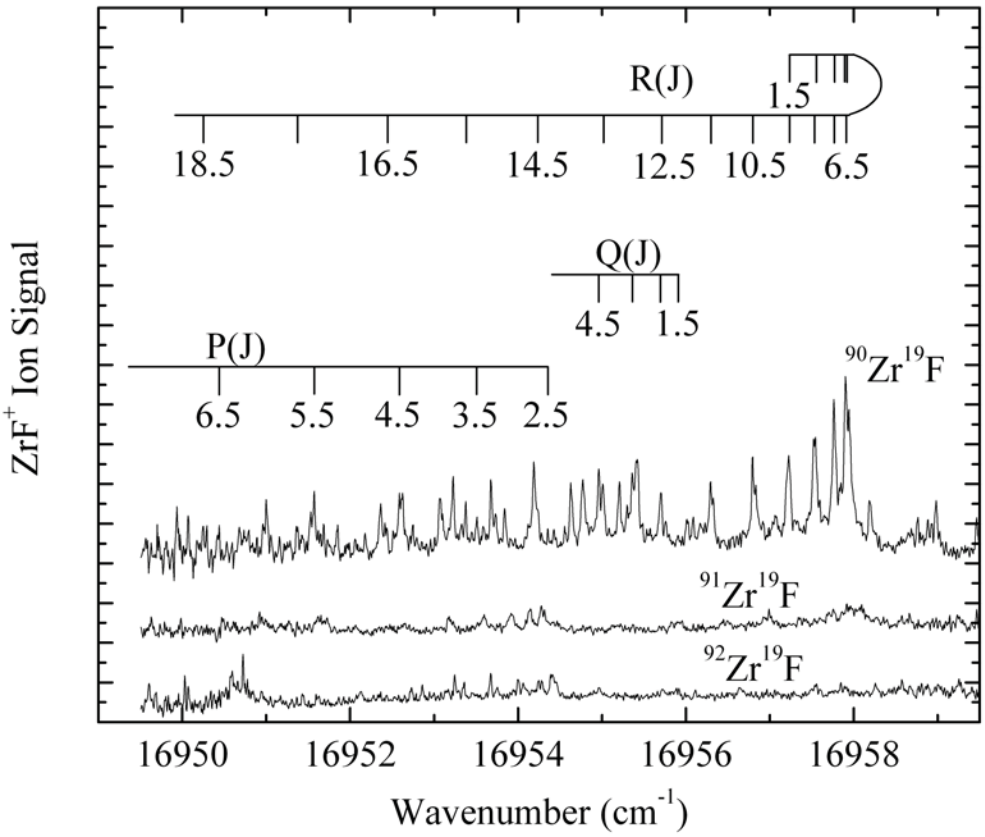

Figure B.30 Rotationally resolved spectra of the various ZrF isotopic modifications for the 7-0 band of the B – X system. Line assignments are provided for the higher wavenumber band that was identified in this spectral range for the $^{90}Zr^{19}F$ isotopic modification, which is the most abundant isotopomer.

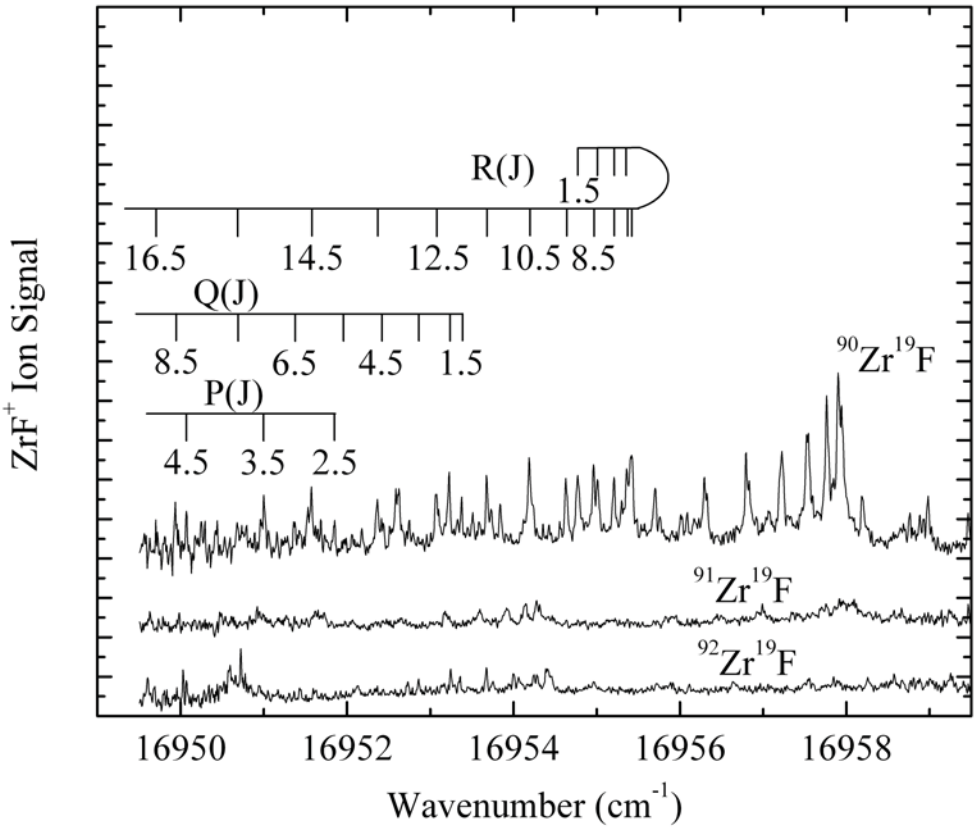

Figure B.31 Rotationally resolved spectra of the various ZrF isotopic modifications for the 7-0 band of the B – X system. Line assignments are provided for the lower wavenumber band that was identified in this spectral range for the $^{90}Zr^{19}F$ isotopic modification, which is the most abundant isotopomer.

Table B.17 Assigned Rotational Lines of the 7-0 Band of the B – X System of ZrF.[a]

Line	$^{90}Zr^{19}F$ (band B)	$^{90}Zr^{19}F$ (band A)	$^{91}Zr^{19}F$	$^{92}Zr^{19}F$
P(2.5)	16951.848(10)			
P(3.5)	16951.004(3)	16953.510(5)		16950.031(10)
P(4.5)	16950.070(-5)	16952.586(-9)		
P(5.5)		16951.573(-24)		
P(6.5)		16950.439(-7)		
Q(1.5)	16953.377(39)			16952.432(8)
Q(2.5)	16953.226(-39)	16955.702(-8)	16952.063(-5)	
Q(3.5)	16952.852(16)	16955.361(19)	16951.726(21)	
Q(4.5)	16952.436(22)	16954.961(14)	16951.368(-23)	
Q(6.5)	16951.364(-2)			
Q(7.5)	16950.682(-4)			
Q(8.5)	16949.936(-34)			
R(1.5)	16954.770(-26)	16957.235(16)	16953.597(16)	16953.754(11)
R(2.5)	16955.010(38)	16957.540(19)	16953.921(2)	16954.064(5)
R(3.5)		16957.763(14)	16954.151(-7)	16954.284(-2)
R(4.5)	16955.361(20)	16957.941(2)	16954.278(-3)	16954.410(-4)
R(5.5)	16955.415(-5)	16957.941(3)	16954.313(4)	16954.451(-12)
R(6.5)	16955.361(-12)	16957.904(-12)	16954.278(-8)	16954.389(-8)
R(7.5)	16955.208(-12)	16957.763(-13)	16954.133(1)	16954.244(-11)
R(8.5)	16954.961(-9)	16957.523(-5)	16953.921(-11)	16954.002(-8)
R(9.5)	16954.634(-17)	16957.202(-6)	16953.597(-2)	16953.676(-11)
R(10.5)	16954.189(1)	16956.794(-9)	16953.179(13)	16953.245(0)
R(11.5)	16953.679(-6)	16956.294(-11)		16952.730(5)
R(12.5)	16953.070(-6)	16955.702(-11)		16952.126(10)
R(13.5)	16952.360(3)	16955.010(0)		16951.432(12)
R(14.5)	16951.573(-1)	16954.234(5)		16950.660(3)
R(15.5)	16950.682(7)	16953.377(0)		16949.800(-9)
R(16.5)	16949.698(18)	16952.436(-10)		
R(17.5)		16951.364(20)		
R(18.5)		16950.247(6)		

Table B.17 Continued

Fitted spectroscopic constants[b]				
Constant	$^{90}Zr^{19}F$	$^{91}Zr^{19}F$	$^{91}Zr^{19}F$	$^{92}Zr^{19}F$
ν_0 (cm^{-1})	16953.5862(55)	16956.0881(34)	16952.4488(54)	16952.6086(33)
B' (cm^{-1})	0.26577(4)	0.26641(2)	0.26629(8)	0.26513(2)
r' (Å)				
B_0'' (cm^{-1})	0.31139 (FIXED)	0.31139 (FIXED)	0.31086 (FIXED)	0.31139 (FIXED)

[a] For these bands, lines have been identified using combination differences involving the ground state rotational constant, which is known from studies of the other bands. Although the quality of the rotational fits are good, the assignment is not considered as secure as in the other bands that were investigated. Therefore, it was decided to exclude these bands from the overall fit that determined B''. Nevertheless, the bands of $^{90}Zr^{19}F$ (two bands), $^{91}Zr^{19}F$, and $^{92}Zr^{19}F$, could be fitted to extract spectroscopic constants. In this process, the ground state rotational constant was held fixed at the value determined from studies of the other bands. Residuals, ν(calculated) – ν(measured), are given in parentheses following each line position, in units of 0.001 cm^{-1}.

[b] Error limits (1σ) are provided for spectroscopic constants, in units of the last digit quoted. B_0'' was constrained to the value determined from the fits of the A – X 3-0 and 4-0 bands, the C – X 4-0 band, and one (*e/f*) component of the C – X 6-0 band.

Table B.18 Numerical Hartree-Fock Radial Wavefunctions, $rR_{n\ell}(r)$, and Calculated Ligand-Field Parameters for Zr^+ $4d^15s^2$, ^2D_g and Zr^+ $4d^25s^1$, ^4F_g.

r (bohr)	$4d^15s^2$, ^2D_g term		$4d^25s^1$, ^4F_g term	
	$rR_{5s}(r)$	$rR_{4d}(r)$	$rR_{5s}(r)$	$rR_{4d}(r)$
0.00000	0.000000	0.000000	0.000000	0.000000
0.00046	0.003664	0.000000	0.003505	0.000000
0.00049	0.003896	0.000000	0.003726	0.000000
0.00052	0.004142	0.000000	0.003961	0.000000
0.00055	0.004403	0.000000	0.004211	0.000000
0.00059	0.004681	0.000000	0.004476	0.000000
0.00063	0.004975	0.000000	0.004758	0.000000
0.00067	0.005287	0.000000	0.005057	0.000000
0.00071	0.005619	0.000000	0.005373	0.000000
0.00075	0.005970	0.000000	0.005709	0.000000
0.00080	0.006342	0.000000	0.006066	0.000000
0.00086	0.006737	0.000000	0.006443	0.000000
0.00091	0.007156	0.000000	0.006844	0.000000
0.00097	0.007599	0.000000	0.007268	0.000000
0.00103	0.008069	0.000000	0.007717	0.000000
0.00110	0.008566	0.000000	0.008193	0.000000
0.00117	0.009093	0.000001	0.008696	0.000001
0.00124	0.009650	0.000001	0.009229	0.000001
0.00132	0.010239	0.000001	0.009792	0.000001
0.00141	0.010861	0.000001	0.010387	0.000001
0.00150	0.011519	0.000001	0.011016	0.000001
0.00160	0.012214	0.000001	0.011681	0.000001
0.00170	0.012947	0.000002	0.012382	0.000002
0.00181	0.013721	0.000002	0.013122	0.000002
0.00193	0.014536	0.000002	0.013902	0.000002
0.00205	0.015395	0.000003	0.014723	0.000003
0.00218	0.016300	0.000004	0.015588	0.000003
0.00233	0.017251	0.000004	0.016498	0.000004
0.00248	0.018251	0.000005	0.017455	0.000005
0.00263	0.019301	0.000006	0.018459	0.000006
0.00280	0.020403	0.000008	0.019512	0.000007
0.00299	0.021557	0.000009	0.020616	0.000008
0.00318	0.022765	0.000011	0.021772	0.000010
0.00338	0.024028	0.000013	0.022980	0.000012
0.00360	0.025347	0.000016	0.024241	0.000015
0.00383	0.026722	0.000019	0.025556	0.000018
0.00408	0.028153	0.000023	0.026925	0.000021
0.00434	0.029640	0.000027	0.028347	0.000026
0.00462	0.031182	0.000033	0.029822	0.000031

Table B.18 Continued

r (bohr)	$4d^{1}5s^{2}$, $^{2}D_g$ term		$4d^{2}5s^{1}$, $^{4}F_g$ term	
	$rR_{5s}(r)$	$rR_{4d}(r)$	$rR_{5s}(r)$	$rR_{4d}(r)$
0.00492	0.032779	0.000040	0.031348	0.000037
0.00524	0.034427	0.000048	0.032924	0.000044
0.00558	0.036124	0.000057	0.034548	0.000053
0.00594	0.037868	0.000069	0.036216	0.000064
0.00632	0.039654	0.000082	0.037923	0.000077
0.00673	0.041476	0.000099	0.039666	0.000092
0.00716	0.043328	0.000118	0.041438	0.000110
0.00762	0.045203	0.000142	0.043231	0.000132
0.00812	0.047092	0.000170	0.045037	0.000158
0.00864	0.048984	0.000204	0.046846	0.000190
0.00920	0.050866	0.000244	0.048646	0.000227
0.00979	0.052725	0.000292	0.050424	0.000272
0.01042	0.054545	0.000350	0.052164	0.000325
0.01109	0.056307	0.000418	0.053850	0.000389
0.01181	0.057991	0.000500	0.055461	0.000465
0.01257	0.059575	0.000597	0.056975	0.000555
0.01338	0.061032	0.000712	0.058369	0.000663
0.01424	0.062336	0.000850	0.059616	0.000791
0.01516	0.063455	0.001013	0.060686	0.000943
0.01614	0.064357	0.001206	0.061549	0.001123
0.01718	0.065005	0.001436	0.062169	0.001336
0.01829	0.065362	0.001707	0.062510	0.001589
0.01947	0.065386	0.002028	0.062534	0.001888
0.02073	0.065036	0.002408	0.062199	0.002241
0.02206	0.064268	0.002855	0.061464	0.002657
0.02349	0.063035	0.003382	0.060286	0.003148
0.02500	0.061292	0.004002	0.058619	0.003725
0.02661	0.058995	0.004730	0.056423	0.004403
0.02833	0.056099	0.005584	0.053653	0.005197
0.03016	0.052564	0.006583	0.050273	0.006126
0.03210	0.048352	0.007749	0.046246	0.007212
0.03417	0.043434	0.009109	0.041542	0.008477
0.03637	0.037785	0.010690	0.036141	0.009949
0.03872	0.031393	0.012525	0.030028	0.011657
0.04122	0.024256	0.014650	0.023203	0.013635
0.04388	0.016388	0.017103	0.015679	0.015918
0.04671	0.007819	0.019928	0.007484	0.018547
0.04972	-0.001401	0.023172	-0.001332	0.021566

Table B.18 Continued

r (bohr)	$4d^{1}5s^{2}$, $^{2}D_g$ term		$4d^{2}5s^{1}$, $^{4}F_g$ term	
	$rR_{5s}(r)$	$rR_{4d}(r)$	$rR_{5s}(r)$	$rR_{4d}(r)$
0.05293	-0.011198	0.026884	-0.010701	0.025021
0.05634	-0.021474	0.031119	-0.020529	0.028963
0.05997	-0.032106	0.035933	-0.030696	0.033444
0.06384	-0.042940	0.041385	-0.041057	0.038519
0.06796	-0.053793	0.047535	-0.051437	0.044243
0.07234	-0.064453	0.054442	-0.061633	0.050672
0.07701	-0.074678	0.062164	-0.071413	0.057860
0.08197	-0.084202	0.070755	-0.080523	0.065856
0.08726	-0.092734	0.080262	-0.088685	0.074706
0.09289	-0.099966	0.090724	-0.095605	0.084446
0.09888	-0.105582	0.102167	-0.100980	0.095099
0.10525	-0.109264	0.114602	-0.104506	0.106675
0.11204	-0.110706	0.128017	-0.105891	0.119165
0.11927	-0.109626	0.142378	-0.104866	0.132537
0.12696	-0.105781	0.157621	-0.101198	0.146732
0.13515	-0.098983	0.173650	-0.094707	0.161659
0.14387	-0.089119	0.190327	-0.085284	0.177193
0.15314	-0.076160	0.207475	-0.072903	0.193168
0.16302	-0.060186	0.224871	-0.057639	0.209377
0.17353	-0.041395	0.242241	-0.039681	0.225567
0.18473	-0.020115	0.259264	-0.019341	0.241439
0.19664	0.003191	0.275568	0.002938	0.256649
0.20932	0.027922	0.290738	0.026583	0.270810
0.22282	0.053347	0.304314	0.050897	0.283496
0.23719	0.078621	0.315804	0.075073	0.294251
0.25249	0.102805	0.324691	0.098214	0.302594
0.26878	0.124898	0.330449	0.119367	0.308036
0.28611	0.143879	0.332553	0.137555	0.310091
0.30456	0.158748	0.330501	0.151825	0.308291
0.32420	0.168578	0.323826	0.161292	0.302202
0.34511	0.172565	0.312114	0.165189	0.291440
0.36737	0.170080	0.295023	0.162912	0.275686
0.39107	0.160708	0.272293	0.154066	0.254696
0.41629	0.144291	0.243765	0.138496	0.228319
0.44314	0.120954	0.209384	0.116318	0.196502
0.47172	0.091124	0.169215	0.087935	0.159300
0.50214	0.055533	0.123447	0.054038	0.116882
0.53452	0.015215	0.072400	0.015604	0.069536

Table B.18 Continued

r (bohr)	$4d^{1}5s^{2}$, $^{2}D_g$ term		$4d^{2}5s^{1}$, $^{4}F_g$ term	
	$rR_{5s}(r)$	$rR_{4d}(r)$	$rR_{5s}(r)$	$rR_{4d}(r)$
0.56900	-0.028518	0.016530	-0.026127	0.017677
0.60569	-0.074107	-0.043566	-0.069681	-0.038156
0.64476	-0.119797	-0.107152	-0.113398	-0.097295
0.68634	-0.163691	-0.173353	-0.155487	-0.158948
0.73061	-0.203833	-0.241167	-0.194100	-0.222206
0.77773	-0.238286	-0.309476	-0.227408	-0.286058
0.82789	-0.265227	-0.377077	-0.253688	-0.349415
0.88128	-0.283040	-0.442709	-0.271413	-0.411138
0.93812	-0.290408	-0.505096	-0.279333	-0.470077
0.99862	-0.286386	-0.562992	-0.276549	-0.525108
1.06303	-0.270461	-0.615225	-0.262566	-0.575182
1.13159	-0.242591	-0.660750	-0.237322	-0.619363
1.20457	-0.203206	-0.698680	-0.201194	-0.656863
1.28226	-0.153196	-0.728322	-0.154982	-0.687069
1.36495	-0.093868	-0.749199	-0.099864	-0.709560
1.45299	-0.026887	-0.761057	-0.037340	-0.724109
1.54670	0.045796	-0.763869	0.030837	-0.730687
1.64645	0.122023	-0.757830	0.102732	-0.729439
1.75264	0.199513	-0.743337	0.176302	-0.720677
1.86567	0.275943	-0.720980	0.249469	-0.704853
1.98600	0.349032	-0.691513	0.320180	-0.682540
2.11408	0.416619	-0.655835	0.386469	-0.654408
2.25043	0.476737	-0.614960	0.446518	-0.621208
2.39557	0.527688	-0.569986	0.498701	-0.583752
2.55007	0.568104	-0.522064	0.541643	-0.542895
2.71453	0.597002	-0.472358	0.574260	-0.499522
2.88961	0.613824	-0.422012	0.595806	-0.454524
3.07597	0.618456	-0.372111	0.605906	-0.408790
3.27435	0.611238	-0.323645	0.604577	-0.363179
3.48553	0.592938	-0.277484	0.592240	-0.318507
3.71033	0.564718	-0.234351	0.569713	-0.275522
3.94962	0.528073	-0.194807	0.538176	-0.234885
4.20435	0.484749	-0.159241	0.499125	-0.197154
4.47551	0.436658	-0.127875	0.454295	-0.162762
4.76416	0.385778	-0.100764	0.405576	-0.132010
5.07142	0.334046	-0.077820	0.354903	-0.105062
5.39850	0.283260	-0.058824	0.304155	-0.081939
5.74667	0.234994	-0.043459	0.255044	-0.062538

Table B.18 Continued

r (bohr)	$4d^1 5s^2$, ^2D_g term		$4d^2 5s^1$, ^4F_g term	
	$rR_{5s}(r)$	$rR_{4d}(r)$	$rR_{5s}(r)$	$rR_{4d}(r)$
6.11730	0.190522	-0.031331	0.209031	-0.046640
6.51183	0.150772	-0.022005	0.167251	-0.033934
6.93181	0.116307	-0.015029	0.130475	-0.024046
7.37887	0.087329	-0.009963	0.099100	-0.016565
7.85477	0.063724	-0.006398	0.073173	-0.011073
8.36136	0.045112	-0.003971	0.052436	-0.007167
8.90062	0.030927	-0.002376	0.036404	-0.004483
9.47466	0.020492	-0.001368	0.024439	-0.002703
10.08572	0.013095	-0.000756	0.015832	-0.001567
10.73619	0.008053	-0.000400	0.009876	-0.000872
11.42862	0.004754	-0.000202	0.005918	-0.000464
12.16570	0.002688	-0.000097	0.003398	-0.000235
12.95032	0.001451	-0.000044	0.001865	-0.000114
13.78554	0.000746	-0.000019	0.000975	-0.000052
14.67464	0.000364	-0.000008	0.000484	-0.000022
15.62107	0.000168	-0.000003	0.000228	-0.000009
16.62854	0.000073	-0.000001	0.000101	-0.000003
17.70099	0.000030	0.000000	0.000042	-0.000001
18.84261	0.000011	0.000000	0.000017	0.000000
20.05785	0.000004	0.000000	0.000006	0.000000
21.35147	0.000001	0.000000	0.000002	0.000000
22.72852	0.000000	0.000000	0.000001	0.000000
24.19438	0.000000	0.000000	0.000000	0.000000
25.75479	0.000000	0.000000	0.000000	0.000000
27.41583	0.000000	0.000000	0.000000	0.000000
29.18400	0.000000	0.000000	0.000000	0.000000
31.06620	0.000000	0.000000	0.000000	0.000000
33.06980	0.000000	0.000000	0.000000	0.000000
Calculated ligand field parameters, B_0^k (cm^{-1}):				
Parameter	Calculated from $4d^1 5s^2$, ^2D_g term		Calculated from $4d^2 5s^1$, ^4F_g term	
	ZrF	ZrCl	ZrF	ZrCl
B_0^0 (5s)	56864	49102	56135	48787
B_0^0 (4d)	62128	50780	61869	50715
B_0^2 (4d)	20325	11713	22093	13101
B_0^2 (4d, 5s)	-20543	-13520	-22276	-15217
B_0^4 (4d)	9990	4479	11612	5562

Table B.18 Continued				
Ligand field angular factors, C^{k}_{0} (nℓλ; nℓ′ λ):				
C^{0}_{0} (nℓλ; nℓλ)	1		C^{2}_{0} (4dσ; 5sσ)	1/√5
C^{2}_{0} (4dσ;4dσ)	2/7		C^{4}_{0} (4dσ; 4dσ)	2/7
C^{2}_{0} (4dπ; 4dπ)	1/7		C^{4}_{0} (4dπ; 4dπ)	-4/21
C^{2}_{0} (4dδ; 4dδ)	-2/7		C^{4}_{0} (4dδ; 4dδ)	1/21

APPENDIX C

PdSi SPECTRA, LINE POSITIONS, AND SPECTROSCOPIC CONSTANTS

C.1 Vibronically Resolved Spectra of PdSi

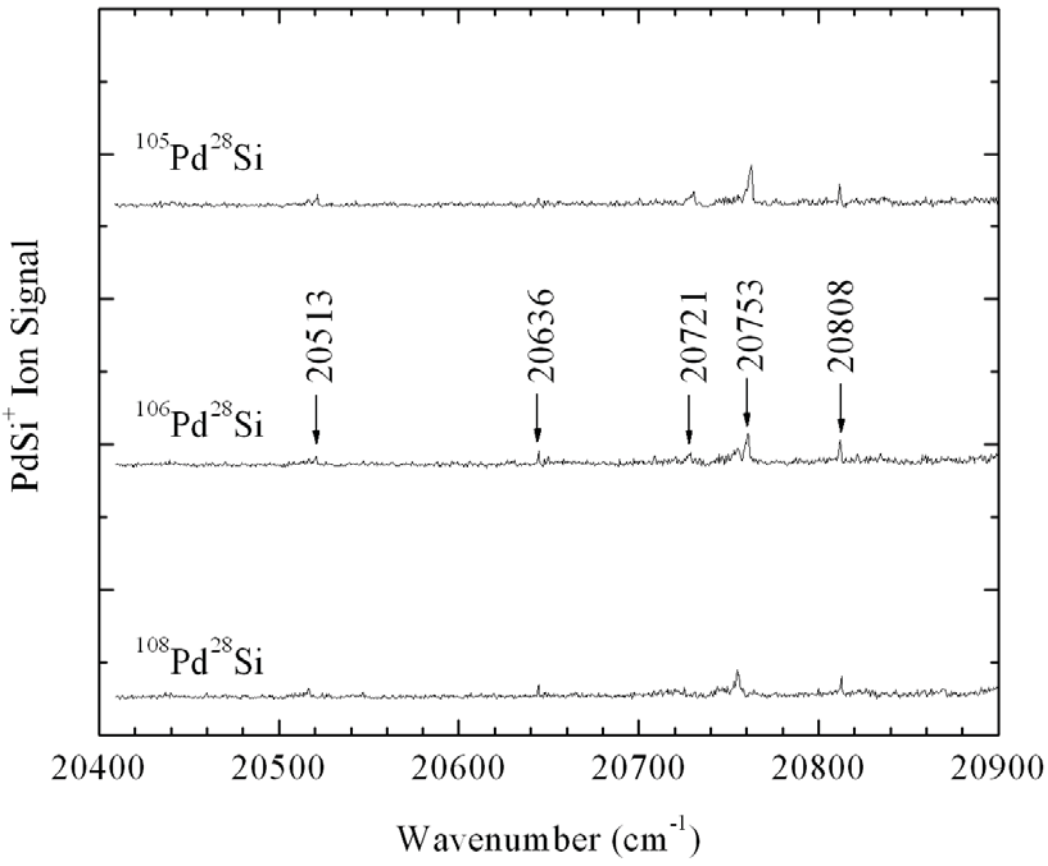

Figure C.1 Vibronic spectra of $^{105}Pd^{28}Si$, $^{106}Pd^{28}Si$, and $^{108}Pd^{28}Si$ over the 20400 – 20900 cm^{-1} range.

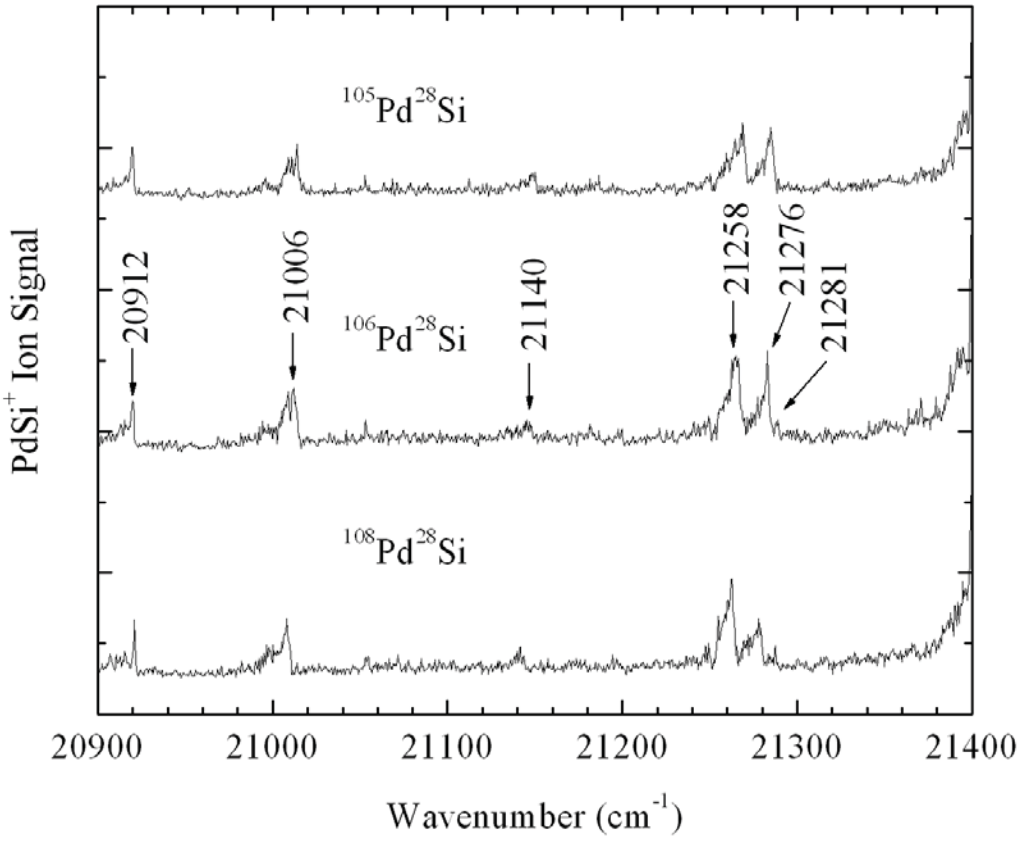

Figure C.2 Vibronic spectra of $^{105}Pd^{28}Si$, $^{106}Pd^{28}Si$, and $^{108}Pd^{28}Si$ over the 20900 – 21400 cm^{-1} range.

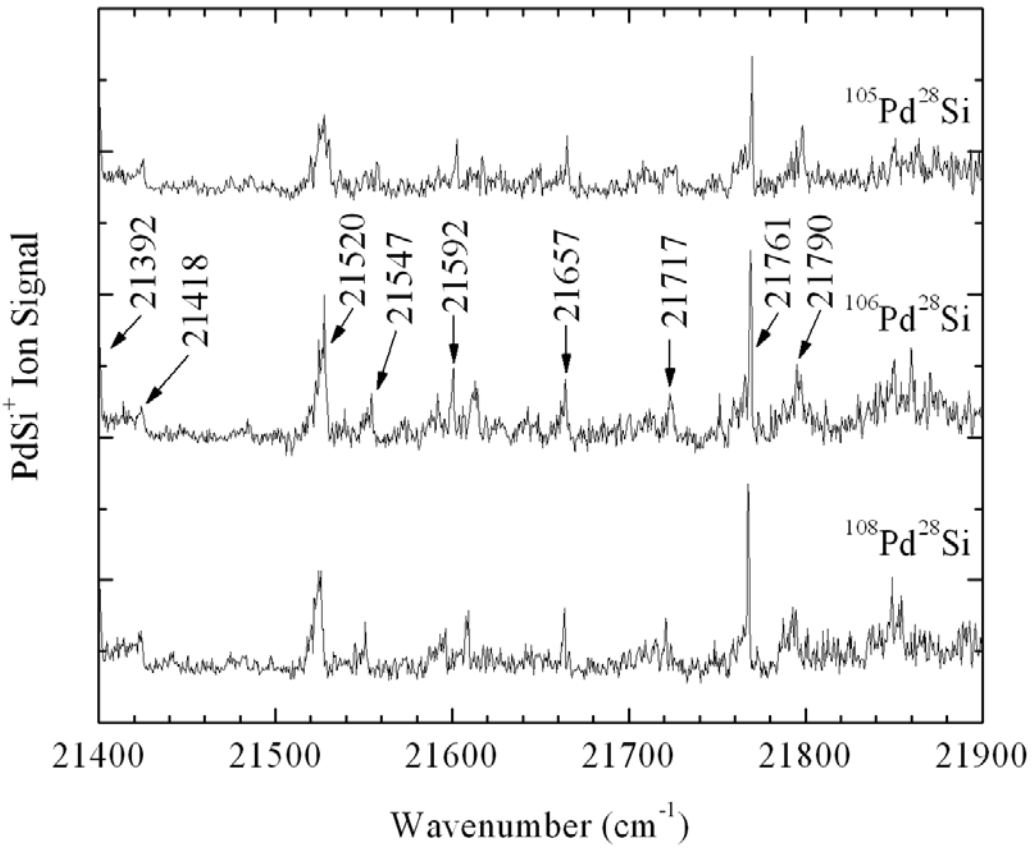

Figure C.3 Vibronic spectra of $^{105}Pd^{28}Si$, $^{106}Pd^{28}Si$, and $^{108}Pd^{28}Si$ over the 21400 – 21900 cm^{-1} range.

Table C.1 Vibronic Band Heads of $^{105}Pd^{28}Si$, $^{106}Pd^{28}Si$, and $^{108}Pd^{28}Si$, in Wavenumbers (cm^{-1}).

Band	$^{105}Pd^{28}Si$	$^{106}Pd^{28}Si$	$^{108}Pd^{28}Si$	Intensity
	21790.63	21789.82	21786.88	weak
$[21.4]0^{+}\leftarrow X^{1}\Sigma^{+}$ 1-0 band Rotationally resolved, perturbed	21762.00	21761.25	21759.89	strong
	21718.98	21717.22	21713.13	weak
	21657.24	21656.61	21655.6	weak
	21594.69	21592.71	21588.45	weak
	21550.63	21546.63	21543.16	very weak
	21522.74	21520.73	21517.88	strong
	21417.52	21417.69	21416.81	medium
$[21.4]0^{+}\leftarrow X^{1}\Sigma^{+}$ 0-0 band Rotationally resolved, perturbed	21393.08	21392.99	21393.02	very strong
	21281.46	21281.34	21281.08	very weak
Rotationally resolved	21278.50	21276.23	21271.69	strong
	21256.91	21257.76	21256.18	strong
	21142.54	21140.39	21136.02	weak
	21007.61	21005.92	21002.08	medium
	20912.18	20912.44	20913.29	medium
	20803.81	20804.13	20804.72	weak
	20754.75	20753.19	20747.87	weak
	20722.67	20721.07	20717.35	very weak
	20636.46	20636.45	20636.45	very weak
	20513.52	20512.65	20508.87	very weak

C.2 Rotationally Resolved Spectra

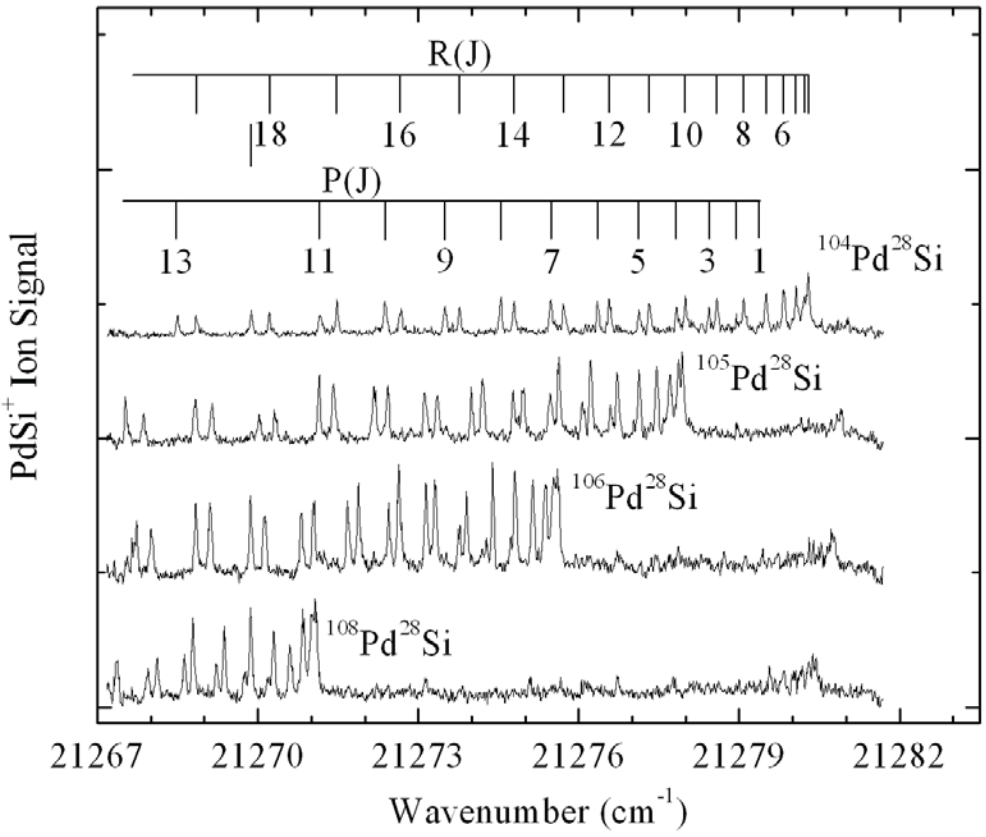

Figure C.4 Rotationally resolved spectra of the various PdSi isotopic modifications for the 21276 cm^{-1} band. Line assignments are provided for the $^{104}Pd^{28}Si$ isotopic modification.

Table C.2 Measured Line Positions and Fitted Parameters for the 21276 cm^{-1} Band of PdSi [a]

Line	$^{104}Pd^{28}Si$	$^{105}Pd^{28}Si$	$^{106}Pd^{28}Si$	$^{108}Pd^{28}Si$
P(1)	21279.395(0)	21277.031(3)	21274.727(-17)	21270.192(-7)
P(2)	21278.947(10)	21276.595(1)	21274.275(-1)	21269.758(-6)
P(3)	21278.434(-1)	21276.075(-1)	21273.763(-10)	21269.224(10)
P(4)	21277.829(-4)	21275.471(-5)	21273.145(2)	21268.630(1)
P(5)	21277.126(4)	21274.772(1)	21272.444(11)	21267.948(-4)
P(6)	21276.358(-8)	21273.999(-5)	21271.681(-2)	
P(7)	21275.479(5)	21273.123(7)	21270.809(9)	
P(8)	21274.540(-7)	21272.181(0)	21269.862(8)	
P(9)	21273.499(-2)	21271.145(1)	21268.837(2)	
P(10)	21272.380(-4)	21270.026(1)	21267.734(-12)	
P(11)	21271.164(4)	21268.827(-6)		
P(12)	21269.876(0)	21267.528(3)		
P(13)	21268.500(-2)			
R(0)	21280.003(13)			
R(1)	21280.189(9)			
R(2)	21280.293(1)	21277.935(-5)	21275.608(-3)	21271.069(3)
R(3)	21280.306(-1)	21277.935(6)	21275.608(8)	21271.069(14)
R(4)	21280.224(7)	21277.870(-4)	21275.531(11)	21271.011(-2)
R(5)	21280.063(8)	21277.704(3)	21275.377(6)	21270.849(1)
R(6)	21279.833(-7)	21277.456(6)	21275.146(-8)	21270.600(7)
R(7)	21279.503(-8)	21277.127(4)	21274.811(-2)	21270.296(-2)
R(8)	21279.082(-3)	21276.720(-4)	21274.393(2)	21269.868(-2)
R(9)	21278.583(-6)	21276.222(-8)	21273.904(-9)	21269.375(-6)
R(10)	21277.997(-7)	21275.628(0)	21273.313(-3)	21268.788(-2)
R(11)	21277.320(-2)	21274.961(-4)	21272.637(4)	21268.117(3)
R(12)	21276.569(-9)	21274.206(-6)	21271.878(8)	21267.363(6)
R(13)	21275.724(-8)	21273.349(9)	21271.043(3)	
R(14)	21274.792(-5)	21272.431(-1)	21270.125(-3)	
R(15)	21273.774(-1)	21271.410(7)	21269.110(2)	
R(16)	21272.667(6)	21270.318(2)	21268.020(-3)	
R(17)	21271.481(8)	21269.142(-6)		
R(18)	21270.213(4)	21267.868(0)		
R(19)	21268.858(4)			

Table C.2 Continued

Fitted parameters				
ν_0 (cm^{-1})	21279.7484(16)	21277.3858(13)	21275.0619(23)	21270.5340(29)
B_0'' (cm^{-1})	0.176401(74)	0.176033(64)	0.175582(134)	0.174402(353)
r_0'' (Å)	2.08220(44)	2.08226(38)	2.08287(80)	2.08585(211)
B' (cm^{-1})	0.133681(66)	0.133381(57)	0.133049(116)	0.132098(292)
r' (Å)	2.39187(59)	2.39214(51)	2.39274(104)	2.39668(265)
χ^2	3.98E-05	2.32E-05	5.90E-05	6.65E-05

[a] Residuals in the fit are given in parentheses following each rotational line position, in units of 0.001 cm^{-1}. Uncertainties in the fitted parameters (1σ error limits) are provided in parentheses in units of the last digit in the number quoted.

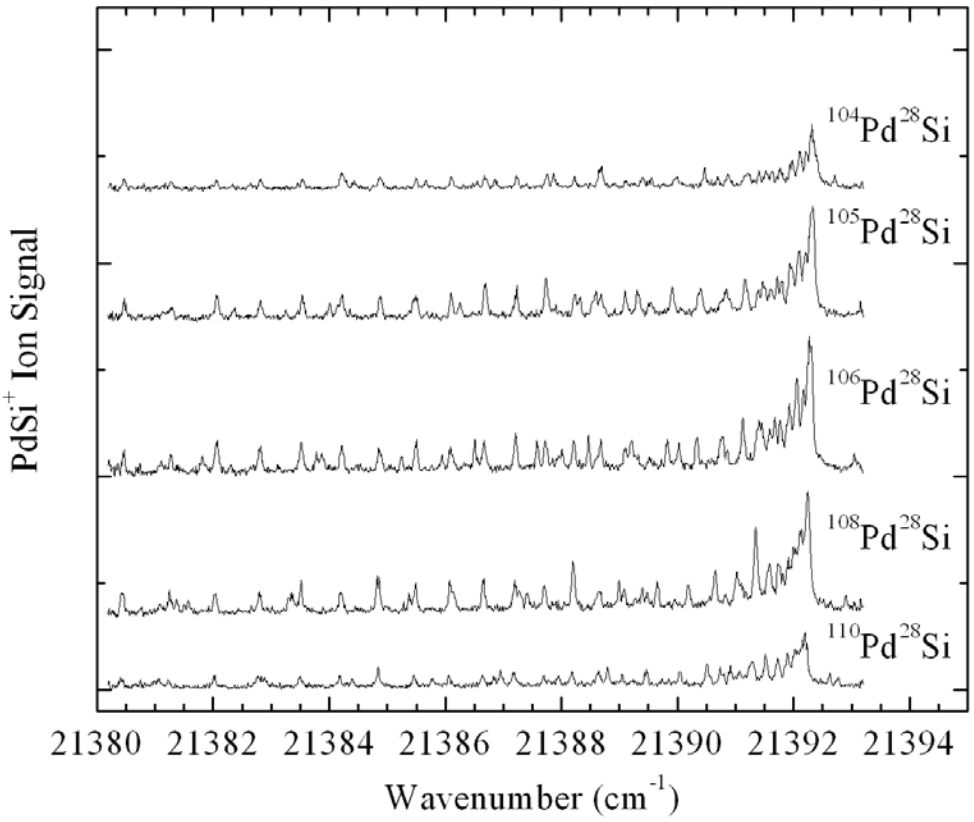

Figure C.5 Rotationally resolved spectra of the various PdSi isotopic modifications for the 21392 cm^{-1} 0-0 band of the $[21.4]0^+ \leftarrow X^1\Sigma^+$ band system. Extra lines are observed in all of the isotopomers, indicating that perturbations are present.

Table C.3 Deperturbation of the 21392 cm^{-1} Band for the $^{108}Pd^{28}Si$ Isotopomer.[a]

J′	Upper/lower level of the interacting pair	E(J′) from P(J′+1) (cm^{-1})	E(J′) from R(J′-1) (cm^{-1})	E(J′) averaged (cm^{-1})
0	Lower	21390.2118		21390.2118(24)
1	Lower	21390.5290		21390.5290(-29)
2	Lower	21391.1787	21391.1773	21391.1780(11)
3	Lower	21392.1413	21392.1430	21392.1421(-23)
4	Lower	21393.4464	21393.4408	21393.4436(94)
5	Lower	21395.0453	21395.0470	21395.0461(1)
6	Lower	21396.9825	21396.9777	21396.9801(3)
7	Lower	21399.2319	21399.2469	21399.2394(43)
8	Lower	21401.8058	21401.8179	21401.8118(1)
9	Lower	21404.7013	21404.7131	21404.7072(-18)
10	Lower	21407.9014	21407.9297	21407.9155(-109)
11	Lower	21411.4558	21411.4582	21411.4570(-64)
12	Lower	21415.3127	21415.3197	21415.3162(-27)
13	Lower	21419.4911	21419.4944	21419.4927(8)
14	Lower	21423.9610	21423.9795	21423.9702(-108)
15	Lower	21428.7744	21428.7933	21428.7838(-5)
16	Lower	21433.8941	21433.9201	21433.9071(73)
17	Lower		21439.3328	21439.3328(84)
18	Lower		21445.0510	21445.0510(-33)
19	Lower		21451.0963	21451.0963(116)
20	Lower		21457.4071	21457.4071(-20)
21	Lower		21464.0198	21464.0198(11)
22	Lower		21470.8993	21470.8993(-30)
23	Lower		21478.0500	21478.0500(49)
24	Lower		21485.4297	21485.4297(13)
25	Lower		21493.0259	21493.0259(-42)
26	Lower		21500.8260	21500.8260(-1)
27	Lower		21508.7900	21508.7900(-43)
28	Lower		21516.9144	21516.9144(-47)
29	Lower		21525.2015	21525.2015(64)
19	Upper	21466.2729		21466.2729(7)
20	Upper	21471.7282		21471.7282(4)
21	Upper	21477.4862		21477.4862(-9)

Table C.3 Continued

Fitted parameters			
Fit omitting high J′ levels:			
ν_0 (cm^{-1})	21390.2131		
B′ (cm^{-1})	0.16110		
r′ (Å)	2.1703		
Full deperturbation:			
T_0^- (cm^{-1})	21391.3595		
B^- (cm^{-1})	0.16269	r^- (Å)	2.1596
T_0^+ (cm^{-1})	21414.0884		
B^+ (cm^{-1})	0.13180	r^+ (Å)	2.3994
H_{12} (cm^{-1})	5.241		

[a] Residuals in the full deperturbation fit are given in parentheses following the average value of E(J′), in units of 0.0001 cm^{-1}.

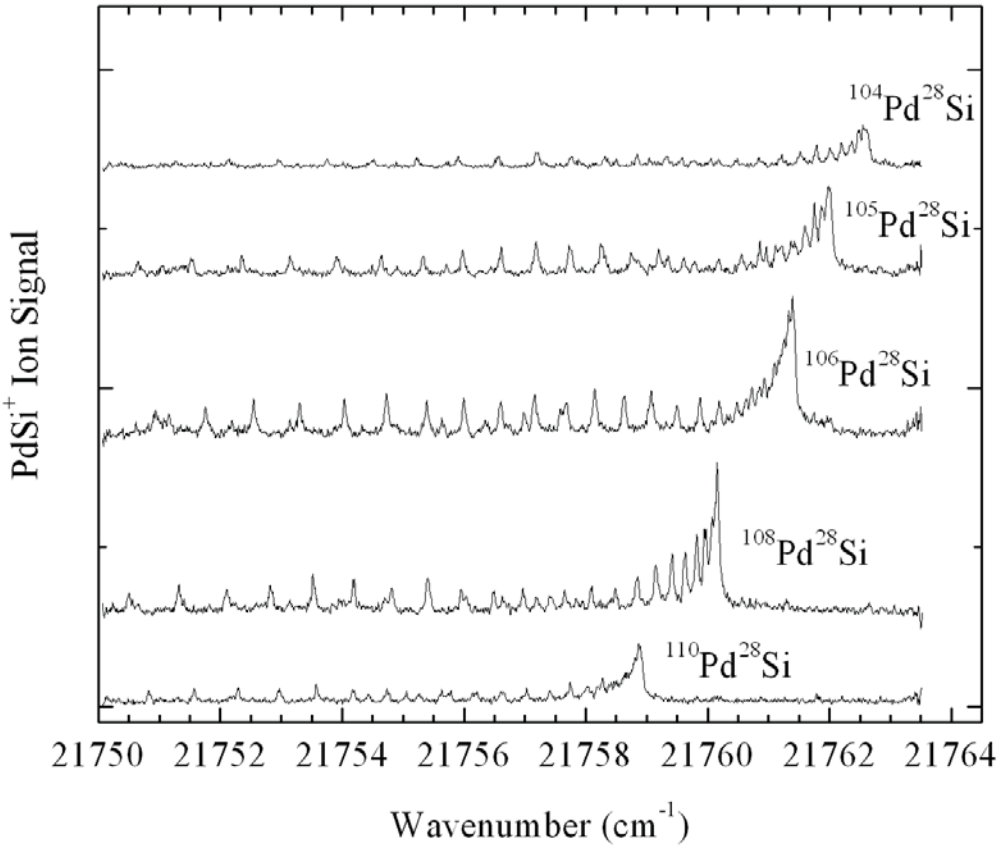

Figure C.6 Rotationally resolved spectra of the various PdSi isotopic modifications for the 21761 cm^{-1} 1-0 band of the $[21.4]0^{+} \leftarrow X^{1}\Sigma^{+}$ band system. Extra lines are observed in all of the isotopomers, indicating that perturbations are present.

Table C.4 Deperturbation of the 21761 cm^{-1} Band for the $^{108}Pd^{28}Si$ Isotopomer.[a]

J′	Upper/lower level of the interacting pair	E(J′) from P(J′+1) (cm^{-1})	E(J′) from R(J′-1) (cm^{-1})	E(J′) averaged (cm^{-1})
1	Lower	21758.8955	21758.8786	21758.8871(64)
2	Lower	21759.5168	21759.5116	21759.5142(26)
3	Lower	21760.4700	21760.4623	21760.4662(82)
4	Lower	21761.7247	21761.7134	21761.7191(-5)
5	Lower	21763.2941	21763.2937	21763.2939(-24)
6	Lower	21765.1915	21765.1859	21765.1887(8)
7	Lower	21767.3916	21767.3920	21767.3918(-23)
8	Lower	21769.9095	21769.9115	21769.9105(-42)
9	Lower	21772.7493	21772.7475	21772.7484(-8)
10	Lower	21775.8934	21775.8975	21775.8955(-19)
11	Lower	21779.3596	21779.3666	21779.3631(46)
12	Lower	21783.1201	21783.1340	21783.1271(-52)
13	Lower	21787.1908	21787.2254	21787.2081(-98)
14	Lower		21791.6143	21791.6143(-4)
15	Lower		21796.3260	21796.3260(39)
16	Lower		21801.3421	21801.3421(31)
17	Lower		21806.6563	21806.6563(-83)
18	Lower		21812.3002	21812.3002(25)
19	Lower		21818.2336	21818.2336(-36)
20	Lower		21824.4763	21824.4763(-54)
21	Lower		21831.0293	21831.0293(-5)
22	Lower		21837.9013	21837.9013(214)
23	Lower		21845.0245	21845.0245(-58)
24	Lower		21852.4751	21852.4751(-39)
25	Lower		21860.2283	21860.2283(41)
26	Lower		21868.2612	21868.2612(-24)
27	Lower		21876.5967	21876.5967(17)
28	Lower		21885.2142	21885.2142(-17)

Table C.4 Continued

Fitted parameters			
Fit omitting high J′ levels:			
ν_0 (cm^{-1})	21758.5796		
B′ (cm^{-1})	0.15733		
r′ (Å)	2.1961		
Full deperturbation:			
T_0^- (cm^{-1})	21764.1397		
B^- (cm^{-1})	0.16116	r^- (Å)	2.1698
T_0^+ (cm^{-1})	21780.6331		
B^+ (cm^{-1})	0.14428	r^+ (Å)	2.2933
H_{12} (cm^{-1})	11.0915		

[a] Residuals in the full deperturbation fit are given in parentheses following the average value of E(J′), in units of 0.0001 cm^{-1}.